SPACE WEATHER EFFECTS ON THE SOUTH ATLANTIC ANOMALY AND THE LOW-EARTH ORBIT SATELLITES

キロロス, ミナ, ジョージ, ザキ, ギルギス

九州大学
KYUSHU UNIVERSITY

SPACE WEATHER EFFECTS ON THE SOUTH ATLANTIC ANOMALY AND THE LOW-EARTH ORBIT SATELLITES

Kirolosse Mina Georges Zaki GIRGIS

A DISSERTATION SUBMITTED TO
THE DEPARTMENT OF EARTH SYSTEM SCIENCE AND TECHNOLOGY
AND THE COMMITTEE OF
THE INTERDISCIPLINARY GRADUATE SCHOOL OF ENGINEERING SCIENCES
OF
KYUSHU UNIVERSITY
IN PARTIAL FULFILLMENT OF THE REQUIREMENTS FOR
THE DEGREE OF DOCTOR OF PHILOSOPHY

JAPAN
August, 2020

九州大学
KYUSHU UNIVERSITY

九州大学大学院博士課程
総合理工学府博士論文
博士（学 術）

南大西洋異常と地球低軌道衛星に対する宇宙天気の影響

キロロス　ミナ　ジョージ　ザキ　ギルギス
（大気海洋環境システム学専攻）
令和02年度

SPACE WEATHER EFFECTS ON THE SOUTH ATLANTIC ANOMALY AND THE LOW-EARTH ORBIT SATELLITES

Approved by:

Prof. Tohru Hada, chair
Department of Advanced Environmental Science and Engineering
Faculty of Engineering Sciences
Kyushu University

Assoc. Prof. Shuichi Matsukiyo
Department of Advanced Environmental Science and Engineering
Faculty of Engineering Sciences
Kyushu University

Assoc. Prof. Akimasa Yoshikawa
Department of Earth and Planetary Sciences
Faculty of Sciences
Kyushu University

南大西洋異常と地球低軌道衛星に対する宇宙天気の影響

論文調査委員

教授 羽田 亨 （主査）
九州大学大学院総合理工学研究院
環境理工学部門

准教授 松清 修一 （副査）
九州大学大学院総合理工学研究院
環境理工学部門

准教授 吉川 顕正 （副査）
九州大学大学院理学研究院
地球惑星科学部門

Abstract

Since the beginning of the last century, humankind is continuously racing toward building, developing, and launching satellites to explore the space, starting from the near-Earth space environment to the most distant celestial objects. Daily, new insights are discovered and knowledge about space is growing. It is now well-understood that space is not a vacuum, but it is filled with a plasma, a high-temperature gas that conducts electricity. In particular, highly energetic plasma is trapped by the magnetic field near the Earth, forming the radiation belts (a.k.a. the Van Allen belts). Spacecraft operations in these regions could easily be subjected to harmful situations.

This thesis focuses on the energetic protons in the inner trapped radiation belt. One of the main aspects of the inner radiation belt is the South Atlantic Anomaly (SAA), a region with significant reduced geomagnetic field intensity. Near the SAA, the inner radiation belt is close to the Earth's surface so that the energetic protons can precipitate inside the anomaly as they do in cavities. Thus, this region imposes an additional dangerous radiation source on the Low-Earth Orbit (LEO) spacecraft missions.

The radiation belts are not stationary, but they behave dynamically in response to variations of the space weather conditions. In this work, the numerical approach was considered by developing test particle simulation codes to compute the particle trajectories. The magnetic field models implemented are the combination of the internal (primary) magnetic field model, IGRF-V12, and the external (disturbed) magnetic field model, the Tsyganenko model series. In addition to the magnetic field, the inductive electric field is included in the simulations by direct numerical integration of the Biot-Savart law. The obtained numerical results were compared with satellite observations.

The thesis is organized as follows: In the first chapter, basic concepts on the South Atlantic Anomaly are explained, such as how it is formed and its anomaly effects. In Chapter 2, the numerical methods used are described, and the definitions of some useful parameters are introduced. The essential methods are the implementation of the magnetic field models, the electric field models, and the test particle simulation models. Chapter 3 discusses the long-term variations of the SAA's magnetic response to the solar wind dynamic pressure and the Interplanetary Magnetic Field (IMF) for 11 years. We implement the Tsyganenko model (T96) to study the variations of the SAA center movement, the SAA area, and the minimum magnetic field inside the SAA. Chapter 4 analyzes the medium-term changes of the SAA magnetic response to solar wind dynamic pressure, IMF conditions, Dst index, and geodipole tilting angle by implementing the Tsyganenko models T96, T01 and TS05. In Chapter 5, we calculate the proton trajectories in the realistic magnetic field to determine the proton flux inside the SAA. We also study the effect of the geodipole tilting angle and the geomagnetic storm effects on the proton flux response inside the anomaly and compare the numerical results with spacecraft observations. Chapter 6 extends our test particle simulation model to cover the main phases of a selected geomagnetic storm using the guiding center approximation model (Tao-Chan-Brizard model) to compute the proton trajectories in the realistic magnetic model. Comparisons are made between the runs with and without the electric field to discuss the roles of the inductive electric field. In Chapter 7, we calculate the radiation environment of the SAA on the LEO spacecraft missions. According to the proton flux obtained from the numerical simulations, we can estimate the absorbed radiation dose rates and the Single Event Upset (SEU) rates.

The main results obtained are as follows: First, the geodipole tilting angle and the Dst index are the most influencing parameters on the magnetic field variations inside the SAA, and the magnetic variations in the SAA could be driven by the magnetic poles with respect to space weather conditions. Second, we elucidate the basic features of the proton flux anomaly using the test particle simulations. For a small geodipole tilting angle, the proton flux was increased in the SAA. Furthermore, the electric field effect on the inner proton belt is significant, and hence, on the proton flux response in the SAA as well. Finally, it is found that the proton flux variations inside the SAA are directly influencing and proportionally changing the radiation environment of a selected LEO spacecraft mission. Thus, the proton flux increase in the SAA leads to an increase in the Single Event Upset (SEU) and absorbed radiation dose rates.

Acknowledgements

First and foremost I would like to thank my supervisor Prof. Tohru Hada. It is my honor to be his doctorate student. Professor Hada has taught me intensively space plasma physics science. I appreciate all his contributions of time, ideas, patience and encouragement in order to make my doctorate course experience productive and stimulating. I am also thankful for the excellent example he has provided as a successful famous physicist and great professor.

Second, I want to thank Assoc. Prof. Shuichi Matsukiyo for all his efforts to make succeeding my doctorate research. I learned a lot from him especially FORTRAN coding and MPI parallelization techniques to succeed developing the test particle simulation codes; it is always my pleasure to continue learning from a unique scientist and professor like him.

Third, I would like to express my special appreciation to Assoc. Prof. Akimasa Yoshikawa for his detailed and insightful comments. His profound evaluation of my doctoral research helped me greatly in preparing this final version of my thesis.

I would like also to thank Prof. Haruichi Washimi for his advice, ideas, suggestions and fruitful discussions. Prof. Washimi was always encouraging me to move on in my research, to contribute and to achieve success.

I would like to appreciate the efforts of Prof. Shinji Saito for his great and continuous support since the beginning of my doctorate course. Prof. Saito helped me diligently in running Tsyganenko models and in coding the test particle simulation programs precisely the guiding center theory formulation. Prof. Saito was always helpful and ready to offer his great support.

Lastly, I want to thank Prof. Öztürk Kaan for his great support and time for providing me detailed answers about guiding center theory and his valuable recommendations for implementing the numerical integrators.

Contents

List of Figures

List of Tables

List of Acronyms

Dst: Disturbance Storm-Time

HEO: Highly Elliptical Orbiting (spacecraft)

IGRF: International Geomagnetic Reference Field

IMF: Interplanetary Magnetic Field

ISS: International Space Station

L: L-shell, or Mcllwain L-parameter

LEO: Low Earth Orbit

NOAA: National Oceanic and Atmospheric Administration satellite (spacecraft)

R3DR2: Radiation risk radiometer-dosimeter (instrument)

Re: Earth Radius ($\approx$ 6371 km)

SAA: South Atlantic Anomaly

SEE: Single Event Effect

SEU: Single Event Upset

T79,T89,T96,T01,TS05: Tsyganenko models developed in 1979, 1989, 1996, 2001, 2005 respectively.

Chapter 1

Introduction

At the east-side of the Brazilian coast, a localized oval-shaped geographic zone is located, where the geomagnetic field strength is weak enough so that it is expanding at all altitudes, as shown in Figure 1.1. This decrease in the magnetic field strength attracts the particles from the inner radiation belt, and allows this donut-shaped Van Allen belt to approach to the Earth's surface, as illustrated in Figure 1.2; then, an intensive particle flux is created. Figure 1.3 is an adequate representation of the approach of the trapped proton radiation belt as computed by the AP8 model. Such unique phenomenon is well-known called, the South Atlantic Anomaly (SAA) [Heirtzler et al., 2002], a permanent feature of the geomagnetic field. As previously explained, this anomaly is considered as a combined cause-effect physical process. By turns, such particle density increase is greatly affecting the radiation environment in the Low-Earth Orbit (LEO) space missions for both, spacecraft and human operations (Figures 1.4 and 1.5).

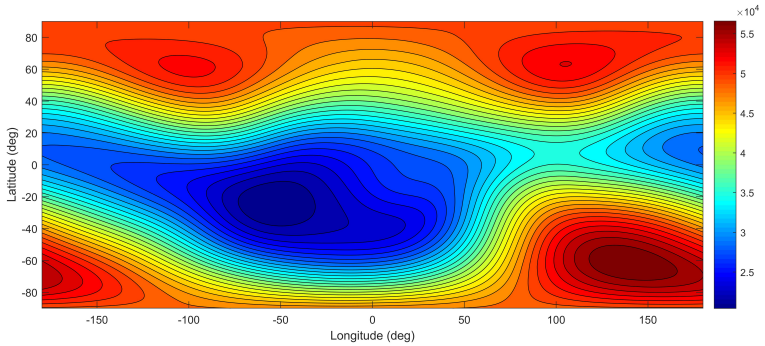

Figure 1.1: Earth's magnetic field intensity (in nT) at 800 km altitude computed by World Magnetic Field Model (WMM)

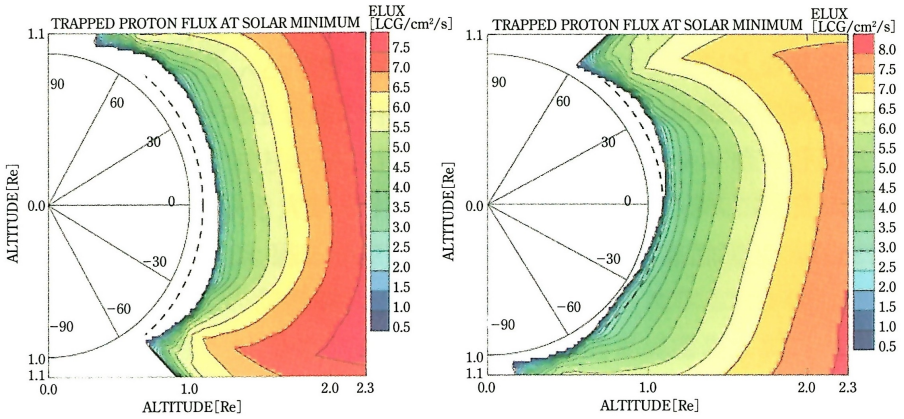

Figure 1.2: The two figures illustrate inner proton radiation belt fluxes calculated by AP8 trapped proton model at two different longitudinal positions: 315°(South America) and 135°(Japan) [Geo, 2010]

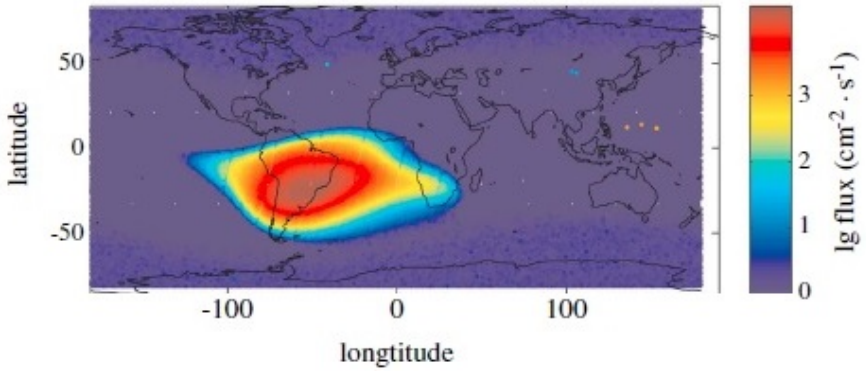

Figure 1.3: Distribution of SAA proton (> 10 MeV) fluxes during a geomagnetically quiet period in November 2009 measured by NOAA spacecraft [Qin et al., 2014]

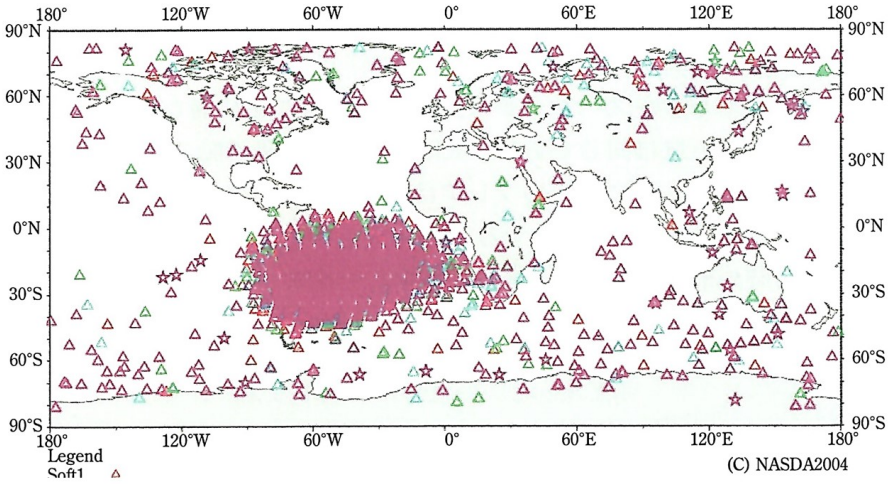

Figure 1.4: Single Event Effects (SEE) detected by International Space Station (ISS) [Geo, 2010]

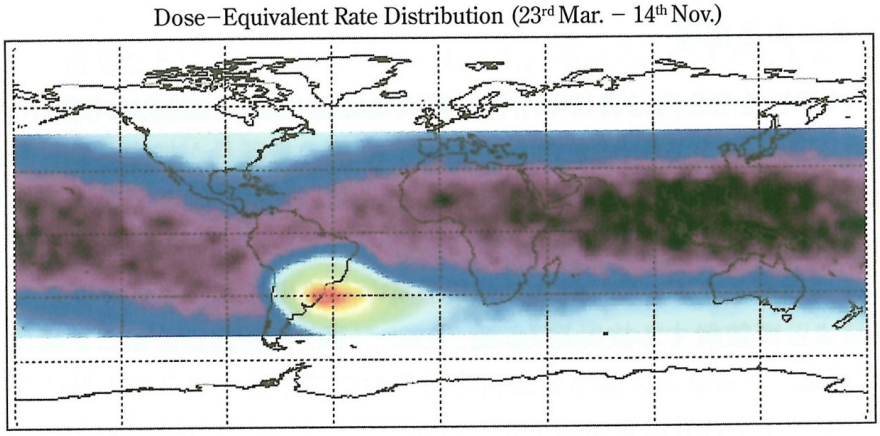

Figure 1.5: Radiation doses measured by International Space Station (ISS) [Geo, 2010]

Globally, we have three main modules which will be carried out during this research to investigate about the SAA physical processes: the SAA magnetic response, the SAA proton flux response and the radiation environment calculation. The three modules are strictly connected together. The section 1.3 demonstrates the recent efforts and the fruitful contributions that studied extensively the SAA.

1.1 How is the SAA created ?

1.1.1 Old Theory

During the last century, the South Atlantic Anomaly was interpreted by tens of published work as a localized dominant non-dipole effect, which pushes the particles from the inner radiation belt to precipitate into the anomaly region.

The Dictionary of Geophysics, Astrophysics and Astronomy [Ridpath, 2012] defines the South Atlantic Anomaly (SAA) as:

> *"A region within the inner Van Allen Belt, which reached its minimum altitude (250 km) over the Atlantic Ocean off the coast of Brazil. This positioning arises because of the offset between Earth's magnetic and geographical axes. Artificial satellites in low-inclination and low-altitude orbits pass frequently through the South Atlantic Anomaly, with a consequent risk to their electronic components (including degradation of solar cells) from energetic trapped particles . . . "*

Moreover, The Dictionary of Astronomy [Matzner, 2001] defines also the SAA as:

> *"The Van Allen belts are energetic particles trapped by the Earth's magnetic field. The offset between the Earth's geographical and magnetic axes leads to an asymmetry in the belt position, and the South Atlantic Anomaly is the resulting region of minimum altitude (about 250 km). Some of the quasi-trapped charged particles mainly electrons in the keV range from the radiation belts may dip to very low height at around 100 km in the Earth's atmosphere, where collisions with neutral particles can cause ionization and photochemical excitation. The anomaly extends as far as the coast of Africa. The South Atlantic Anomaly in this a region of energetic particles through which low-orbiting satellites frequently pass, and the radiation density can be harmful to electronics and to human crew . . . "*

The cause of the magnetic anomaly is the asymmetry of the geomagnetic field as discussed in many literature sources, e.g. [Clément, 2007]: (1) the tilt angle between the Earth's rotation axis and the magnetic axis ($\approx 11^{\circ}$) as shown by [Norberg, 2013], [Barratt and Pool, 2008] and [Messenger and Ash, 2013] and (2) the offset distance between the geographical center (= center of mass) and the geomagnetic center ($\approx$ 500 km), as reported by [Barratt and Pool, 2008], [Logsdon, 1998] and [Messenger and Ash, 2013]. This asymmetry in the geomagnetic field created a high intensity radiation region which can reach exceptionally low altitudes due to the low magnetic field strength [Scherer et al., 2005]. [Bone, 2007] determined that due to this offset, the inner radiation belt could penetrate to a minimum altitude of $\approx$ 250 km above the Atlantic Ocean near the Brazilian Coast.

The NASA technical report [NASA, 1967] illustrated this displacement feature as shown in Figure 1.6. Even if the inner trapped radiation belt is symmetrically distributed azimuthally, however, there is an exception to this at low altitudes. It is well known that the magnetic field of the Earth is approximately described by a dipole magnet at the Earth's center. The displacement and the tilting of the idealized dipole field from and with respect to the Earth's rotational axis. Due to this virtual dipole displacement, a portion of the inner radiation belt is getting closer to the surface of the Earth from one side. Furthermore, such anomaly is permanently located at the same region because the geomagnetic field is rotating with the Earth. Adding that, this radiation belt part can extend to the top of the atmosphere.

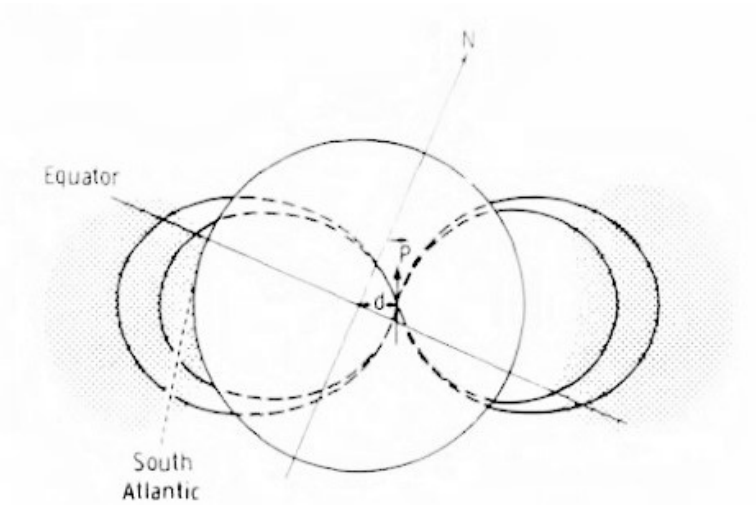

Figure 1.6: South Atlantic Anomaly (SAA) diagram

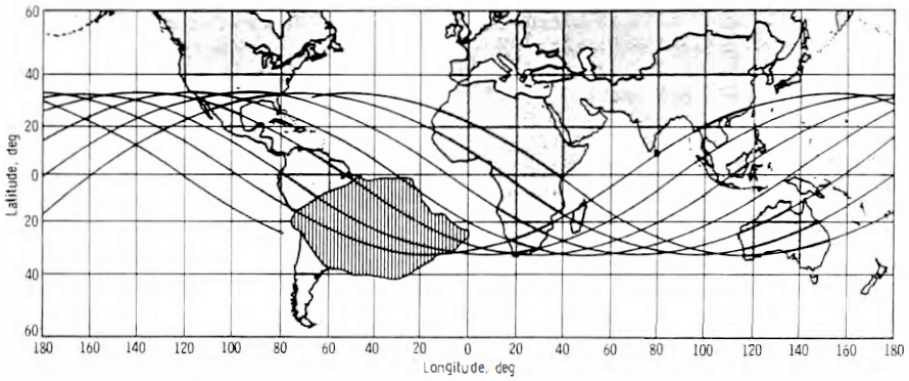

Figure 1.7: Location of radiation fluxes in the South Atlantic Anomaly for 160 nautical mile altitude, 28.5°orbital ground track.

Actually, a new understanding of the anomaly begins to be revealed: the fixed and imaginary bar magnet inside the Earth apparently passes not through the very center of our planet, theoretically because of an irregularity in its spinning, liquid, metal core [Chaisson, 1998]. A more detailed explanation about the non-dipole effect was discussed by [Rauschenbakh et al., 2006], who argued that the main influence comes from the significant contributions of the quadrupole ($n = 2$) and octupole ($n = 3$) terms as well as the higher order terms $(5, 4)$, $(6, 5)$ and $(4, 3)$ which are related with local, crustal and magnetic anomalies.

Thus, the internal magnetic field dynamics (core field) are newly understood to play a major role in interpreting the presence of the SAA, as shown in the next section.

1.1.2 New Theory

Recently, the SAA enigma was better resolved from another perspective. The anomaly at the surface is considered as the response of inverse flux patches at the Core-Mantle Boundary (CMB) of the radial component of the Earth's magnetic field, which is located approximately under the South Atlantic Ocean; such effect could generate the hemisphere asymmetry of the realistic Earth's magnetic field. As greatly explained by [A. Tarduno et al., 2015], the CMB under the South of Africa is identified by a reduced seismic wave anomaly which is called the African Large Low Shear Velocity Province (LLSVP). This feature is a very essential element to evaluate several tomograhic models as shown in Figures 1.8 and 1.9.

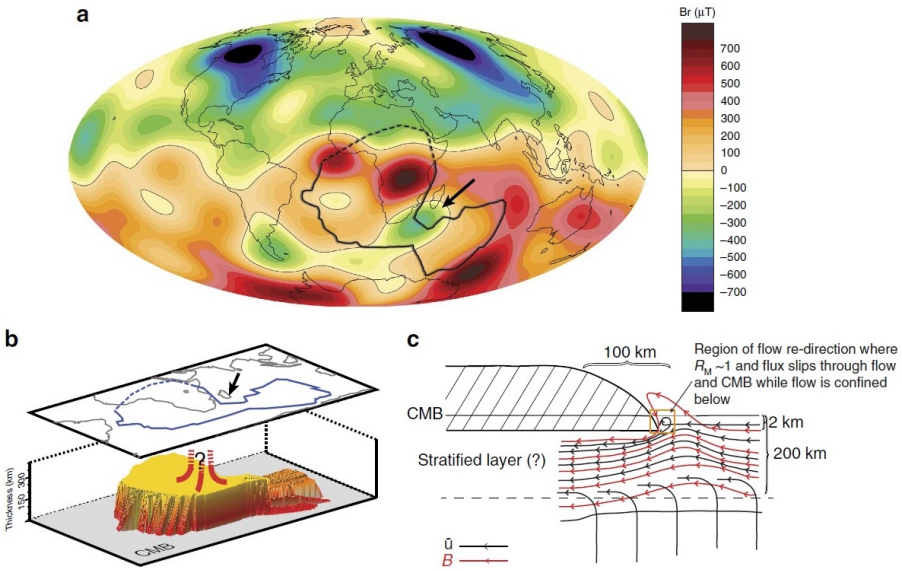

Figure 1.8: The figure illustrates the possible scenario for the flux expulsion. The edges of the African LLSVP are visualized as sites of flux expulsion. (a) Radial component of the geomagnetic field at the core–mantle for 1980 shown with sharp edges of the African LLSVP (black outline). Northern boundary of the LLSVP (dashed) is unknown in these models. The black arrow indicates the region of reversed flux at the CMB. (b) The edges of the African LLSVP at CMB. (c) Schematic model of the beginning stages of the flux expulsion at the steep edge of the African LLSVP. A 300 km base of LLSVP is shown as diagonal stripes [A. Tarduno et al., 2015].

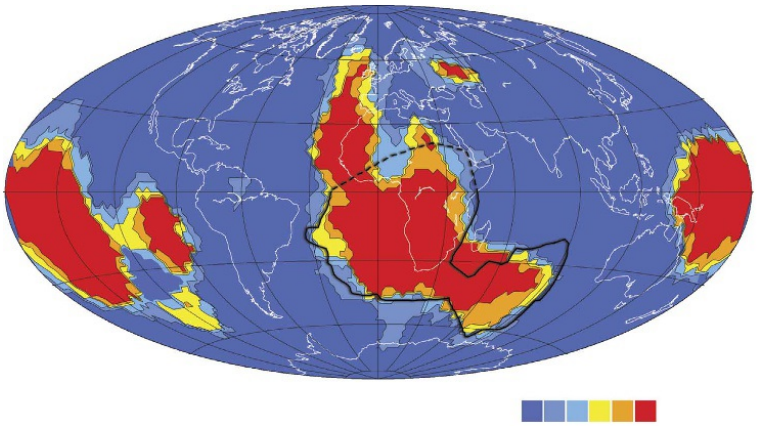

Figure 1.9: A vote map of cluster analysis of shear wave profiles (1,000–2,800 km depth). The map shown with the edge of African LLSVP at CMB. The cluster analyses assess five global tomographic models, with the colour-coded voting map representing the number of models, which assign a lower than average shear wave velocity to the pixel. The voting map highlights the consistency between the global models in defining the African LLSVP, as well as the similar, but more spatially complex, Pacific LLSVP.

It is clear from Figure 1.10 that the African LLSVP is surrounded by large steep coasts, located near the reversed geomagnetic flux underneath South Africa, which is directly related to the presence of the South Atlantic Anomaly (SAA): these sharp coastal gradients build small-scale vortices in the geomagnetic flow; thus, the core flow near the African LLSVP will be responsible to create such normal magnetic components. These flux ejections might be the main reason of the occurrence of the reversed and normal core patch pairs. The summation of both geomagnetic fluxes causes locally this decrease in the radial magnetic component intensity, hence, the formation of the anomaly. The main two reversed patches are clearly observed at South Africa and South America, as illustrated in Figures 1.8 and 1.9. Same interpretation was also discussed by several authors such as [Aubert, 2015], [Brown et al., 2018] and [Pavón-Carrasco and De Santis, 2016].

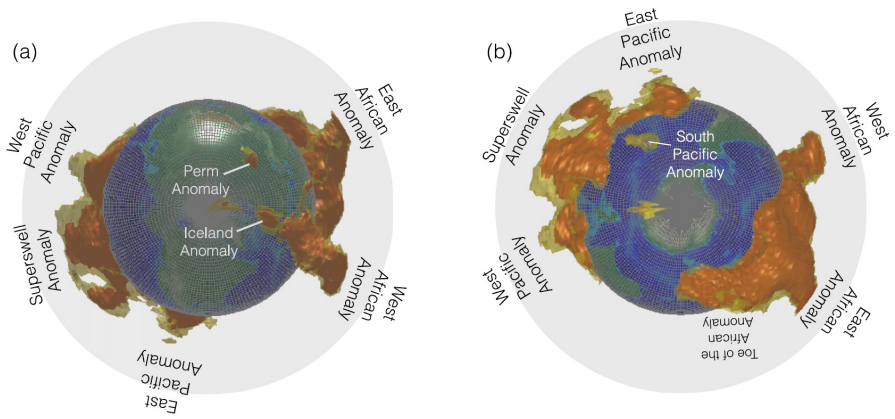

Figure 1.10: Contour of the votes for the slow cluster for majority (m = 3, transparent yellow) and for consensus (m = 5, red): the anomalies viewed (a) from the North pole and (b) from the South pole. These plots emphasize the larger size of the African anomalies compared to the Pacific anomalies. Surface topography is projected onto the CMB for reference [Cottaar and Lekic, 2016].

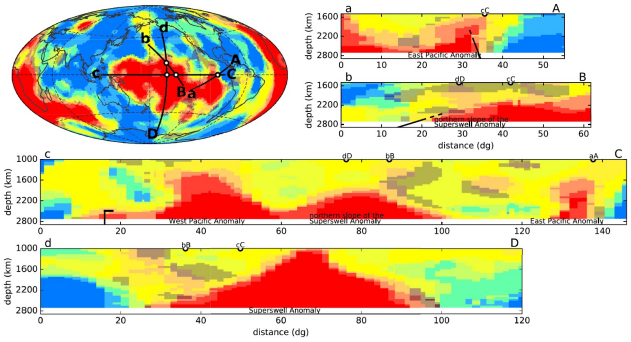

(a) Cross-sections across the Pacific LLSVP showing the vote results for the model proposed by [Cottaar and Lekic, 2016]. Map view shows clustering results at a depth of 2700 km. Panels (aA), (bB) and (cC) are cross-sections of the clustering. Panel (cC) runs west to east across the LLSVP, illustrating the West Pacific anomaly, the Superswell anomaly and the East Pacific anomaly. Black lines represent the boundaries. Cross-section (dD) runs north–south across the Superswell anomaly. The color scale is shown in Figure 1.12

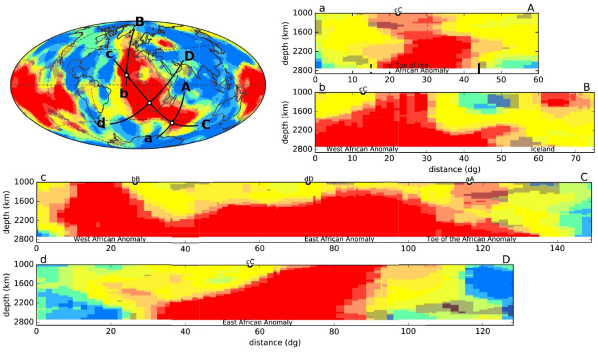

(b) Cross-sections across the African LLSVP showing the vote results for VS models. Map view shows clustering results at a depth of 2700 km. Panels (aA), (bB) are selected cross-section of the clustering. Panel (cC) runs from the West African anomaly across South Africa and beneath the Indian Ocean. Cross-section (dD) runs from the southwest to the northeast across eastern Africa, shows the anomalous nature of the East African anomaly: it tilts towards the northeast [Cottaar and Lekic, 2016]. The color scale is shown in Figure 1.12

Moreover, another study revealed that the relation between the minimum intensity at the Earth's surface and Reversed Flux Patches (RFPs) is not really straightforward. The SAA can eventually be explained by several intense patches (reversed and normal) which can determine the location of the minimum surface intensity. The longitude of the SAA minimum appears near the longitude of the Patagonia RFP due to the low-latitude normal flux patches (NFPs) near Africa and mid-Atlantic which diminish the effect of the Africa RFPs, as shown in Figure 1.13. The latitude of the SAA minimum is lower than the Patagonia RFP latitude due to the South Pacific high-latitude NFP and the axial dipole effect. The motion of the SAA minimum is explained by the motions and changes in intensity of these robust geomagnetic flux patches. Figure 1.14 illustrates the secular variations of the SAA path that can be explained by advection, while its intensity decrease requires magnetic diffu-

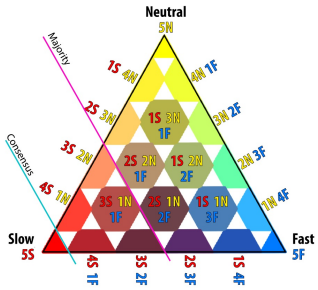

Figure 1.12: Color bar used to display the results of the cluster analysis across five tomographic models. The corners of the triangles indicate the colors that represent regions where all tomographic models agree on a single cluster [Cottaar and Lekic, 2016].

sion.

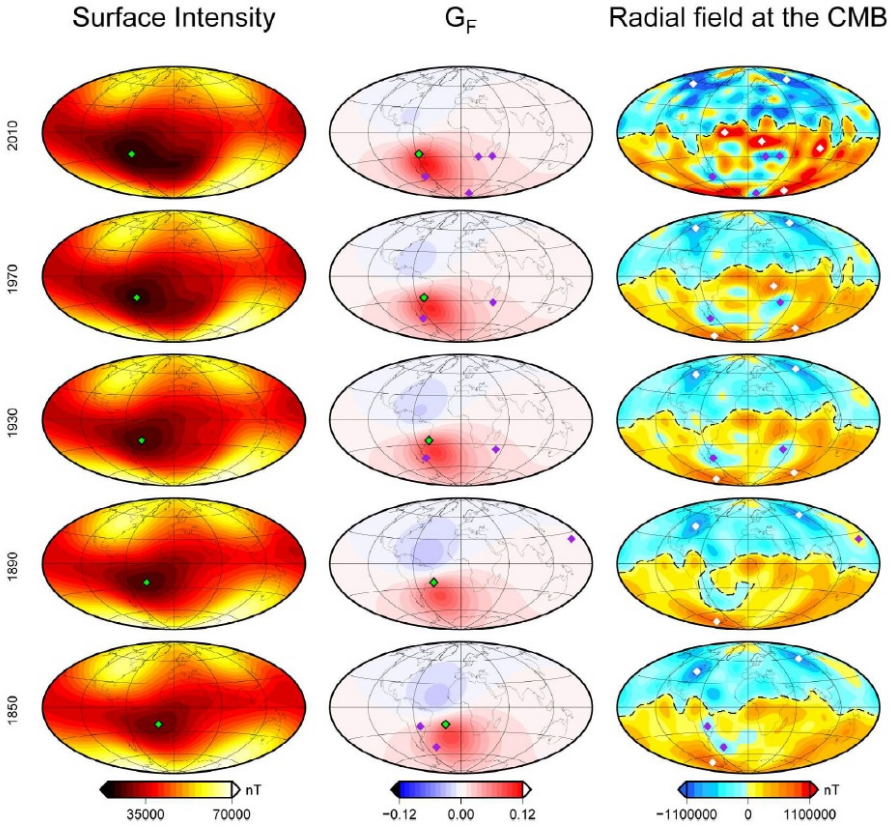

Figure 1.13: The figure demonstrates the field intensity at the Earth's surface (left), the intensity kernel G_F (middle) and the radial field at the CMB (right) for the years 1850, 1890, 1930, 1970 (gufm1) and 2010 (CHAOS5). The SAA minimum is indicated by green diamonds (left and middle) and the identified reversed flux patches (RFPs) and normal flux patches (NFPs) are determined by purple diamonds (middle and right) and white diamonds (right), respectively. The dashed lines correspond to the identified magnetic equator (right). Both CMB and surface fields are in nT [Terra-Nova et al., 2017].

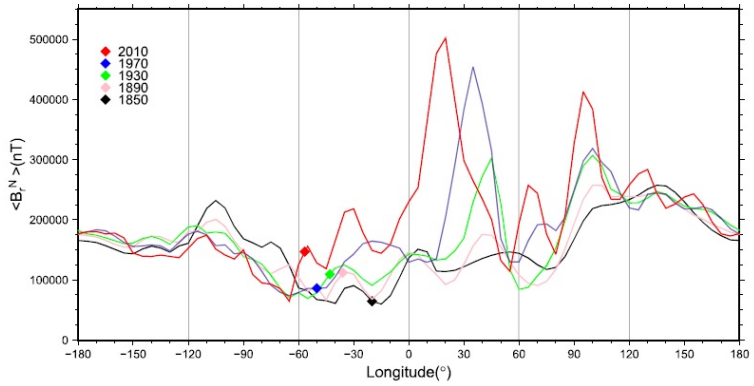

Figure 1.14: Integrated normal flux B_r^N at the core-mantle boundary calculated over the Southern Hemisphere versus longitude. Each colored line corresponds to a specific year as shown in the legend. Diamonds indicate the longitudes of the SAA minimum [Terra-Nova et al., 2017].

1.2 The Anomaly Effects

1.2.1 Particle Dynamics

This magnetic distortion has a direct impact on the Van Allen belts, namely, the inner radiation belt, because it becomes closer to the Earth's surface. Supposing that the Earth's magnetic field strength is horizontal, then

the loss cone angle should be longitudinally equal. However, the realistic geomagnetic field strength varies depending on the longitude, where the minimum is occurring in the SAA [Gemelos, 2011]. Adding that, for a given particle pitch angle and L shell value, the mirror altitude is considered as a surface of constant B. The latter is the lowest in the SAA [Pisacane, 2005]. The particles drift around the Earth on paths along the magnetic field lines, where they can reach much closer to the Earth's surface in the SAA comparing to other longitudes. Figure 1.15 clearly demonstrates the deviation of the drift contours of the equatorially trapped particles in the magnetosphere (by including only the internal magnetic field) compared to that in a pure and centered dipole field, at distances $L = 1, 2, 7$. It is clearly observed that the largest deviations are occurring close to the planet surface, where the particle drift orbits are at much lower altitudes at the SAA. Moreover, at $L = 7$, the largest deviations are caused by the dipole field offset from the Earth's center [de Pater and Lissauer, 2010].

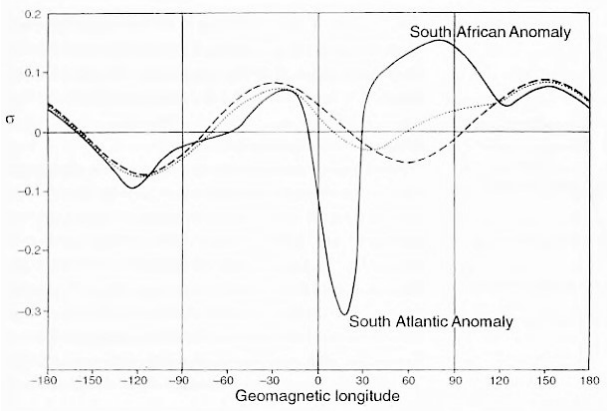

Figure 1.15: Deviation of a particle's drift path in the Earth's magnetic field, compared to the drift orbit in a pure dipole filed, at distances $L = 1$ (solid curve), 2 (dotted) and 7 (dashed) [de Pater and Lissauer, 2010].

1.2.2 Radiation Effects

The LEO (Low Earth Orbit) spacecraft missions are always and significantly affected by such anomaly. For example, the space shuttle missions, where the laptop computer is mounted on, is from time to time crashed because of the high-energy cosmic ray particles, precisely in the SAA [Lowman, 2002], [Barratt and Pool, 2008] and [de Pater and Lissauer, 2010]. The SAA, in fact, is one of the reasons why the space shuttle can lower its orbit to avoid this high-energy particles that are harmful for humans as well as electronics [Chaisson, 1998]. Furthermore, Skylab was passing through several portions of the Van Allen belts and also a portion of the SAA near the northern and the southern extreme of its orbit [SP., 1962]. Figure 1.16 illustrates the upsets locations observed by TAOS satellite. The data were collected after examining about 1300 single event upsets from one computer mounted on the TAOS mission; the results showed that approximately 50 % were occurred in the SAA, considering that only 5 % of its orbital time was spent in the anomaly region. The same radiation level was also found by [Gradwell and Rainford, 2016], where they estimated that by the passage through the SAA, it can account for about 50 % of the radiation dose that is occurred for a selected orbit, which depends on the shielding depth of the dose considered. Another important example is Hubble Telescope which spends about 15 % of its orbital time in the anomaly, and is actually considered as a great challenge for the mission data measurements. During operation, Hubble's instruments are turned on while crossing the SAA, although the acquired data are not meaningful. Besides, the transit time spent in this critical region of orbital path can directly interrupt its pointing control system, thus, the main objective of the entire mission [Chaisson, 1998]. Figure 1.17 also demonstrates the particle energy in space environment and the corresponding hazards for spacecraft.

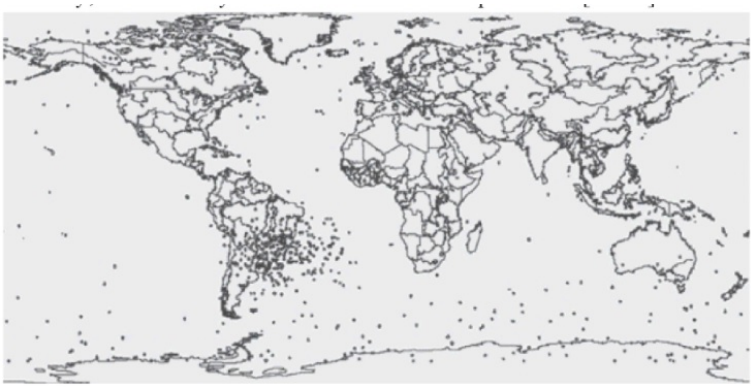

Figure 1.16: Upset rates for TAOS mission

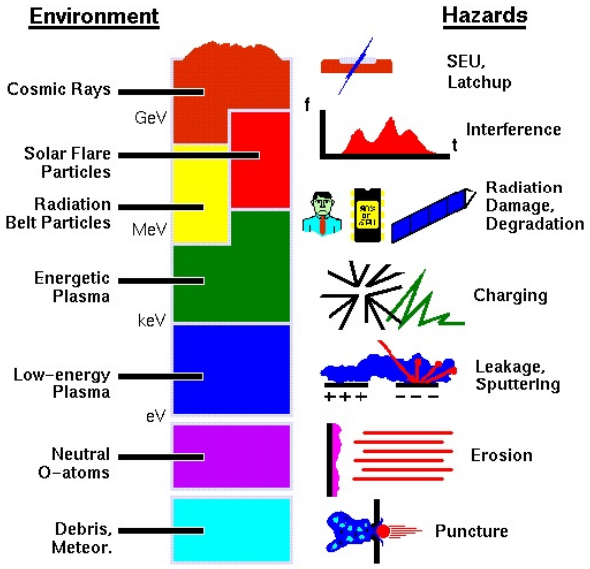

Figure 1.17: Environment radiation effects [Pisacane, 2014]

1.2.3 Atmosphere Effects

The close contact of the inner radiation belt can also induce several modifications in the atmosphere, where the particle deposition can dig further into the atmosphere. For a given particle pitch angle and L shell value, the mirror altitude is a surface of constant magnetic field intensity [Pisacane, 2005]. In addition, it is known that the main source of the trapped protons in the inner belt could be the Cosmic Ray Albedo Neutron Decay (CRAND). Another phenomenon is the enhanced EUV flux during solar flares that can heat the dayside atmosphere and then affect the proton fluxes in the SAA [Zou et al., 2015].

1.3 Literature Review

The main scope of this research is to find the response of the SAA with respect to the space weather environmental conditions. Few papers studied such subject. We will briefly discuss here those contributions:

1.3.1 SAA and Space Weather: Short-Term Study

1. [Dachev, 2018]: In this research, two spectrometers mounted on the International Space Station (ISS) at the altitude $\approx$ 350 km, were measuring the proton flux ($<$ 70 MeV) [Dachev et al., 2002] inside the SAA during four main magnetic storms from 2008 to 2015. The main findings were that the maximal proton flux value and the corresponding area were decreasing during the main phase and both parameters were increasing during the storm sudden commencement. Figure 1.18 illustrates the response of the SAA proton flux during the magnetic storm phases. The time-scale of the results is in days.

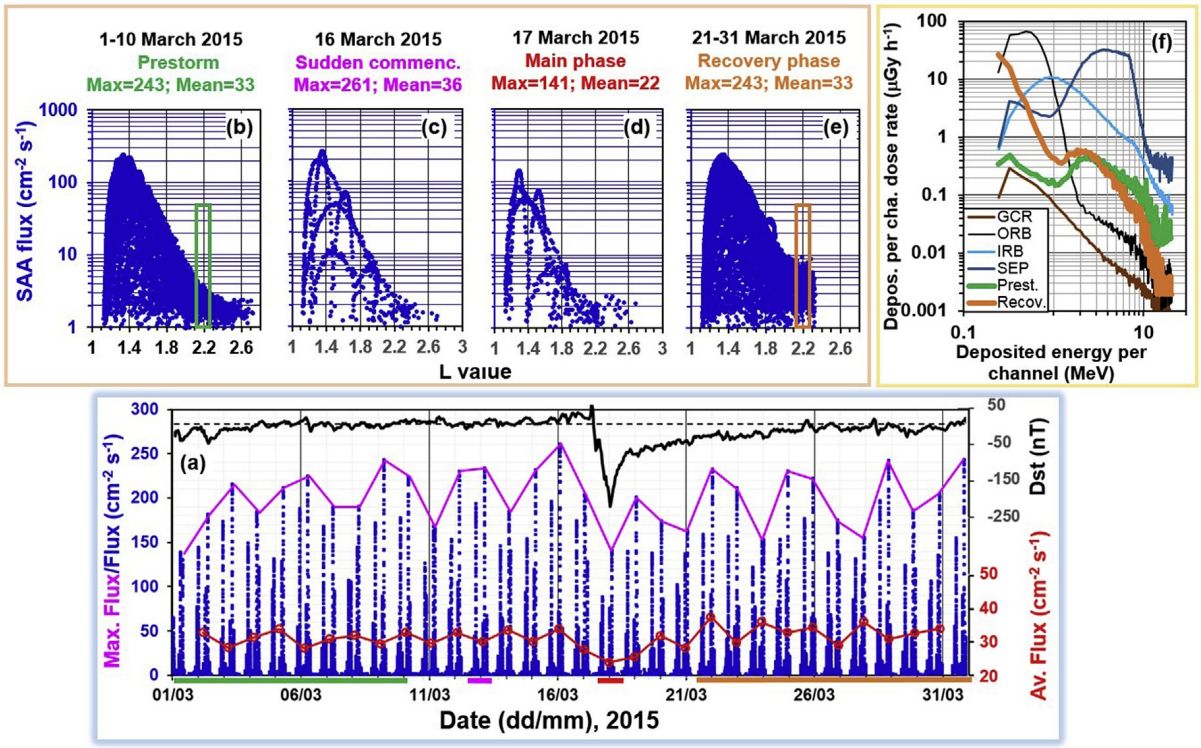

Figure 1.18: Panel (a) demonstrates the short-term geomagnetic storm variations of the Inner Radiation Belt (IRB) parameters as observed by the R3DR2 instrument in the period March 1-April 1, 2015. Panels (b–e) represent the flux (blue points) versus the L-value for the four geomagnetic storm phases. Panel (f) shows the deposited energy spectra shapes for the period June 21–30, 2015 named Galactic Cosmic Ray (GCR), relativistic electrons and/or Bremsstrahlung in the outer radiation belt (ORB), protons in the South Atlantic Anomaly region of the inner radiation belt (IRB) and Solar Energetic Particle (SEP) events. These spectra were compared with: (1) the Prest. (Prestorm) spectrum (plotted with a heavy green line), obtained during the prestorm phase (March 1–10, 2015) in the L range 2.1–2.3 (shown with a green rectangular at Panel (b)); (2) Recov. (Recovery) spectrum (plotted with a heavy orange line), obtained during the recovery phase (March 21–31, 2015) in the L range 2.1–2.3 (shown with an orange rectangular at Panel (e)). The color lines below the horizontal axes show the continuity of the significant periods [Dachev, 2018].

2. [Zou et al., 2015]: The authors demonstrated the SAA proton flux (all energy channels) response, measured by the spacecraft NOAA 17, operating at $\approx$ 800 km during two main geomagnetic storms occurred in 2005. The main result was that the SAA maximum proton flux value and the corresponding area were decreased during magnetic storms. The time-scale of the results is also in days. Figure 1.19 summarizes their conclusions.

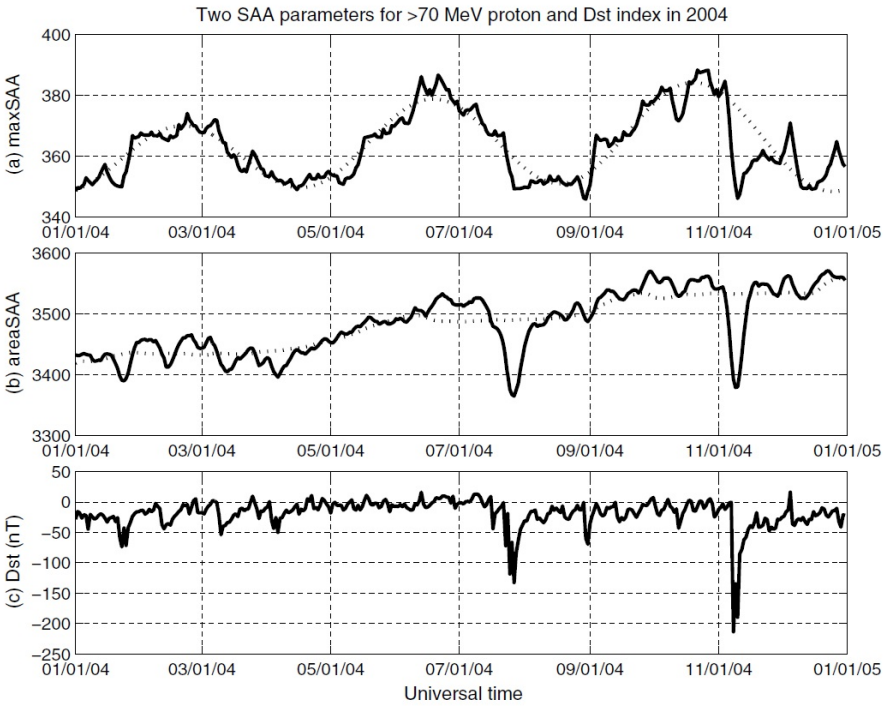

Figure 1.19: The 5 day running averages of (a) maximum proton flux value (maxSAA) and (b) corresponding area below a selected threshold (areaSAA) for $>$ 70 MeV protons measured by NOAA 17 in 2004, along with the daily (c) *Dst* indix profile. The solid lines in Panels (a, b) are the temporal variations of the maxSAA and areaSAA, and the dotted lines show the best fit of the 120 day variations of them [Zou et al., 2015].

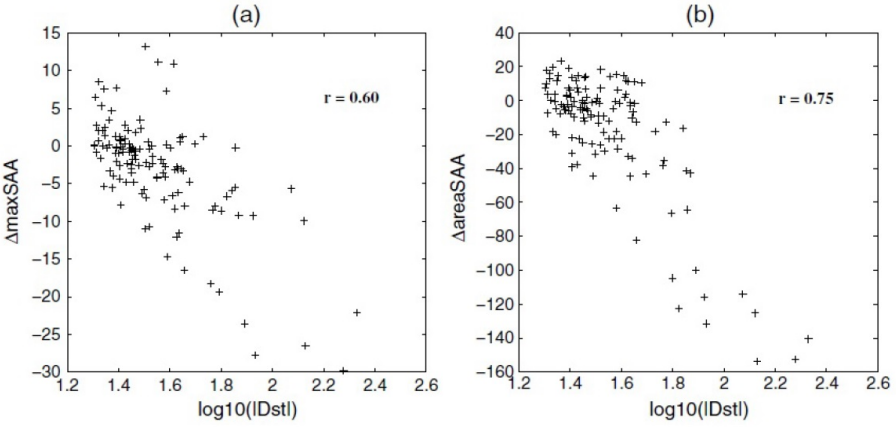

Figure 1.20: Correlation results between the maximum proton flux value and corresponding area with respect to *Dst* index. It was found that the correlation coefficients are respectively, 0.6 and 0.75 [Zou et al., 2015].

3. [Suparta et al., 2017]: The authors conceived a model for forecasting the trapped particle flux distribution in equatorial LEO based on the hierarchical Bayesian spatio-temporal (HBST) statistical model; the model was developed to estimate the risk occurred on satellite bodies. Their model was applicable to the low and to the medium energy electrons and protons under all solar activity conditions. The model used NOAA 15 - 17 spacecraft data, which classified particle energies as $>$ 30 keV (mep0e1) and $>$ 300 keV (mep0e3) for electrons and 80 - 240 keV (mep0p2) and 800 - 2500 keV (mep0p4) for protons in the SAA region. The purpose of this research was to investigate the model accuracy and forecast during quiet period (15 - 19 May 2009) and period of high solar activity (26 - 30 October 2003). The forecast was interpolated by the Kriging technique to assess the corresponding particle distribution. The average mean relative error values was found to be 20 - 30% for both periods and a similar pattern as that of the National Oceanic and Atmospheric Administration (NOAA) maps.

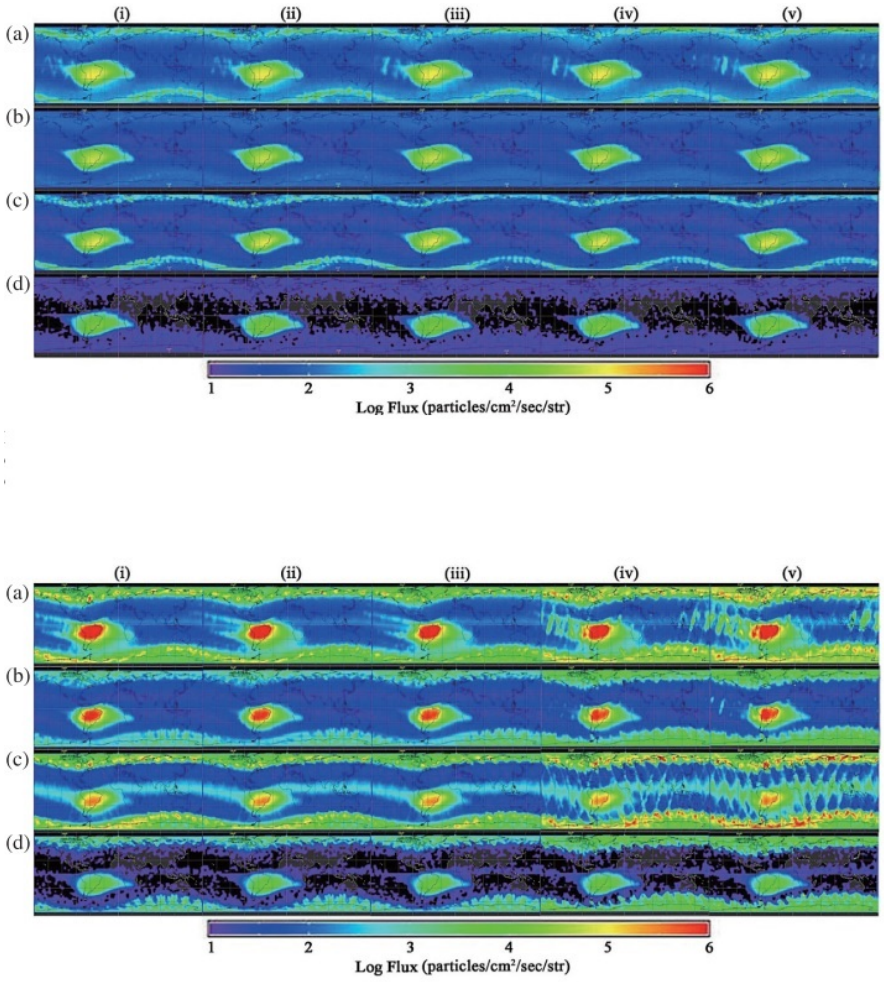

Figure 1.21: Upper Panel: NOAA's particle flux distribution for (a) of mep0e1, (b) of mep0e3, (c) of mep0p2, and (d) mep0p4 on the quiet days of (i) 15 May 2009, (ii) 16 May 2009, (iii) 17 May 2009, (iv) 18 May 2009, and (v) 19 May 2009. Lower Panel: NOAA's particle flux distribution for (a) of mep0e1, (b) of mep0e3, (c) of mep0p2, and (d) mep0p4 on the days of high solar activity of (i) 26 October 2003, (ii) 27 October 2003, (iii) 28 October 2003, (iv) 29 October 2003, and (v) 30 October 2003 [Suparta et al., 2017].

4. [Schaefer et al., 2016]: In this research, a new SAA particle flux intensity model for low Earth orbit was developed by particle noise pulses in an ultraviolet photomultiplier. The data set was daily monitoring of the particle radiation strength at a fixed altitude and local specific time. It was observed that (1) an enhancement in SAA intensity over the solar cycle 23's decline into a deep solar minimum and the cycle 24 subsequent rise, (2) a slow motion drift of the SAA centroid with time, (3) a higher particle flux at solar minimum than at solar maximum, and (4) a yearly cyclical variation. These particle rates were deduced from electric noise pulses generated in the photometers when an energetic charged particle hit the detector and causes an electron to be liberated from the detector material. The model described here can be used to monitor and even spatially predict the changes in particle fluxes seen by instruments in LEO missions through the SAA.

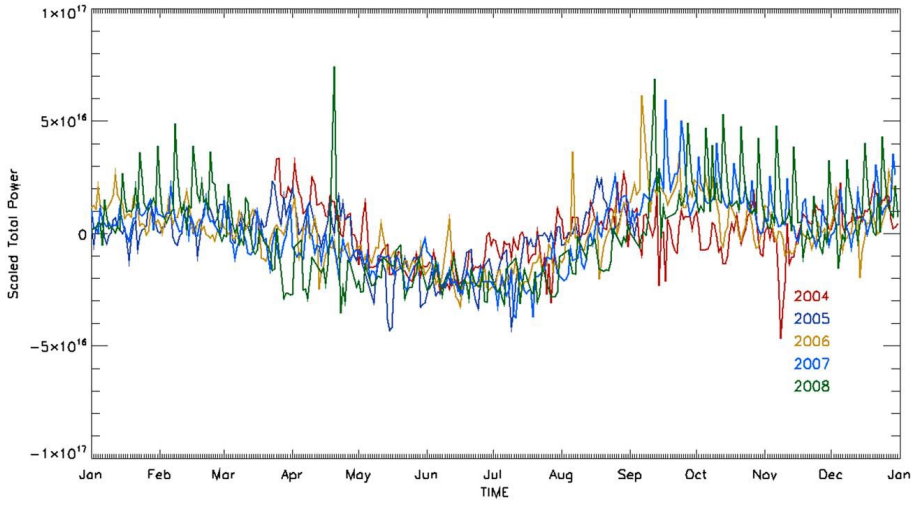

Figure 1.22: The figure demonstrates the SAA intensity changes over the course of a year. The yearly average counts were subtracted and the years 2004–2008 were plotted as a function of day of year. It is observed two maxima, spaced wider than half a year. The later maximum coincided with the autumnal equinox, but the earlier maximum occurred around February, earlier than the vernal equinox. During these years, the intensity was increasing, so the end of the year was higher than the beginning, even though the average count rate had been subtracted from each year. The spikes that appeared with an 8 day period are likely an artifact of the DMSP orbital precession period [Schaefer et al., 2016].

1.3.2 SAA and Solar Activity: Long-Term Study

1. [Qin et al., 2014]: The authors investigated the proton flux variations in the inner radiation belt as well as the SAA, with respect to solar cycle. They studied the related long-term variations of the anomaly from measurements carried out by NOAA 15 from 1999 to 2009. It was reported that the SAA peak proton flux variation was anticorrelated with the $F_{10.7}$ during a solar cycle. It was also found a phase lag of 685 days between the solar $F_{10.7}$ flux and the proton flux (Figure 1.24a). Those features were observed similarly for the SAA area variations, which in addition showed a rapid decrease during the solar maximum and a slow increase during the solar minimum. Moreover, the solar wind dynamic pressure enhancement could favor the SAA north-south drift, as shown in Figure 1.24b.
   From Figure 1.23a, it is observed that the SAA area was decreased during the Solar Particle Event (SPE) (top panel).

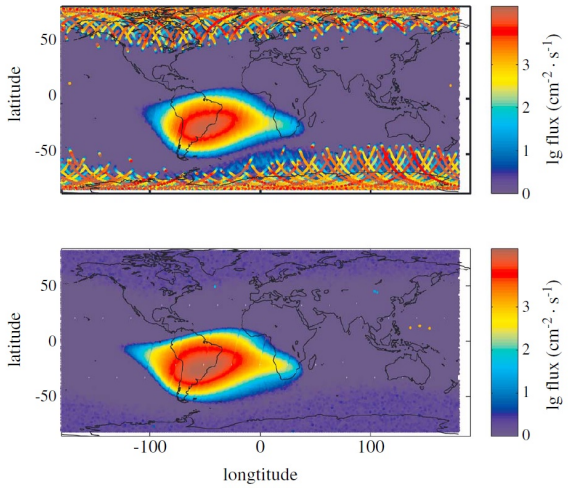

(a) Two examples showing (top) the distribution of SAA proton fluxes during the solar proton events in November 2001 and (bottom) the distribution of SAA proton fluxes during a geomagnetically quiet period in November 2009 [Qin et al., 2014].

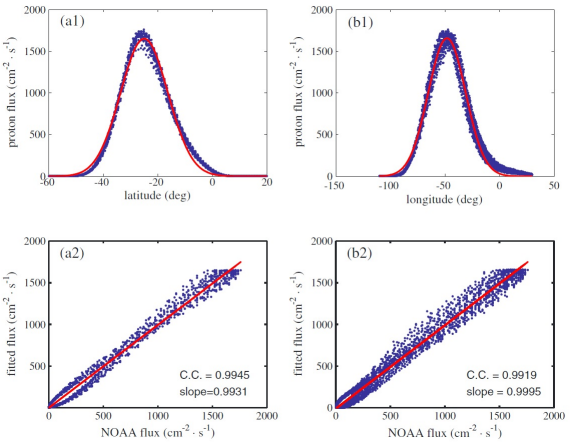

(b) Gaussian fitting results as a function of experimental NOAA flux for protons > 16 MeV over the period from 20 March 2003 to 20 June 2003: (a1, a2) for a longitudinal range of -53°to -47°, and (b1, b2) for a latitudinal range of -28°to -22°[Qin et al., 2014].

The authors also found that the latitudinal and longitudinal proton flux in the SAA could be fitted by

one dimensional Gaussian curve, as shown Figure 1.23b.

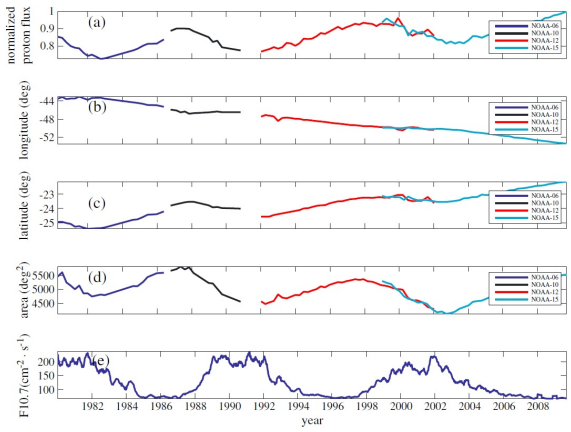

(a) Temporal evolution of (a) the normalized peak proton flux, (b) longitudinal center, (c) latitudinal center and (d) the area of the SAA, and (e) $F_{10.7}$. The blue, black, and red solid lines correspond to the data from NOAA 6, NOAA 10, NOAA 12, and NOAA 15 satellites, respectively [Qin et al., 2014].

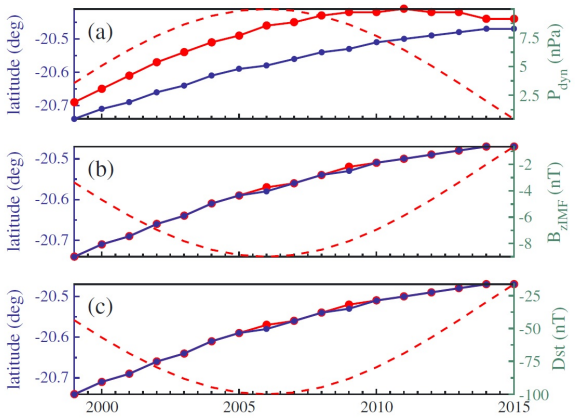

(b) Variations of the latitudinal point of the minimum geomagnetic field (B_{min}) with respect to external factors. The blue solid curves represent the results for the case with P_{dyn} = 0.5 nPa, B_{zIMF} = 0 nT, and Dst = 0 nT. From top to bottom, (a) change P_{dyn} only, (b) change B_{zIMF} only, and (c) change Dst only, as shown by the red dashed curves. The corresponding variations of the latitudinal point of B_{min} are indicated by the red solid curves [Qin et al., 2014].

2. [Campana et al., 2014]: In this research, the authors studied the radiation environment in a LEO (500–600 km altitude, 4˚inclination) as measured by the Particle Monitor (PM) experiment onboard the BeppoSAX satellite, from 1996 to 2002. By using the time series of the particle count rates measured by PM, the researchers could construct the corresponding intensity maps and then, derived the SAA passage number of times and the resulted fluences. The low-latitude SAA regions were found to have an intensity strongly decreasing with altitude and dependent on the magnetic rigidity. The SAA extent, westward drift and strength versus altitude was reported. Furthermore, it was concluded that the SAA proton flux at different altitudes was anticorrelated to the sunspot numbers, as shown in Figure **??**.

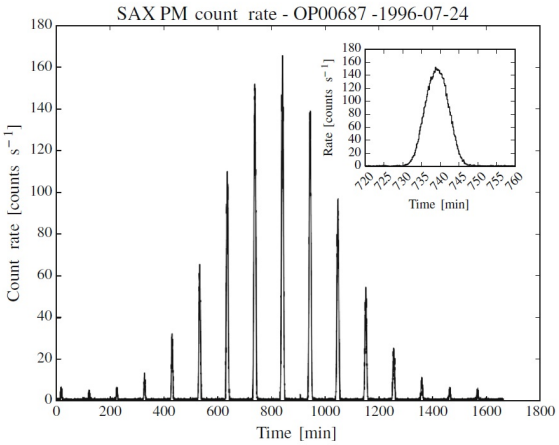

(a) BeppoSAX/PM count rate for the observation period OP00687, corresponding to July 24, 2006. The peaks in the count rate correspond to the various SAA passages. The inset shows in more detail one such passage [Campana et al., 2014].

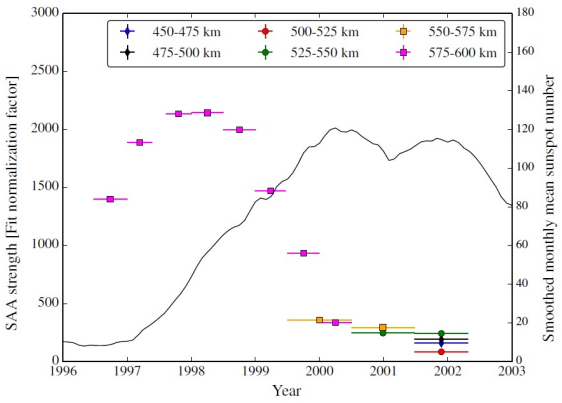

(b) The SAA strength, proportional to the normalization factor A of (1). The solid black line is the average monthly sunspot number, a direct indication of the solar activity [Campana et al., 2014].

3. [Jones et al., 2017]: In this study, the authors examined the SAA location secular drift at 400–600 km altitude over approximately two solar cycles, by using particle count rates in order to trace the geomagnetic field lines in the region near the SAA. The data were measured by the Low-Energy Ion Composition Analyzer sensor on board the SAMPEX (Solar, Anomalous, and Magnetospheric Particle Explorer) spacecraft to measure both the longitudinal and latitudinal drift of the SAA. These measurements were compared

with the IGRF12 (International Geomagnetic Reference Field - version 12) model calculations based on the analysis of the magnetic field minima in the SAA region. The observational data were in good agreement with the model results.

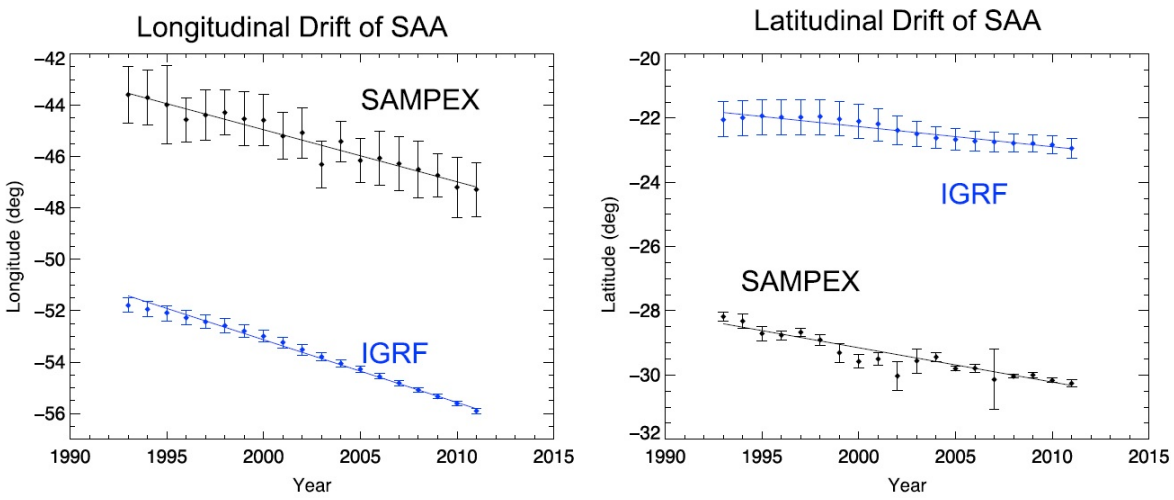

Figure 1.26: Fitted max peak of count rate for longitudes and latitudes 1993–2011 (black), including errors on data. IGRF (blue) minimum magnetic field values with linear fit, including variance on minimum [Jones et al., 2017].

4. [Domingos et al., 2017]: A very recent geomagnetic field model CHAOS-6, whose data were provided by different platforms, such as satellites orbiting the Earth – POES NOAA for 1998–2014 and CALIPSO for 2006–2014. It was found that the main magnetic field changes were responsible for the anomaly observed westward drift. Three modes account for the time evolution of the POES proton flux instrument were related to the solar activity effects. It was revealed that both, the first and second modes had a good correlation with the thermospheric density, which varied with respect to the solar cycle. The first mode represented the total intensity variation of the particle flux in the SAA, and the second the movement of the SAA between different L-shells, as shown in Figures 1.27a and 1.27b. The proposed analysis allowed the authors to assess the westward drift rate, as well as the latitudinal and longitudinal solar cycle oscillations.

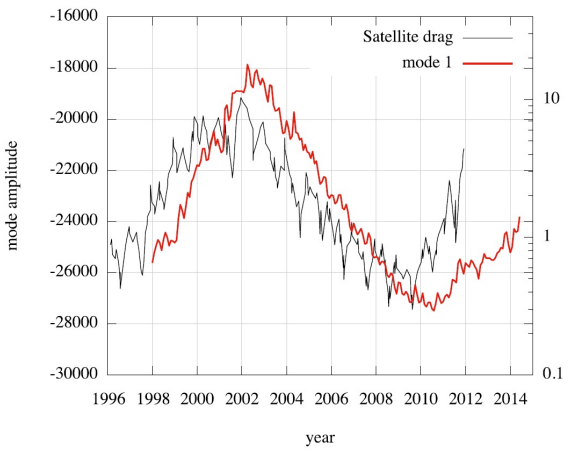

(a) Time series of the first PCA mode of POES L-shell reference frame and the thermospheric density [Domingos et al., 2017].

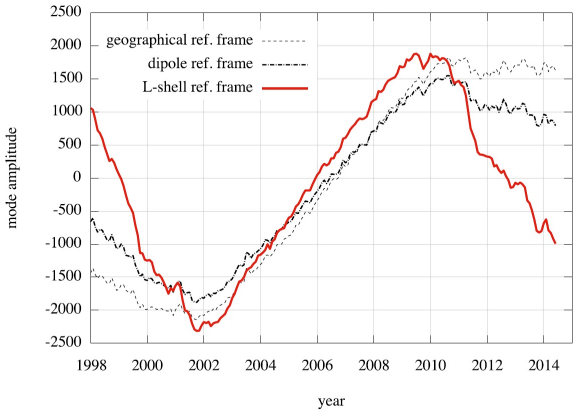

(b) Time series of the second mode for POES: comparison between a regular geographical grid (thinner dashed line), the dipole reference frame (thicker dashed line) and the L-shell reference frame (bold red line) [Domingos et al., 2017].

5. [Cnossen and Matzka, 2016]: In this study, the researchers analyzed the magnetic measurements going back to the eighteenth century which could be useful to examine the upper atmosphere changes. The measurement sites were taken from Rome and Mannheim from May 1782 to May 1783, from Greenwich, St. Helena, Cape of Good Hope, and Singapore from May 1841 to May 1842. The daily magnetic variations in the historical data were compared with modern-day observations from 2010 at nearby stations. The

model simulations determined that the difference between the old and new measurements can be explained at least to some extent by changes in the Earth's main magnetic field. Changes in the main field strength and the northwestward movement of the magnetic equator, in particular in the region of the South Atlantic Anomaly, had caused changes in the positioning, shape, and strength of the equivalent current vortices in the ionosphere that resulted in the magnetic perturbations on the ground. Differences in solar activity between the historical and modern epochs, which were all near solar minima, were too small to have a notable effect on the ground magnetic perturbations. However, in regions where main magnetic field changes had been relatively small for the last $\approx$ 400 years, e.g., in Singapore, the effects of a long-term increase in solar activity from Maunder Minimum conditions to normal solar minimum conditions (an increase in $F_{10.7}$ of $\approx$ 35 solar flux units) were comparable to the effects of geomagnetic main field changes.

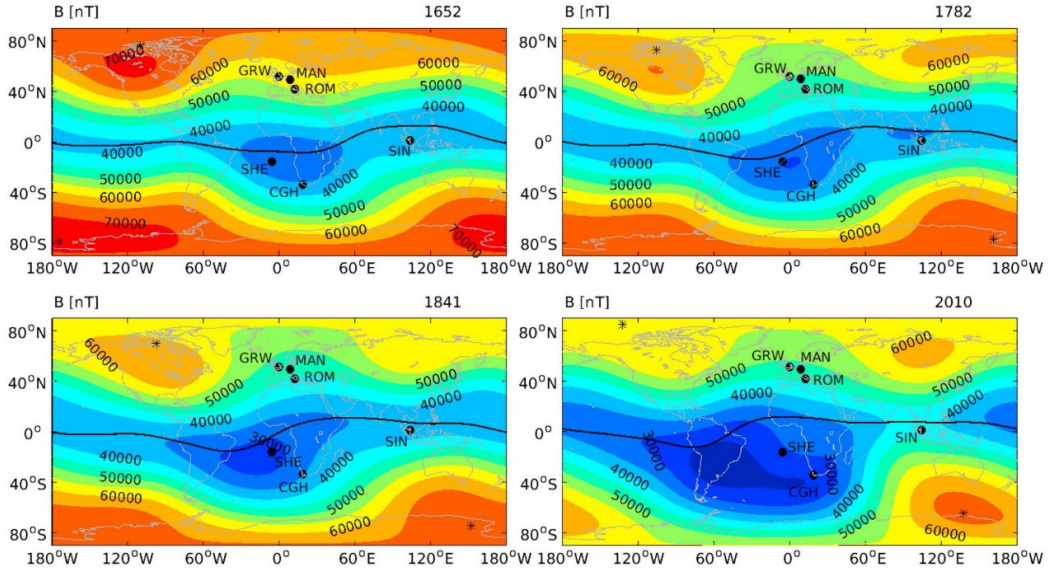

Figure 1.28: Main magnetic field intensity (color contours) in (top left) 1652, (top right) 1782, (bottom left) 1841, and (bottom right) 2010. Also marked are the positions of the magnetic equator (solid line) and magnetic dip poles (stars) according to the GUFM1 model (for 1652, 1782, and 1841) and the IGRF (for 2010). The locations of magnetic stations of the analyzed historical data are indicated with black dots [Cnossen and Matzka, 2016].

1.3.3 The Formation of New Inner Radiation Belt from Solar Proton Event

1. [Pierrard et al., 2014]: The authors discovered significant enhancements in the electron, proton and helium ion fluxes in the South Atlantic Anomaly (SAA) and at high latitudes during SEP (Solar Energetic Particles) events and geomagnetic storms. Measurements were performed by the Energetic Particle Telescope (EPT), which was a new compact and modular ionizing particle spectrometer that was launched on 7 May 2013 to a LEO polar orbit at an altitude. Figure 1.29 demonstrates the proton flux during quiet time (June 2013) and SEP occurrence (September 2013). It should be noted that during the SPE event, the green area of the contour plot of the SAA, whose proton flux was greater than approximately 9.5 $cm^{-2}s^{-1}sr^{-1}MeV^{-1}$ (the bottom panel), was enhanced at the South of the SAA.

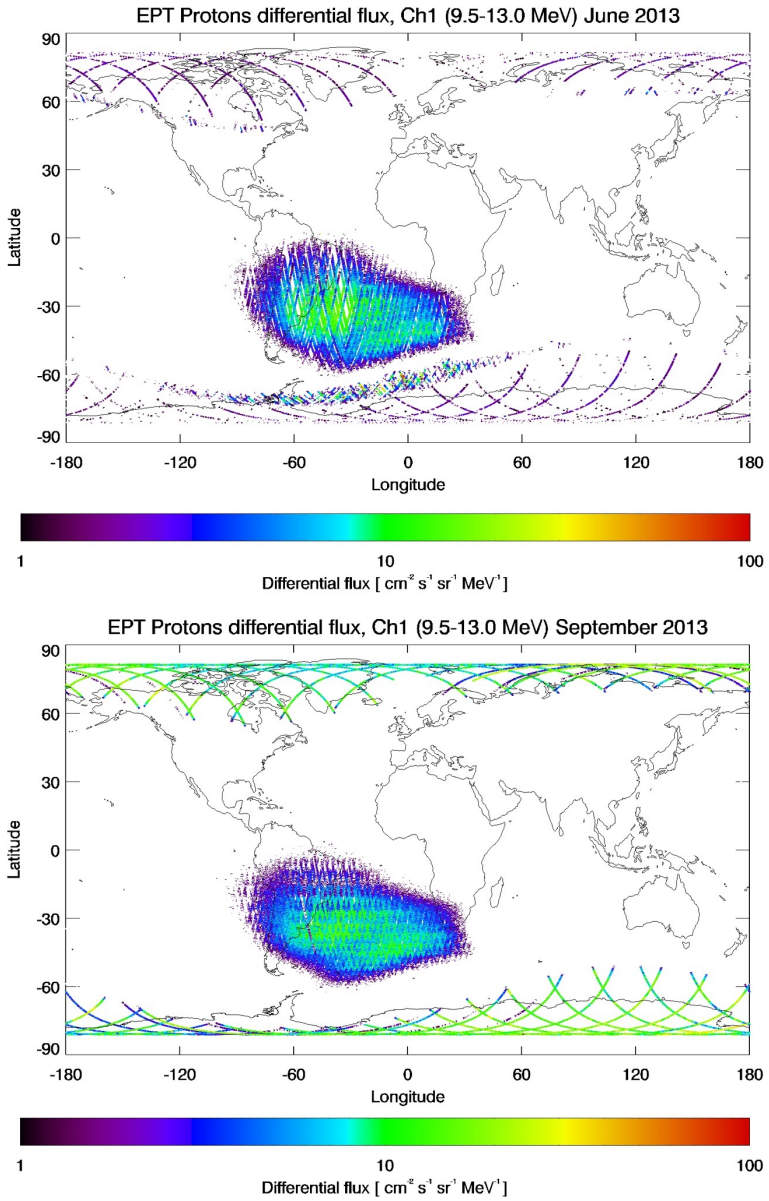

Figure 1.29: Proton flux in Channel 1 (9.5–13 MeV) observed during one month of observations. First panel: June 2013, second panel: September 2013 [Pierrard et al., 2014].

2. [Looper and Blake, 2005]: Observations of the response of the low-altitude radiation population below $L = 3$ during and after the strong solar energetic particle events and geomagnetic disturbances of late October and early November 2003 were studied throughout the 12-year SAMPEX mission. It was revealed that on 29 October 2003, at the approximately 600 km altitude of SAMPEX, the usual belt of energetic protons (above 19 MeV) around $L = 2$ almost completely disappeared, and recovered only after several months.

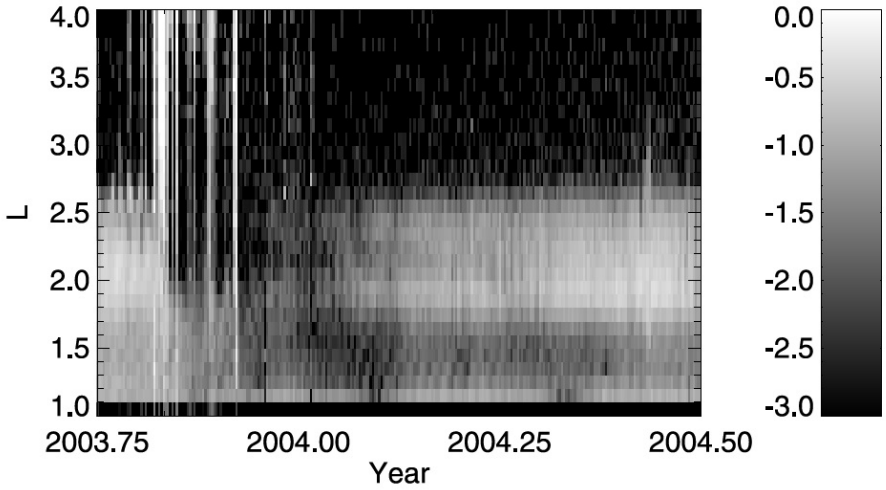

Figure 1.30: Daily averages of 19–29 MeV proton count rate versus L and time for nine months around the October/November 2003 events. Gray scale is the logarithm (base 10) of the count rate per second in all figures [Looper and Blake, 2005].

Figure 1.30 is demonstrating the daily averages of protons at 19–29 MeV as a function of L (IGRF) for a period of nine months around the time of these SEP events. The trapped protons, where the peak was located around $L = 2$, were visible at the event beginning, and the SEP events were visible as bands stretching down from high L (when SAMPEX was over the polar caps). SAMPEX sampled the SAA region, where the trapped protons could be observed at low altitude, with roughly 12-hour resolution, so PET could not pinpoint timing of changes with a resolution of better than one-half day. On 29 October 2003 the low-altitude protons had almost completely disappeared. In Figure 1.30, it can be observed that it took several months for the protons to recover to their initial intensity.

3. [Lorentzen et al., 2002]: The authors reported the formation of new ion radiation belts associated with several solar energetic particle events and large geomagnetic storms in 1998 and 2000. Observations from the following satellites, Polar, Highly Elliptical Orbit (HEO) 1997-068, and the Solar, Anomalous, and Magnetospheric Particle Explorer (SAMPEX), were used to study in detail the inner zone of the radiation belt at low and high altitudes. They focused specifically on the four International Solar Terrestrial Physics events of August and September 1998 and April and July 2000. It was found in several events new 2–15 MeV proton belts at various locations between $L = 2.0$ and $L = 3.5$. The low-altitude SAMPEX observations revealed some features that were not visible at the high altitudes, such as the formation of the radiation belts with multiple peaks in L shell. During the event of July 2000, energetic helium and iron were observed at $L \approx 2$, suggesting that a solar energetic particle could be a source for these injected ions.

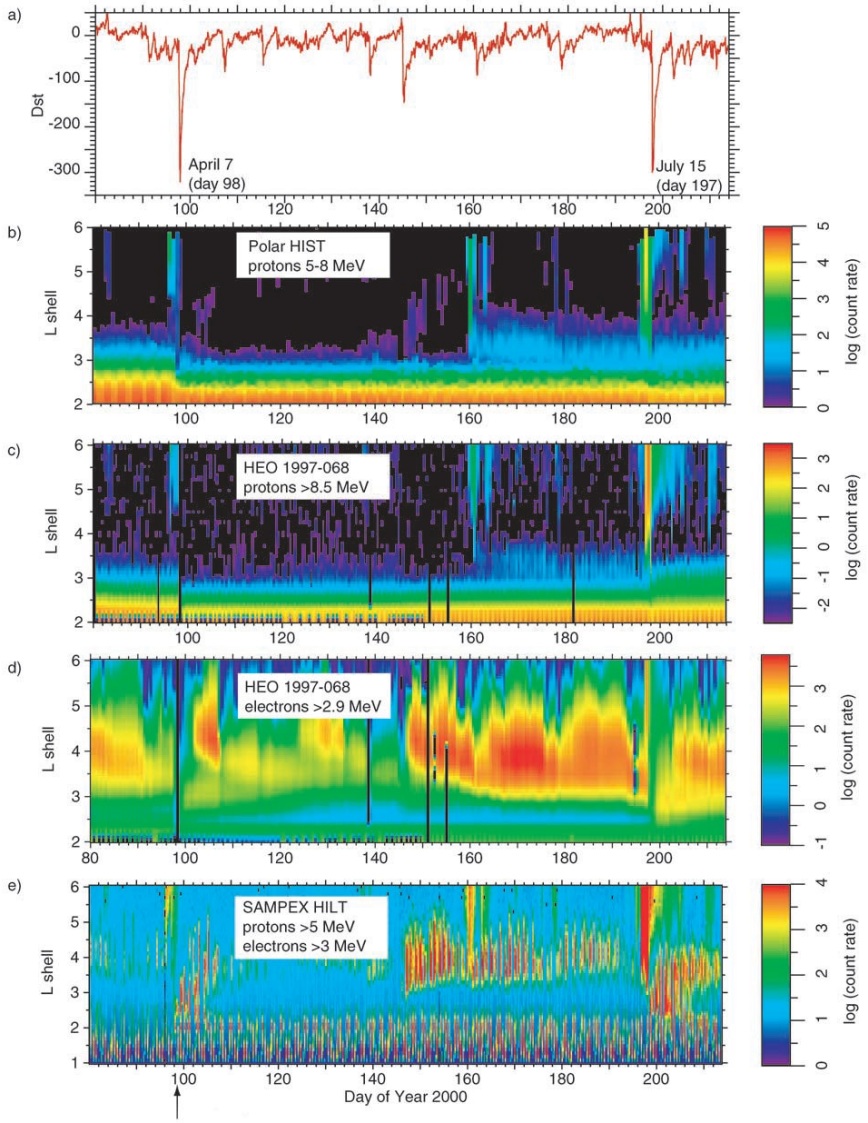

Figure 1.31: (a–e) Summary of *Dst*, Polar, HEO 1997-068, and SAMPEX data from 2000. Polar data was summed over all pitch angles [Lorentzen et al., 2002].

1.3.4 Numerical Simulations of Proton Inner Radiation Belt

1. [Engel et al., 2015]: In this study, the proton loss in the outer part of the inner radiation belt ($L = 2 - 3$) was investigated by using test particle simulations that followed the full Lorentz trajectories with both magnetic (TS05) and electric (inductive) fields, during the solar energetic particles event of 6 April 2000. The electric fields were calculated as inductive fields generated by the time-varying magnetic field data. The simulation results were compared with the proton measurements from the highly elliptical orbit (HEO-3) satellite for three different energy ranges (8.5–35 MeV, 16–40 MeV, and 27–45 MeV) as well as previous modeling work done. It was revealed that the inclusion of the induced electric field caused an additional increase in the proton loss rate in the lower L shells, improving the agreement with satellite data.

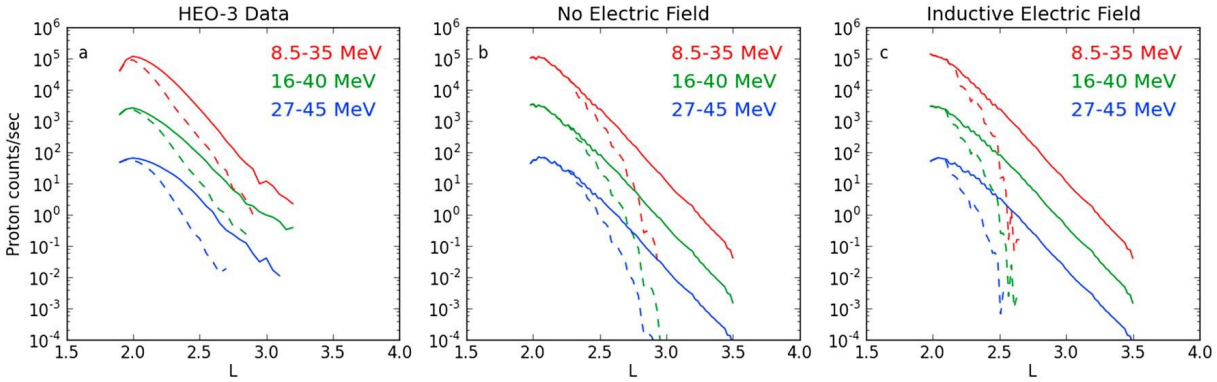

Figure 1.32: L-shell versus flux plots for (a) HEO-3 data, (b) simulations using only TS05, and (c) simulations using TS05 + inductive electric field. The solid line is before the storm, and the dashed line is after the storm when Dst index ≈ -270 nT in April 2000 [Engel et al., 2015].

2. [Hudson et al., 1997]: The authors had performed test particle simulations by using the guiding center approach with the background MHD fields from global three-dimensional simulation, to investigate the storm sudden commencement (SSC) of the great March 24, 1991 event, when a radiation belt was formed. They found that in all cases, a solar proton event was followed by a SSC, leading to the formation of a new proton belt earthward of solar proton penetration. Moreover, it was revealed that both a seed population of solar protons and the SSC shock-induced compression of the magnetosphere were necessary conditions for the formation of a new proton belt. The outer boundary of the inner zone protons were more affected by a SSC and a newly formed belt can be affected by the ensuing or a subsequent storm, which might occur in rapid successions; this was the case in June and July 1991. The acceleration process was effective for both northward and southward IMF, with more energization and inward radial transport for the southward case for otherwise comparable solar wind parameters, because of the initially more compressed magnetopause in the southward case. The inner boundary and stability of the newly formed belt depended on the magnitude of radial transport the time of formation and subsequent ring current perturbation of adiabatic trapping.

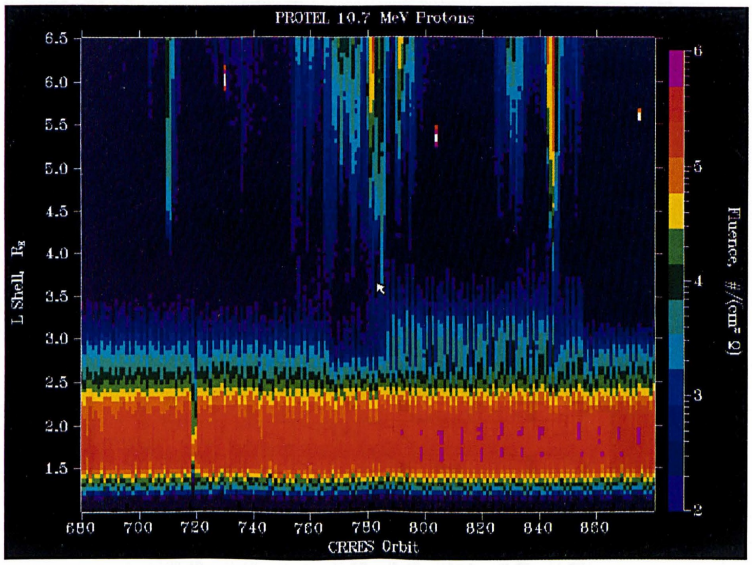

Figure 1.33: Proton fluence in 10.7 MeV channel of Protel instrument on CRRES, for orbits 680 to 880 (May 1 through July 23, 1991). There was a decrease in maximum L of 10.7 MeV protons on orbit 765 (June 4-5), and increase on orbit 783 (June 12), coincident with SSCs noted in the paper. A similar decrease in maximum L was seen on orbit 856 (July 13) [Hudson et al., 1997].

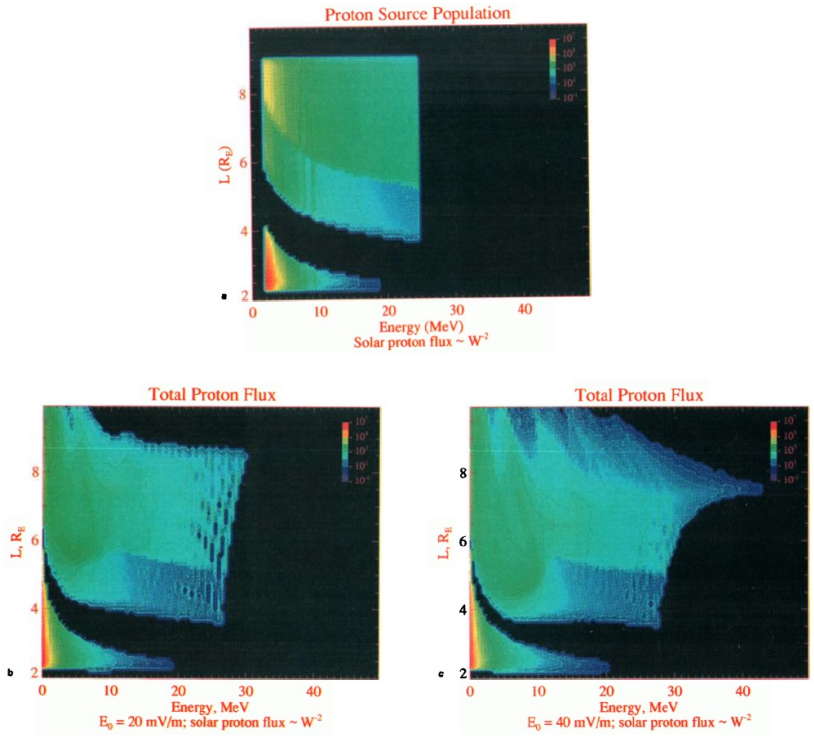

Figure 1.34: Relative proton flux versus energy and L shell: (a) for input source population. There were two solar proton source populations described by energy cutoffs in the text, which modeled the energy dependent radial penetration depth of solar proton flux versus L; a third population models the inner zone. A W^{-2} power law was superimposed on the solar proton source populations, while a W^{-5} power law was used for the inner zone. (b) Flux versus energy and L shell after 300 seconds, averaged over a $\Delta L = 0.1$ and $\Delta W = 0$ using input source population in Panel (a) and analytic field models described in text, with $E_0 = 20$ mV m^{-1} (c) Same as Panel (b) with $E_0 = 40$ mV m^{-1} [Hudson et al., 1997].

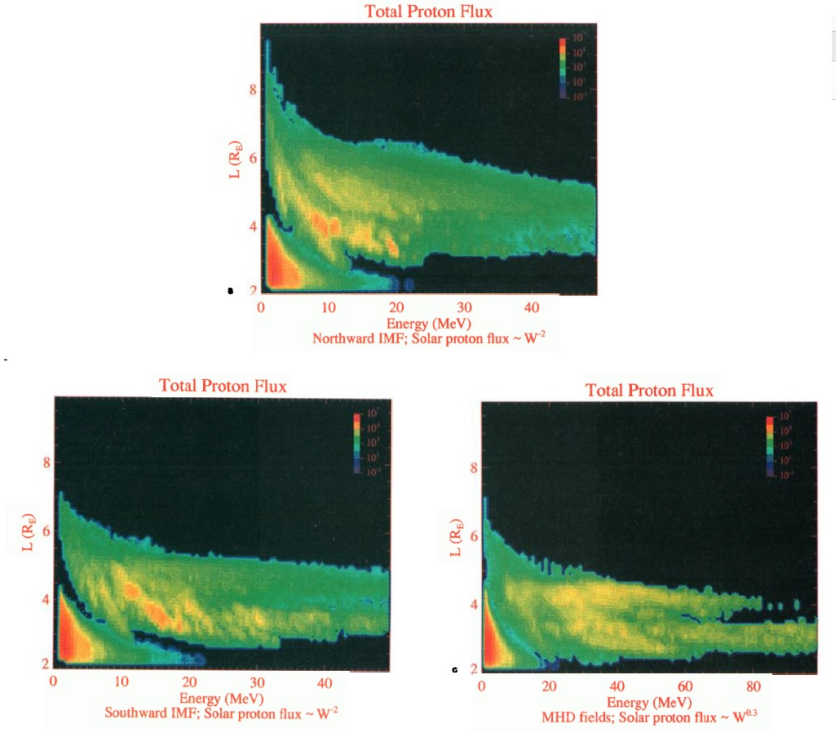

Figure 1.35: Flux versus energy and L shell after 500 seconds using input proton source population in last figure Panel (a) for (a) northward IMF case, (b) southward IMF case and (c) MHD fields, with a solar wind shock speed of 1000 km s^{-1}. (b) Southward IMF case for a solar wind shock speed of 1400 km s^{-1} and a W$^{-0.3}$ solar proton power law weighting, appropriate for the March 1991 event [Hudson et al., 1997].

1.3.5 Inner Proton Radiation Belt Models

1. [Badavi, 2011]: An inner trapped proton flux model GEORAD (GEOmagnetic RADiation) was developed by a suite of codes which computed the cutoff rigidity, the trapped proton and electron environments. The web version of GEORAD was named OLTARIS (On-line Tool for the Assessment of Radiation in Space). GEORAD suite is applicable to radiation environment prediction at Low-Earth Orbit (LEO), Medium-Earth Orbit (MEO) and Geosynchronous-Earth Orbit (GEO) at quiet solar periods. GEORAD interest was in the study of long term effect of the trapped environment and hence it did not include any short term external field contribution due to solar activity. The paper presented the validation of the trapped proton model at LEO by using GEORAD in comparison with reported measurements from the compact environment anomaly sensor (CEASE) science instrument package, flown onboard the tri-service experiment-5 (TSX-5) satellite during the period of June 2000 to July 2006. The authors had emphasized the validation of the differential and integral flux profiles for $\geq$ 40 MeV.

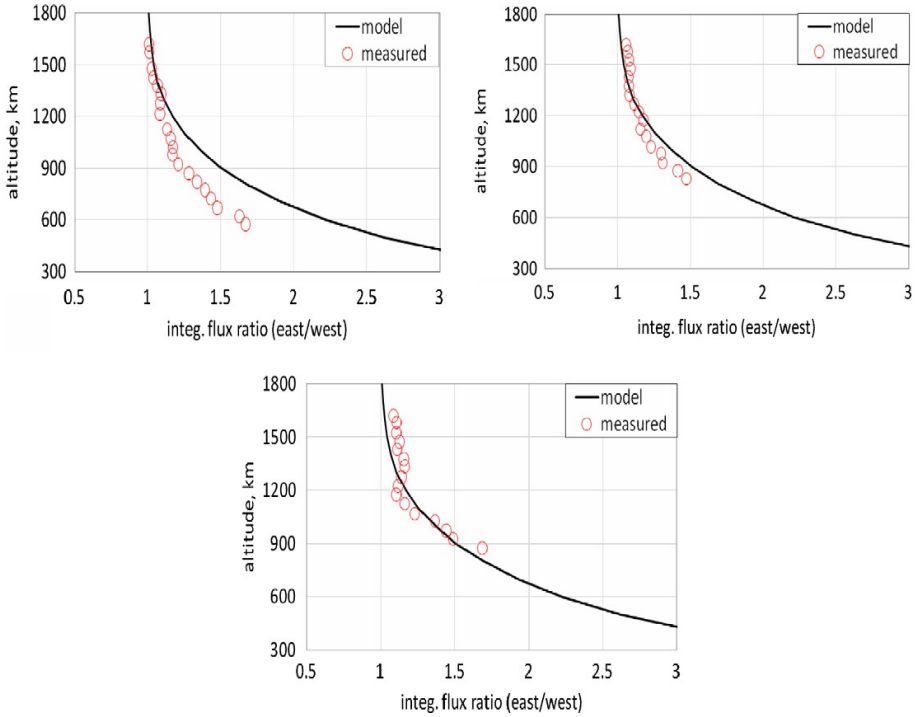

Figure 1.36: Altitude dependent, east/west traveling integral proton (> 40 MeV) flux ratios at geographic coordinates 18 ˚S, 300˚E (top left), 9˚S, 309˚E (top right) and 0˚S, 315˚E (bottom) [Badavi, 2011].

2. **AP Models**:

   Among the more established trapped models are the historic and popular AE8/AP8, dating back to the 1980s, the historic and less popular CRRES electron/proton, dating back to 1990s and the recently released AE9/AP9/SPM. The AE9/AP9/SPM model is a major improvement over the older AE8/AP8 and CRRES models. This model was derived from numerous measurements acquired over four solar cycles dating back to the 1970s, roughly representing 40 years of data collection. In contrast, the older AE8/AP8 and CRRES models were limited to only a few months of measurements taken during the prior solar minima and maxima. In the paper published by [Badavi, 2014], its dual goal was to first validate the AE8/AP8 and AE9/AP9/SPM trapped models against ISS dosemetric measurements for a silicon based detector, and to assess the improvements in the AE9/AP9/SPM model as compared to AE8/AP8 model.

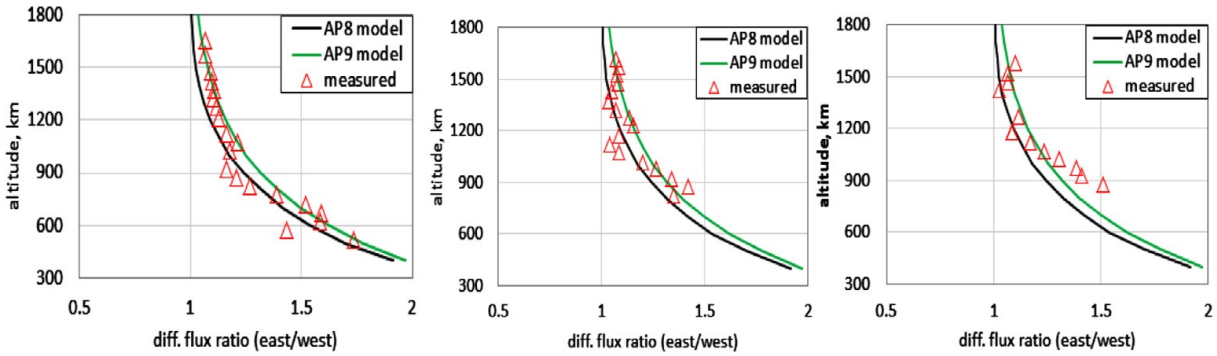

Figure 1.37: Altitude dependent, east/west traveling differential proton (40 MeV) flux ratios at geographic coordinates 18°S, 300°E (top left), 9°S, 309°E (top right) and 0°S, 315°E (bottom) [Badavi, 2014].

Figure 1.37 indicates that within SAA, the proton flux density was lower during solar maximum than solar minimum. This was mostly due to the variation of the atmospheric density in response to solar energy output. During solar maximum, the sun releases energy at a higher frequency. This extra energy excites atmospheric neutral particles, allowing them to attain higher altitudes in the atmosphere and as the result, atmospheric density increases as solar cycle moves toward solar maximum.

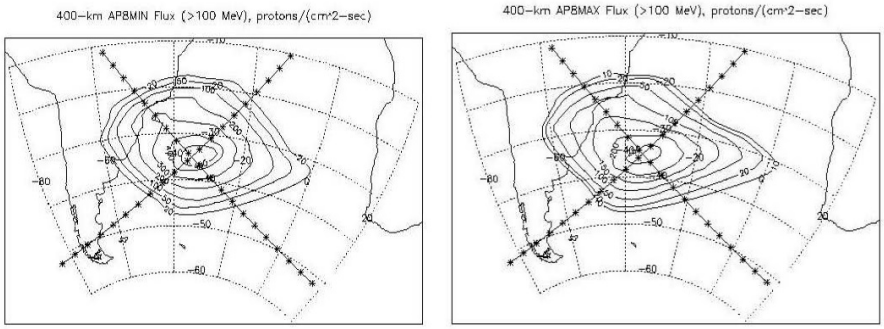

Figure 1.38: SAA contours of AP8MIN and AP8MAX integral flux (> 100 MeV) at 400 km 1.37.

Moreover, [Fennelly et al., 2015] had also demonstrated several AP9 model outputs as shown in Figures 1.39 and 1.40.

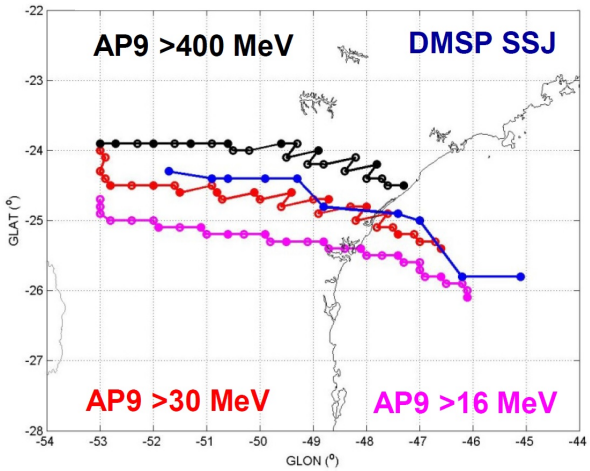

Figure 1.39: Location of SAA peak from 1989 to 2020 computed by AP9 model [Fennelly et al., 2015].

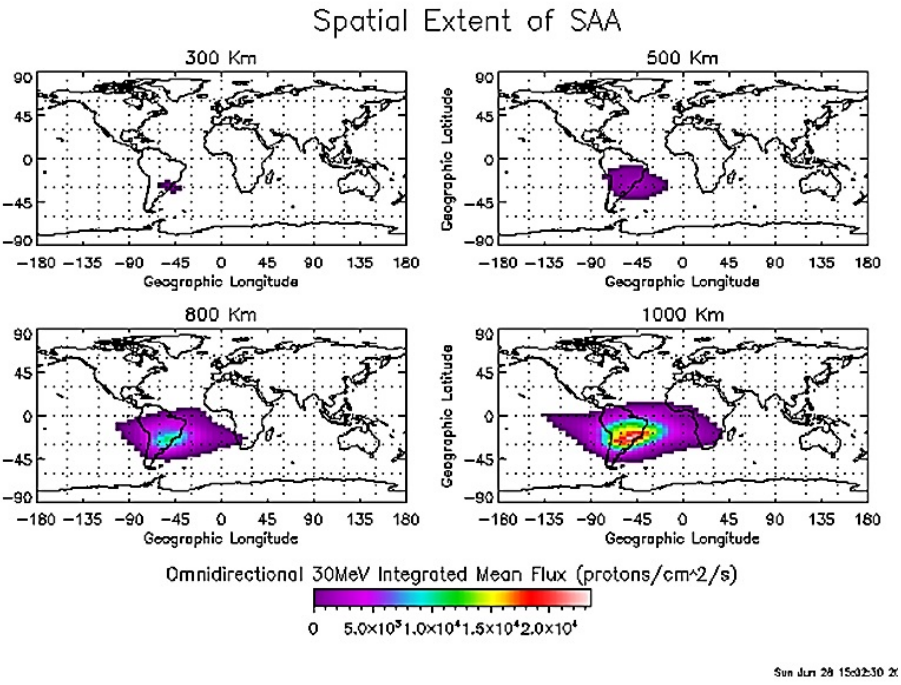

Figure 1.40: Spatial extent of the SAA computed by AP9 model [Fennelly et al., 2015].

1.3.6 SAA and Satellite Risk Radiation

1. [Limousin et al., 2015]: The 6th Japanese X-ray scientific satellite ASTRO-H (JAXA) with the support of the the French Atomic Energy Commission (CEA) was operating at LEO at 550 km altitude. The spacecraft then was passing through the SAA. The purpose of this study was to investigate the effect of the accumulated proton fluence on the spectral response of the CdTe detector performance. The irradiation environment was assessed and the proton flux was simulated on the sensors over the entire mission as well as the secondary neutrons flux due to the primary proton interactions. It was found that the secondary neutrons might be more active to reduce the performance on the long run.

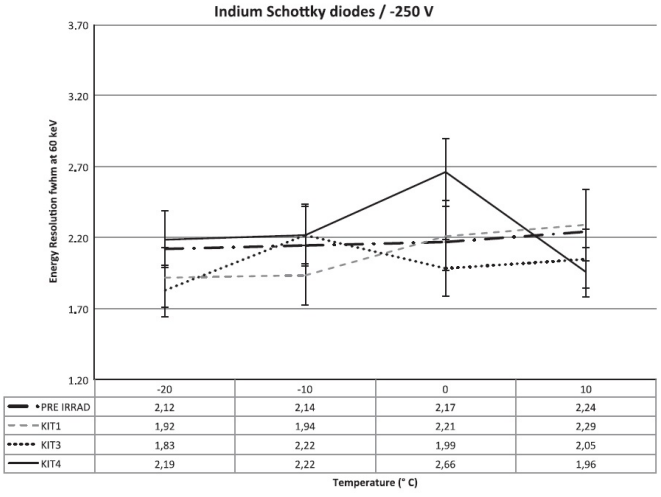

Figure 1.41: Spectral response at 60 keV for Indium Schottky diodes at -250 V against temperature and for different irradiation conditions. Error bars gave the standard deviation of the spectral resolution in a given kit. Relative errors were found to ranging from 8 to 11 % for Indium diodes. [Limousin et al., 2015].

2. [Narici et al., 2015]: A 3D radiation environment study was developed throughout the International Space Station ISS-US Lab and through the ALTEA detector system mounted in Columbus during 2010–2012. The study purpose was investigating the radiation environment in the ISS. The radiation flux was shown

to be roughly similar across the different positions, while the radiation quality, described by the dose equivalent and by the quality factor and most relevant for radiation risk assessment, features a larger variability, in some cases up to a factor of 3. The truss shielding technique was confirmed to be effective. The presence of the radiation from the SAA strongly modified the measured radiation pattern, with a large variability in time.

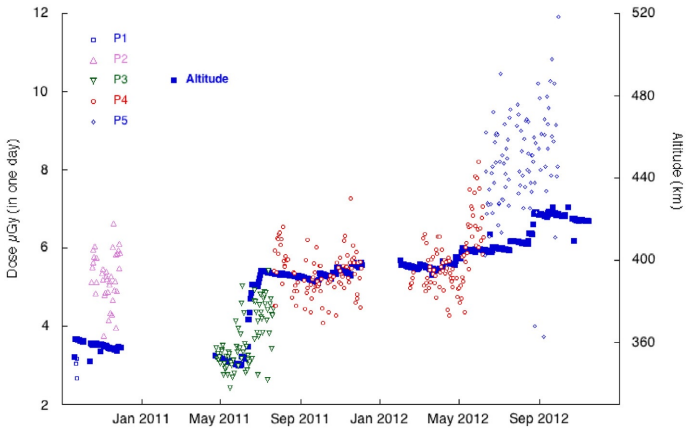

Figure 1.42: The radiation during the passes through the SAA was strongly variable as shown in the current figure. Dose in one day measured in the z-direction during the entire measurement period, over the five different sites. The mean altitude of the ISS was also reported (right axis). Note the lowest point in the quality factor plot during the March 2012 Solar Proton Event (SPE) and *Dst* index = -145 nT, due to the high concentration of protons that featured low Linear Energy Transfer (LET) and therefore a dose equivalent rate value similar to the dose rate one [Narici et al., 2015].

3. [Federico et al., 2015]: The authors analyzed the radiation measurements aboard aircraft during flight routes between airports as well as flights passing through the SAA region. The experimental results were compared to the estimates obtained using the computer codes such as EXPACS for the accumulated dose estimation in the route; the comparison showed that the computational estimates demonstrated a good agreement with the measurements. Furthermore, it was found that there was no observable systematic effect, confirming that there was not influence of the SAA on the radiation dose at flight altitude, at least in calm solar and magnetospheric conditions. The results did not allow concluding if there were any types of influence of the SAA in extreme disturbed solar and magnetospheric conditions which could be the subject for future investigation..

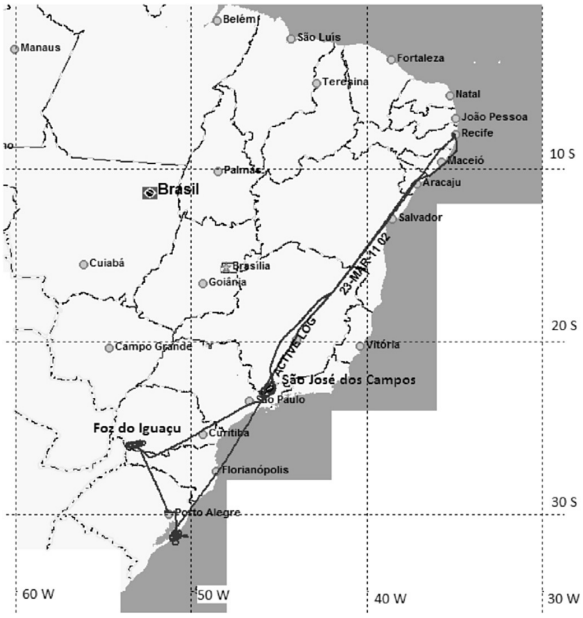

(a) Visualization on the region covered by the flight missions [Federico et al., 2015].

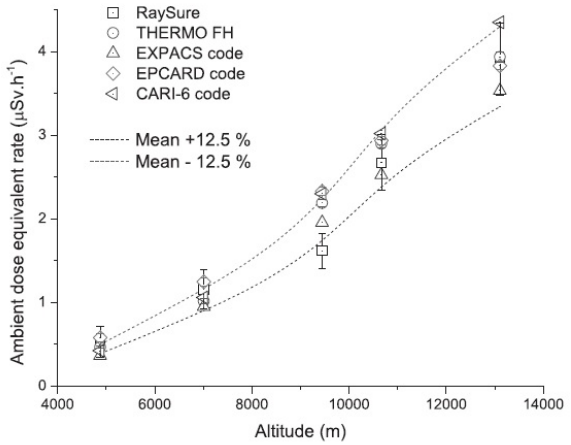

(b) Results for missions 1, 2, 3, 4 and 5, performed near Sao Jose dos Campos city, Brazil (9.6 GV cut-off rigidity). The dashed curves correspond to a fitting of the mean of values (measurements plus computational calculation) on each altitude ± 12.5 %, only to allow visual guidance [Federico et al., 2015].

1.4 Gaps

From all the intensive efforts that were briefly introduced in the previous section of the literature review, we would like to summarize the main gaps from these recent studies:

1. SAA and short-term space weather study: The research that studied the SAA using observations from satellite missions during a year or a geomagnetic storm event, were limited to a specific range of proton energy and a selected altitude. As clearly commented by the authors themselves (underlined text), SAMPEX observations can roughly sample the data in the SAA within 12 hours. During such time scale, the assessed data cannot entirely detect the proton dynamics in the SAA. The main conclusions are that the SAA intensity at both altitudes ≈ 400 and ≈ 800 km were decreased during geomagnetic storms and were increased around the equinox times.

2. SAA and long-term space weather study: The SAA variations with respect to solar cycles and solar activity were studied in detail and the main important common and confirmed conclusion is that the SAA intensity is anti-correlated with solar activity.

3. SAA and Solar Proton Event (SPE): Although the Solar Proton Events (SPE) were essentially affecting the high-latitudes regions, however from the presented researches above, some features could be observed in the anomaly. For example, in Figure 1.29, the differential flux intensity in the SAA was increased, and from Figure 1.42, the radiation dose measured in the SAA were significantly increased.

4. SAA and numerical simulations of the inner radiation belt: The numerical simulations carried out to study the inner radiation belt are of great value. However, as discussed by [Hudson et al., 1997], the authors implemented Northrop-Teller guiding center model [Northrop, 1963b] whose accuracy is low as commented by [Öztürk, 2012], adding that the background magnetic field was computed from MHD simulations whose accuracy in low L shells is generally low and finally the implemented electric field formulation was analytic.

5. Proton trapped radiation models:

   (a) as discussed by [Fennelly et al., 2015], Figure 1.44 demonstrates small deviations between the trapped model AP9 and the measurements from POES satellite. From Figure 1.40, the proton flux resolution for the low altitudes (300 and 500 km) is very low and is probably experiencing lack of data availability.

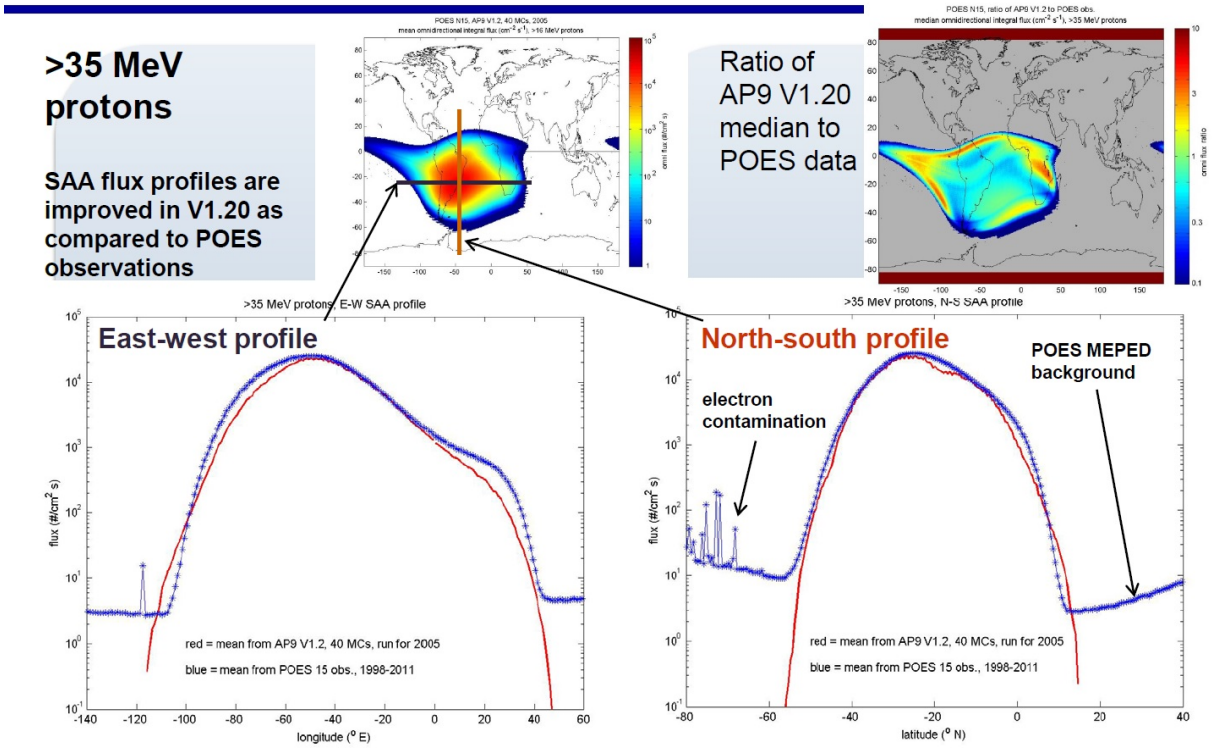

Figure 1.44: AP9 Model Validation [Fennelly et al., 2015].

   (b) as discussed by [Petersen, 2011], the author's main purpose was to confirm about the accuracy of the available and well-established trapped models, namely the AP models, to estimate the Single Event Effects (SEE) on satellite. Below is the summary of his comments:

i. **The East–West effect**: This refers to the fact that particles arrive with greater abundance from the west due to the effects of the Earth's magnetic field and atmosphere. The effects are noticeable from 500 to 1200 km and may be a factor of 2 at the lower altitudes. This may be important for spacecraft that maintain an east–west orientation [Buhler et al., 1997] and [Heckman and Nakano, 1963]. The East–West effect may be very important for some spacecraft in the SAA. At low altitudes the directional difference may be a factor of 2 to 7. It is important to take the anisotropy into account if a spacecraft maintains fixed axis throughout the mission.

ii. **The uncertainty factor**: for protons in AP-8 is quoted as 2. It represents the uncertainty from combining the data sets from many instruments and satellites and is not meant to measure the variation in the actual environment. [Takagi et al., 1993] presented proton results at the equator indicating that the radiation belt was more intense at lower altitudes than modeled by AP8. This may indicate higher proton fluxes in some orbits, although the impact on LEO is not apparent. [Underwood et al., 1993] pointed out that the same parts flown in two distinct orbits had different ratios of predicted to observed upset rates.

iii. **Between a static and stable model**: The AP-8 model is a static model and it is well known that the proton radiation belts are dynamic. One aspect of this is the slight shift of the SAA from the position described by AP-8. An extreme example of the dynamic nature is the production of new radiation belts by the flare on March 24, 1991, whose effects on Single Event Upset (SEU) rates have been described, for example by [Campbell et al., 1992]. The largest uncertainties in the environments arise because of the dynamic nature of the proton radiation belt(s).

iv. **A long-term averaged model**: It appears from the results of these papers and from the near agreement of upset rate predictions and observations that there is nothing drastically wrong with the commonly available space environments. The proton environment may occasionally experience fluctuations that are not described by the static models, but the long-term averages appear to be well described.

v. **As a summary**: There is no evidence of serious problems with the methods of upset rate prediction. The predictions do need data that has been carefully obtained. Although it is possible to make good predictions, there are still a number of possible sources of error. The relatively large number of cases with a large difference between prediction and observation indicates that a great deal of care must be taken with the laboratory measurements, the predictions, and the space measurements.

6. SAA and radiation effects: As already mentioned, the dynamic nature of the inner radiation belts can arise some level of uncertainties in the prediction and the forecast of their response by using the long-term averaged models. Such uncertainties could create a source of unpredicted radiation risks which could reduce the performance of the spacecraft components (= Single Event Upset (SEU)) or in worst case, cause physical damages (= Single Event Latch-up (SEL)); e.g. according to [Federico et al., 2015], the radiation measurements aboard aircraft were addressed to study the SAA during quiet conditions; the authors clearly mentioned that the results did not include the effects of the extreme disturbed solar and magnetospheric conditions (underlined text).

1.5 Motivations

1. Develop a simulation model for the inner proton belt: The SAA is considered as a permanent feature of the inner proton belt along with the geomagnetic field. Hence, the main motivation and the core of the current research are the development of a simulation model to study the inner proton belt dynamics according to space weather activity. This main motivation consists of several minor initiatives:

   (a) **Resolve the gaps existing in the past researches**: The main gaps are that the observations were carried out at a specific altitude (note that the satellite orbit could be subjected to some changes in altitudes), within or greater than the time-scale of days, and the instruments were addressed to measure a specific range of particle energy and fixed detector angle. It should be noted also that the measurements could be subjected to electron contamination as shown in Figure 1.44. We are motivated to resolve the last issues by studying numerically the anomaly by calculating the magnetic and particle flux responses for any particle type, energy and pitch angle at any desired altitudes, by performing test particle simulations.

   (b) **Continue the previous efforts**: We believe that the numerical simulations could add new insights about the particle dynamics inside the SAA, especially during different space weather conditions. For example, [Engel et al., 2015] studied the loss proton process in the outer boundary of the inner radiation belt; starting from this study, we will analyze the inner boundary dynamics of the inner

radiation belt. [Hudson et al., 1997] used the numerical approach as well to simulate the inner proton radiation belt during Sudden Storm Commencement (SSC); we would like to use a better guiding center model, which is the Tao-Brizard-Chan model, for its high level of accuracy. About the magnetic response of the SAA, we would like also to continue the work of [Qin et al., 2014], by implementing real solar wind data and IMF conditions to the realistic geomagnetic model (IGRF+T96/T01/TS05).

(c) **Understand the physical processes occurring inside the SAA**: Most studies related to the SAA were focusing only on the 2D configuration of either the magnetic strength or the proton flux intensity. By using the numerical approach, the 3D configuration could be easily achieved so that we can better understand the dynamic nature of the SAA.

2. Better estimate the SAA dangerous radiation effects on spacecraft: According to the previous research carried out to study the inner radiation belt effect on the radiation environment of the satellite mission at specific orbit, especially by [Petersen, 2011], the better was the inner trapped radiation model, the better prediction would be the Single Event Upset (SEU) rates and the absorbed radiation dose rates, especially during disturbance time such as flare emission, geomagnetic storm and as confirmed during solar minimum activity.

3. Design more effective shielding for spacecraft: Consequently, the earlier assessment of the Single Effect Upset (SEU) rates and the absorbed radiation dose rates could lead to develop efficiently the spacecraft shielding not necessarily by increasing the slab thickness but by finding new approaches and advanced techniques to mitigate the effects of the Single Event Effect (SEE) in general.

1.6 Objectives

The research objectives will be classified into three major milestones:

1. Estimate the magnetic variations of the SAA due to space weather elements: First of all, in order to study the magnetic variations in the SAA, we will implement the realistic geomagnetic models, Tsyganenko models T96, T01 and TS05 combined with the main (internal) magnetic field Internal Geomagnetic Reference Field (IGRF) model. The main parameters of the SAA will be the minimum magnetic field intensity (= SAA center), the latitudinal and longitudinal movement of the SAA center and the area (calculated at the desired altitude and below a selected threshold). The input conditions of the geomagnetic field are real solar wind data. We will perform two different analysis: (1) a long-term study for approximately 11 years: its purpose is to detect the variations of the magnetic SAA parameters with respect to the implemented space weather information. (2) a shorter term study of 4 years: its purpose is to find out statistically the correlation between the input solar wind conditions and the output SAA magnetic parameters, hence, to find out which input parameter will have the dominant effect on the SAA magnetic variations.

2. Estimate the proton flux variations in the SAA during geomagnetic storms: Through understanding the magnetic variations of the SAA corresponding to the input space weather conditions can help us to further investigate the nature of the proton dynamics inside the anomaly, since the main driver of the test particle simulations is the background magnetic field. In this research phase, we will perform two studies: (1) a short-term study (for several proton drift periods corresponding to one minute in real time), to calculate the proton flux in the SAA by changing the magnetic field configuration with respect to various input space weather conditions during selected events which reflect the quiet, moderate and intense geomagnetic activity as well as the seasonal variation. (2) A longer term study within a full geomagnetic storm ($\approx$ 12 hours), in order to understand the proton flux evolution in the SAA corresponding to the selected event. In these last simulations, we implement a background inductive electric field, that is calculated by the time-varying magnetic field information, so that we can observe the electric field effect on the inner trapped proton belt simulation and hence, in the SAA. The output numerical results are compared with the published works by [Zou et al., 2015] and [Dachev, 2018]. The two mentioned authors did examine deeply the proton flux response in the SAA during geomagnetic storms using satellite measurements at two specific altitudes $\approx$ 400 and 800 km. These two research are of great value for our current numerical study.

3. Assess the corresponding variations in radiation dose on the spacecraft: The final phase of the research is to evaluate the radiation environment on spacecraft based on the proton flux and the energy spectrum obtained from the numerical simulations. The main two parameters to be estimated are the Single Event Upset (SEU) rates and the absorbed radiation doses during a selected satellite mission, orbit information, shielding thickness and material. The corresponding groundtrack of the satellite will be combined with proton flux and energy flux contours maps to evaluate the dose accumulation on the satellite.

1.7 Complications

- Problem size: The merits of developing test particle simulation codes to simulate the inner radiation belt response with respect to space weather conditions are various; we believe that the selected approach is very useful for several applications such as the study of the SAA proton flux variations, the current research. Although, the main complications arise if the desired problem time-scale is large and if the required counting data (particle number) to achieve an acceptable interpolation is huge.
- Parallel computing: In order to overcome the previous obstacles, one way is to implement the parallelization techniques by using Message Passing Interface (MPI) into our test particle simulation codes instead of the serial computing method in order to accelerate the codes. As defined by Wikipedia, *"The Message Passing Interface (MPI) is a standardized and portable message-passing standard designed by a group of researchers from academia and industry to function on a wide variety of parallel computing architectures. The standard defines the syntax and semantics of a core of library routines useful to a wide range of users writing portable message-passing programs in C, C++, and Fortran. There are several well-tested and efficient implementations of MPI, many of which are open-source or in the public domain. These fostered the development of a parallel software industry, and encouraged development of portable and scalable large-scale parallel applications".*

The thesis is organized as follows: the "Introduction" in Chapter 1, the "Methods" in Chapter 2, four consecutive chapters corresponding to the objectives explained above: "SAA Magnetic Response: Long-term Variations" in Chapter 3, "SAA Magnetic Response: Mid-term Variations" in Chapter 4, "Test Particle Simulations: Calculation of SAA Proton Flux Response in Drift Period Time Scale" in Chapter 5, "Test Particle Simulations: Calculation of SAA Proton Flux Response during a Geomagnetic Storm" in Chapter 6 and "Assessment of the LEO Spacecraft Radiation Environment due to its Passage in the SAA" in Chapter 7, with the "Summary and Future Directions" in Chapter 8.

Chapter 2

Methods

2.1 Basic Definitions

2.1.1 Coordinate Transformation

The sequence of the coordinate transformation should be as follows: Geodetic (GEOD) to geographic (GEO) to geomagnetic (GSM) coordinates. Since the Earth is approximated by a spheroid, locations near the surface are described in terms of the geodetic latitude, longitude and height, and this is the definition of the "Geodetic" coordinate system. The geodetic latitude is different from the geocentric latitude because the geodetic latitude is defined as the angle located between the equatorial plane and normal to the ellipsoid, whereas the geocentric one is defined as the angle located between the equatorial plane and the line joining the point to the ellipsoid's center. This is the first coordinate transformation, while the second one, is achieved by calculating the dipole tilting angle, which is defined as the angle between the Earth's rotation and magnetic axis.

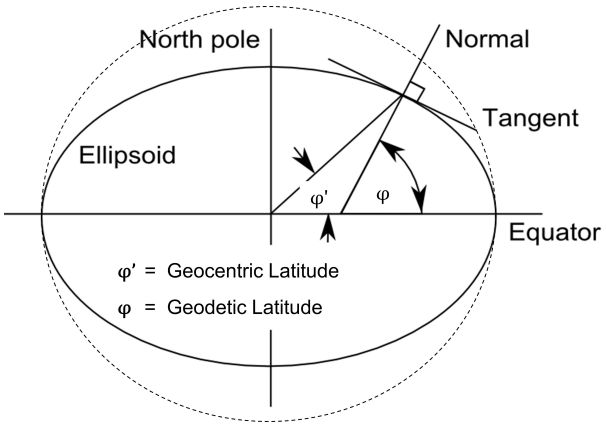

Figure 2.1: The difference between the geocentric and geodetic latitudes

2.1.2 Geodipole Tilting Angle Definition

The x-axis is pointed from the Earth toward the Sun, which means that the "geodipole" tilting angle, which is the angle between the dipole and vertical axes, varies with respect to time, due to the angle located between the Earth's equatorial plane and the ecliptic plane 23.5°, added with the angle located between the rotation and dipole axes 10.5°. The geodipole tilting angle is defined as positive when the northern hemisphere is tilted toward the Sun [Cnossen and Richmond, 2012], [Cnossen et al., 2012] and [Qin et al., 2014].

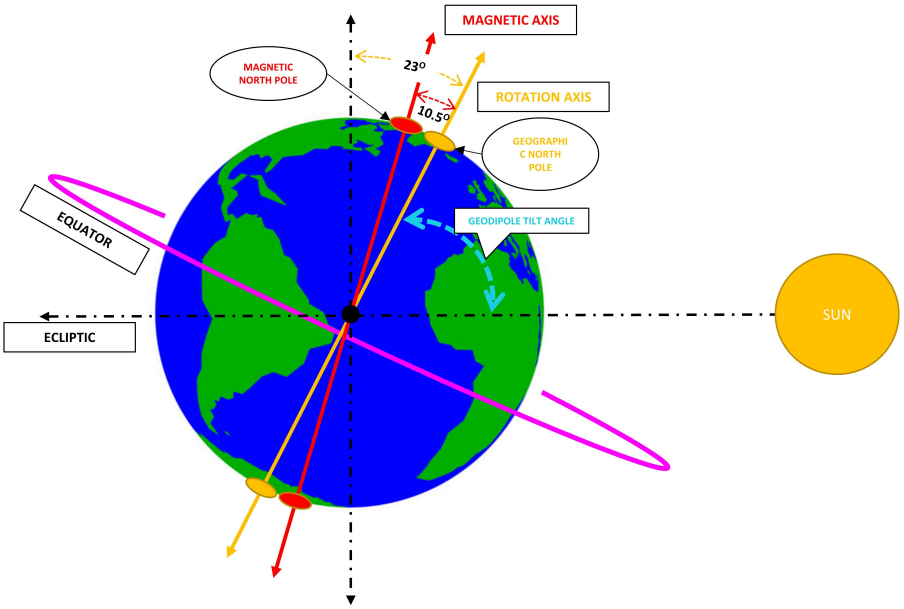

Figure 2.2: A simple representation of the geodipole tilting angle

2.1.3 *Dst* Index Definition

The *Dst* index is a magnetic activity index which is derived from near-equatorial geomagnetic observatories network that can measure the intensity of the global symmetrical equatorial electrojet, the "ring current".
The *Dst* (**D**isturbance **S**torm **T**ime) equivalent equatorial magnetic disturbance indices are derived from hourly scalings of low-latitude horizontal magnetic variation. They show the effect of the globally symmetrical westward flowing high altitude equatorial ring current, which causes the "main phase" depression worldwide in the H-component field during large magnetic storms. The geomagnetic index database available in the following website [1], provides the final hourly *Dst* indices for the period 1957 through 2014, as derived by M. Sugiura and T. Kamei, WDC-C2 for Geomagnetism, Faculty of Science, Kyoto University, Kyoto 606, Japan.
Hourly H-component magnetic variations are analyzed to remove annual secular change trends from records of a worldwide array of low-latitude observatories. A cosine factor of the site latitude transforms residual variations to their equatorial equivalents and harmonic analysis isolates the term used as the *Dst* index. Sugiura described *Dst* derivation in ANNALS OF THE IGY [2].
Inside the Earth's magnetosphere, various currents are occurring. Figures 2.3a demonstrate the ring current whose activity is measured by the *Dst* index. As shown in Figure 2.3b, for a typical magnetic storm, the *Dst* index shows a sudden rise, corresponding to the *Storm Sudden Commencement (SSC)* or the *initial storm phase*, and then decreases sharply as the ring current intensifies; this is the *main storm phase*. Once the IMF turns northward again and the ring current begins to recover, the *Dst* index begins a slow rise back to its quiet time level, which is called *the recovery storm phase.*

[1] http://wdc.kugi.kyoto-u.ac.jp/dstdir/
[2] From official NOAA website: https://www.ngdc.noaa.gov/stp/geomag/dst.html

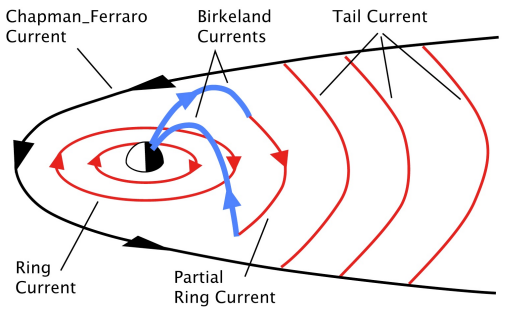

(a) Schematic illustration of the current system in the Earth's magnetosphere

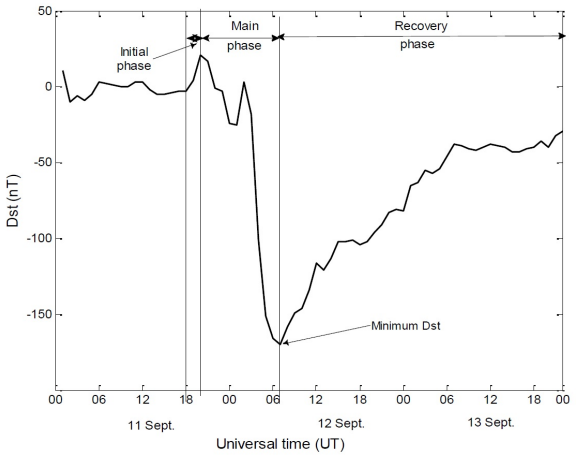

(b) A typical magnetic storm event showing the three storm phases: the initial, the main and the recovery phases [Okpala and Ogbonna, 2018].

2.2 Magnetic Field Models

2.2.1 Internal Magnetic Field Models

2.2.1.1 CHAOS Magnetic Field Model

CHAOS magnetic field model defines the static (core and crustal) field (up to degree n = 50), with an accurate estimation of the temporal changes during 6.5 years. The model name was selected to reflect the uncertainty and the chaotic nature of the geomagnetic field, by implementing the high-precision magnetic measurements from the three satellites Ørsted, CHAMP and SAC-C taken between 1999 March and 2005 December [Olsen et al., 2006]. The updated time-dependent geomagnetic field CHAOS-6 included more than two years of magnetic data from the Swarm mission, and monthly means from 160 ground observatories as available in March 2016 [Finlay et al., 2016]. According to the official website [3], the most recent models (after 2019) are still under review.

2.2.1.2 World Magnetic Field Model (WMM)

According to the official website of National Oceanic and Atmospheric Administration (NOAA)[4], the World Magnetic Field Model is a collaborative product of the United States' National Geospatial-Intelligence Agency (NGA) and the United Kingdom's Defence Geographic Centre (DGC). The WMM was conceived by the National Centers for Environmental Information (NCEI, Boulder CO, USA) and the British Geological Survey (BGS, Edinburgh, Scotland). The World Magnetic Model is a standard model used by the U.S. Department of Defense, the U.K. Ministry of Defence, the North Atlantic Treaty Organization (NATO) and the International Hydrographic Organization (IHO). This model is applied in attitude, navigation and heading referencing systems. The model is produced each 5-year, where the current model is expiring on December 31, 2024.

2.2.1.3 International Geomagnetic Reference Field (IGRF) Model- Version 12

The 12^{th} Generation of the International Geomagnetic Reference Field (IGRF) has been developed by the International Association of Geomagnetism and Aeronomy (IAGA). It is a standard mathematical model that describes the Earth's main (internal) magnetic field using spherical harmonics formulation. The model is of series order 12 and the Gaussian coefficients are determined using magnetic field data from ground stations and from satellites around the world. Further detailed information is available in the main paper published by the authors [Thébault et al., 2015] and also NOAA website [5]. Furthermore, in December 2015, IAGA released the new IGRF model V-13.

2.2.1.4 IGRF versus WMM

It was clearly explained in the official website that both models are estimated from the most recent data and are of comparable quality. The differences between IGRF and WMM are within expected model inaccuracy.

[3] https://www.space.dtu.dk/english/research/scientific_data_and_models/magnetic_field_models
[4] https://www.ngdc.noaa.gov/geomag/WMM/DoDWMM.shtml
[5] Same previous website

The WMM is a predictive-only model and is valid for the current epoch (= 2020.0 to 2025.0). The IGRF is retrospectively updated and the latest update, IGRF-12 is valid for the years 1900 to 2020.

According to the above brief information about the three geomagnetic models, we select the IGRF-V12 model to describe the internal geomagnetic field in all our simulations.

2.2.1.5 Mathematical Model: Spherical Harmonic Field Models

The main references of this part are selected from [Finlay, 2011, Chulliat et al., 2015]. The figures plotted in this section are the corresponding outputs of WMM using *Wolfram Mathematica* Notebook.

Representing Periodic Functions in 1D: Any periodic function $f(t)$ over an interval T can be defined from a sum of sinusoidal functions with integer wavenumber m, which is commonly known as Fourier series expansion:

$$f(t) = \sum_{m=0}^{\infty} \left(a_m \cos\left(\frac{\pi m t}{T}\right) + b_m \sin\left(\frac{\pi m t}{T}\right) \right)$$

Since sinusoidal basis functions are orthogonal, thus, integrating their product over the interval of T gives 0, unless the two basis functions are identical:

$$\int_0^T \cos\frac{2\pi m t}{T} \cos\frac{2\pi m t}{T} dt = \begin{cases} \frac{T}{2} & \text{, if } m = n \neq 0 \\ 0 & \text{, if } m \neq n \\ T & \text{, if } m = n = 0 \end{cases}$$

The orthogonality permits us to easily evaluate the weighting coefficients if $f(t)$ is defined.

Wrapping T Around a Longitude Circle: Imagine wrapping the periodic function $f(t)$ around a circle of longitude as shown in Figure 2.4: In that case, we equate t with longitude ϕ and set $T = 2\pi$.

$$f(\phi) = \sum_{m=0}^{\infty} \left(a_m \cos m\phi + b_m \sin m\phi \right)$$

Considering such series representing functions of longitude at all co-latitudes, then,

$$f(\theta, \phi) = \sum_{m=0}^{\infty} \left(a_m(\theta) \cos m\phi + b_m(\theta) \sin m\phi \right)$$

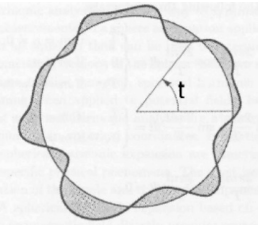

Figure 2.4: Periodic function around a circle

Functions of co-latitude on a sphere are need not be periodic unlike functions of longitude. Then, simple sinusoidal basis is not good choice. To represent the latitude functions, Legendre functions will be selected.

Solution of Laplace's Equation in Spherical Geometry:

$$\boxed{\frac{1}{r^2}\frac{\partial}{\partial r}\left(r^2 \frac{\partial u}{\partial r}\right) + \frac{1}{r^2 \sin\theta}\frac{\partial}{\partial \theta}\left(\sin\theta \frac{\partial u}{\partial \theta}\right) + \frac{1}{r^2 \sin^2\theta}\frac{\partial^2 u}{\partial \phi^2} = 0}$$

The solution procedure is realized by separation of variables method, which leads to the final solution, as follows:

$$u(r, \theta, \phi) = (Ar^l + Br^{-(l+1)})(C \cos m\phi + D \sin m\phi)[EP_l^m(\cos\theta) + FQ_l^m(\cos\theta)]$$

where the three bracketted factors are connected only through the integer parameters l and m, $0 \leqslant |m| \leqslant l$.

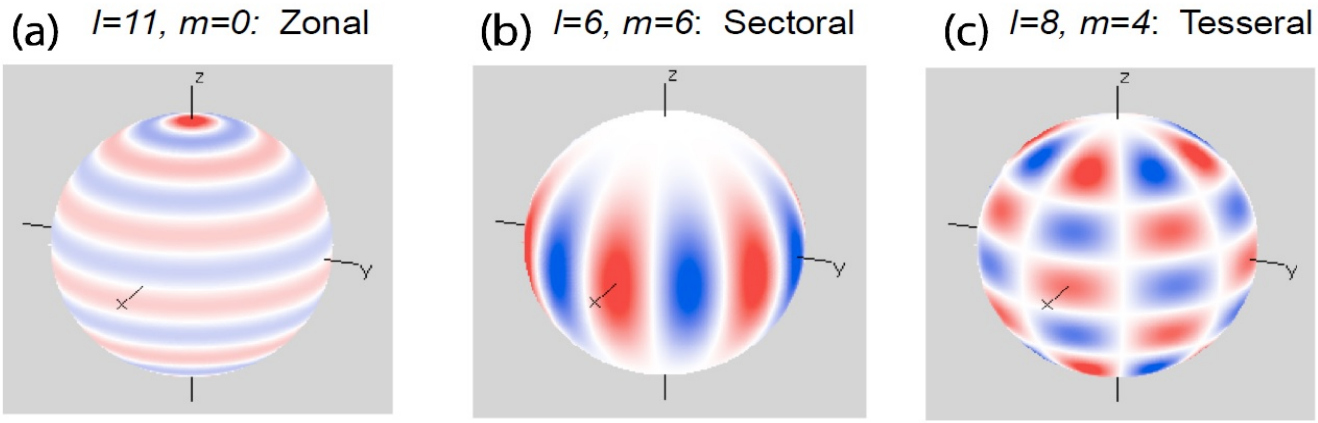

Figure 2.5: An illustration of spherical harmonics for different series

Associated Legendre Functions:

$$P_{l,m}(\mu) = (1-\mu^2)^{\frac{m}{2}} \frac{\partial^m}{\partial \mu^m}\left(\frac{1}{l!2^l}\frac{d^l}{d\mu^l}(\mu^2-1)^l\right)$$

where $\mu = \cos\theta$; m is the order of polynomial (in our case, m is the index specifying the azimuthal wave number), and it equals to 0 for $m > l$. In fact, magnitude varies rapidly with l; to combat this, an extra "Schmidt quasi-normalization" is applied:

$$P_l^m(\theta) = \begin{cases} P_l^m(\theta) & \text{, if } m = 0 \\ \left(2\frac{(l-m)!}{l+m}\right)^{\frac{1}{2}} P_l^m(\theta) & \text{, if } m > 0 \end{cases}$$

Definition of Spherical Harmonics: Substituting linear combinations of associated Legendre functions as the representation of latitudinal variations into the general solution along with a Fourier series representation of the longitudinal variations yields the following spherical harmonic expansion of a function on a spherical surface:

$$\boxed{f(\theta,\phi) = \sum_{l=0}^{\infty}\sum_{m=0}^{\infty}\left(g_l^m \cos m\phi + h_l^m \sin m\phi\right) P_l^m(\theta)}$$

The two first summations are the sum over all possible integer wavelength in co-latitude and longitude; the second term is the Fourier series in longitude (labeled m), and the last term is for the associated Legendre function in co-latitude (labeled l, m).

Examples of Spherical Harmonics:

$$f(\theta,\phi) = g_1^0\cos\theta + g_1^1\cos\phi\sin\theta + h_1^1\sin\phi\sin\theta + g_2^0\tfrac{3\cos^2\theta-1}{2} + g_2^1(\cos\phi)(\sqrt{3}\sin\theta\cos\theta) + g_2^1(\sin\phi)(\sqrt{3}\sin\theta\cos\theta) + g_2^2(\cos 2\phi)(\tfrac{\sqrt{3}\sin^2\theta}{2}) + h_2^2(\sin 2\phi)(\tfrac{\sqrt{3}\sin^2\theta}{2}) + \ldots$$

Each pair of integers (l, m) identifies a particular spherical harmonic Y_n^m. For $m > 0$, a single spherical harmonic consists of both $a\cos m\phi$ and $a\sin m\phi$ part.

Properties of Spherical Harmonics:

- Vanish on $(l-m)$ lines of latitude and $2m$ lines of longitude
- $(l-m)$ = even, then symmetric about equatorial plane
- $(l-m)$ = odd, then antisymmetric about equatorial plane
- $(2l+1)$ coefficients associated with each degree l

Representing the Geomagnetic Field in Spherical Geometry: In source free regions and when there are no magnetic monopoles then:

$$\mathbf{B} = -\nabla V \text{ and } \nabla \bullet \mathbf{B} = 0$$

Assuming these conditions are both appropriate for modeling the geomagnetic field, then the magnetic potential for Earth's magnetic field will satisfy Laplace's equation in spherical geometry:

$$\boxed{\nabla^2 V = \frac{1}{r^2}\frac{\partial}{\partial r}\left(r^2\frac{\partial V}{\partial r}\right) + \frac{1}{r^2\sin\theta}\frac{\partial}{\partial\theta}\left(\sin\theta\frac{\partial V}{\partial\theta}\right) + \frac{1}{r^2\sin^2\theta}\frac{\partial^2 V}{\partial\phi^2} = 0}$$

The general solution (see earlier aside) to this takes the following form involving spherical harmonics:

$$\boxed{V = \sum_{l=1}^{\infty}\sum_{m=0}^{l}\left[\left(\frac{a}{r}\right)^{l+1}\left(g_l^m\cos m\phi + h_l^m\sin m\phi\right)P_l^m(\theta) + \left(\frac{r}{a}\right)^{l}\left(q_l^m\cos m\phi + s_l^m\sin m\phi\right)P_l^m(\theta)\right]}$$

- The first term stands for the internal sources and the second one stands for the external sources
- Weighting coefficients are known as Gauss coefficients and measured in nT
- a = constant reference radius (e.g. Earth's surface = 6371 km)
- We have 2 spherical harmonic expansions in the general solution to Laplace's equation in spherical geometry.
- Fields associated with internal and external sources have different radial dependence.
- This allows internal (e.g. core) and external (e.g. magnetospheric) sources to be efficiently separated, provided observations at different altitudes are available.
- Except during geomagnetic storms the internal field consists of around 97 % of the total field observed at Earth's surface.

Relating Global Models to Observations: Using $\mathbf{B} = -\nabla V$ in spherical geometry and the spherical harmonic expansion for V (internal part), then the spherical polar components of the field can written e.g.

$$B_r = -X = -\frac{\partial V}{\partial r},\ B_\theta = Y = -\frac{1}{r\cos\phi}\frac{\partial V}{\partial\theta} \text{ and } B_\phi = -Z = -\frac{1}{r}\frac{\partial V}{\partial\theta}$$

Together with similar expressions for the other spherical polar co-ordinates, this and the relations below can be used to construct expressions for the observable field components in terms of the Gauss coefficients.

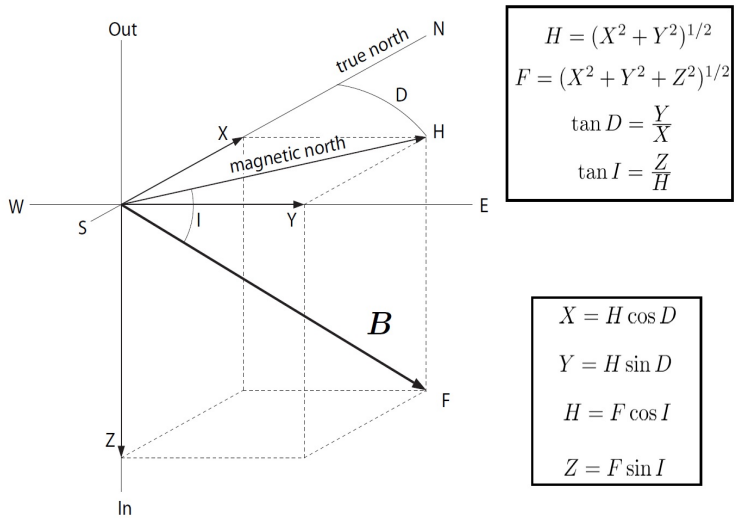

Figure 2.6: Magnetic field directions at a given point as defined in the model

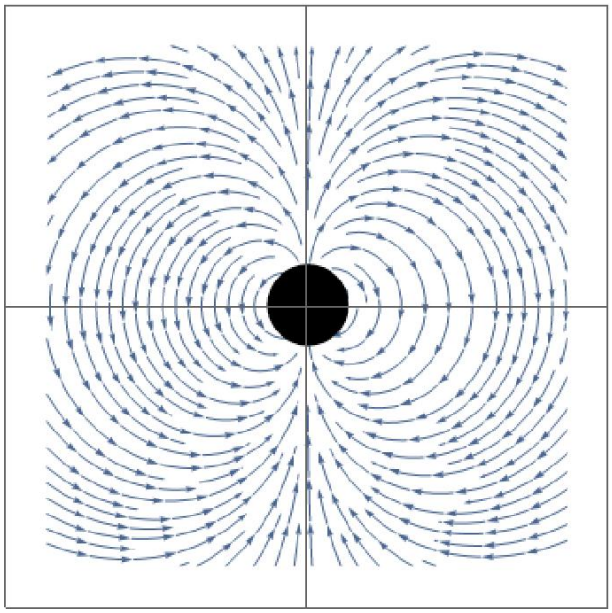

Figure 2.7: Magnetic field fines for ideal dipole case

Graphical Results:

1. **Ideal Dipole** $(m = 1, l = 0)$:

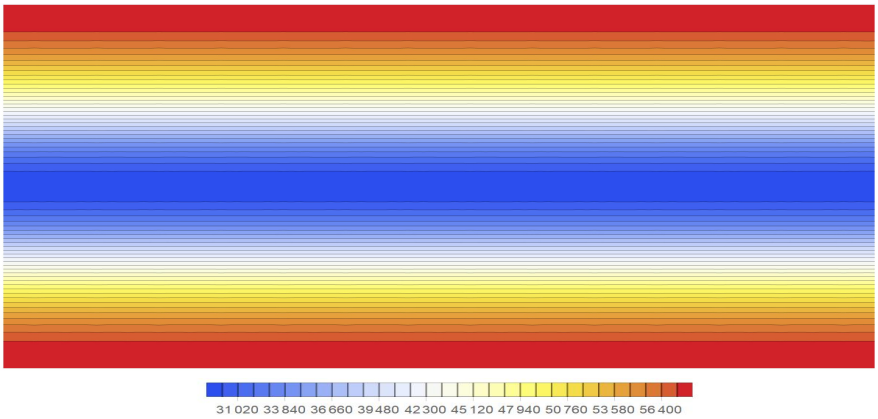

Figure 2.8: Magnetic field strength contours for ideal dipole case

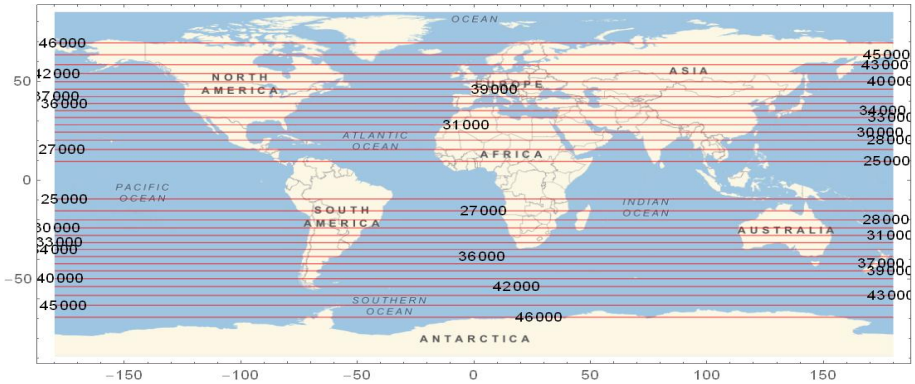

2. **Tilted Dipole** $(m = 1, l > 0)$: The $m = 1$ and $l > 0$ terms give the tilted dipole field; the tilt angle, for the given data for the year 2015, is [Bertotti and Farinella, 1990]:

$$\theta_M = \arctan\left(\frac{\sqrt{(g_1^1)^2 + (h_1^1)^2}}{g_0^1}\right) = 9.6879^o$$

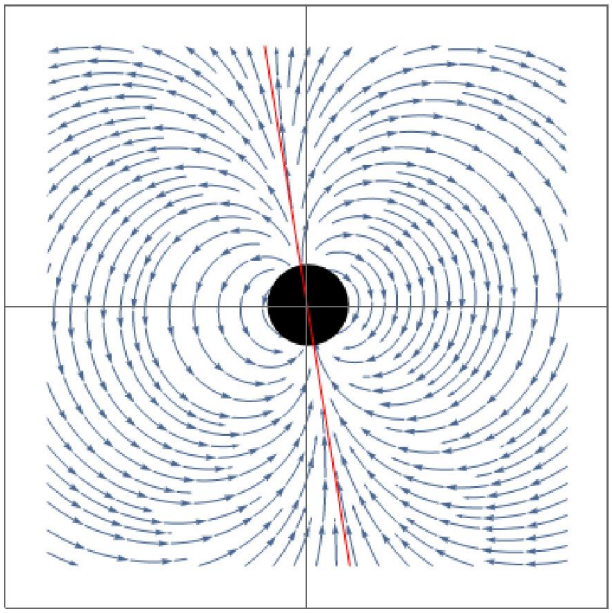

Figure 2.9: Magnetic field fines for tilted dipole case

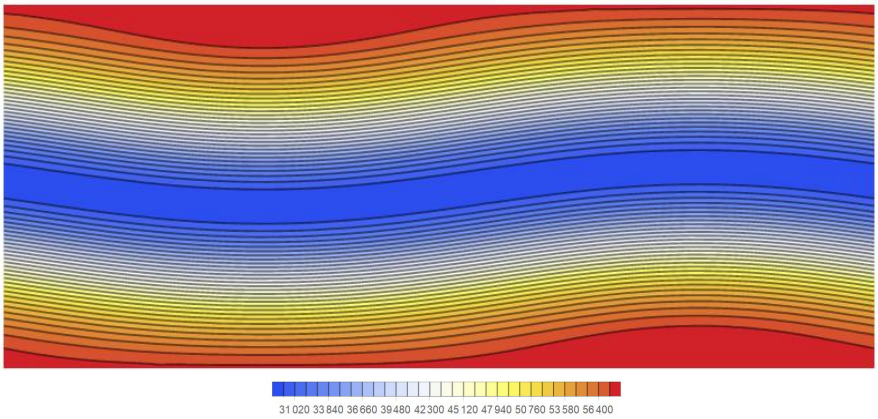

Figure 2.10: Magnetic field strength contours for tilted dipole case

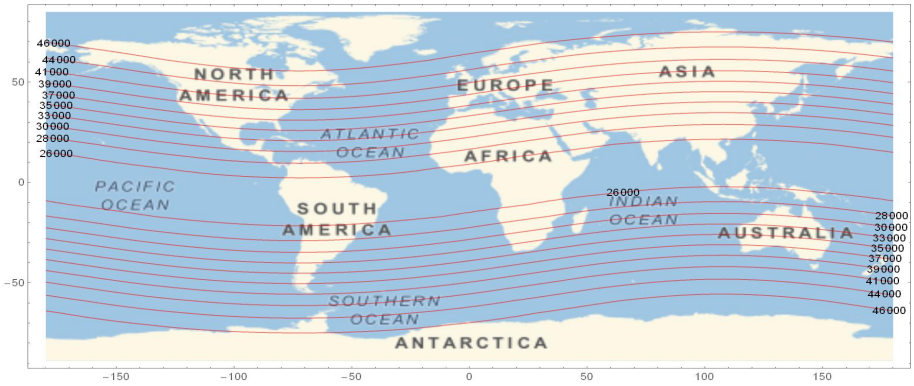

Figure 2.11: Magnetic field strength projected on world map for tilted dipole case

3. **Quadrupole: Titled + Displaced Dipole** $(m = 2, l > 0)$:

   The quadrupole terms $m = 2$ correspond in part to a displacement of the dipole from the center of the earth by an amount of about $0.07R$ [Bertotti and Farinella, 1990].

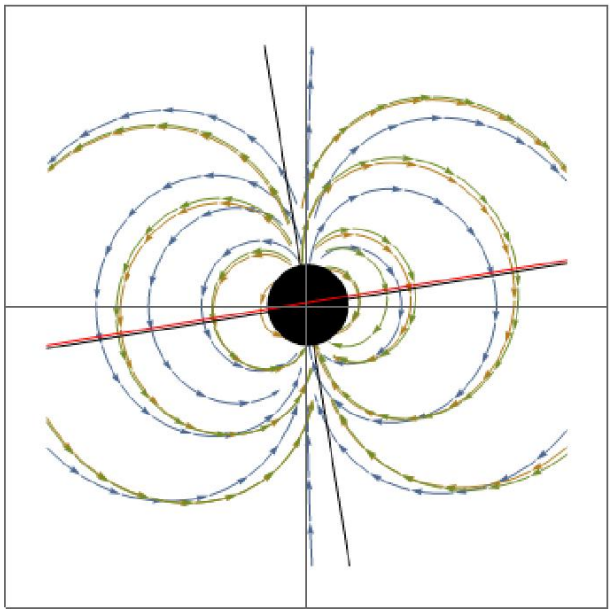

Figure 2.12: Magnetic field fines for quadrupole case

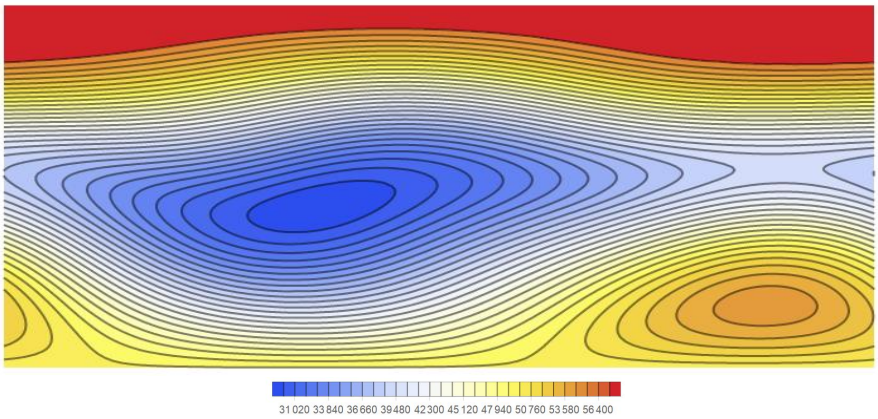

Figure 2.13: Magnetic field strength contours for quadrupole case

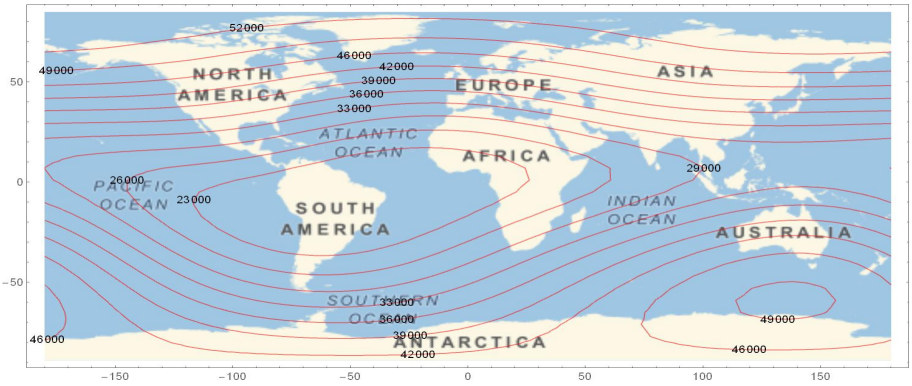

Figure 2.14: Magnetic field strength projected on world map for quadrupole case

4. **Octupole** $(m = 3, l > 0)$:

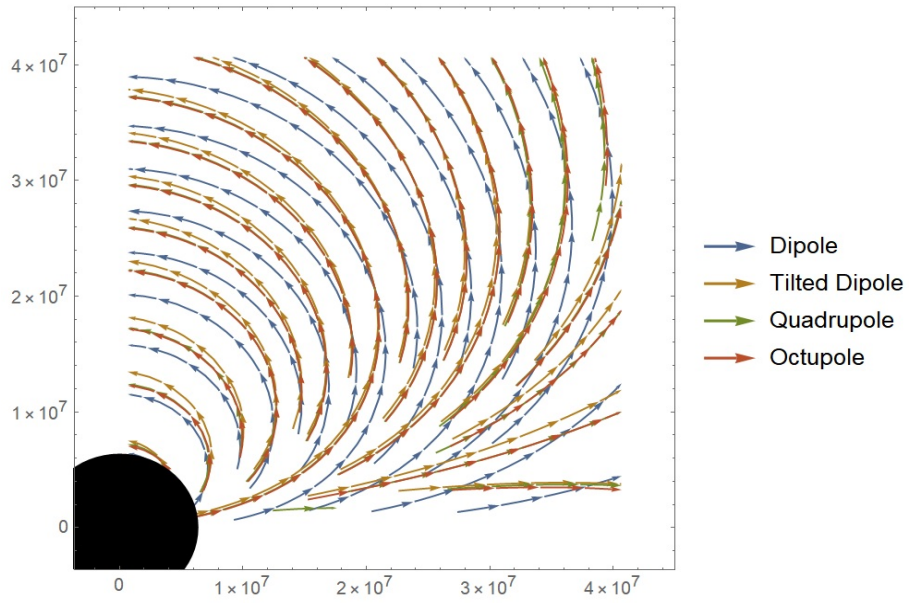

Figure 2.15: Magnetic field lines for the dipole, tilted dipole, quadrupole and octupole models

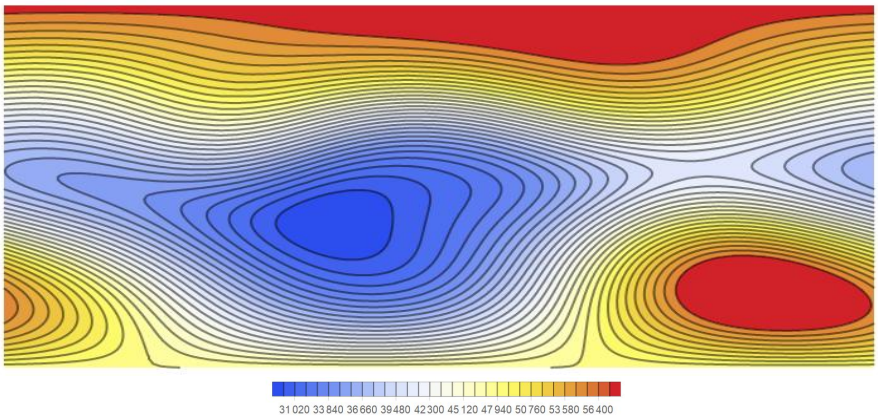

Figure 2.16: Magnetic field strength contours for octupole case

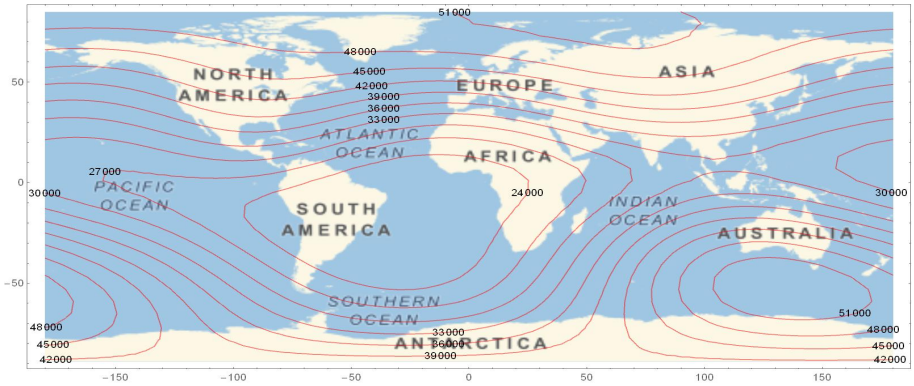

Figure 2.17: Magnetic field strength projected on world map for octupole case

5. **Final Model** $(m = 12, l > 0)$:

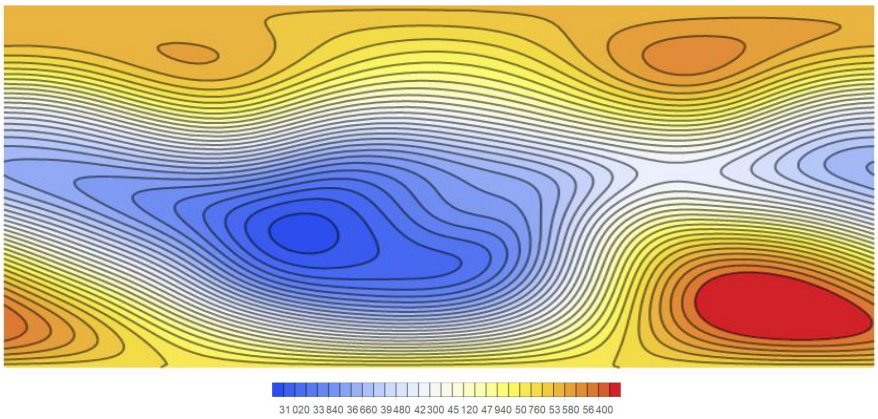

Figure 2.18: Magnetic field strength contours for the full series

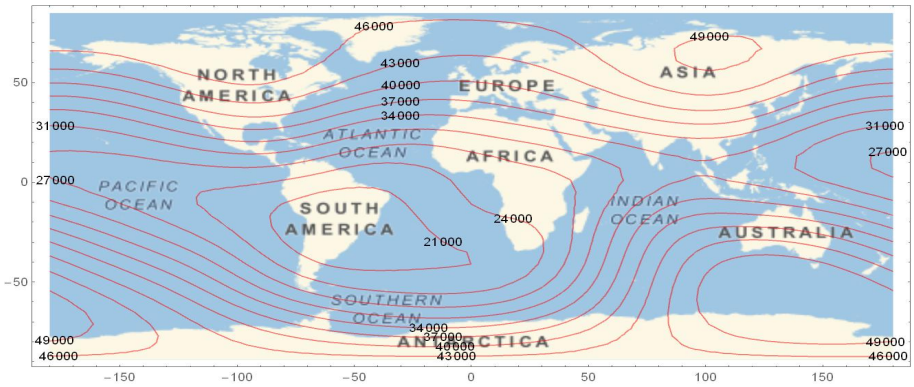

Figure 2.19: Magnetic field strength projected on world map for the full series

2.2.2 External Field Model: Tsyganenko Models

The Tsyganenko model is a semi-empirical representation of the magnetic field configuration. The model is based on various satellite measurements such as IMP, HEOS, ISEE, POLAR, Geotail, etc. It consists of several external magnetospheric sources, such as: the ring current, the magnetopause currents, the magnetotail current system and the field-aligned currents. The author of this model Prof. N. A. Tsyganenko also affords subroutines available in "GEOPACK-2008" package which calculates the Earth's internal magnetic field, by using the International Geomagnetic Reference Field (IGRF) model with additional coordinate transformation subroutines [Tsyganenko, 1996]. In the T96 model, the magnetosphere's boundary is considered on the dayside as a semi-ellipsoid, which is combined with the magnetotail by a cylindrical surface. The external magnetic field is formed by the summation of the symmetric ring current, the Chapman-Ferraro current, the cross-tail current sheet, the large-scale field-aligned currents and the partial penetration of the IMF into the model magnetosphere. The model main parameters are the solar wind ram pressure and velocity components, IMF transverse components, the *Dst* index and the geodipole tilting angle, in addition of the position and date [Tsyganenko, 1996] and [Tsyganenko, 1995]. Figures 2.20 and 2.21 are samples of Tsyganenko model run. The official website of the author is available here [6].

[6] http://geo.phys.spbu.ru/~tsyganenko/modeling.html

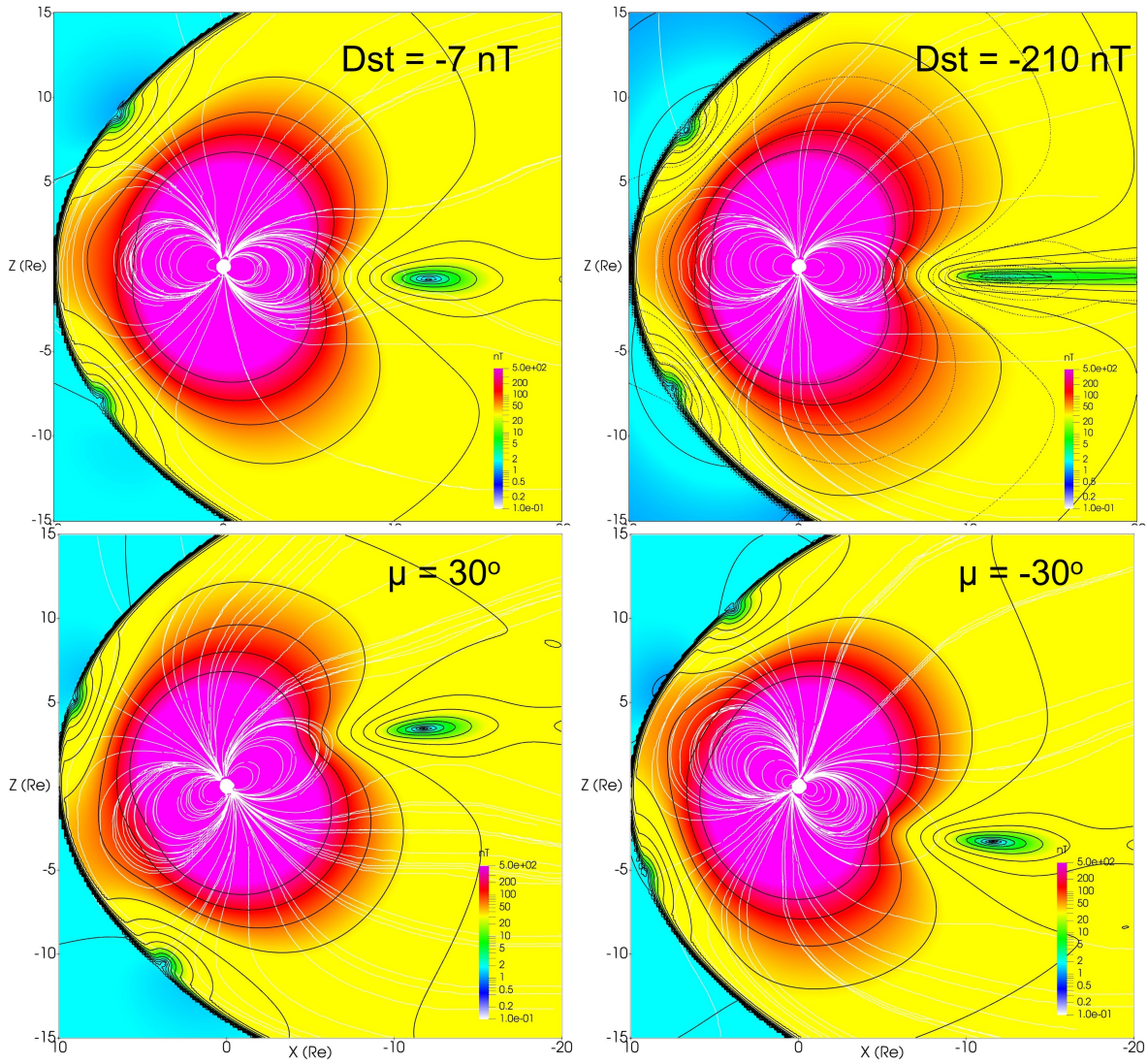

Figure 2.20: *Dst* index and geodipole tilting angle effects on external magnetic field

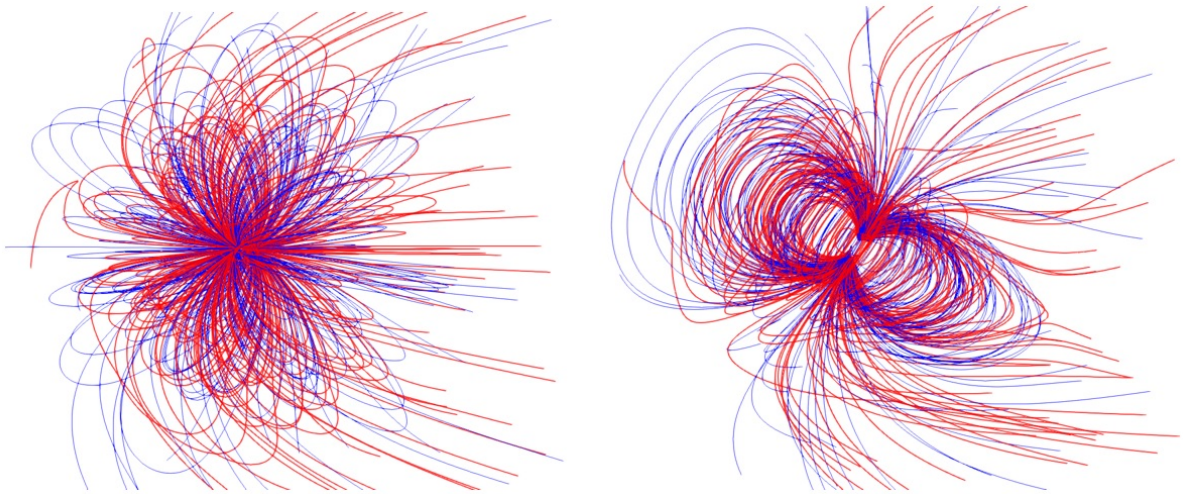

Figure 2.21: Magnetic field lines confinement due to increase in dynamic pressure: low (blue) and high (red)

The more recent model T01 [Tsyganenko, 2002a] [Tsyganenko, 2002b] is better resolving the inner magnetosphere region and the magnetotail, while TS05 [Tsyganenko and Sitnov, 2005], the inner magnetosphere response during magnetic storms.

2.3 Electric Field Models

2.3.1 Brief Introduction about the Electric Currents in the Magnetosphere

The geomagnetic field confinement due to its interaction with the solar wind and thus the formation of the magnetosphere, is accompanied by electric currents which flow in the magnetosphere. These currents are considered as important drivers of the dynamics of plasma around the Earth. The electric currents transport the charge, the mass, the momentum, and the energy, and by turn, they themselves generate magnetic fields which can distort significantly the preexisting fields.
When the solar wind approaches the Earth, it cannot easily penetrate the geomagnetic field. Hence, the magnetopause is formed, which is behaving like a surface boundary by separating the two different zones. The solar wind dynamic pressure compresses the geomagnetic field from the dayside, and this is corresponding to the *magnetopause current* that is flowing across the magnetopause. On the other hand, the magnetic field lines in the nightside are stretched and a long magnetotail is formed, where the *magnetotail current* occurs. The magnetotail current is consisting of two parts: the first part is flowing in the tail center from the dawn to the dusk across the magnetosphere and the other part is making two loops, one above and one below the magnetotail center, by closing the central current through the magnetopause. The ions, protons and electrons, which are emitted from the solar wind and the Earth's ionosphere, are the main source of the magnetospheric plasma. The particles gyrate around and bounce along the magnetic field lines and drift around the Earth. Westward drift of ions and protons and the eastward drift of electrons, along with their gyration motion in a region where a pressure gradient is occurring, cause a net charge transport and thus, the *ring current* is flowing around the Earth. Along magnetic field lines, there are the *field-aligned currents*, which are mainly carried by electrons, and they connect the magnetospheric currents with the ionospheric currents. Since the Earth's magnetosphere is always acting according to the changes in the solar activity, the magnetospheric current systems can be seriously changed with the generation of new transient current systems [Ganushkina et al., 2018]. The main currents are shown in Figure 2.22.

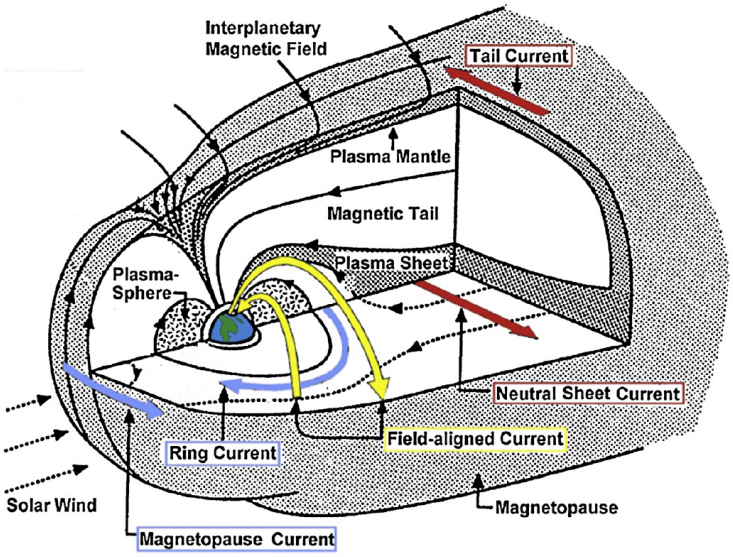

Figure 2.22: Schematic illustration of magnetospheric current systems contributing to the near-Earth magnetic field. The major current systems are highlighted by different colors [Lühr et al., 2017]

Several electric field models were developed by using various approaches; according to Figure 2.23, [Yu et al., 2017] conceived a self-existing electric field model and compare the results with well-established models, namely, the Volland-Stern model and the Weimer potential model. The mentioned models will be briefly discussed in the following sections.

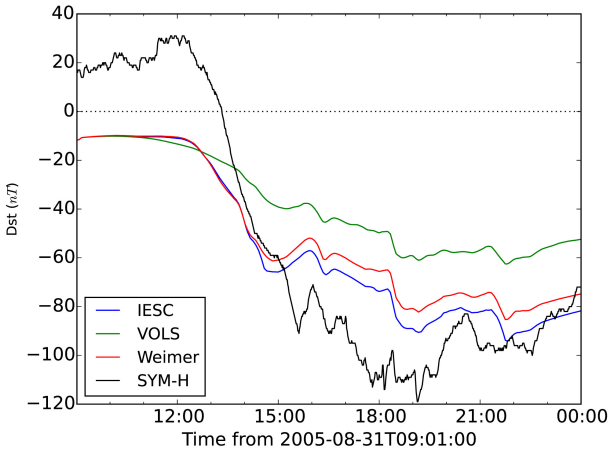

Figure 2.23: Measured SYM-H index (black) and simulated Dst index using different electric field models. "IESC" stands for self-consistent electric field, "VOLS", for Volland-Stern electric field, and "Weimer", Weimer potential model [Yu et al., 2017].

2.3.2 Ring Current Models

Several ring current models were developed. We report here as an example the recent model of [Yu et al., 2017]; the model is a self-consistent electric field coupling between the midlatitude ionospheric electrodynamics and inner magnetosphere dynamics represented in a kinetic ring current model. Figure 2.24 describes the model features.

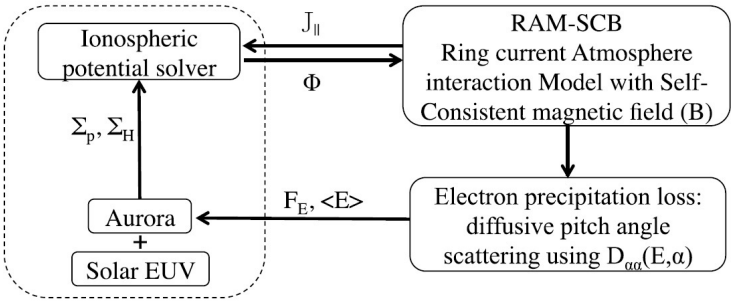

Figure 2.24: The coupling within the RAM-SCB-E model. The part within the dashed box is used to implement the self-consistency of electric field using inputs of $J_{\|}$ and precipitation energy flux F_E from the kinetic ring current model [Yu et al., 2017].

2.3.3 Volland-Stern Model: Global Electric Field Model

[Volland, 1973] and [Stern, 1975] constructed a simplified analytic model of the magnetospheric electric field in which detailed consideration of magnetospheric plasma convection is eliminated by the assumption of a semi-empirical electric field that fits the observations. The proposed electric field is consisting of the convection and the corotational fields as shown in the following mathematical expression:

$$\Phi = \kappa\Big(\frac{1}{x} - \frac{x^{\gamma}}{\gamma}\sin\phi\Big), \tag{2.1}$$

where Φ is the electric field potential, $x = R/R_0$ with ϕ the plane angle (Magnetic Local Time (MLT)) are the polar coordinates in 2D and κ is a constant derived from the Kp index.
The corresponding particle flow pattern is formulated by the following expression:

$$\frac{x^{\gamma}}{\gamma}\sin\phi - \frac{1}{x} + \frac{\mu^{'}}{x^3} = c, \tag{2.2}$$

where $\mu^{'}$ is the normalized magnetic moment. Figure 2.25 illustrates the families of curves for various initial conditions (different magnetic moment).

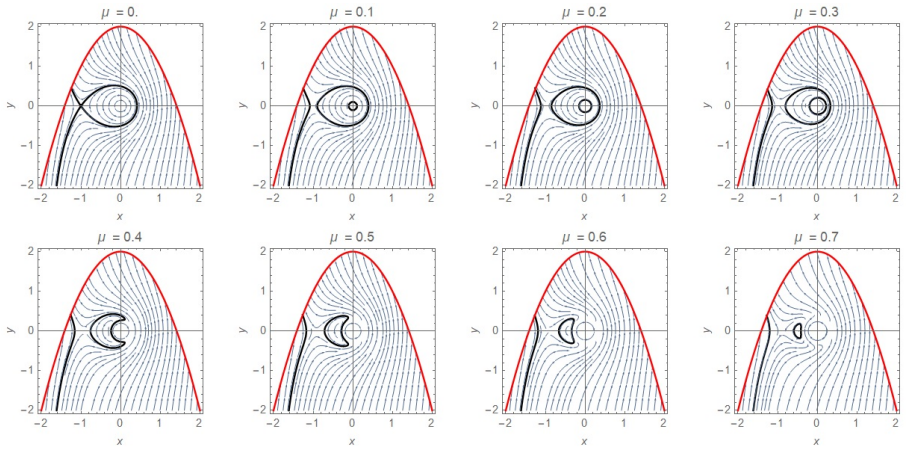

Figure 2.25: Volland-Stern Model isoboundaries: the particles are moving along constant total energy lines corresponding to different magnetic moment $\mu^{'}$

2.3.4 MHD Self-Consistent Model: FAC Model

The height-integrated ionospheric electrodynamics model is an electric field pattern that is usually derived from a Poisson equation at the ionospheric altitude, given two major quantities $J_{\parallel}$ and Σ:

$$\nabla \cdot \left(\Sigma \cdot \nabla \Phi \right) = -J_{\parallel} \sin I, \tag{2.3}$$

where $J_{\parallel}$ is the Field Aligned Currents (FACs) into and out of the ionosphere and Σ is the tensor of height-integrated ionospheric conductance, including both Hall and Pedersen conductances, and I is the inclination angle of the magnetic field in the ionosphere. Figure 2.26 from Wikipedia[7] illustrates the FACs flowing in and out the ionosphere .

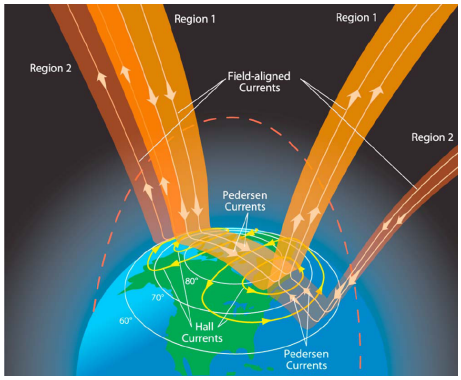

Figure 2.26: Schematic representation of the Birkeland or Field-Aligned Currents (FACs) and the ionospheric current systems connected to Pedersen and Hall currents.

The current model is widely implemented in several MHD global simulations to simulate the solar wind-magnetosphere interaction by computing the FACs that connect the inner simulation boundary with the ionosphere electrodynamics.

2.3.5 Weimer Model

Weimer models are semi-empirical electric potential models addressed for the high-latitude ionosphere. The model was developed by [Weimer, 1995], using satellite measurements of the ionospheric electric fields, simultaneously with the measurements of solar wind and interplanetary magnetic field (IMF) conditions. The control parameters to run the model include the solar wind plasma number density N, velocity V_x, the transverse orientation of the solar wind magnetic field B_{yIMF}, B_{zIMF}, and the orientation of the Earth's magnetic axis. The model output consists of the ionospheric electrostatic potential in kilovolts (kV). For further information please visit the following website [8]. Figure 2.27 is a demonstration of the model output with respect to the input space weather conditions.

[7] https://en.wikipedia.org/wiki/Birkeland_current
[8] https://ccmc.gsfc.nasa.gov/models/modelinfo.php?model=Weimer

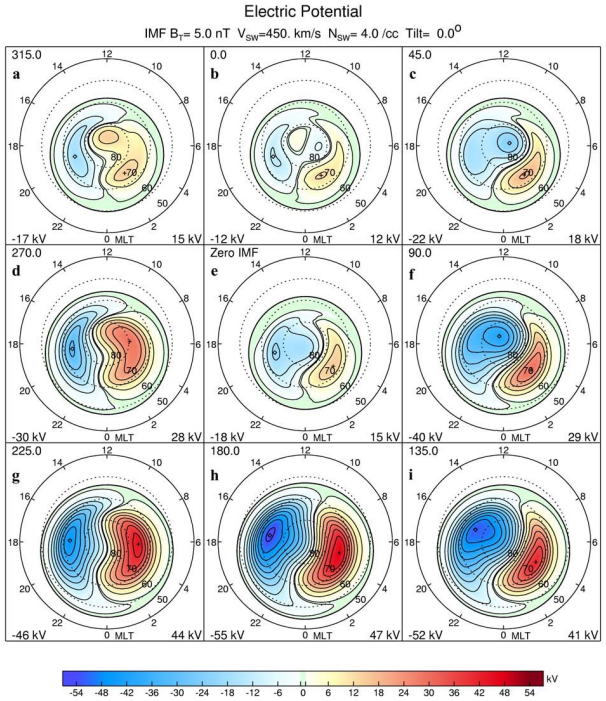

Figure 2.27: (a–i) Polar cap electric potentials in the Northern Hemisphere, mapped as a function of Altitude-Adjusted Corrected Geomagnetic Coordinates (AACGM) latitude and MLT. Figures 2a–2d and 2f–2i show the patterns for eight different clock angle orientations of the IMF vector in the GSM Y-Z plane; the angle in degrees is indicated in the top left corner of each map. The IMF has a fixed magnitude of 5 nT, the solar wind velocity is 450 km s^{-1}, the solar wind number density is 4 cm^{-3}, and the dipole tilt angle is 0°. Figure 2e shows the potential for zero IMF, with the same solar wind conditions. Minimum and maximum potential values are printed in the bottom left and right corners of each map, with locations indicated by the diamonds and pluses [Weimer, 2005].

2.3.6 Inductive Electric Field

The Ultra Low Frequency (ULF) is a radio frequency in the lower range of the radio spectrum from about 300 Hz to 3 kHz. In this frequency range, the magnetic and electric field variations have different source mechanisms and generate various temporal and spatial structures occurring in the inner magnetosphere. Such fluctuations can be generally categorized as either waves or as quasi-periodic perturbations, which are created by the ULF variations in the solar wind several parameters (e.g., compression in the magnetopause due to solar wind dynamic pressure (P_{dyn}) increase). Huge efforts are continuously devoted to evaluate the radial transport due to the ULF waves depending on several theoretical and observational approaches. [Ukhorskiy et al., 2006] studied the impact of the large-scale induced ULF fields, provided by the global and realistic time-varying reproduction of both the electric and magnetic fields in the inner magnetosphere. Hence, they developed a new methodology to calculate the self-consistent inductive electric field according to the time evolution of the geomagnetic field models by implementing the storm-time magnetic field model TS05 [Tsyganenko and Sitnov, 2005].
According to [Ukhorskiy et al., 2006], the advantages of this approach are summarized as follows:

1. This new technique was found to be computationally efficient to quantify the electron dynamic effects in the outer radiation belt.

2. The TS05 includes several self-consistent magnetic field physical sources, so that it permits to study the effects of the field disturbance causes in the selected magnetic field model to indicate their relative roles in the radial transport in the radiation belts.

3. TS05 can be used as a dynamical disturbed magnetic field model, since its ten input parameters are corresponding to the solar wind conditions. The resulted magnetic field configuration is computed based on the seven major magnetospheric current systems driven by the different input parameters for various time scales [Tsyganenko and Sitnov, 2005].

4. TS05 implies spatial coherence of magnetic field variations over the whole domain of the magnetosphere structure and hence it does not include wave phenomena. Therefore, the analysis presented in the mentioned paper was restricted to the phenomena that are longer than the characteristic wave propagation time.

5. The authors successfully examined the drift resonance of the P_{dyn}-induced electric field effects on the outer electron radiation belt which generated a radial motion across the drift shells. From their simulations, large transport rates were reproduced which means that the global magnetospheric compression due to the P_{dyn} variations was found to be one of the dominant processes of the radial transport occurred in the outer radiation belt.

6. Steady-state versus disturbed magnetosphere: the trapped relativistic electron motions in a steady-state magnetosphere are mainly described by the gradient curvature drift however the $\mathbf{E} \times \mathbf{B}$ force due to the convection electric field is generally small. On the other hand, in the disturbed case, the global variations produced in the geomagnetic field can produce large-scale electric fields which may manifest resonance with a quasi-periodic electron motion. That is why it is possible to neglect the electric fields which can be considered static on the time scales of electron drift motion ($>$ 10 min for a 1.5 MeV electron at L = 6) as well as proton drift motion ($>$ 10 sec for a 100 MeV proton at L = 3), while analyzing the radial transport in the belt by quantifying the ULF oscillations in the global electric fields. Thus, we can assume that ULF variations of electric field induced by global perturbations of geomagnetic field can be estimated using the inductive component of the field.

7. In magnetospheric plasma science, it is widely known that the electric fields have both potential and inductive components. However, by following the global MHD simulations, the time required for the magnetospheric convection to reach a new steady state characterized by the potential electric field after an impulsive change in solar wind conditions can exceed 1 hour. Furthermore, spacecraft observations concluded that the electric field oscillations were inductive on minute time scales caused by the rapid changes in the magnetic field at substorm onset.

In addition, [Engel et al., 2015] has also investigated the proton loss in the inner radiation belt by implementing the same approach. According to this study, the merits of this method are also summarized as follows:

1. The buildup and the decay of the ring current during geomagnetic storms creates a time-varying magnetic field where the inclusion of the inductive electric field is associated. The authors found that this electric field model imposed a significant effect on the inner zone proton belt state mainly due to the particle losses.

2. In their work, they resolved the differences between model results and observations by simulating the inner zone proton belt losses including the inward and outward radial motions due to ring current changes, since the ring current buildup and decay during a geomagnetic storm had a significant impact on the L shell and energy dependence of the inner zone proton belt, following the storm.

The inductive electric field is evaluated directly from Faraday's law with $\partial B(r,t)/\partial t$ being an output of the global time-dependent model of geomagnetic field. The Biot-Savart integration is performed in all the simulation domain in order to compute the associated inductive electric field generated from the realistic magnetic field e.g. IGRF+TS05. The mathematical expression is shown as follows:

$$\mathbf{E}(\mathbf{r},t) = -\frac{1}{4\pi}\frac{\partial}{\partial t}\int_V \frac{\mathbf{B}(\mathbf{r}^{'},t)\times(\mathbf{r}-\mathbf{r}^{'})}{|\mathbf{r}-\mathbf{r}^{'}|^3} d^3r^{'}, \tag{2.4}$$

where $\mathbf{E}$ is the electric field computed at the desired location $\mathbf{r}$ and time t, $\mathbf{B}$ is the magnetic field defined at all grid point $\mathbf{r}^{'}$; the integration is performed over the entire simulation domain of the selected geomagnetic field model.

2.3.6.1 Simple Dipole Field Example

The results are validated with the published results of [Engel et al., 2015] for the calculation of the inductive electric field in a pure dipole field configuration due to the temporal change in the B_z component.

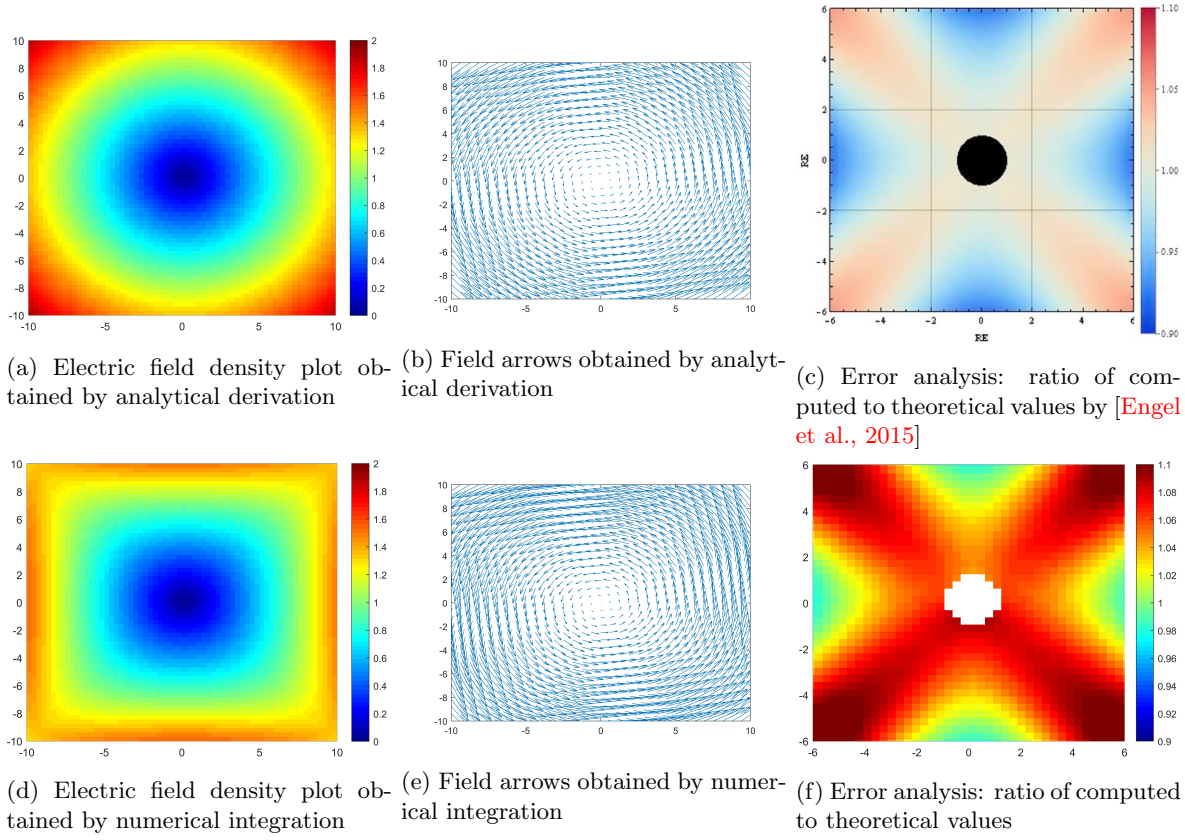

(a) Electric field density plot obtained by analytical derivation

(b) Field arrows obtained by analytical derivation

(c) Error analysis: ratio of computed to theoretical values by [Engel et al., 2015]

(d) Electric field density plot obtained by numerical integration

(e) Field arrows obtained by numerical integration

(f) Error analysis: ratio of computed to theoretical values

Figure 2.28: Comparison of the inductive electric field models obtained from analytical and numerical integrations

2.3.6.2 Realistic Geomagnetic Field Examples

Solar Wind Dynamic Pressure Effect: The results are validated with the published results of [Ukhorskiy et al., 2006] for the calculation of the inductive electric field for a a realistic geomagnetic field due to the increase of the solar wind dynamic pressure from 2 to 4 nPa in 4 minutes.

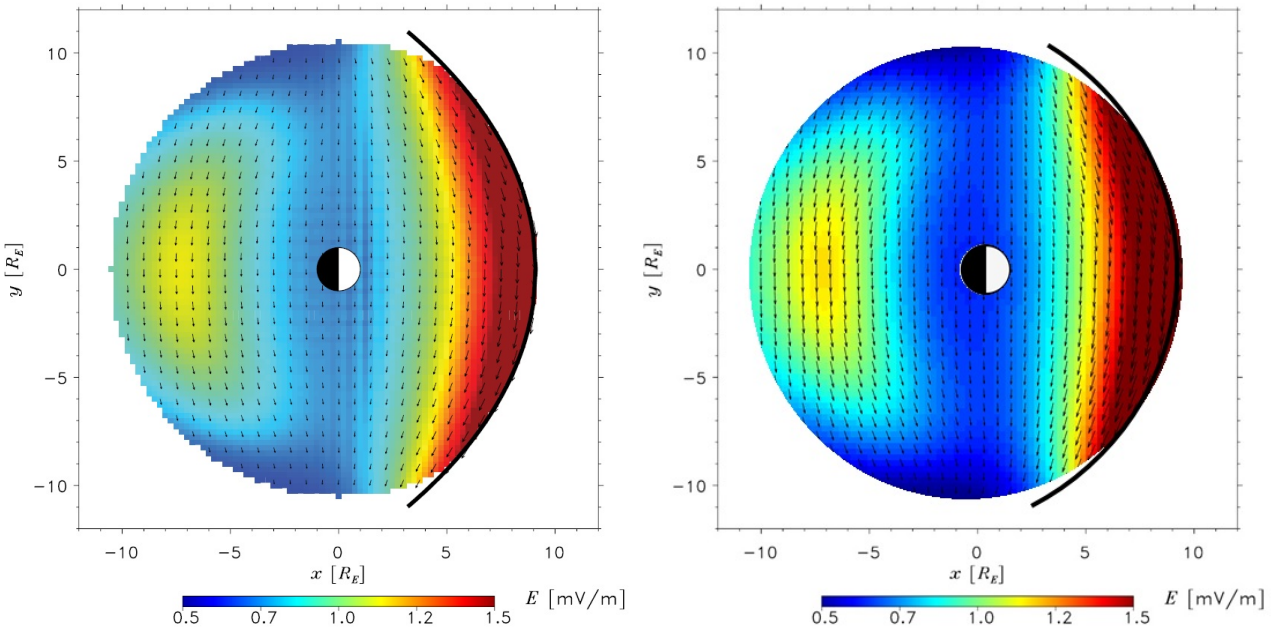

(a) Equatorial electric field plot and field directions as computed by [Ukhorskiy et al., 2006]

(b) Equatorial electric field plot and field directions as computed by the authors

Figure 2.29: A comparison with the numerical inductive electric field model obtained by published works

From Figure 2.29, we observe the enhancement of the magnetopause and the magnetotail currents in the dayside and in the nightside respectively due the dynamic pressure increase.

Dst Index Effect: An additional example shows the inductive electric field in the magnetosphere due to the decrease of the Dst index from -7 to -210 nT.

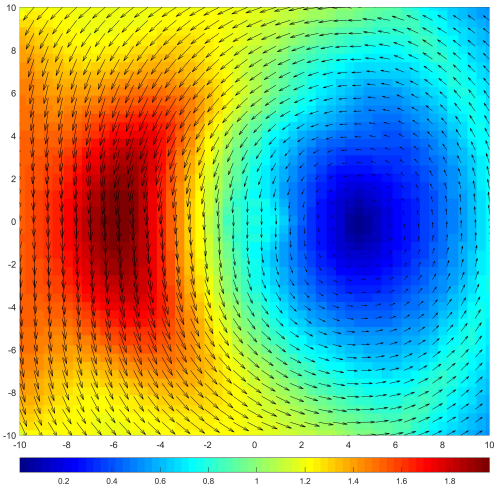

Figure 2.30: Equatorial electric field (in mV/m) contour plot due to the decrease of the Dst index

It is remarked from Figure 2.30 that the decrease in the Dst index leads to a significant decay in the magnetopause current in the dayside, accompanied by large enhancement in the magnetotail current in the nightside.

2.3.6.3 Comparison between several integration methods

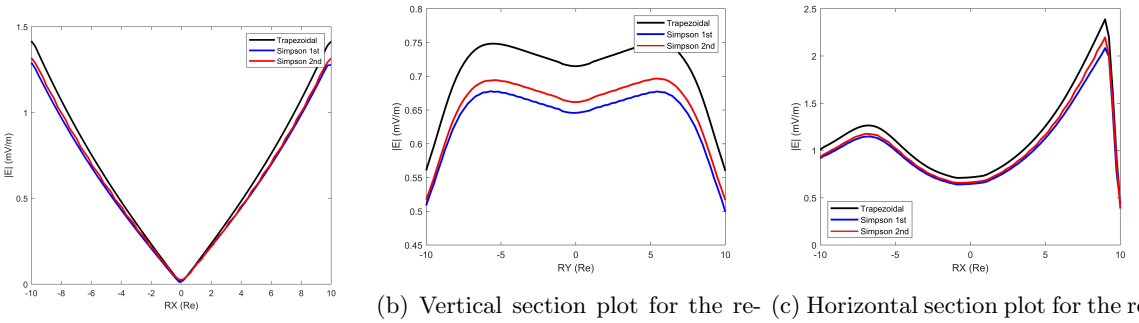

(a) For a dipole field case

(b) Vertical section plot for the realistic geomagnetic field variation of the P_{dyn} from 2 to 4 nPa

(c) Horizontal section plot for the realistic geomagnetic field variation of the P_{dyn} from 2 to 4 nPa

Figure 2.31: A comparison between integrator method for the two examples: dipole and realistic geomagnetic field

Figure 2.31 demonstrates the results solved by several integration methods: trapezoidal, Simpson 1st and 2nd rules. As argued by many references e.g. Wolfram Web Resource [9], the Simpson 2nd is the best among the selected methods since it uses 4 points for integration, while the Simpson 1st rule uses 3 points and the trapezoidal, 2 points. Therefore, it is clear that the trapezoidal rule overestimates the results and the Simpson 1st rule underestimates them.

[9]Weisstein, Eric W. "Newton-Cotes Formulas." From MathWorld–A Wolfram Web Resource: https://mathworld.wolfram.com/Newton-CotesFormulas.html

2.4 Test Particle Equations of Motion

2.4.1 Full Particle Model

The test particle equations are introduced as follows:

$$m\frac{d\gamma\mathbf{v}}{dt} = q(\mathbf{E} + \mathbf{v} \times \mathbf{B}) \tag{2.5}$$

$$\frac{d\mathbf{r}}{dt} = \mathbf{v} \tag{2.6}$$

where m is the particle mass, q is the particle charge, $\mathbf{B}$ is the magnetic field, $\mathbf{E}$ is the electric field, $\mathbf{v}$ is the particle velocity, $\mathbf{r}$ is the particle position and γ is the relativity factor.

2.4.1.1 Normalized Test Particle Equations of Motion

The variables are normalized as follows:

$$t = T_0\hat{t}, \quad \mathbf{r} = R_0\hat{\mathbf{r}}, \quad \mathbf{v} = V_0\hat{\mathbf{v}}, \quad \mathbf{B} = B_0\hat{\mathbf{B}} \tag{2.7}$$

where

T_0 is obtained from the gyrofrequency, and equal to,

$$T_0 = \frac{2\pi m}{qNB} \tag{2.8}$$

and N is the division number of the particle circular motion.

R_0 = Earth Radius ≈ 6371 km

V_0 = Speed of Light $\approx 3 \times 10^8$ m/s

B_0 = Maximum Earth's magnetic field value at its surface ≈ 0.65 Gauss

The final normalized equations, with no electric field, are introduced as shown:

$$\frac{d\gamma\hat{\mathbf{v}}}{d\hat{t}} = 2\pi\big(\hat{\mathbf{v}} \times \hat{\mathbf{B}}\big) \tag{2.9}$$

$$\frac{d\hat{\mathbf{r}}}{d\hat{t}} = \hat{\mathbf{v}} \tag{2.10}$$

2.4.2 Guiding Center Model

2.4.2.1 Northrop-Teller Model

The guiding center equations were formulated by [Northrop, 1963a, Northrop, 1963b] as follows:

$$\dot{\mathbf{X}} = \frac{\gamma m v^2}{2qB^2}\Big(1 + \frac{v_\parallel^2}{v^2}\Big)\hat{\mathbf{b}} \times \nabla B + v_\parallel \hat{\mathbf{b}} \tag{2.11}$$

$$\dot{v_\parallel} = -\frac{\mu}{\gamma^2 m}\hat{\mathbf{b}} \cdot \nabla B \tag{2.12}$$

where $\mathbf{B}$ is the magnetic field, $\mathbf{E}$ is the electric field, $\mathbf{X}$ is the guiding center position, $p_\parallel$ is the parallel momentum, μ is the first invariant of the guiding center motion, m is the particle mass, q is the charge and γ is the relativity factor.

2.4.2.2 Brizard-Chan Model

The guiding center equations were formulated by [Brizard and Chan, 1999] as follows:

$$\dot{\mathbf{X}} = \frac{p_{\parallel}}{\gamma m}\frac{\mathbf{B}^*}{B_{\parallel}^*} + \frac{\widehat{\mathbf{b}}}{q\gamma B_{\parallel}^*} \times \mu \nabla B$$

$$\dot{p_{\parallel}} = -\frac{\mu \mathbf{B}^*}{\gamma B_{\parallel}^*} \cdot \nabla B \tag{2.13}$$

with,

$$\mathbf{B}^* = \mathbf{B} + \frac{p_{\parallel}}{q} \nabla \times \widehat{\mathbf{b}} \tag{2.14}$$

and,

$$B_{\parallel}^* = \mathbf{B}^* \cdot \widehat{\mathbf{b}} = B + \frac{p_{\parallel}}{q}\left(\widehat{\mathbf{b}} \cdot \nabla \times \widehat{\mathbf{b}}\right) \tag{2.15}$$

where $\mathbf{B}$ is the magnetic field, $\mathbf{E}$ is the electric field, $\mathbf{X}$ is the guiding center position, $p_{\parallel}$ is the parallel momentum, μ is the first invariant of the guiding center motion, m is the particle mass, q is the charge and γ is the relativity factor.

2.4.2.3 Tao-Chan-Brizard Model

The relativistic formulation of the guiding center position and the parallel momentum are introduced by the authors [Tao et al., 2007], as follows:

$$\dot{\mathbf{X}} = \frac{p_{\parallel}}{\gamma m}\frac{\mathbf{B}^*}{B_{\parallel}^*} + \mathbf{E}^* \times \frac{\widehat{\mathbf{b}}}{B_{\parallel}^*}$$

$$\dot{p_{\parallel}} = q\mathbf{E}^* \cdot \frac{\mathbf{B}^*}{B_{\parallel}^*}, \tag{2.16}$$

where

$$\mathbf{B}^* = \mathbf{B} + \frac{p_{\parallel}}{q} \nabla \times \widehat{\mathbf{b}} \tag{2.17}$$

$$\mathbf{E}^* = \mathbf{E} - \frac{1}{q}\left(p_{\parallel}\frac{\partial \widehat{\mathbf{b}}}{\partial t} + \frac{\mu}{\gamma}\nabla B\right), \tag{2.18}$$

and,

$$B_{\parallel}^* = \mathbf{B}^* \cdot \widehat{\mathbf{b}} = B + \frac{p_{\parallel}}{q}\left(\widehat{\mathbf{b}} \cdot \nabla \times \widehat{\mathbf{b}}\right) \tag{2.19}$$

where $\mathbf{B}$ is the magnetic field, $\mathbf{E}$ is the electric field, $\mathbf{X}$ is the guiding center position, $p_{\parallel}$ is the parallel momentum, μ is the first invariant of the guiding center motion, m is the particle mass, q is the charge and γ is the relativity factor.

2.4.2.4 An important note about GC theory

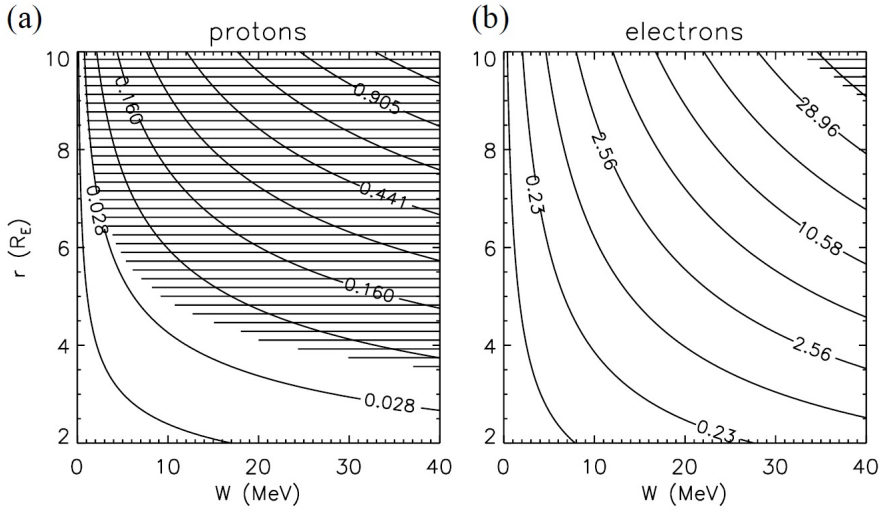

Figure 2.32: Lines of constant first adiabatic invariant (in MeV=nT) for protons (a) and electrons (b) in a dipole field of moment $B_0 = 30500$ nT. The hatched area indicates those regions where the guiding center approximation breaks down [Elkington et al., 2002].

According to [Elkington et al., 2002], the guiding center theory is applicable to simulate the inner proton radiation belt ($L < 3$) even for high energies (> 40 MeV). The last important point is the appropriate selection of the integrator schemes that will be implemented in the simulations, as shown in the next section.

2.4.3 Numerical Schemes

2.4.3.1 Runge-Kutta 4$^{\text{th}}$ order scheme

The 4$^{\text{th}}$ order Runge-Kutta formula is shown by [Press et al., 1997] as follows:

$$\begin{aligned} k_1 &= hf(x_n, y_n) \\ k_2 &= hf(x_n + \frac{h}{2}, y_n + \frac{k_1}{2}) \\ k_3 &= hf(x_n + \frac{h}{2}, y_n + \frac{k_2}{2}) \\ k_4 &= hf(x_n + h, y_n + k3) \\ y_{n+1} &= y_n + \frac{k_1}{6} + \frac{k_2}{3} + \frac{k_3}{3} + \frac{k_4}{6} + O(h^5) \end{aligned} \tag{2.20}$$

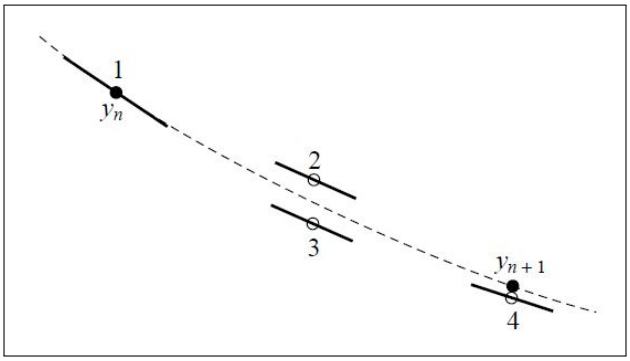

Figure 2.33: Fourth-order Runge-Kutta method. In each step the derivative is evaluated four times: once at the initial point, twice at trial midpoints, and once at a trial endpoint. From these derivatives the final function value (shown as a filled dot) is calculated [Press et al., 1997].

2.4.3.2 Adaptive step-size Runge-Kutta 4th order scheme

A good ODE integrator should exert some adaptive control over its own progress, making frequent changes in its step-size. Usually the purpose of this adaptive step-size control is to achieve some predetermined accuracy in the solution with minimum computational effort [Press et al., 1997].

The general form of a fifth-order Runge-Kutta formula is:

$$\begin{aligned} k_1 &= hf(x_n, y_n) \\ k_2 &= hf(x_n + a_2 h, y_n + b_{21} k_1) \\ &\dots \\ k_6 &= hf(x_n + a_6 h, y_n + b_{61} k_1 + \dots + b_{65} k_5) \\ y_{n+1} &= y_n + c_1 k_1 + c_2 k_2 + c_3 k_3 + c_4 k_4 + c_5 k_5 + c_6 k_6 + O(h^6) \end{aligned} \tag{2.21}$$

The embedded fourth-order formula is:

$$y^*_{n+1} = y_n + c^*_1 k_1 + c^*_2 k_2 + c^*_3 k_3 + c^*_4 k_4 + c^*_5 k_5 + c^*_6 k_6 + O(h^5) \tag{2.22}$$

and so the error estimate is:

$$\begin{aligned} \Delta_1 &= y_{n+1} - y^*_{n+1} = \sum_{i=1}^{6} (c_i - c^*_i) k_i \\ \Delta_0 &= \epsilon h \frac{dy}{dx} \end{aligned} \tag{2.23}$$

where ϵ is a very small number ($= 10^{-4}$).
The new step-size is calculated as follows:

$$h_0 = \begin{cases} S h_1 \left| \dfrac{\Delta_0}{\Delta_1} \right|^{0.20}, & \text{if } \Delta_0 \geq \Delta_1 \\ S h_1 \left| \dfrac{\Delta_0}{\Delta_1} \right|^{0.25}, & \text{if } \Delta_0 < \Delta_1 \end{cases} \tag{2.24}$$

where S is a safety factor ($= 0.90$).
The equation 2.24 is used in two ways: If Δ_1 is larger than Δ_0 in magnitude, the equation tells how much to decrease the stepsize when we retry the present (failed) step. If Δ_1 is smaller than Δ_0, on the other hand, then the equation tells how much we can safely increase the stepsize for the next step.

Cash-Karp Parameters for Embedded Runga-Kutta Method

i	a_i	b_{ij}					c_i	c^*_i
1							$\frac{37}{378}$	$\frac{2825}{27648}$
2	$\frac{1}{5}$	$\frac{1}{5}$					0	0
3	$\frac{3}{10}$	$\frac{3}{40}$	$\frac{9}{40}$				$\frac{250}{621}$	$\frac{18575}{48384}$
4	$\frac{3}{5}$	$\frac{3}{10}$	$-\frac{9}{10}$	$\frac{6}{5}$			$\frac{125}{594}$	$\frac{13525}{55296}$
5	1	$-\frac{11}{54}$	$\frac{5}{2}$	$-\frac{70}{27}$	$\frac{35}{27}$		0	$\frac{277}{14336}$
6	$\frac{7}{8}$	$\frac{1631}{55296}$	$\frac{175}{512}$	$\frac{575}{13824}$	$\frac{44275}{110592}$	$\frac{253}{4096}$	$\frac{512}{1771}$	$\frac{1}{4}$
$j =$		1	2	3	4	5		

Figure 2.34: Adaptive Runge-Kutta Scheme Coefficients [Press et al., 1997]

2.4.3.3 Boris-Bunemann Scheme

While the equation of motion in the electromagnetic field can be solved by using any numerical methods developed for Ordinary Differential Equations (ODE), there is an efficient and accurate scheme particularly suited for this problem, Buneman-Boris method [Hada and Matsukiyo, 2017].

The equations are discretized as follows:

$$\begin{aligned} \frac{\mathbf{v}^{k+\frac{1}{2}} - \mathbf{v}^{k-\frac{1}{2}}}{h} &= \frac{q}{m}(\mathbf{E}^k + \frac{\mathbf{v}^{k+\frac{1}{2}} - \mathbf{v}^{k-\frac{1}{2}}}{2} \times \mathbf{B}^k) \\ \frac{\mathbf{r}^{k+1} - \mathbf{r}^k}{h} &= \mathbf{v} \end{aligned} \tag{2.25}$$

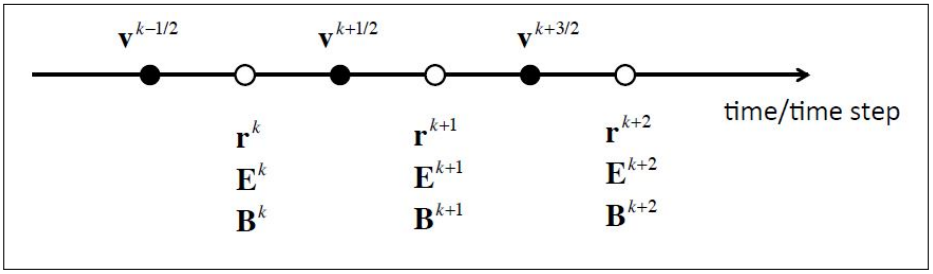

Figure 2.35: Buneman-Boris discretization method [Hada and Matsukiyo, 2017]

The discretization procedure is summarized as follows:

$$\begin{aligned} \mathbf{F}^k &= \frac{hq}{2m}\mathbf{E}^k \\ \mathbf{T}^k &= \frac{hq}{2m}\mathbf{B}^k \\ \mathbf{v}^- &= \mathbf{v}^{k-1/2} + \mathbf{F}^k \\ \mathbf{v}^0 &= \mathbf{v}^- + \mathbf{v}^- \times \mathbf{T}^k \\ \mathbf{v}^+ &= \mathbf{v}^- + \frac{2}{1+\mathbf{T}^2}\mathbf{v}^0 \times \mathbf{T}^k \\ \mathbf{v}^+ &= \mathbf{v}^{k+1/2} + \mathbf{F}^k \\ \mathbf{r}^{k+1} &= \mathbf{r}^k + h\mathbf{v}^k \end{aligned} \tag{2.26}$$

2.4.3.4 Adaptive Step-size Boris-Buneman Scheme using Error variation not including the scheme order (p = 1)

The local error estimate can be used to decide how step-size h should be modified to achieve the desired accuracy. For example, if a local tolerance tol is allowed, we could let h evolve roughly similar to [10]:

$$h_{n+1} = 0.85\ h_n\ min\left(max\left(\frac{tol}{\tau_{n+1}^{(1)}}, 0.3\right), 2.0\right) \tag{2.27}$$

The 0.85 is a safety factor to ensure success on the next try. The minimum and maximum are to prevent extreme changes from the previous stepsize. This should, in principle give an error of about $0.85 \times tol$ in the next try. If $\tau_{n+1}^{(1)} < tol$, we consider the step successful, and the error estimate is used to improve the solution:

$$y_{n+1}^{(2)} = y_{n+1}^{(1)} + \tau_{n+1}^{(1)} \tag{2.28}$$

2.4.3.5 Adaptive Step-size Boris-Buneman Scheme using Error variation including the scheme order (p = 2)

To provide a faster computation run, we will try to build an adaptive step-size of the Buneman-Boris method. The conventional step size control is realized by changing the time step in a way that as estimate for the local error is below a tolerance e_{tol}. The local error is assumed to be proportional to h^r, where r depends on the order of the method. Based on the estimate en for the current local error, a new step size is predicted by a formula like:

$$h_{n+1} = 0.85\ h_n\left(\frac{e_{tol}}{e_n}\right)^{1/r} \tag{2.29}$$

where 0.85 is a safety factor. To prevent the instability, as demonstrated in 2.4.3.4, we have imposed a top and bottom boundary for the step-size [Toggweiler, 2011].

[10] https://en.wikipedia.org/wiki/Adaptive_step_size

2.4.3.6 Adaptive Step-size Boris-Buneman Scheme using Magnetic Field variation

In this section, the proposed adaptive version of the Buneman-Boris method is achieved by the variation of the background magnetic field. To prevent the instabilities, we have imposed a maximum step-size, as follows:

$$h = S\ max\left(\frac{1}{NB_i}, \frac{1}{NB_0}\right) \tag{2.30}$$

where

S is a safety factor

N is the division number of the particle cyclotron motion

B_i is the normalized magnetic field magnitude at each time-step

B_0 is the initial magnetic field magnitude

2.4.3.7 Burlisch-Stoer Integrator

According to [Press et al., 1997], the authors believe that the Bulirsch-Stoer method [Stoer and Bulirsch, 1980] is the best known tool to achieve high-accuracy solutions for ordinary differential equations with minimal computational effort.

The current method is consisting of three main features:

1. The first feature is to consider the final answer of a numerical calculation as an analytic function (if a complicated one) by adjusting the stepsize h. That analytic function is controlled by calculating various values of h. When the function is being known, it is fit to some analytic form, and then it is evaluated at that mythical and golden point when $h = 0$ (see Figure 2.36). This is what is called the Richardson's deferred approach.

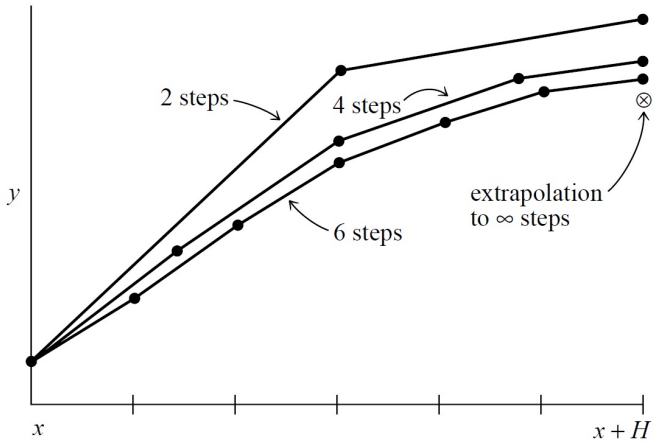

Figure 2.36: Richardson extrapolation as used in the Bulirsch-Stoer method. A large interval H is spanned by different sequences of finer and finer substeps. Their results are extrapolated to an answer that is supposed to correspond to infinitely fine substeps. In the Bulirsch-Stoer method, the integrations are done by the modified midpoint method, and the extrapolation technique is rational function or polynomial extrapolation [Press et al., 1997].

2. The second feature is the kind of the chosen fitting function. Bulirsch and Stoer considered the merit of the rational function extrapolation in Richardson type applications. That merit is realized by breaking the chain of the power series and its limited radius of convergence, out only to the distance of the first pole in the complex plane. Rational function fits are good approximations to the analytic functions even after the various terms in powers of h all have comparable magnitudes. However, more recent experience suggests that for smooth problems straightforward polynomial extrapolation is slightly more efficient than the rational function extrapolation. In the textbook of [Press et al., 1997], the written subroutine of the method is adopting the polynomial extrapolation as the default.

3. The third idea is to use a method whose error function is strictly even, allowing the rational function or the polynomial approximation to be in terms of the variable h^2 instead of just h.

2.4.4 Numerical Examples

2.4.4.1 Full Particle Examples

2.4.4.1.1 Uniform Magnetic Field Problem

Problem Setup: In this problem, the magnetic field has only one component in $z-$ direction and the velocity field has only one component in $y-$ direction. To compare the results of each scheme, the computation is stopped until a full orbit is achieved.

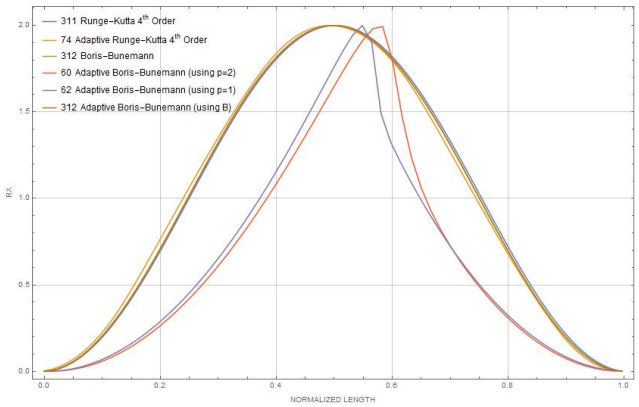

(a) Particle position in $x-$ direction

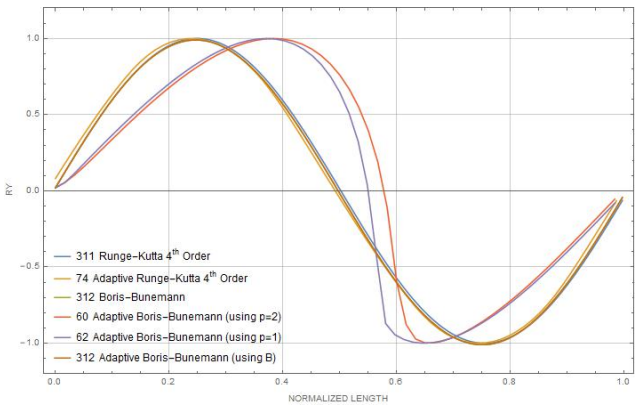

(b) Particle position in $y-$ direction

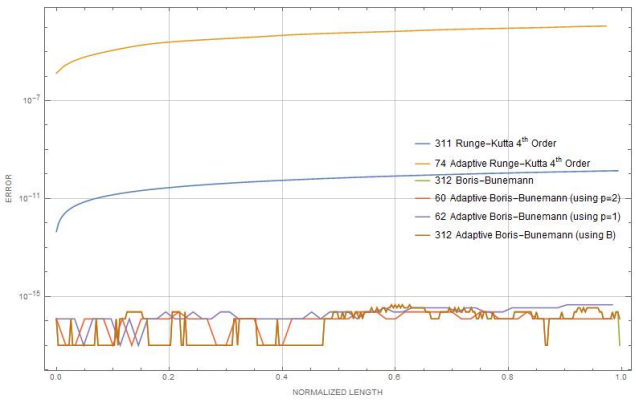

(c) Error analysis for each scheme

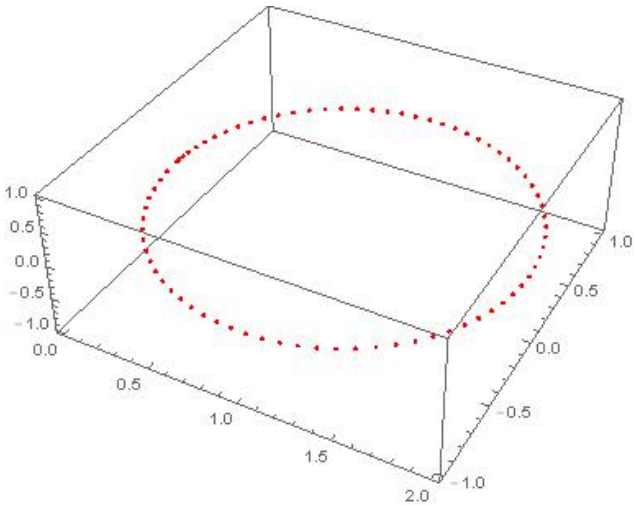

(d) 3D Plot

Figure 2.37: Test particle in a constant magnetic field problem

Discussion: As shown from Figure 2.37, we deduce the following:

1. From the gyroradius equation, which is given by, $r_g = \dfrac{mv_\perp}{qB}$, the radius of this problem should be equal to 1.0, and all schemes have provided the same result.
2. It is clear that the two versions of the adaptive Buneman-Boris scheme using the error terms, are relatively different from the other four schemes.
3. The adaptive methods of Runge-Kutta and the Buneman-Boris scheme using the error terms (74, 60 and 62 respectively), have the lowest time-step number required to perform a complete orbit.
4. The adaptive Runge-Kutta scheme lead to the highest error, then its constant step-size version, and finally, the family of Buneman-Boris method, has achieved the minimum error.

2.4.4.1.2 Dipole Magnetic Field Problem

Problem Setup: In this problem, the Earth's magnetic field model is a pure dipole field, where its potential is,

$$V = -7.613 \times 10^{24} \left(\frac{\cos\theta}{r^2} \right) \tag{2.31}$$

And, the magnetic field is calculated by the gradient of the potential,

$$\mathbf{B} = -\nabla V \tag{2.32}$$

The velocity field has only one component in $z-$ direction $= 0.12 \times 10^8$ m/s, which corresponds to $\approx 0.75\ MeV$ for a proton. To compare the results of each scheme, the computation is stopped until a full orbit is reached.

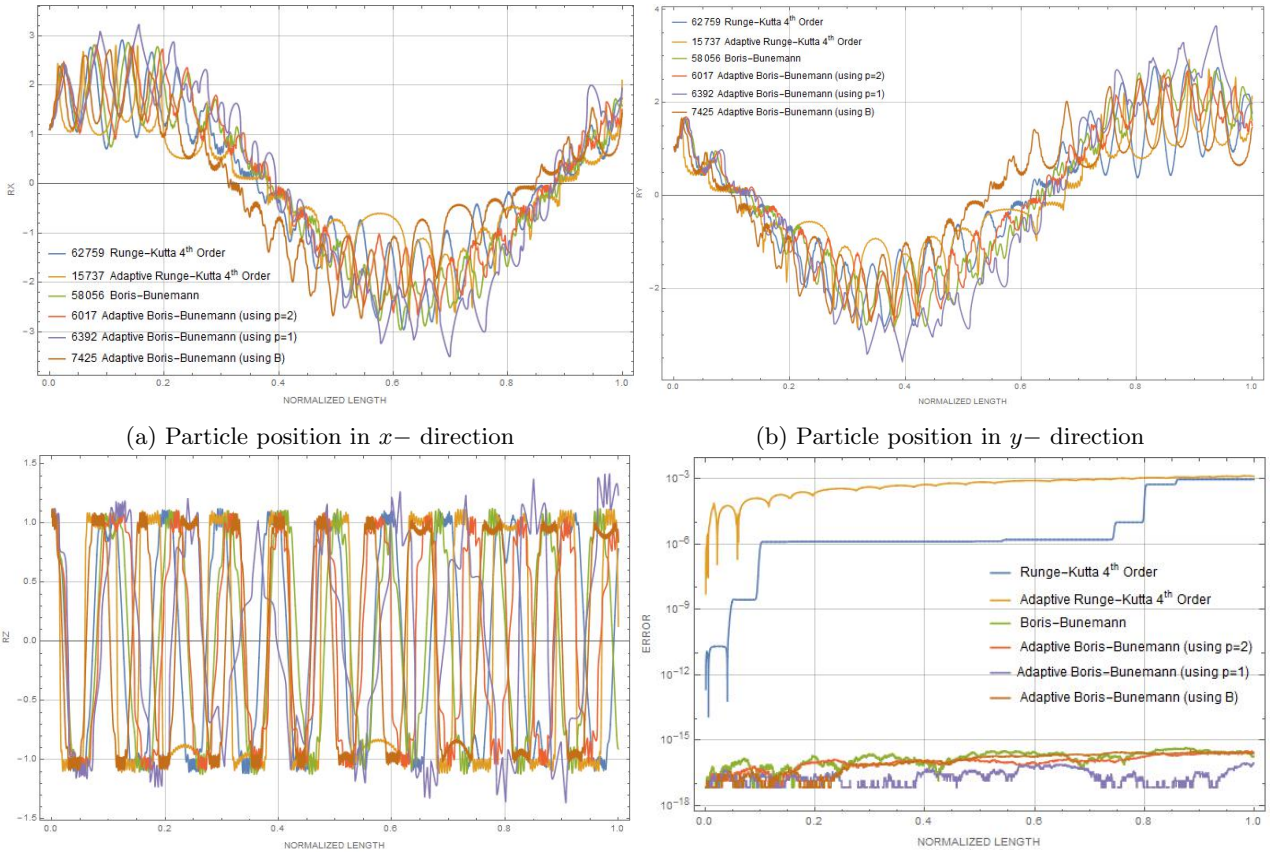

(a) Particle position in $x-$ direction

(b) Particle position in $y-$ direction

(c) Particle position in $z-$ direction

(d) Error comparison of each scheme

Figure 2.38: Test particle in a dipole magnetic field problem

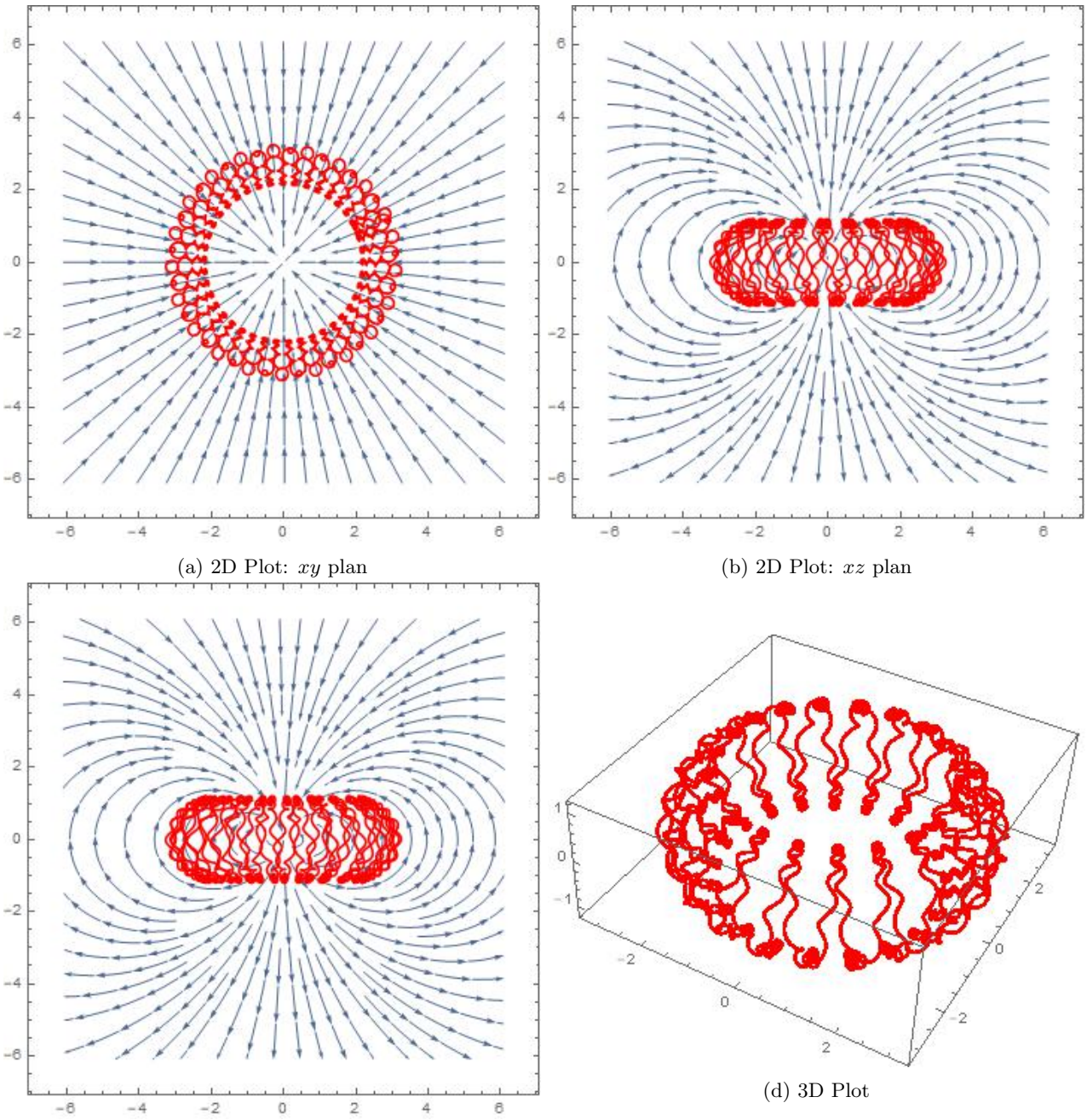

(a) 2D Plot: xy plan

(b) 2D Plot: xz plan

(c) 2D Plot: yz plan

(d) 3D Plot

Figure 2.39: Further results of test particle in a dipole field problem using the conventional Buneman-Boris method for a proton with an energy of 1.3 MeV

Discussion: From the Figure 2.38, we deduce the following:

1. from Figure 2.38a, we remark that the adaptive Buneman-Boris scheme using the error analysis without including the scheme order, is quite deviating in comparison with the other schemes;
2. it is clear that the adaptive Buneman-Boris using the error analysis including the scheme order, has achieved the minimum number of time-steps, required to perform a full orbit ($n_t = 6017$); in second place, the adaptive Buneman-Boris using the error analysis without including the scheme order ($n_t = 6392$), then, the adaptive Buneman-Boris scheme using the magnetic field variation ($n_t = 7425$) and finally, the adaptive Runge-Kutta scheme ($n_t = 15737$). and,
3. from figure 2.38d, as in the previous problem, the adaptive Runge-Kutta scheme has the highest error relatively with other schemes.

2.4.4.2 Guiding Center Examples

1. Overview:

Example 1: 10 MeV proton with $\alpha = 90^o$

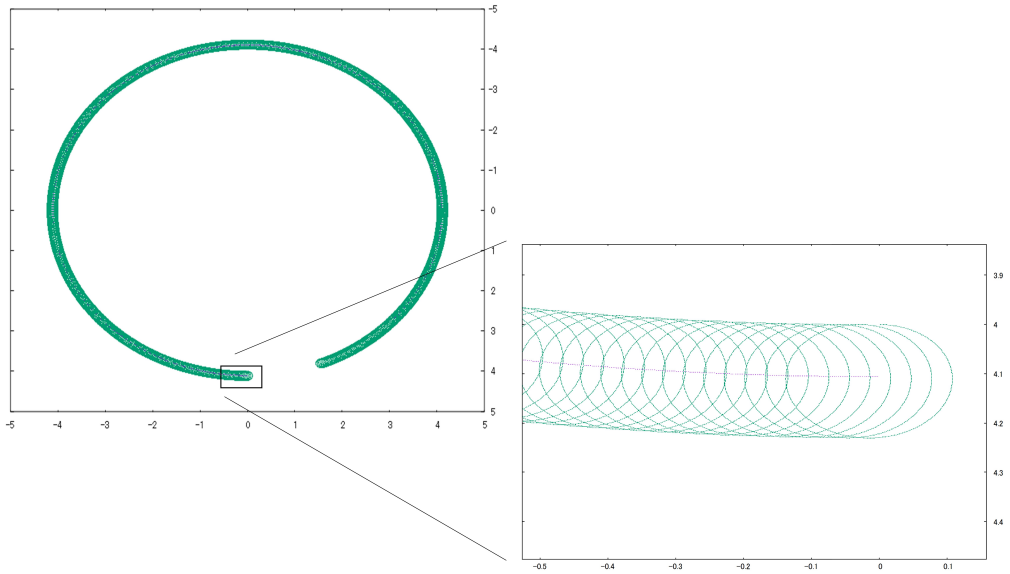

Figure 2.40: XY plane of guiding center proton trajectory

Example 2: 10 MeV proton with $\alpha = 30^o$

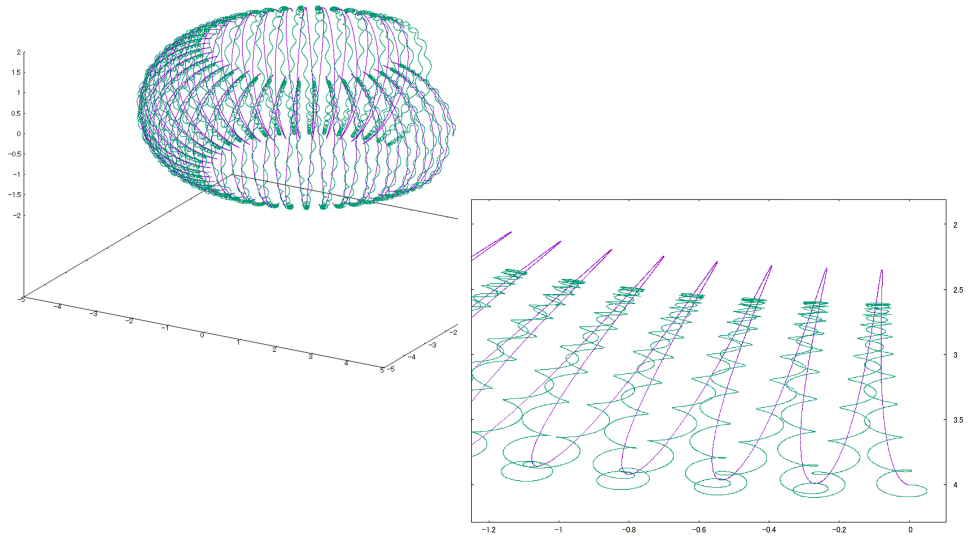

Figure 2.41: Isometric view of the guiding center proton trajectory

Example 3: 10 MeV proton with $\alpha = 30^o$ initially located at $R_x = 2$ Re and 4 Re

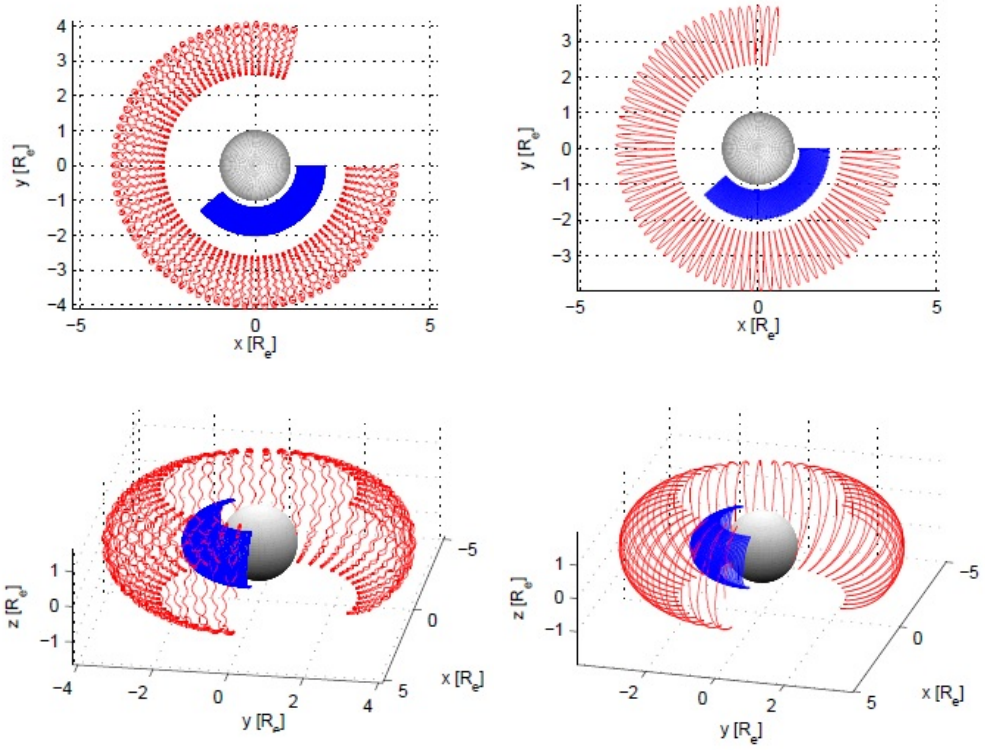

Figure 2.42: Comparison between the full particle model and the guiding center model [Öztürk, 2012]

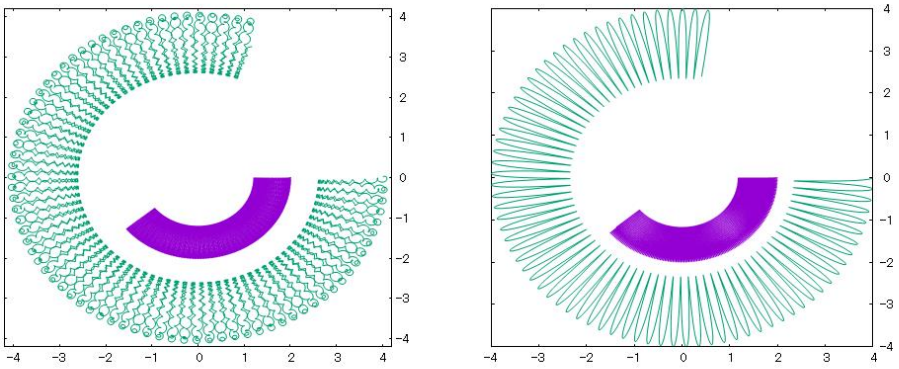

(a) 2D plot of FP trajectory in xy plan

(b) 2D plot of GC trajectory in xy plan

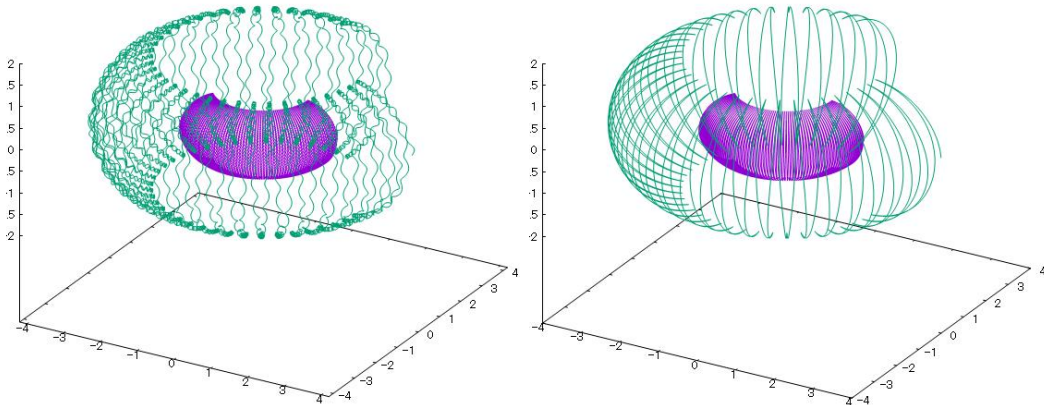

(c) 3D plot of FP trajectory

(d) 3D plot of GC trajectory

Figure 2.43: Validation of the numerical results according to [Öztürk, 2012]; "FP" stands for Full Particle model and "GC" for Guiding Center model

2. Performance Comparison

Dipole Field: Particle information: electron located at 6.6 Re with 2 MeV, where time step is equal to:

$$dt = \frac{2\pi\gamma m}{\epsilon q B_i}$$

where, B_i is the magnetic field magnitude at the initial particle position, and $\epsilon = 1$. This value is then normalized by multiplying the corresponding particle cyclotron frequency:

$$\Omega_0 = \frac{qB_0}{2\pi\gamma m},$$

where, B_0 is the magnetic field magnitude at Earth's surface ($\approx 3.07 \times 10^{-5}$ T)

Pitch Angle (α)	Max. Error in %
30°	1.2×10^{-4}
60°	2.5×10^{-5}
90°	3.5×10^{-5}
120°	2.5×10^{-5}
150°	1.2×10^{-4}

Realistic Field (IGRF+TS05): In the realistic magnetic field (IGRF+TS05), a proton located at 2 R_e with 10 MeV and $\alpha = 30^o$ and fixed time steps for 260 sec by RK4 and Adaptive RK4 (ARK4).

Time Step	Max. Error Ratio
Constant (RK4)	1.5
Adaptive (ARK4)	1

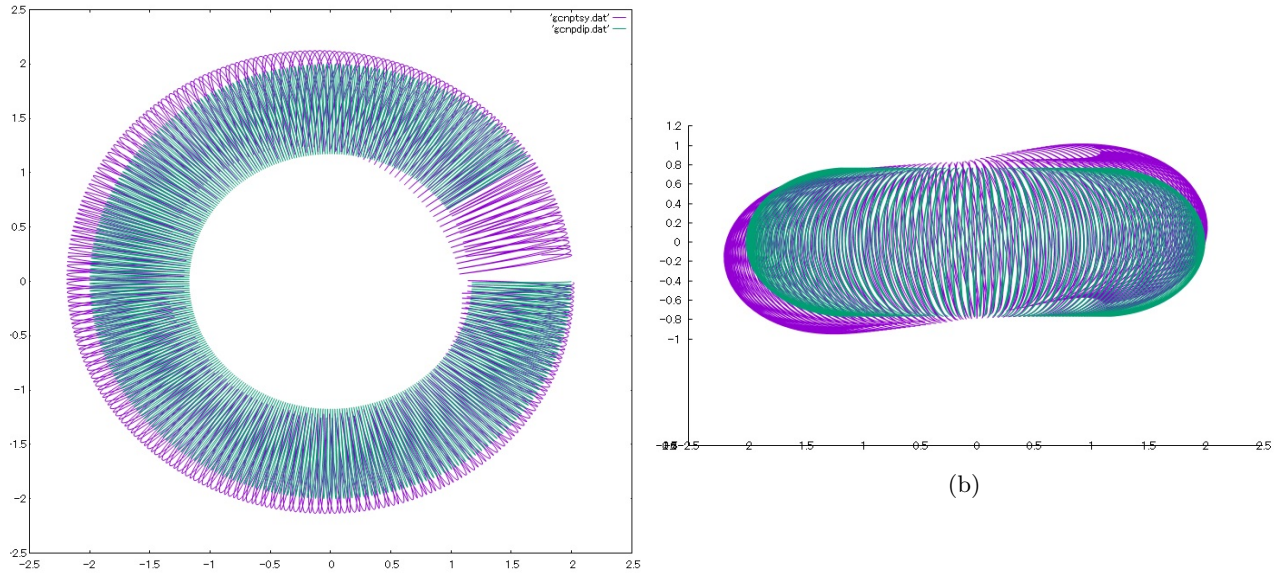

(a) (b)

Figure 2.44: The realistic geomagnetic field effect on the proton trajectory

Real and Dipole field Effects In a real field (IGRF+TS05), a proton located at 2 R_e with 10 MeV and $\alpha = 30^o$ and fixed time steps for 1 hour solved by ARK4.

	Dipole	Real(IGRF+TS05)
$T_s(s)$	1.0	1.05
Max. Error (%)	1.6×10^{-7}	1.288

Full Particle vs Guiding Center Models: We compare both approaches, in three points: computational time, time steps number and maximum error in energy conservation, in a dipole and realistic magnetic fields. In a dipole field, a proton located at 4 R_e with 10 MeV and $\alpha = 30^o$ and fixed time steps for 1 hour.

	Full(BB)	GC(RK4)
N_t	same	same
$T_s(s)$	2.0	3.6
Max. Error (%)	6.0×10^{-12}	7.0×10^{-4}

The main advantage of the full trajectory model solved by BB method is the energy conservation, as shown in the table above. However, to obtain a stable solution, step size should be small enough in order to resolve correctly the helical cyclotron motion of the particle; on the other hand, the advantage of the GC method is that we can use larger time steps to calculate the guiding center motion of the particle, since the helical trajectory is no longer taken into consideration, hence, we can gain a significant computation speed up.
In a realistic field (IGRF+TS05), a proton located at 2 R_e with 10 MeV and $\alpha = 30^o$ and fixed time steps for 1 day. For BB method, the normalized time step $\Delta\hat{t}$ is the inverse of the number of divisions N_c of one cyclotron orbit. So, for $N_c = 20$, then $\Delta\hat{t} = 0.05$. We found that, for this number of divisions, the particle trajectory could not be stabilized. We decreased N_c to 50.

	Full(BB)	GC(RK4)
Δt	0.02	1.85 ($\approx 100\times$)
$T_s(s)$	327	113 ($\approx 3\times$)
Max. Error (%)	7.0×10^{-12}	3.85

Grid Resolution Effect: In a realistic field (IGRF+TS05), a proton located at 2 R_e with 10 MeV and $\alpha = 30^o$ and fixed time steps for 1 hour solved by RK4.

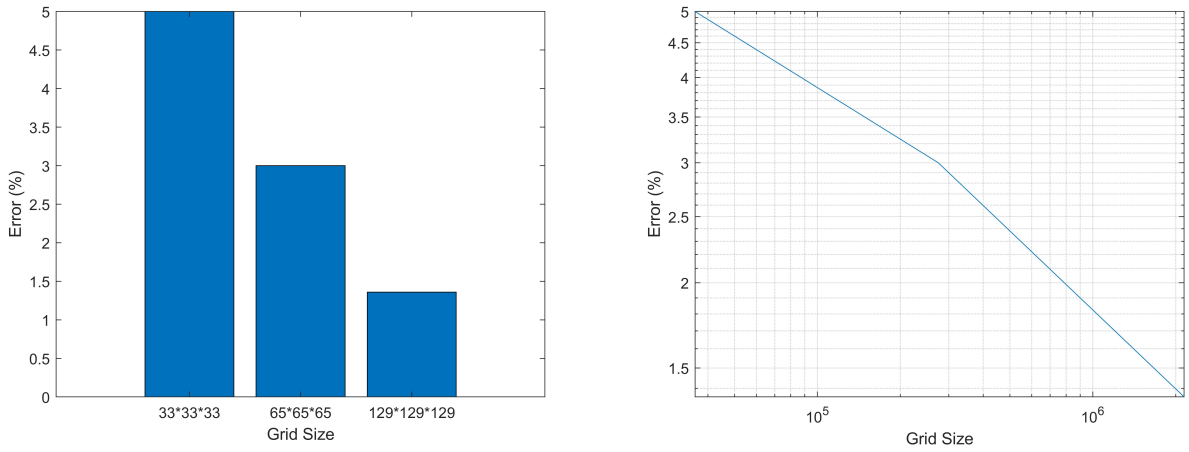

(a) (b)

Figure 2.45: The grid resolution effect on the code performance

	$33 \times 33 \times 33$	$65 \times 65 \times 65$	$129 \times 129 \times 129$
$T_s(ratio)$	1	1	1
Max. Error (%)	5	3	1.4

The computational time is nearly the same, and the conservation of energy is better by ≈ 3.5 times for an increase of 8 times the grid size.

Particle Kinetic Energy Effect: In a realistic field (IGRF+TS05), a proton located at 2 R_e and $\alpha = 30$°and fixed time steps for 1 hour with grid size $129 \times 129 \times 129$.

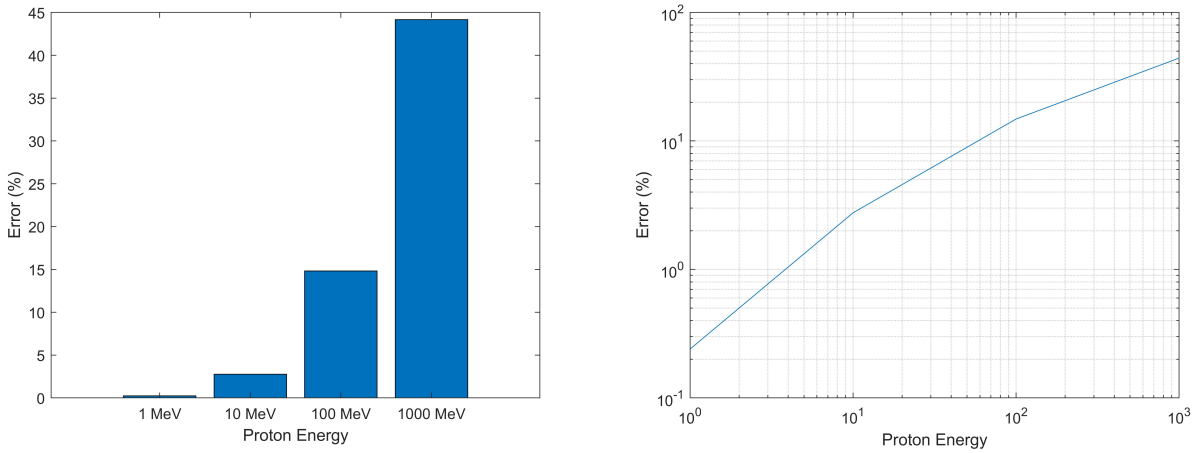

(a) (b)

Figure 2.46: The energy effect on the code performance

	1 MeV	10 MeV	100 MeV	1000 MeV
Max. Error (%)	0.25	3	15	44

Proton/Electron Effect: In a realistic field (IGRF+TS05), a proton and an electron located at 2 R_e and α = 30˚and fixed time steps for one day with grid size $81 \times 81 \times 81$ solved by RK4.

	Electron	Proton
Time (ratio)	220	1
Max. Error (%)	0.01	0.6

Burlirsch-Stoer Method: A proton is located at 4 Re with 10 MeV and $\alpha = 30^o$, for 1 hour of simulation time in a dipole field.

	RK4	BS
Time (ratio)	1	1
Number of time steps (Nt)	270000	150000
Max. Error (%)	6.8×10^{-4}	1.1×10^{-5}

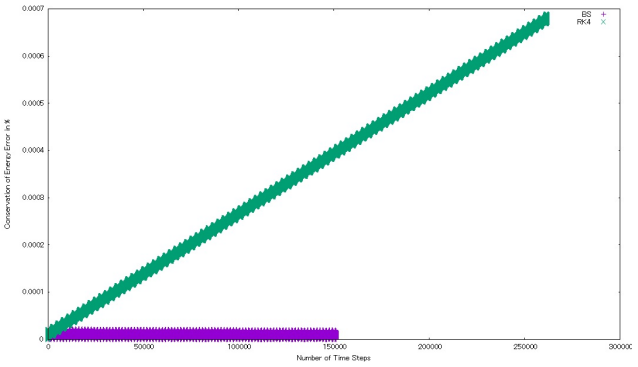

(a) Error percentage versus number of time steps

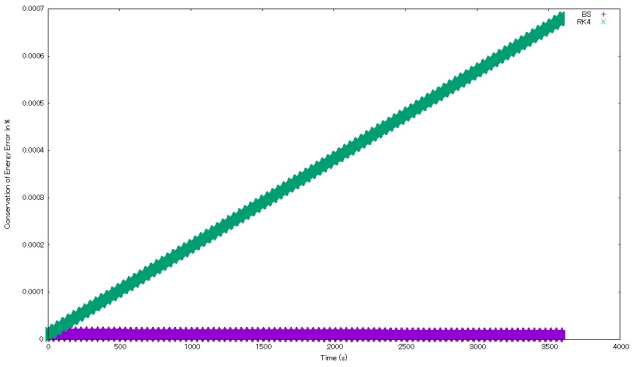

(b) Error percentage versus time

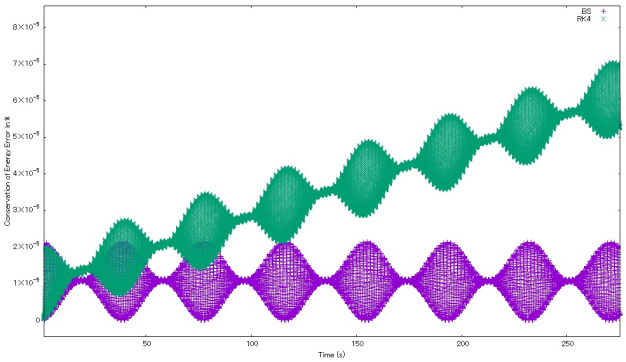

(c) Error percentage versus time (for 260 seconds)

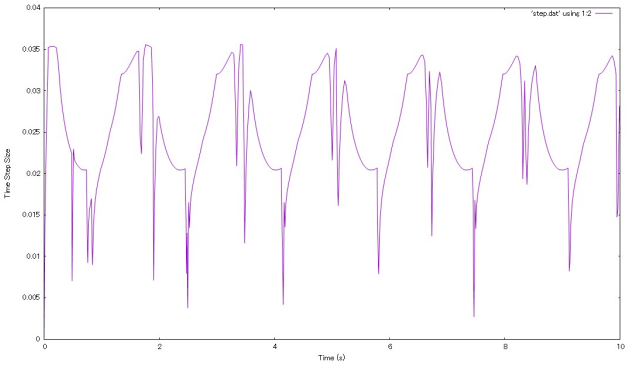

(d) The adaptive time step calculation versus time (10 seconds)

Figure 2.47: The merit of implementing Bulirsch-Stoer method for a 10 MeV proton case

For a 250 MeV proton case, we obtained the following results:

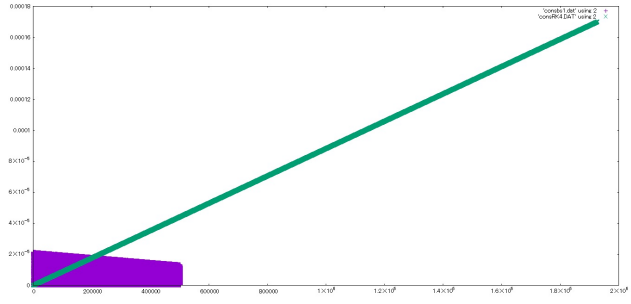

(a) Error percentage versus time steps: a comparison between BS and ARK4 schemes

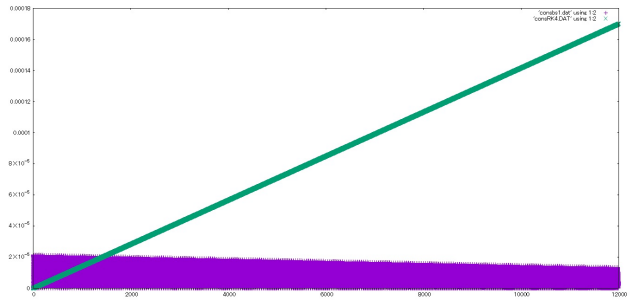

(b) Error percentage history for BS and ARK4 schemes

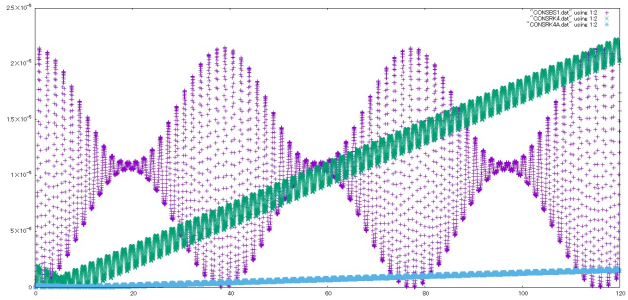

(c) Error percentage history (120 seconds) for BS, RK4 and ARK4 schemes

Figure 2.48: The merit of implementing Bulirsch-Stoer method for a 250 MeV proton case

It is shown from the results that BS method is energy conservative and uses less number of time steps (nearly the half), in comparison with the classical RK4, implemented by most authors, studying the particle dynamics in radiation belts.

Electric Field Inclusion by Tao-Chan-Brizard Model

Uniform Electric Field Case: An example for a 10 MeV proton, initial $R_x = 4$ in a pure dipole field solved for 240 sec with an additional uniform electric field $E_x = 0.05$ (normalized) solved by Tao-Chan-Brizard model and computed by RK4.

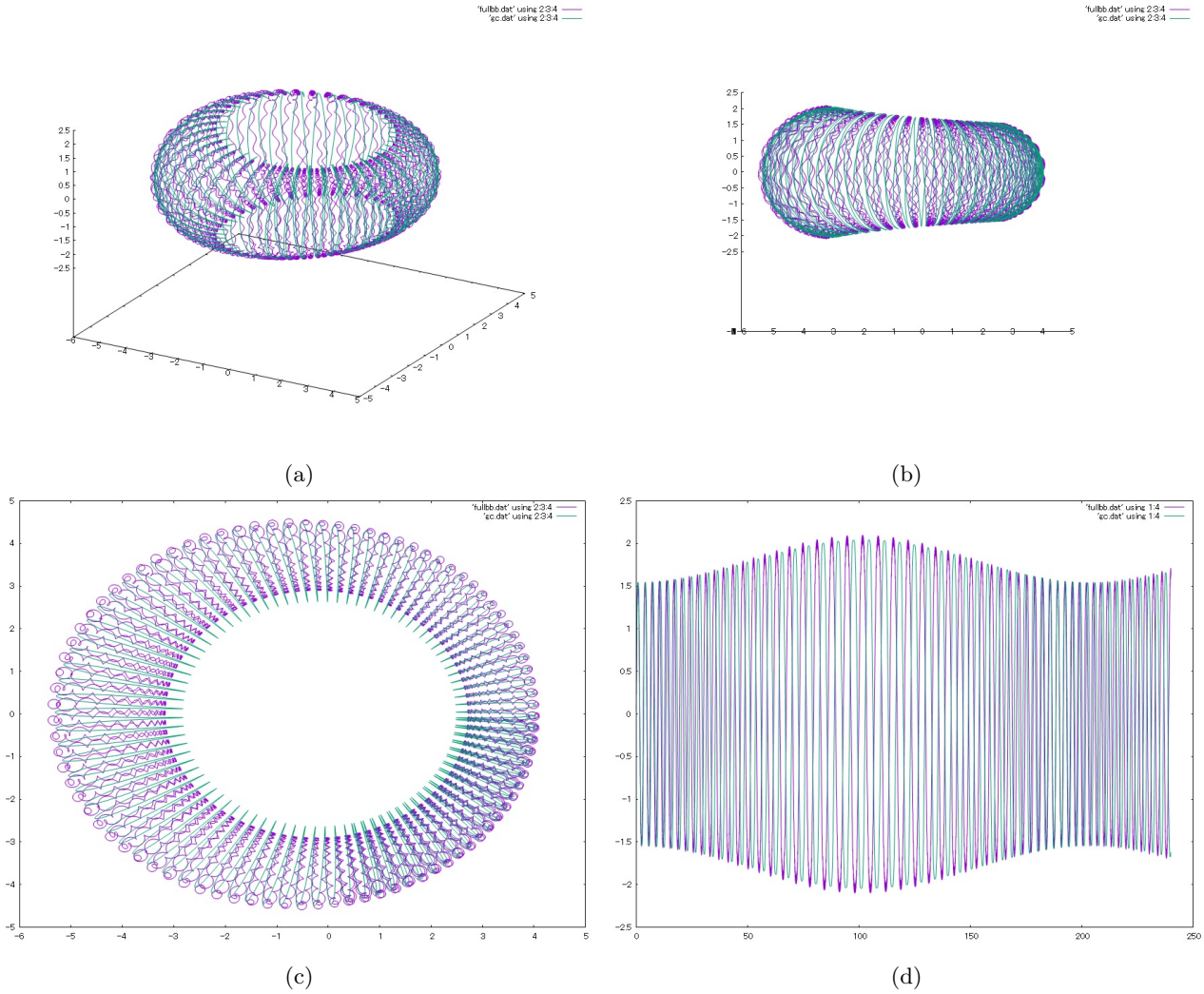

(a) (b)

(c) (d)

Figure 2.49: The effect of a uniform electric field on a 10 MeV proton trajectory in a pure dipole field

Realistic (= inductive) Electric Field Case: An example for a 10 and 100 MeV proton, initial $R_x = 4$ in a pure dipole field solved for 240 sec with an additional inductive electric field solved by Tao-Chan-Brizard guiding center model.

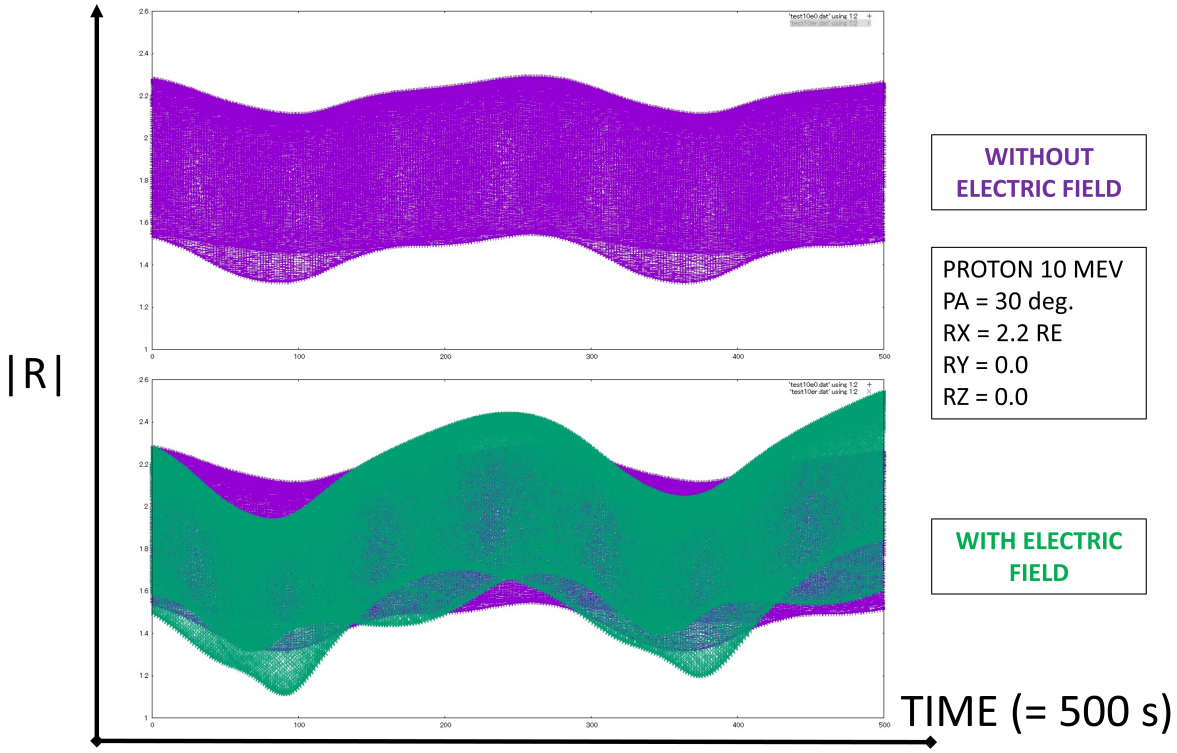

Figure 2.50: Particle distance from the Earth center for a 10 MeV proton without and with the inclusion of the inductive electric field

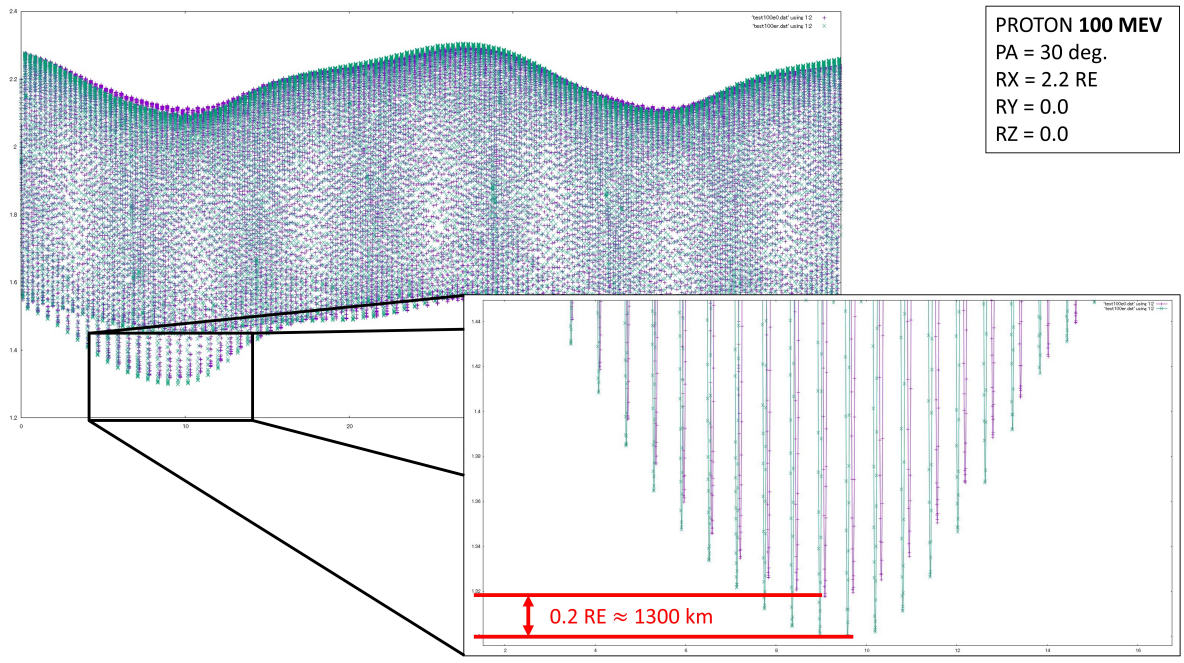

Figure 2.51: Particle distance from the Earth center for a 100 MeV proton without and with the inclusion of the inductive electric field. The zoomed figure highlights the penetration increase effect of the proton in the South Atlantic Anomaly

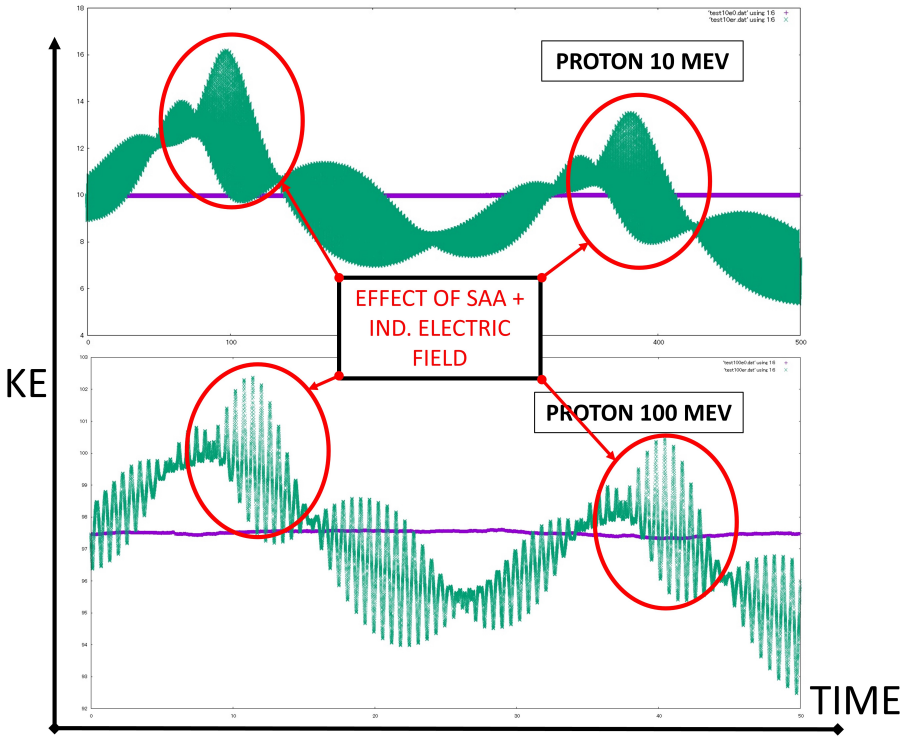

Figure 2.52: Proton kinetic energy evolution for 10 and 100 MeV proton without and with the inclusion of the inductive electric field

From both Figures 2.51 and 2.52, we observe that inside the South Atlantic Anomaly, the inductive electric field intensity is high; a single proton trajectory in the low-altitude L-shells is directly affected by both effects of the SAA region: the decrease in the magnetic field intensity and the associated increase in the inductive electric field intensity.

Chapter 3

SAA Magnetic Response: Long-term Variations

3.1 Introduction

The Earth trapped radiation belts are consisting of huge number of energetic charged particles which are harmful to Low Earth Orbit (LEO) missions. The Earth's magnetic field is not a simple dipole, due to the tilt of the dipole field axis with respect to the Earth's rotation axis, $\approx 10.5°$and the offset distance between the geographic and magnetic centers of the planet $\approx$ 500 km. Therefore, the minimum magnetic field value is found at the South of the Atlantic Ocean; hence, energetic particles from the inner radiation belt are easily precipitated into this zone, where it becomes an additional serious source of radiation for spacecraft and human operations. This phenomenon is called the South Atlantic Anomaly (SAA).

In this research phase, we investigate the long-term variations of the solar wind effects on the South Atlantic Anomaly (SAA) using Tsyganenko model (T96) [Tsyganenko, 1996], a semi-empirical model of external geomagnetic field model. The main variables of the SAA discussed here, as shown in Figures 3.3 and 3.4 are:

1. the latitude and the longitude (= movement) of the SAA's center,
2. the minimum magnetic field value, and
3. the corresponding area,

with respect to altitude and the temporal variation of several solar wind parameters: density, three velocity components and IMF transversal components, from 1999 to 2015, including the temporal variation of the geodipole tilting angle.

The objective of this work is to better understand the SAA behavior under the input space weather conditions, by finding a correlation between the SAA phenomenon and the input solar wind parameters; the study of the SAA magnetic response is important to understand the proton flux dynamics inside the anomaly in order to improve the spacecraft shielding design, thus, to save its components from early damage.

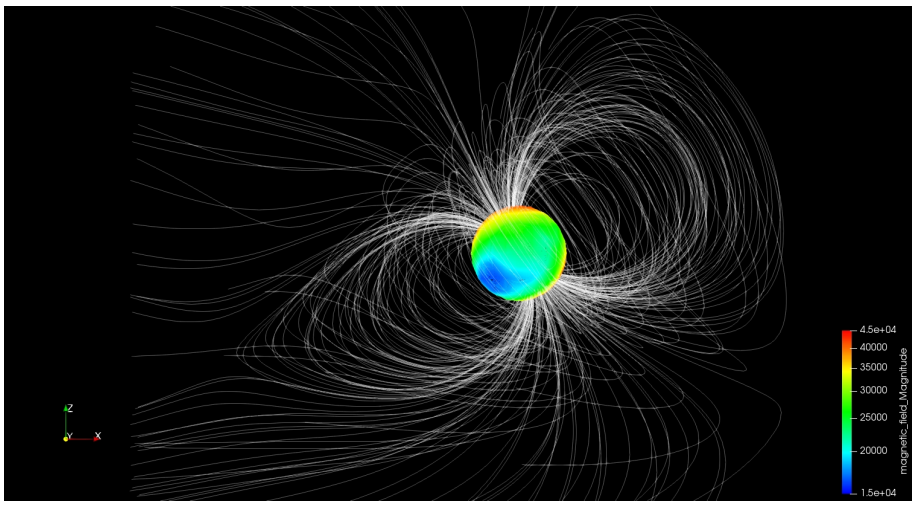

Figure 3.1: The SAA observed from the outer space: spherical contour plot at ≈ 1 Re overplotted by the magnetic field lines (white) computed by Tsyganenko and IGRF models

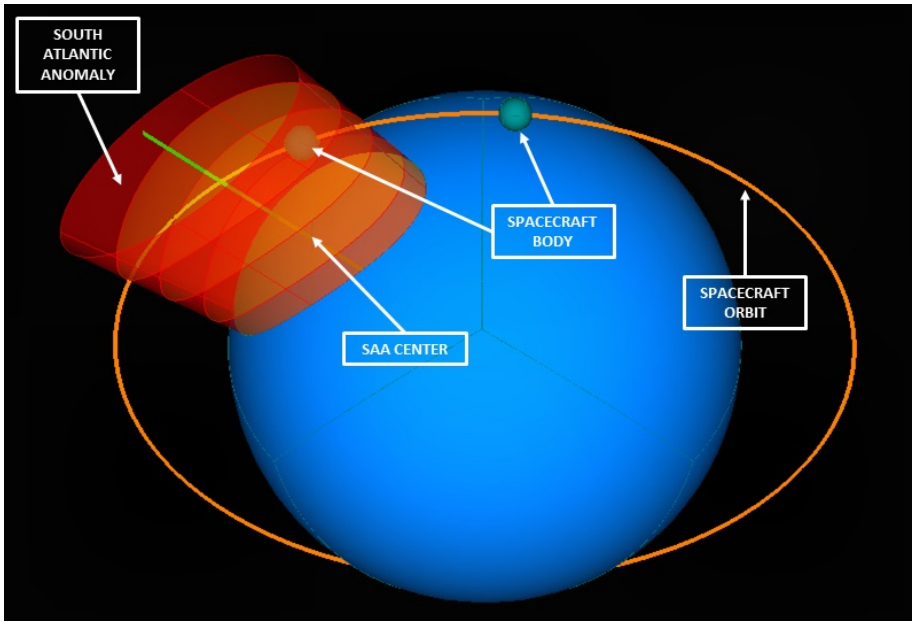

Figure 3.2: A schematic figure showing the anomaly in a 3D configuration intersected by a spacecraft orbit

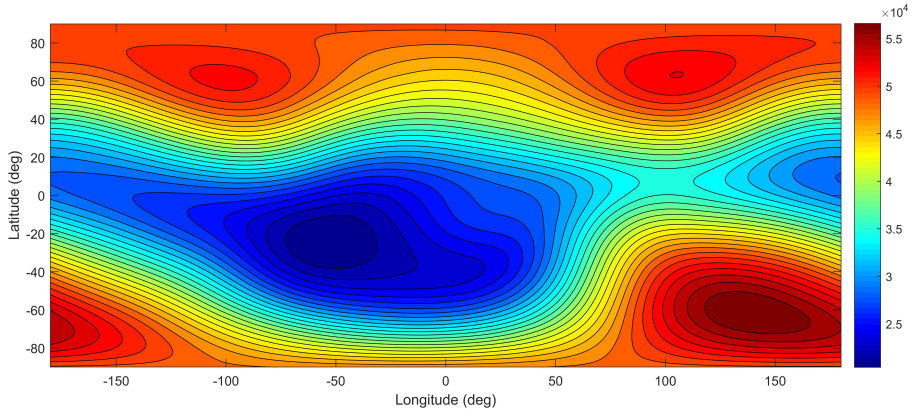

Figure 3.3: The South Atlantic Anomaly (SAA) magnetic field intensity map at altitude of 800 km

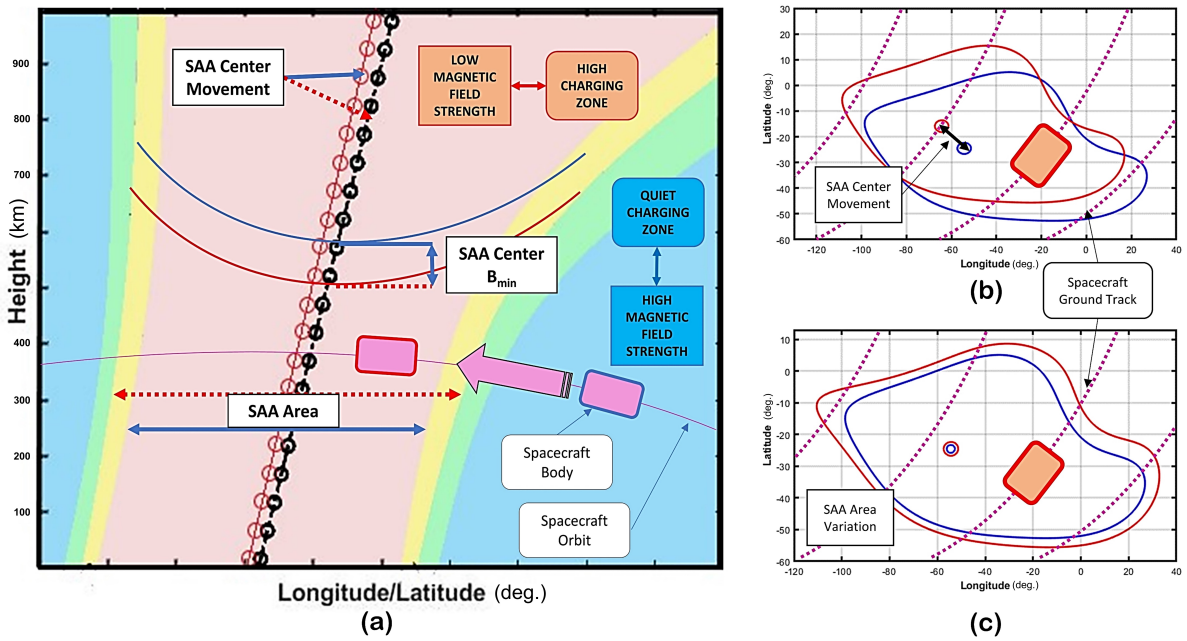

Figure 3.4: Several 2D representations of SAA showing its main four parameters: the SAA center movement, the minimum magnetic field strength at the SAA center and the area evaluated at specific altitude

This work was published in the proceedings of the 4th International Exchange and Innovation Conference on Engineering & Sciences (IEICES), entitled "Long-Term Variations of the Solar Wind Effects on South Atlantic Anomaly (SAA) using Tsyganenko Model" [Girgis and Hada, 2018].

3.2 Validation Phase

Validation phase will be realized by comparing the results with [Qin et al., 2014].

3.2.1 Internal Magnetic Field (IGRF)

First, the minimum magnetic field B_{min} position of the SAA is calculated, using the International Geomagnetic Reference Field (IGRF) model. The top panel of Figure 3.5 shows the secular variation of the latitudinal variation B_{min} corresponding to an altitude of 808 km and a longitude of -52°, and the bottom panel shows the secular variation of the longitudinal B_{min} corresponding to the same altitude and a latitude of -230°, from the years 1999 to 2009. It is clearly shown that the internal magnetic field drifts westward and northward slowly without the addition of the external magnetic field.

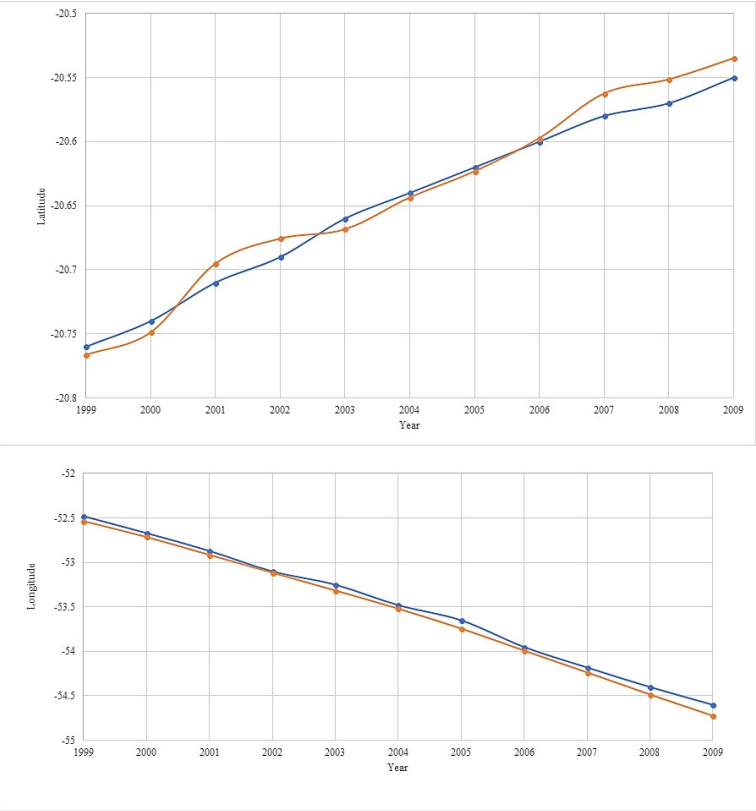

Figure 3.5: Secular variation of the latitudinal (top) and longitudinal (bottom) B_{min} position of the SAA using IGRF model. The blue line corresponds to the original paper results and the orange line, the calculated results.

3.2.2 External Magnetic Field (T96) + Internal Magnetic Field (IGRF)

Next, the external magnetic field T96, as proposed by [Qin et al., 2014], is added to the internal magnetic field, to reproduce a more realistic scenario of the Earth's magnetic field, thus, to study the movement (latitude + longitude) of the B_{min} of the SAA. Two variables are considered here: the dynamic pressure and B_{zIMF}. [Qin et al., 2014] assumed two sinusoidal profiles to simulate the temporal variation of each parameter; e.g. the solar wind dynamic pressure equation is:

$$P_{dyn} = 2 + 8 \sin \frac{\pi(year - 1998)}{16} \tag{3.1}$$

and similarly for B_{zIMF}. Furthermore, each parameter is studied separately to understand its influence on the SAA's movement, in comparison with the "quiet" case, where the dynamic pressure = 0.5 nPa, $B_{zIMF} = 0.0$ and $Dst = 0.0$.

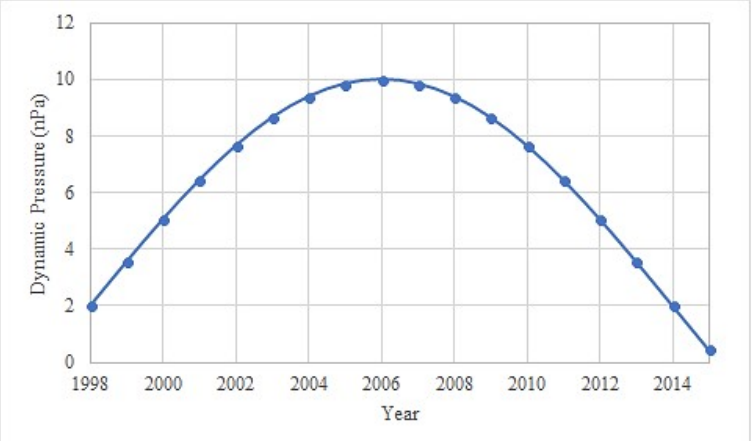

Figure 3.6: Solar wind dynamic pressure profile as proposed by [Qin et al., 2014]

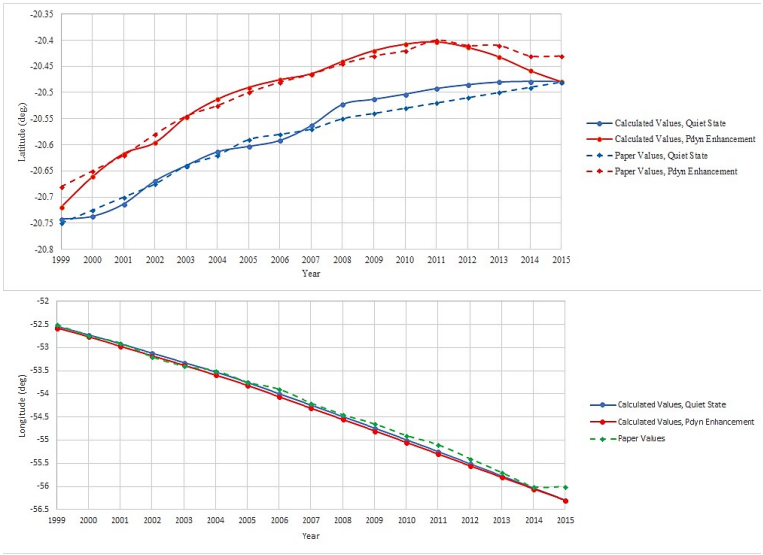

Figure 3.7: SAA's movement temporal variation, including external magnetic field contribution. The solid lines in both panels are the calculated values, where the blue color corresponds to the quiet case ($P_{dyn} = 0.5$ nPa, $B_{zIMF} = 0.0$ and $Dst = 0.0$), and the red one to dynamic pressure enhancement, whereas the dashed blue and red lines represent the results of the quiet and dynamic pressure enhancement cases, respectively, as published in [Qin et al., 2014].

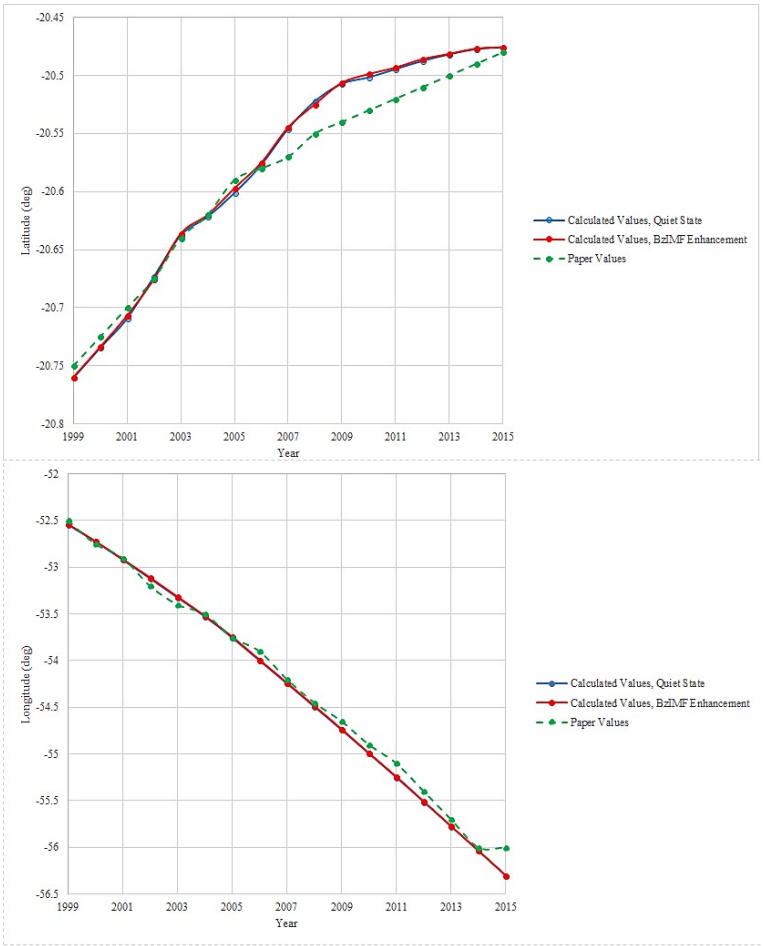

Figure 3.8: SAA's movement temporal variation, including external magnetic field contribution. The solid lines in both panel are the calculated values, where the blue color corresponds to the quiet case ($P_{dyn} = 0.5$ nPa, $B_{zIMF} = 0.0$ and $Dst = 0.0$), and the red one to B_{zIMF} enhancement, whereas the dashed green line represents the results of both the quiet and B_{zIMF} enhancement cases, respectively, as published in [Qin et al., 2014] (which are nearly superposed).

Comments There is a minor deviation in results, which is may be due to some missing information from [Qin et al., 2014], such as (a) the specific chosen time of the year (month, day), (b) the grid size, and (c) the geodipole tilt angle value.

3.3 Main Results

3.3.1 Global study of solar wind parameters effects on SAA

In this section, all solar wind parameters are included in the calculations, with respect to time; *Dst* index is maintained as -10 nT in all calculations and the geodipole tilting angle is updated with respect to time. The target of this study is to create a global understanding of the behavior of the SAA due to the solar wind parameters variations.

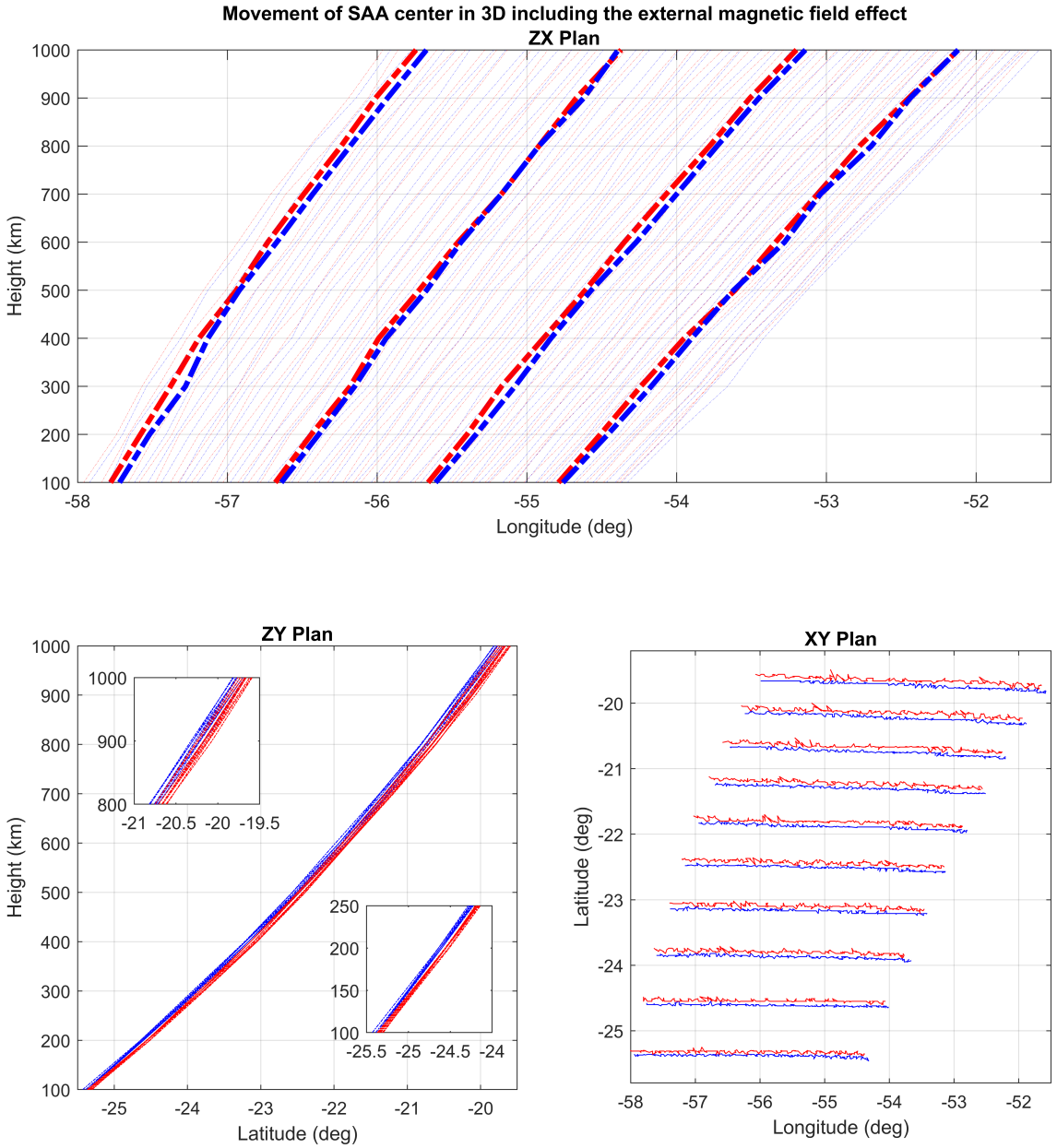

Figure 3.9: Three views of SAA, showing the effect of the external magnetic field on the movement of SAA's center (red lines), with respect to altitude. The thick lines in the top panel (ZX plan) represent the SAA's center each approximately 4 years.

From Figure 3.9, we can extract some useful information:

- From the top panel (ZX plan), SAA's center is accelerating toward the West, and the external magnetic field effect enhances this acceleration.
- From the lower left panel (ZY plan), SAA's center is mostly affected by the external magnetic field at higher altitudes.
- From the lower right panel (XY plan), SAA's center is accelerating toward the North, precisely, at the higher altitudes, and, the external magnetic field effect enhances this acceleration, too.

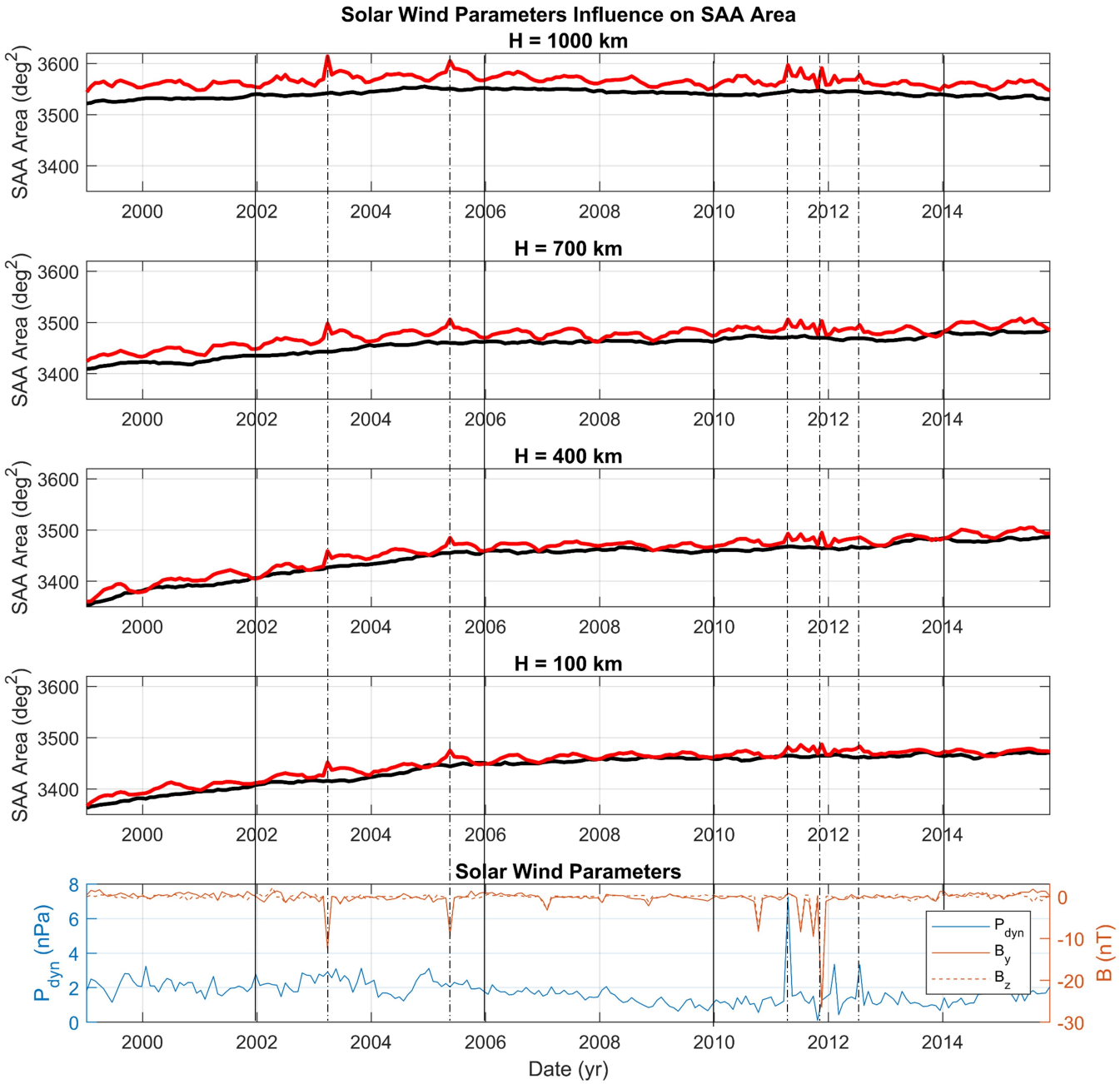

Figure 3.10: The effect of adding external magnetic field on the SAA's area from year 1999 to 2015 (red lines) and internal magnetic field only (blue lines), with respect to altitude.

From Figure 3.10, it is observed clearly that:

- the ram pressure and IMF are affecting the SAA's area; the rapid increase in SAA's area is corresponding to the external magnetic field enhancements, shown here as dashed lines.
- Moreover, at the higher altitudes, the increase in SAA's area is greater.

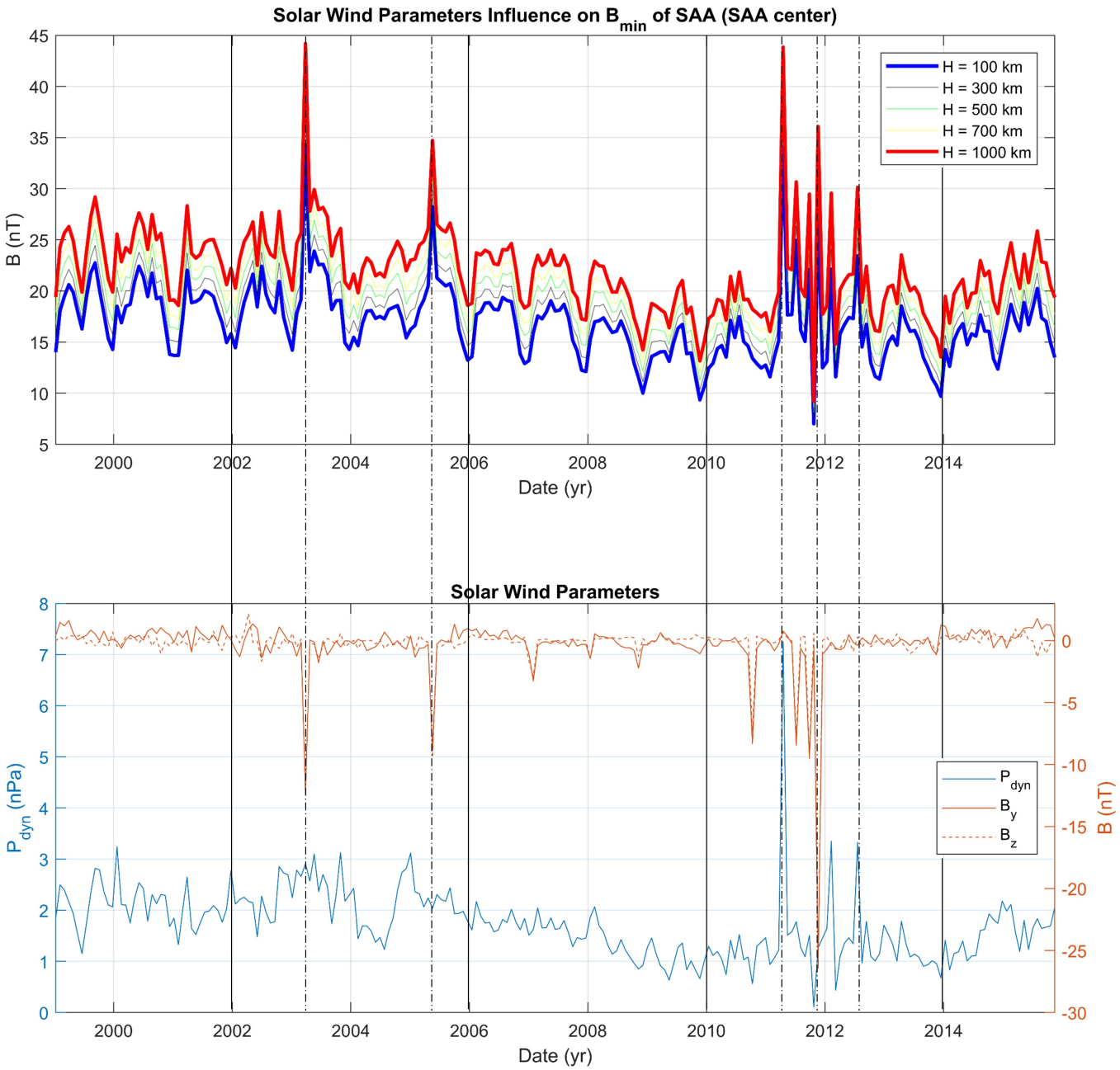

Figure 3.11: The effect of external magnetic field on the absolute difference of B_{min} (calculated based on the internal magnetic field only and with the external magnetic field) of the SAA's center from year 1999 to 2015, with respect to altitude.

From Figure 3.11, it is shown that:

- the ram pressure and IMF are affecting B_{min} of the SAA's center; the rapid increase in B_{min} of the SAA's center is corresponding to the external magnetic field enhancements, shown here as dashed lines.
- Likewise, at the higher altitudes, the increase in B_{min} of the SAA's center is larger.

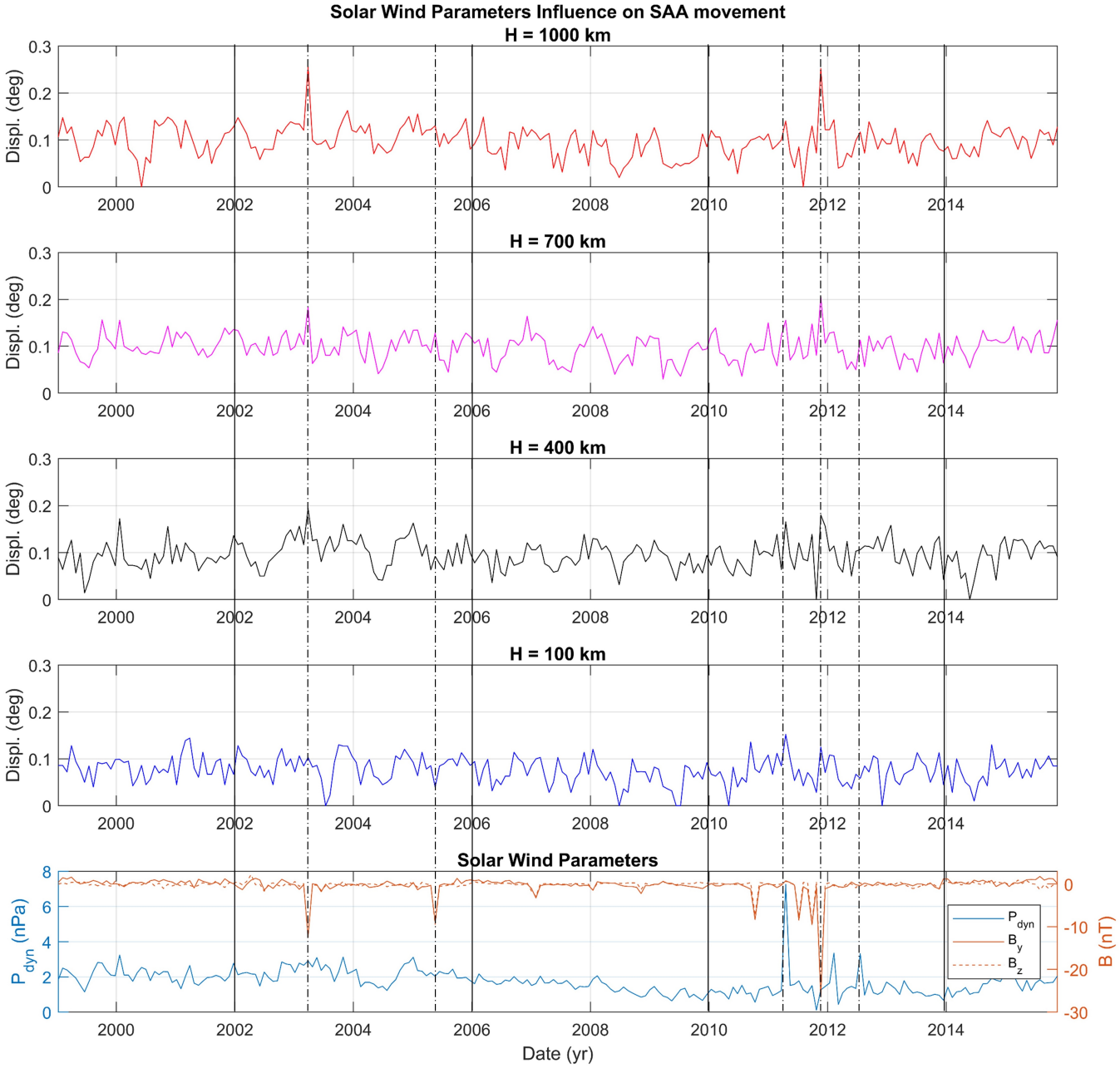

Figure 3.12: The effect of external magnetic field on the movement of SAA's center from year 1999 to 2015, with respect to altitude.

From Figure 3.12, it is remarked that:

- the ram pressure and IMF are affecting the movement of SAA's center; the rapid variation in the movement of the SAA's center is corresponding to the external magnetic field enhancements, shown here as dashed lines.
- Similarly, at the higher altitudes, the variation in the movement of the SAA's center is greater.

3.4 Parametric Study of the Influence of the Solar Wind Parameters on SAA

In this section, each solar wind parameter is included in the Tsyganenko model individually, with respect to time, and the other parameters are set as constant values. The objective of this study is to determine the solar wind parameters which have the stronger influence on the phenomenon.

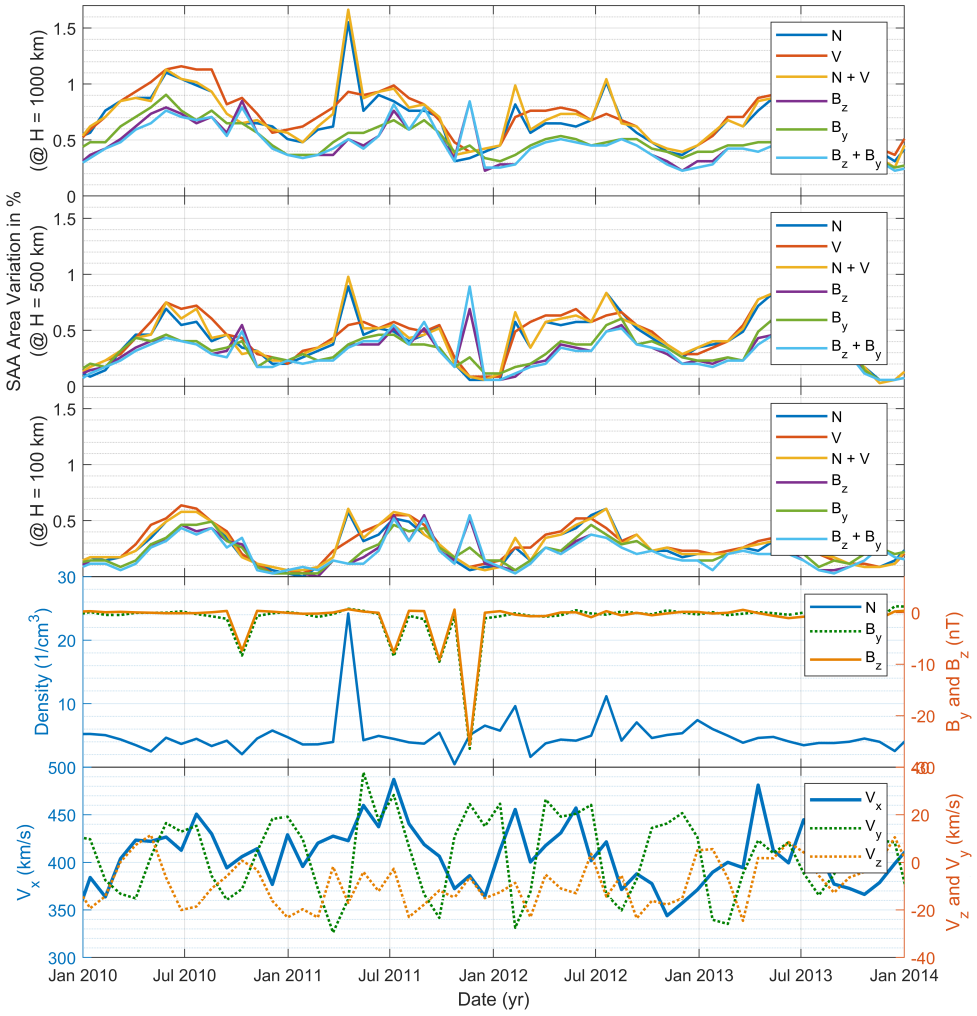

Figure 3.13: The effect of each solar wind parameter on SAA's area from year 2010 to 2014, with respect to altitude.

From Figure 3.13, the ram pressure (density case (N) and density with velocity case (N+V)) has a greater influence on the SAA's area, than the IMF.

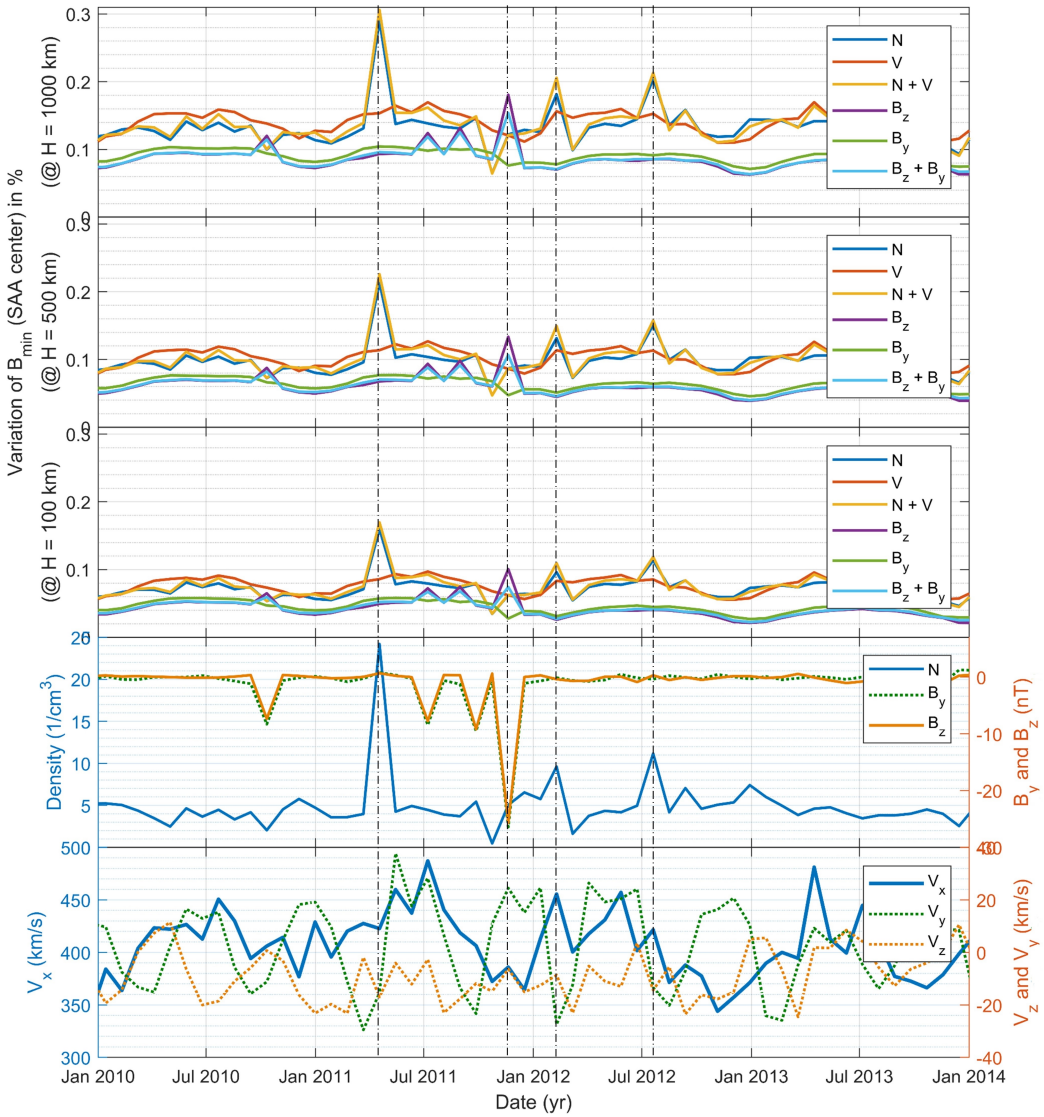

Figure 3.14: The effect of each solar wind parameter on Bmin of SAA's center from year 2010 to 2014, with respect to altitude.

From Figure 3.14, the ram pressure (density case (N) and density with velocity case (N+V)) has also a greater influence on the B_{min} of the SAA's center, than the IMF.

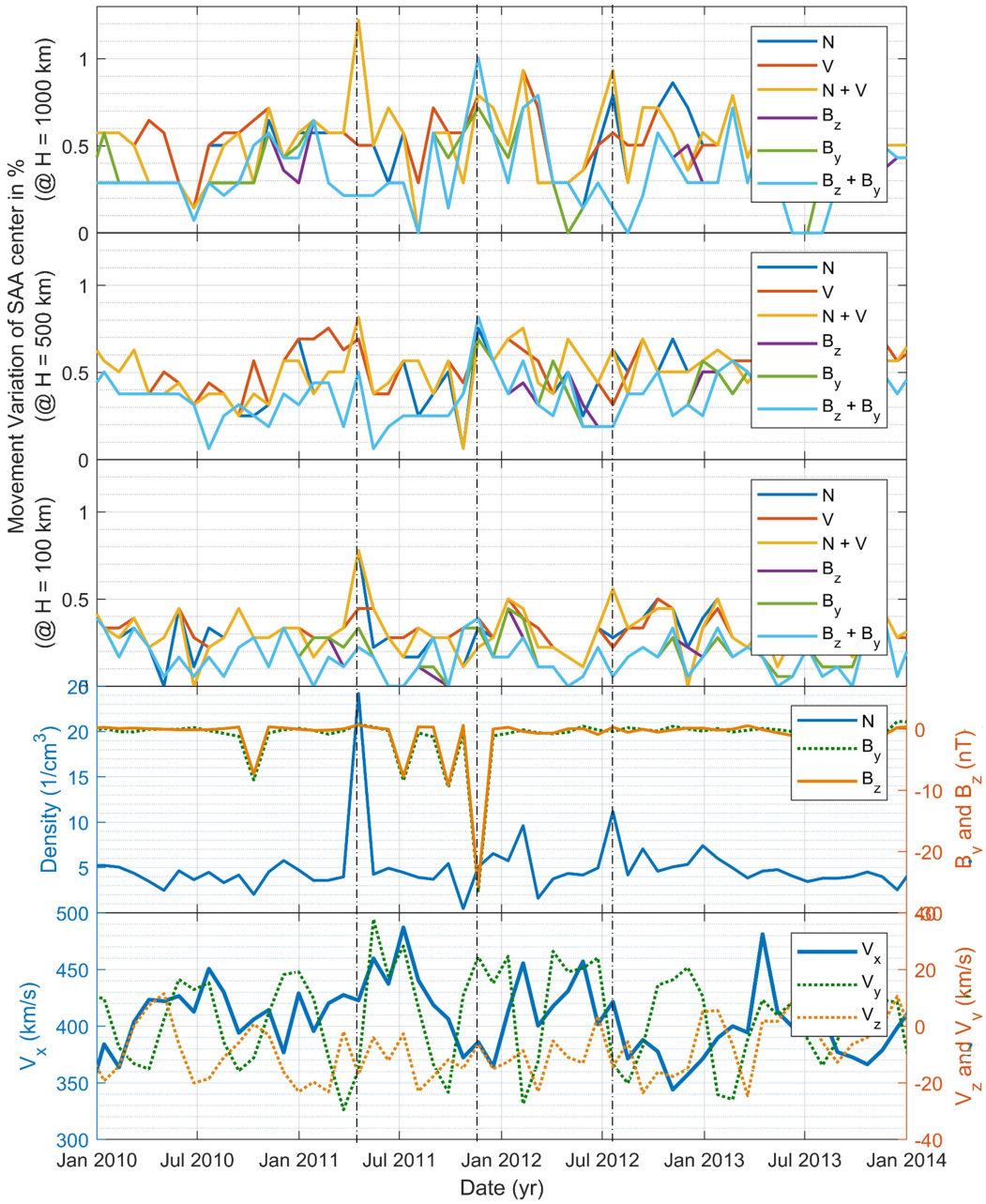

Figure 3.15: The effect of each solar wind parameter on the movement of SAA's center from year 2010 to 2014, with respect to altitude.

From Figure 3.15, the ram pressure (density case (N) and density with velocity case (N+V)) has, as well, a greater influence on the movement of the SAA's center, than the IMF.

3.5 Conclusions

To analyze the long-term variation of the South Atlantic Anomaly (SAA), from the point of view of the magnetic field, we have adopted IGRF and T96 model to study the SAA's behavior, by implementing real solar wind data, from ACE spacecraft from the years 1999 to 2015. Our main conclusions can be summarized as follows:

- The anomaly is strongly correlated with the external magnetic field, even if the region of interest is lying below 1.15 Re (approximately 1000 km). This is due to the variation of the magnetic field lines corresponding to the input solar wind conditions.
- SAA is also correlated to the variation of the geodipole tilting angle, since the magnetosphere structure and shape, are directly depending on it.

- All the SAA parameters, movement, B_{min} and area, are more affected by the external magnetic field at the higher altitudes, because, as long as we move toward the Earth's center, the internal magnetic field is more dominant and therefore, SAA becomes less dependent on the outer solar wind conditions.
- It was deduced from the parametric analysis that the ram pressure is more affecting the SAA than IMF; however, the global study of the solar wind parameters is more realistic than the parametric one, to study the SAA variations, as it might be a significant coupling between the solar wind dynamic pressure and IMF components. Consequently, further analyses are strongly recommended to better understand the SAA behavior under severe space weather conditions; such as adopting T01 and T05 models and studying the short-range variations of the solar wind parameters effects on the SAA.

Chapter 4

SAA Magnetic Response: Mid-term Variations

4.1 Introduction

From Africa through the South of the Atlantic Ocean to South America, the Earth's lowest magnetic field intensity is located; this phenomenon is called the South Atlantic Anomaly (SAA). The most recent interpretation of this permanent feature of the geomagnetic field is the presence of negative geomagnetic fluxes at the core-mantle boundary under the Earth's surface at this region, which in turn, decreases locally the field strength [Terra-Nova et al., 2017], [A. Tarduno et al., 2015], [Cottaar and Lekic, 2016], [Aubert, 2015].

The research about the SAA is always attracting the scientists from different backgrounds, such as (1) in geomagnetism, where [Pavón-Carrasco and De Santis, 2016] studied the possible geomagnetic reversal, (2) in space plasma physics, to understand the close approach of the inner radiation belt, and (3) in spacecraft design, to mitigate the radiation effects on the on-board instrument at Low Earth Orbit (LEO), etc. In this chapter, we are concentrating on studying statistically the space weather effects on the magnetic field response of the South Atlantic Anomaly.

Since the space weather conditions are always influencing the trapped radiation belts in the inner magnetosphere, much research had been carried out in studying the effects of space weather on the South Atlantic Anomaly. [Qin et al., 2014] studied the magnetic field long-term response of the SAA center location by proposing sinusoidal profiles of the solar wind ram pressure, the z-component of the Interplanetary Magnetic Field (IMF), B_{zIMF}, and the Dst index, using the Tsyganenko model (T96), as well as [Schaefer et al., 2016] and [Ye et al., 2017]. In addition, [Zou et al., 2015] found a direct correlation between the Dst index and the two SAA parameters, the maximum proton flux value and corresponding area, by using measurements from NOAA 17 satellite data. The results of the two mentioned studies were obtained at specific altitudes, and for two SAA parameters each. Moreover, [Nakano and Heckman, 1968] and [Dragt, 1971] examined as well the solar cycle variation effects on the SAA proton flux; [Grigoryan et al., 2008], on its westward drift rate; [Badhwar, 1997] and [Casadio and Arino, 2011], on its northward drift rate; as well as [Huston et al., 1996] and [Huston and Pfitzer, 1998], the anti-correlation between the solar radio flux $F_{10.7}$ and the proton flux. Lastly, as reported in the previous chapter, we studied the solar wind ram pressure and the IMF transversal components on the SAA magnetic field response using the Tsyganenko model T96 by maintaining a constant Dst index [Girgis and Hada, 2018].

We should confirm the accuracy of the Tsyganenko models at low altitudes since their implementation is the essential part of this study. We summarize here the main points:

1. As described in detail by the model developer e.g. the review paper [Tsyganenko, 2013], the net external magnetic field is described as the superposition of various magnetospheric currents: the magnetopause current, the large-scale field-aligned currents, the ring current and the tail currents.

2. The calculation of the Isotropic precipitation Boundary (IB) is one of the methods that validates the model accuracy with respect to the low-altitude spacecraft measurements: for example, [Sergeev and Tsyganenko, 1982] compared the adiabatic drift shells obtained from the T79 model [Tsyganenko, 1979] for the mirrored particles at the altitude 400 km, with the experimental data, and found a good agreement with an error of 1° at high latitudes. Moreover, [Weiss et al., 1997] compared the modeled Isotropic precipitation Boundary (IB) from the T89 [Tsyganenko, 1989] with the low-altitude DMSP spacecraft (830

km) data and estimated the error of the median latitudinal deviation to be ≈ 2°. In addition, [Shevchenko et al., 2010] estimated the Isotropic precipitation Boundary (IB) by the T96 model [Tsyganenko, 1996] and compared it with THEMIS observational data at the ionospheric altitudes and found a reasonable agreement with an latitudinal error ≈ 1°. [Kubyshkina et al., 2009] found an error ≈ 1° in quiet space weather conditions by implementing the same T96 model, compared with NOAA spacecraft measurements; the error could reach several degrees during substorm conditions. [Ganushkina et al., 2005] estimated the maximum error ≈ 0.7°, when *Dst* was equal to -16 nT, by adopting the T01 model. For the selected *Dst* index range, the model underestimated the tail current, where this issue was later improved by the TS05 model [Tsyganenko and Sitnov, 2005].

3. The calculation of the geomagnetic cutoff latitude is also another technique that tests the accuracy of the Tsyganenko models at low-altitudes by comparing the obtained results with the spacecraft measurements, as demonstrated by [Smart and Shea, 2005], where the mentioned authors adopted the T89 model with the IGRF model, and then compared the given results with the SAMPEX spacecraft data at the altitude 450 km. The authors found that the computed and the measured cutoff latitudes showed a similar global pattern, while during the magnetic active cases, the assessed error was slightly increased. Additional studies on this topic were reported in [Smart and Shea, 1994, Kress et al., 2015].

4. The parametrization of the Tsyganenko models by the solar wind drivers and/or ground-based indices is considered as a strong advantage. This merit permits us to understand the magnetospheric structure associated to the quiet space weather conditions and the magnetic storm events. It is widely understood that there is no perfect model that could fulfill all the user requirements, thus, we are concentrating our efforts to understand statistically and quantitatively the SAA general response, due to the solar wind parameter variations and the seasonal changes.

In this chapter, we are extending the investigation of the space weather impact on the magnetic response of the SAA, by examining its dependency with the altitude and by introducing the SAA variables as follows: (1) the SAA area computed below a selected threshold of the magnetic intensity; (2) the minimum magnetic field strength at the SAA center (B_{min}); and (3) the location (latitude and longitude) of the SAA center described as the point where the magnetic field intensity is minimized. Moreover, the space weather inputs parameters include the two transversal components of the Interplanetary Magnetic Field (IMF), B_{yIMF} and B_{zIMF}, as well as the three velocity components of the solar wind, the solar wind dynamic pressure, the *Dst* index, and the geodipole tilting angle (μ).

The framework in this research phase was achieved by implementing three versions of the Tsyganenko models, T96 [Tsyganenko, 1996], T01 [Tsyganenko, 2002a, Tsyganenko, 2002b], and TS05 [Tsyganenko and Sitnov, 2005] to describe the external magnetic field, then, the output results of each model are compared. The global representation of the geomagnetic field is completed by combining the International Geomagnetic Reference Field (IGRF-12) to define the main (internal) magnetic field.

This work was published in the Earth, Planets and Space (EPS) Journal, entitled "Solar wind parameter and seasonal variation effects on the South Atlantic Anomaly using Tsyganenko Models" [Girgis et al., 2020].

4.2 Material and Methods

The localized decreased intensity in the magnetic field (= SAA) attracts the particles from the inner trapped belt. Therefore, the magnetic field is playing the major role in the particle flux response of the SAA. Hence, the purpose of this study was to evaluate the correlation level of each SAA variable with respect to each space weather parameter.

First of all, the SAA variables are demonstrated as shown in Figure 3.4 in the previous chapter; Panel (a) illustrates the minimum magnetic field at the SAA center, the corresponding area, calculated below the magnetic field limit (= 7/6 ≈ 1.167 B_{min}), and the movement (latitudinal and longitudinal variations) of the SAA center. In the same panel, a typical spacecraft is also shown at the Low Earth Orbit (LEO) (colored in magenta) that passes through the SAA; the dangerous situation arises when the spacecraft body (rectangular shape colored with magenta) enters the high radiation zone (colored in light red), whereas the less dangerous radiation zone is located outside the SAA (colored in light blue). The variations of the SAA center movement and the corresponding area are also illustrated in Panels (b) and (c), respectively, with the addition of a typical ground track of a LEO satellite. It should be noted that the figure demonstrates the SAA magnetic variations (red and blue contour lines) for illustrative purposes only and not according to realistic situations.

4.2.1 SAA Variables

The variations of the SAA variables estimated in this study were due to the external magnetic field temporal change. The variations were computed by subtracting the corresponding values calculated first by adopting the main (internal) magnetic field only, as defined by the IGRF-12 model, from the values calculated by adding the external magnetic field when described by the Tsyganenko models, in addition of the main (internal) magnetic field. Next, the normalization was achieved by dividing the given value by the corresponding SAA variables, calculated according to the main (internal) magnetic field. The following equations are implemented:

$$\Delta \left[\bar{X}_j\right]_{\%} = \frac{\left[X_j\right]_{e+i} - \left[X_j\right]_i}{\left[X_j\right]_i} \times 100 \tag{4.1}$$

$$\left[X_j\right] = \begin{bmatrix} A \\ B_{min} \\ \theta \\ \phi \end{bmatrix} \tag{4.2}$$

where,

X_j is a vector of the four SAA variables ($j = 4$),

A is the area,

B_{min} is the minimum magnetic field intensity (= SAA center),

θ is the latitude of the SAA center,

ϕ is the longitude of the SAA center,

$[X]_{e+i}$ is the SAA variable computed based on the external and the internal magnetic field, and,

$[X]_i$ is the SAA variable computed based on internal magnetic field only

4.3 Input Data

The required input information to run the Tsyganenko model are the real solar wind data, such as the solar wind three velocity components, the ram pressure, the IMF transversal components, B_{yIMF} and B_{zIMF}. The daily data was provided by the ACE spacecraft from the years 2010 to 2014, in addition to the Dst index and the geodipole tilting angle (μ), as calculated by the GEOPACK package subroutines. All previous information is plotted as demonstrated in Figure 4.1.

It was expected that the variations of the input space weather parameters not only will influence the global magnetic field representation but would also induce some variations in the inner magnetosphere. Since the global structure of the Earth's magnetic field was described according to the given space weather parameters, a statistical study was performed, in order to obtain the correlation between each of the input space weather parameters and the SAA output variables, besides illustrating their temporal evolution, as shown in the next section.

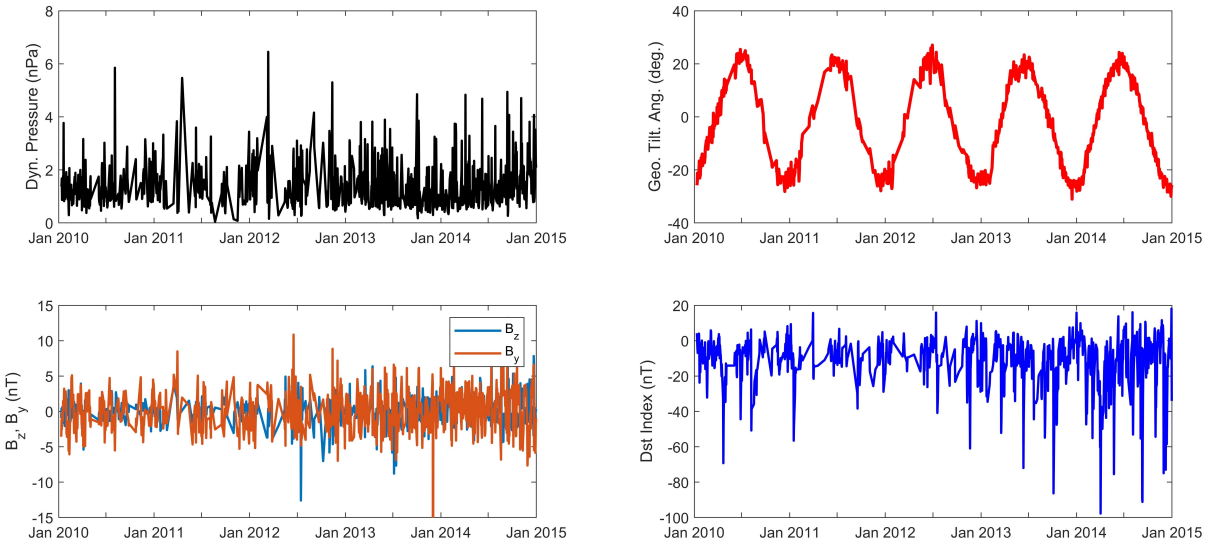

Figure 4.1: The left panel shows the daily solar wind data from the ACE spacecraft, and the right panel, the geodipole tilting angle (computed by the GEOPACK package subroutines), with the *Dst* index profiles from 2010 to 2014.

4.4 Results

Figure 4.2 shows the two SAA variable profiles: the area and the B_{min} variations plotted in Panels (a) and (b), respectively. The calculations here were demonstrated for the altitude 800 km, by implementing the three Tsyganenko models, T96, T01 and TS05.

First, it was found that the changes of the SAA variables were larger when T96 and T01 were adopted, in comparison with the TS05. Second, the latter results clearly exhibit a smoother sinusoidal pattern, revealing the strong impact of the geodipole tilting angle on the magnetic field response of the SAA.

Further interpretations are quantitatively assessed to determine the correlation level between the SAA response and the input space weather conditions by performing a statistical study. The famous Pearson correlation coefficient was calculated for the two vectors, one standing for every temporal variation of the SAA output variables, as discussed previously in the Equations 4.1 and 4.2, and the other one, for every temporal variation of the input space weather parameter, according to a selected altitude, and calculated corresponding to each Tsyganenko model, T96, T01 and TS05.

Figures 4.3 and 4.4 display the correlation coefficient for every SAA output variable, associated with each input space weather parameter: the solar wind dynamic pressure, B_{yIMF}, B_{zIMF}, the geodipole tilting angle, and the *Dst* index, at altitudes of 100, 400, 700 and 1000 km, by implementing every Tsyganenko model, T96, T01 and TS05. It was revealed that from the T96 calculations that the solar wind ram pressure was influencing all SAA variables nearly at all altitudes. Adding that, the IMF had a very weak impact on all SAA variables, regardless of the adopted Tsyganenko model. Although, a moderate absolute correlation was still found (≈ 0.4) between B_{yIMF} and the SAA B_{min} when TS05 was adopted. Certainly, the three models did agree that both, the *Dst* index and the geodipole tilting angle effects were dominant at all altitudes and for all SAA variables. Tsyganenko models T96 and T01 highlighted the *Dst* index effects on all SAA variables; on the other hand, the TS05 results reduced the *Dst* index effect on the SAA magnetic behavior.

Table 4.1 represents the correlation analysis, as shown in Figures 4.3 and 4.4, obtained by the three Tsyganenko models, T96, T01 and TS05 at an altitude of 800 km. The colored values in the table identify the weak (blue, $0.1 - 0.4$), moderate (green, $0.4 - 0.7$), and strong (red, $0.7 - 1$) absolute correlation. It was again concluded numerically that the three models T96, T01 and TS05 did agree together that the *Dst* index and the geodipole tilting angle (μ) were the most influencing space weather parameters on the SAA magnetic response. Furthermore, it was found that the SAA center longitudinal movement was the least SAA variable influenced by the external space weather conditions. In this study, since we focused on the inner magnetosphere configuration dynamics, it is proposed to take into account both model: T01 [Tsyganenko, 2002a, Tsyganenko, 2002b], which better resolves the inner magnetosphere and magnetotail structures, in addition to TS05 [Tsyganenko and Sitnov, 2005], that better describes the inner magnetosphere response, corresponding to the strong storm

events.

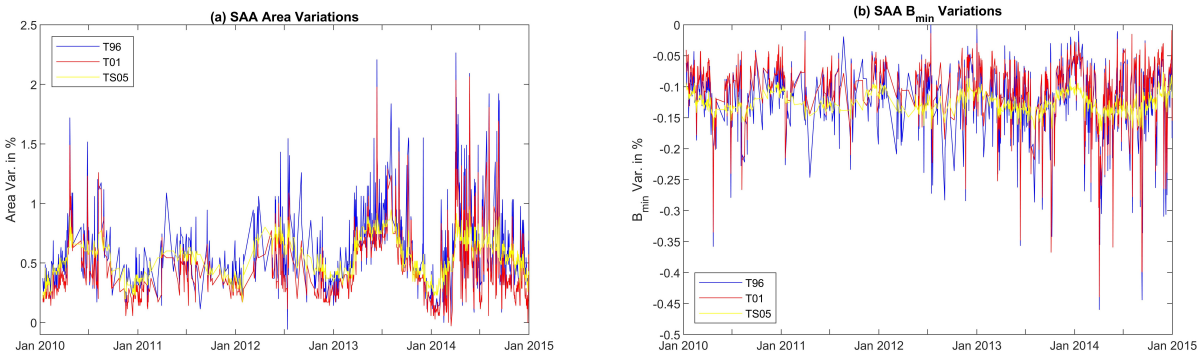

Figure 4.2: (a) the area and (b) the B_{min}, by adopting the Tsyganenko models T96, T01, and TS05, at an altitude of 800 km.

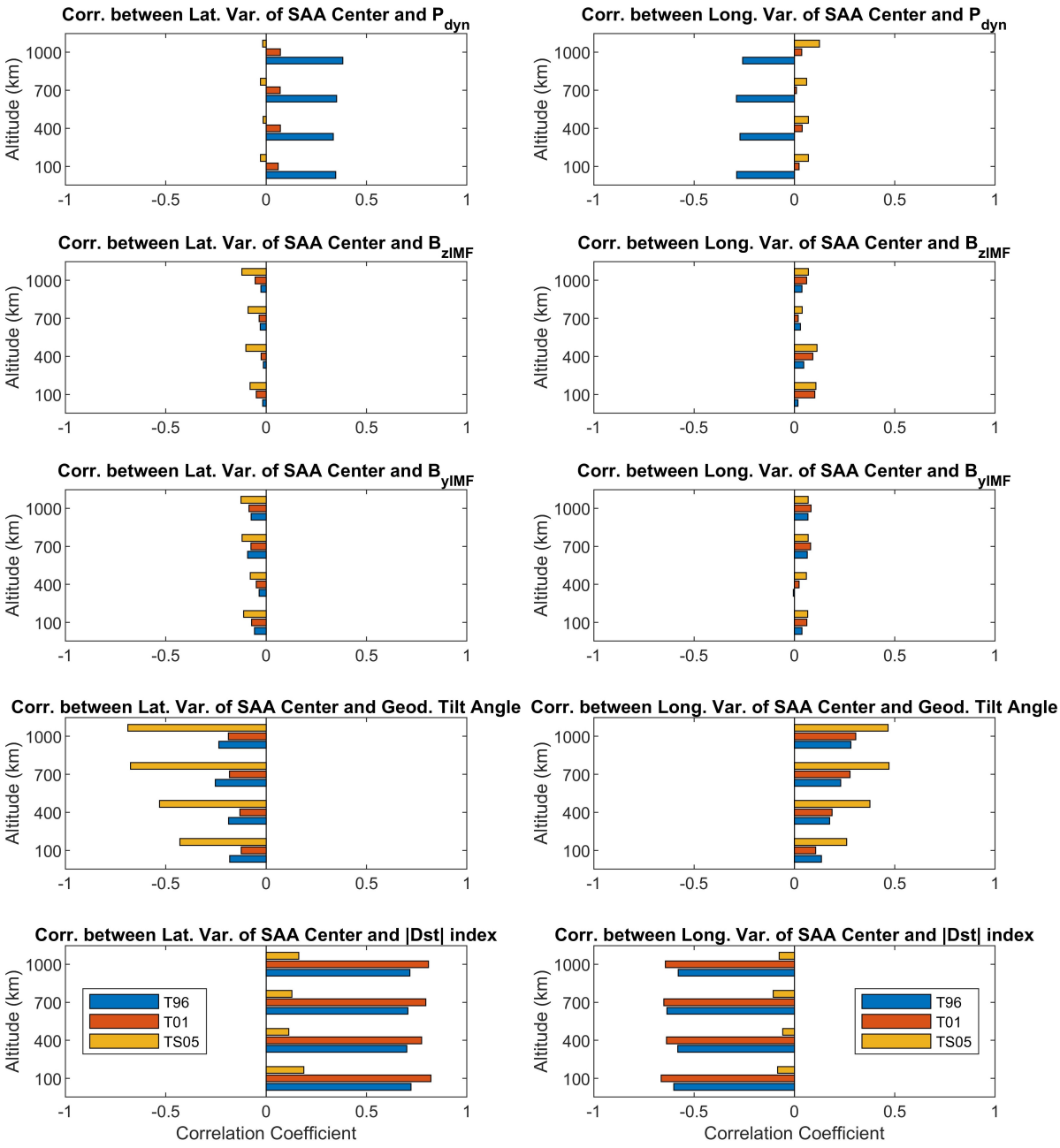

Figure 4.3: The statistical study illustrates the correlation coefficients of the latitudinal and longitudinal SAA center movements according to the altitudes for the Tsyganenko models, T96, T01 and TS05, referencing the different space weather parameters

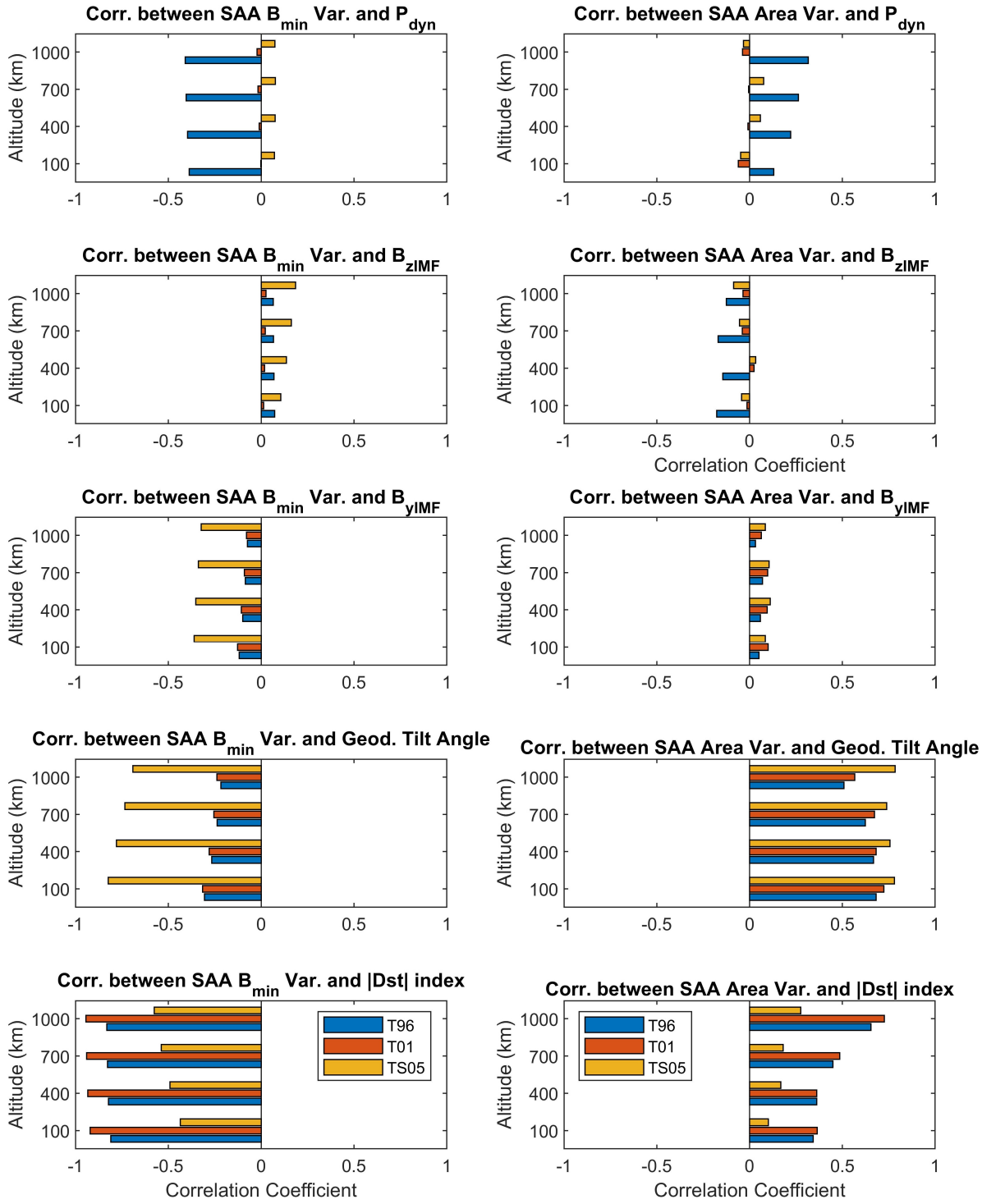

Figure 4.4: The statistical study illustrates the correlation coefficients of the area and the B_{min} of the SAA center according to the altitudes for the Tsyganenko models, T96, T01 and TS05, referencing the different space weather parameters.

4.5 Discussion

4.5.1 Comparison of the results using Tsyganenko models T96, T01 and TS05

When implementing T01 and TS05, the SAA variables became much less affected by the solar wind dynamic pressure and the IMF transversal components, in comparison with the T96, where the results were more influenced by the geodipole tilting angle and the *Dst* index. This result was also confirmed by [Kronberg et al., 2015] who found that ion accelerations in the inner radiation belt was strongly related to the AE index and less

Table 4.1: Correlation coefficient results of the different Tsyganenko models T96, T01 and TS05, demonstrating the effects of space weather parameters on the SAA variables at an altitude of 800 km.

	Space Weather Parameters														
	P_{dyn}			**B_{zIMF}**			**B_{yIMF}**			**|Dst|**			μ		
	T96	T01	TS05	T96	T01	TS05	T96	T01	TS05	T96	T01	TS05	T96	T01	TS05
SAA Area	**0.32**	-0.04	-0.03	-0.13	0.04	-0.09	0.03	0.06	0.09	**0.65**	**0.72**	**0.28**	**0.51**	**0.57**	**0.78**
SAA B_{min}	**-0.41**	-0.02	0.07	0.07	0.03	0.18	-0.07	-0.08	**-0.32**	**-0.83**	**-0.94**	**-0.58**	**-0.22**	**-0.24**	**-0.69**
SAA Center Long. Mov.	**0.38**	0.07	-0.02	-0.03	-0.05	-0.12	-0.07	-0.09	-0.12	**0.72**	**0.8**	0.16	**-0.24**	-0.19	**-0.69**
SAA Center Lat. Mov.	**-0.26**	0.04	0.12	0.04	0.06	0.07	0.07	0.08	0.07	**-0.58**	**-0.64**	-0.08	**0.28**	**0.31**	**0.47**

to the variations in the IMF components and the solar wind dynamic pressure. This conclusion means that the magnetotail structure could play an important role in the SAA magnetic field response, and hence, the inner magnetosphere.

In order to explain the results from each magnetic model, it is important to understand the physical description of the three Tsyganenko models. As explained in [Tsyganenko, 1996], T96 was developed to study the space weather effects on the general magnetosphere configuration. Later on, T01 and TS05 were built to better describe the inner magnetosphere response related to space weather conditions [Tsyganenko, 2002a, Tsyganenko, 2002b, Tsyganenko and Sitnov, 2005]. One of the main physical differences between the models TS05 and T01 is the involvement of different temporal responses of independent geomagnetic field sources in the TS05 model. Thus, [Tsyganenko and Sitnov, 2005] explicitly argued that TS05 was more accurate and physically consistent, since both the temporal resolution and the spatial configuration would become equally important for defining the magnetic field during storm events.

4.5.2 About the *Dst* index and the geodipole tilting angle effects on the SAA: A direct relationship with the magnetic pole variations

The earlier statistical analysis showed that the *Dst* index and the geodipole tilting angle were the most influencing space weather parameters on the SAA magnetic response. The effects of both previous parameters on the general geomagnetic activity were also reported by [Malin and Isikara, 1976] as well as [Shore et al., 2016]. This was where it was explained that the ring current is moving latitudinally along the year, due to the tilt of the Earth rotational axis with respect to the ecliptic plane, so that the compression of the magnetosphere by the solar wind pushes the ring current during the Northern Hemisphere summer toward the south, then six months later toward the north.

Since the SAA is not an separated feature from the global geomagnetic field, the magnetic poles may "lead" the SAA response. Accordingly, we additionally studied the magnetic poles' response related to the space weather condition. Typically, the variables were: the maximum magnetic field intensity B_{max}, the location (latitudinal and longitudinal movements) where the magnetic field was maximized, and the areas of the magnetic poles, defined as the region where the magnetic field was larger than 6/7 (≈ 0.88) of B_{max}. We have implemented the same input information as was shown in Figure 4.1.

Several interesting features were found from the magnetic pole temporal variation due to the input space weather conditions: first, the magnetic poles are clearly affected by the space weather parameters, namely, the *Dst* index and the geodipole tilting angle, as shown in Figure 4.5. The latter figure demonstrates the temporal changes in both magnetic pole variables at the altitude 1000 km, as well as the correlation coefficients between the magnetic pole output variables and the input space weather parameters, at the three altitudes, 100, 500 and 1000 km, as demonstrated in Figure 4.6. Second, it is easier to understand the relationship between both variables, the area and the maximum magnetic field strength variations. From Figures 4.5 and 4.6, a clear pattern can be remarked: the variations in the area are anti-correlated with respect to the changes in the magnetic field, not only for the magnetic poles but also for the SAA, as shown earlier in the previous section.

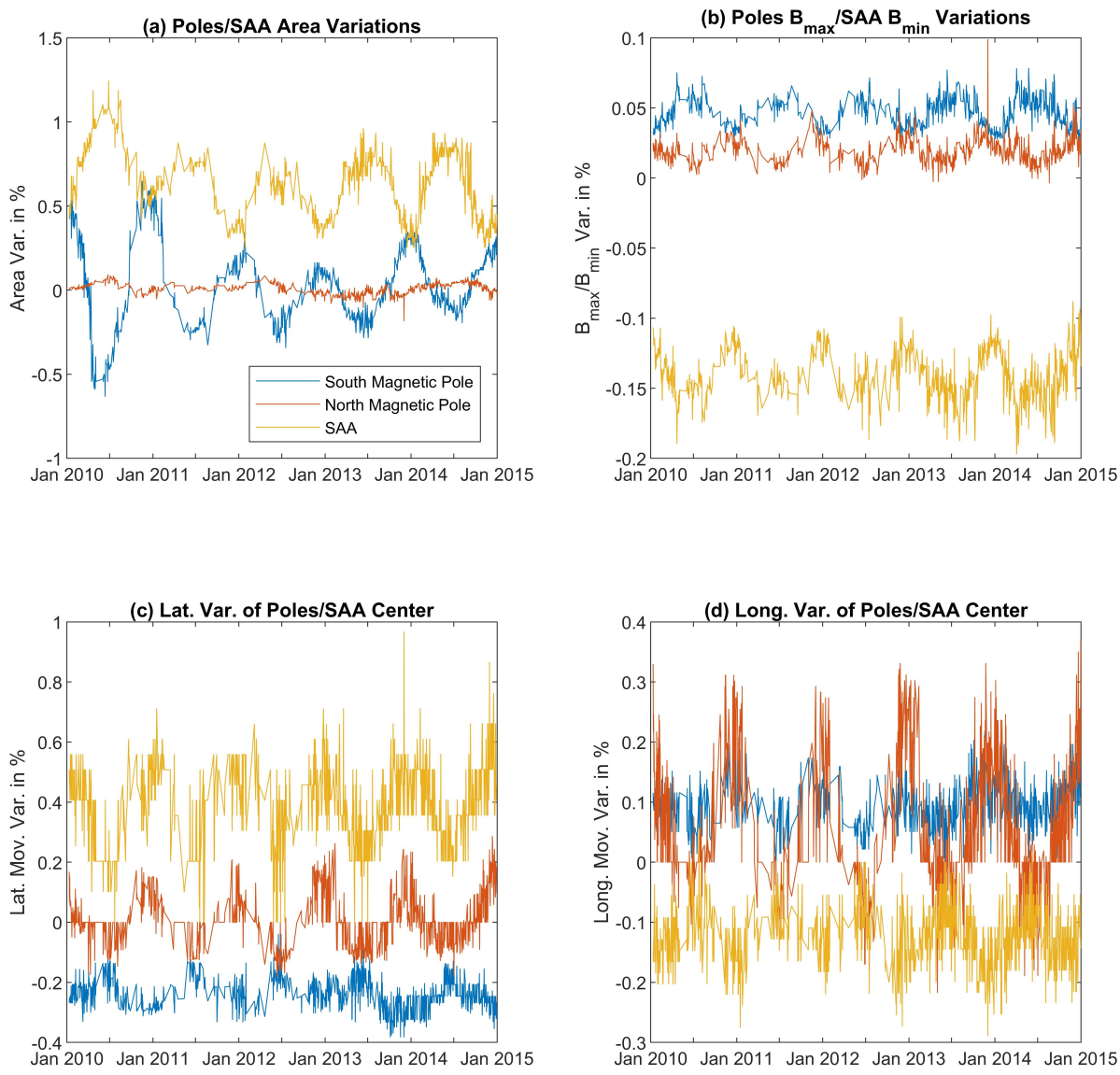

Figure 4.5: Magnetic poles and the SAA variation profiles for the four variables: the area, the minimum/maximum magnetic field, the latitudinal and longitudinal center movement at a 1000 km altitude.

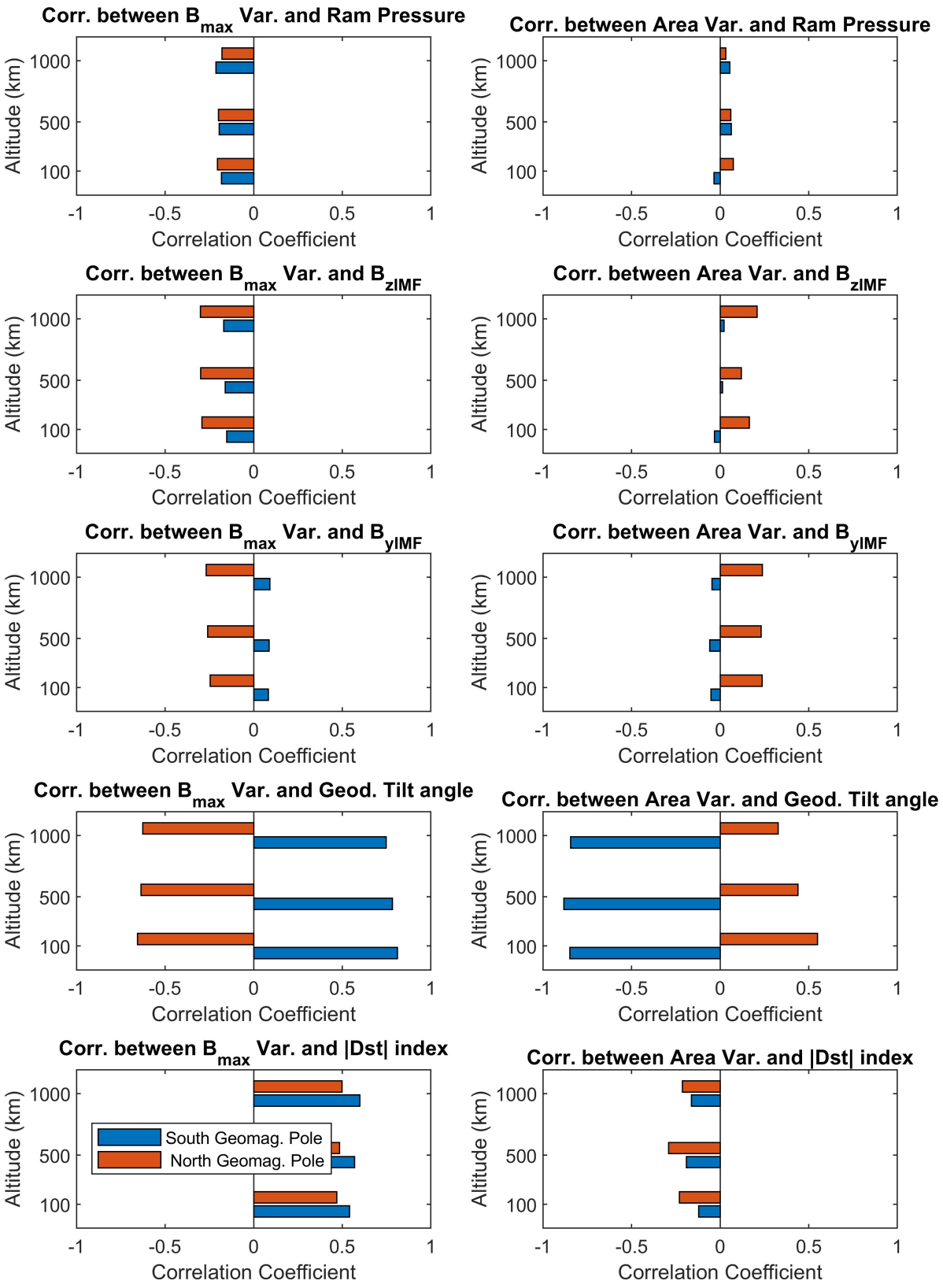

Figure 4.6: Correlation coefficients between the magnetic pole area and B_{max} variations, with respect to the space weather parameters, and according to altitudes of 100, 500, and 1000 km.

4.5.3 Geodipole tilting angle effects on the magnetic poles and the SAA

Figure 4.7 illustrates the effects of the geodipole tilting angle on both magnetic poles. Panels (a) and (b) show the magnetic field contour lines (in black solid lines) and the magnetic field lines (in white lines) for the positive

and the negative geodipole tilting angle cases, 29.5˚and -29.5˚, respectively. Panels (c) and (d) are typically the projected contour plots of the magnetic field in geodetic latitude and longitude representation. The white lines are the initial magnetic pole boundaries, and the black dotted lines correspond to the boundaries that include the negative and positive geodipole tilting angle effects, as illustrated in Panels (c) and (d), respectively. Since the variations of the magnetic field cannot be detected visually in the projected geographical maps, the drawn boundaries in both last two panels do not correspond to the computed magnetic field variations in Panels (a) and (b), but they are actually just drawn to highlight the magnetic pole effects on the SAA area.

The SAA area and the B_{min}/B_{max} variables can be interpreted as a "mountain" for both magnetic poles, where their height describes the magnetic field intensity and their width describes the area; furthermore, the "valley" describes the SAA, where its depth corresponds to the weak magnetic field intensity and its width, the area.

From this simple idea, if one chooses a positive geodipole tilting angle (Panel (a)), which means when the Earth axis is pointing toward the sun, the distance between the north magnetic pole and the magnetopause boundary is getting smaller, so that the height of the mountain (= B_{max}) decreases and its width (= area) increases. On the other hand, the same conclusion can be derived for the south magnetic pole, where its height is increased and its area is decreased, for the same conditions. Since the variations of the south magnetic pole area are larger than the north one, as shown in Figure 4.6, as a result the SAA area is getting larger, as is demonstrated in Panel (c) of Figure 4.7; hence, the SAA B_{min} is decreased. The same interpretation can also be made for the negative geodipole tilting angle case, see Panel (b) and its corresponding Panel (d).

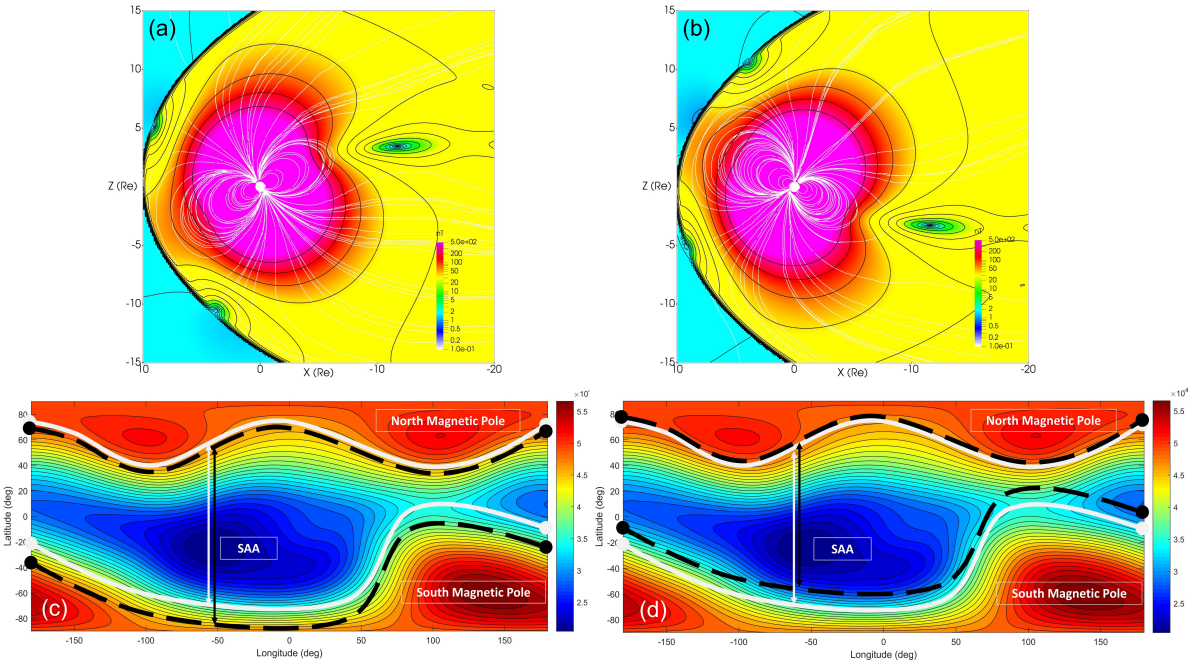

Figure 4.7: The figure shows the effects of the geodipole tilting angle on the magnetic poles and the SAA. Panels (a) and (b) show the contour plots of the magnetic strength (black lines) and the field lines (white lines) for the two geodipole tilting angles, 29.5˚and -29.5˚, respectively. Panels (c) and (d) correspond to the contour mapping of the magnetic strength, according to Panels (a) and (b), respectively, where the white lines represent the initial position of the magnetic pole boundaries and the dotted black lines, constitute the variations of the magnetic pole boundaries. Note: the contour lines and the colors are plotted according to the logarithmic scale.

4.5.4 The *Dst* index effects on the magnetic poles and the SAA

Figure 4.8 interprets the effects of the *Dst* index on the magnetic poles and the SAA, which is explained similarly to Figure 4.7. Panels (a) and (b) demonstrate the contour plots of the the field lines and the magnetic strength for two distinct cases of *Dst* index, -7 nT and -210 nT, respectively. In Panel (b), the thick black lines correspond to the magnetic strength contour plot when the *Dst* index = -210 nT and the dotted black lines, *Dst* index = -7 nT.

From Figures 4.6 and 4.8, it is clearly observed that when the *Dst* index is decreased, the magnetotail structure is getting thinner and more extending to the night side, so that both magnetic pole areas are decreased and the

corresponding B_{max} is increased. Consequently, the SAA area is increased and SAA B_{min} is decreased.

From this section, we can conclude that the *Dst* index and the geodipole tilting angle are both affecting the SAA, mainly due to the magnetic pole variations.

Several research had already confirmed that the *Dst* index and the geodipole tilting angles are influencing the polar cusp and cap, such as the study of the seasonal variations and interplanetary condition effects on the cusp regions by using observations from Polar satellite [Stubbs et al., 2004], and the interpretation of the storm activity effects on the general magnetic field representation using Tsyganenko model T96 by [Feshchenko et al., 2000]. Furthermore, [Meng, 1982, Meng, 1984, Stasiewicz, 1991] concluded that the latitudinal variations of the polar cusp zone are mostly affected by the *Dst* index using observations, in addition to the size of the polar cap that was investigated by [Kamide et al., 1999], as well as the diurnal variations of the polar cap and the cusp boundaries, by [Sergeev, 1990], besides the Polar Cap (PC) indices, that can characterize the space weather activity [Stauning et al., 2008].

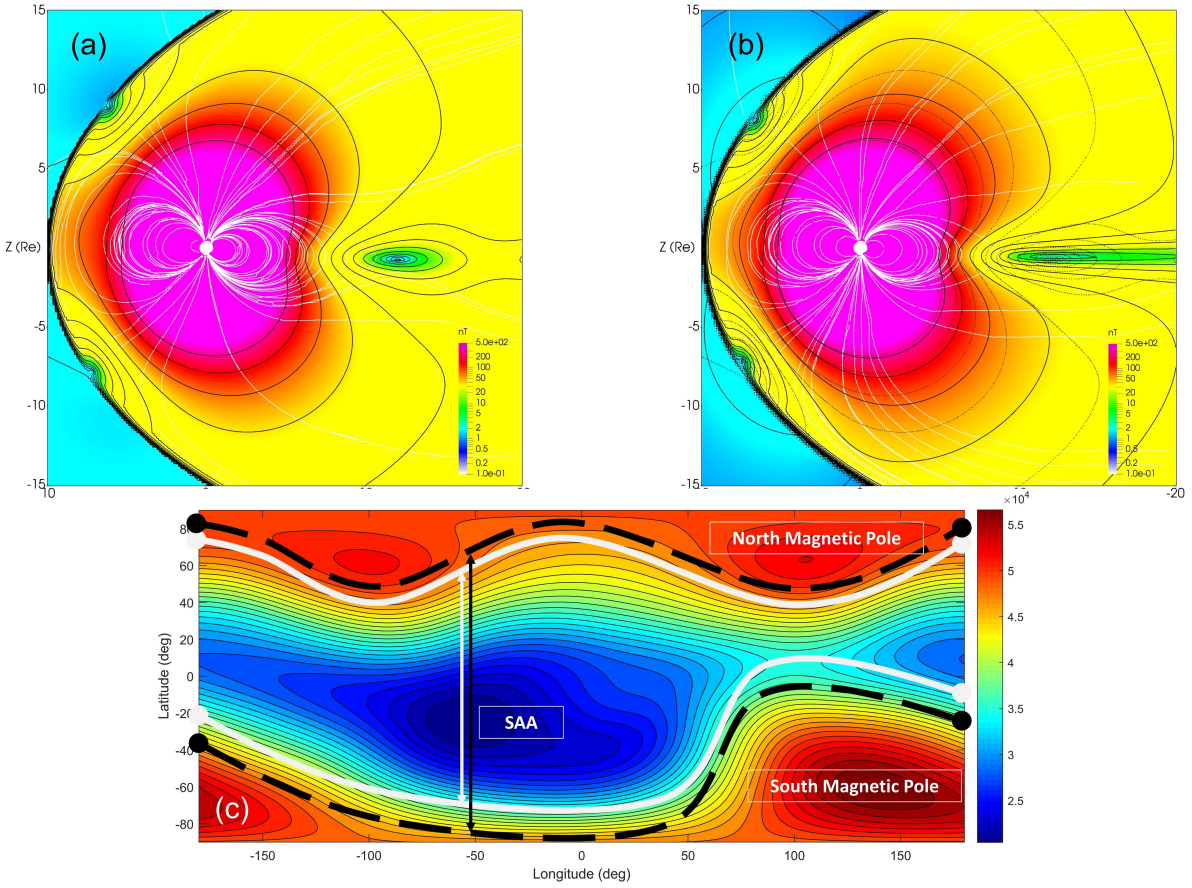

Figure 4.8: The figure shows the effects of the *Dst* index effect on the magnetic poles and the SAA. Panels (a) and (b) show the contour plots of the magnetic strength (black lines) and the field lines (white lines) for the two *Dst* index cases, -7 nT (dotted lines) and -210 nT (solid black lines), respectively. Panel (c) corresponds to the contour mapping of the magnetic strength, according to Panel (b), where the white lines represent the initial position of the magnetic pole boundaries and the dotted black lines, the variations of the magnetic pole boundaries. Note: the contour lines and the colors are plotted according to the logarithmic scale.

4.5.5 Diurnal variation effects on SAA Response

The analysis discussed in the previous section was realized at a specific condition during the day, UT = 00:00:00. However, it was also interesting to investigate if the anomaly was also diurnally affected. Thus, the SAA diurnal variations during 5 January 2010 was studied, by adopting model TS05.

Figure 4.9 illustrates the variations of the SAA variables throughout a day (white area) and a night (gray shaded area), calculated using TS05. Even though the variations were quantitatively low, it is detected a direct correlation between the SAA variables and the day/night succession. The SAA B_{min} and the SAA center

latitudinal movement were strongly influenced and correlated with the hourly variations, where the maximum variations occurred when the SAA was facing the sun. However, the SAA area variations had another pattern, which is consisted of two minima, when the SAA was exactly at dayside and at nightside, although the largest variations were also found at daytime. The longitudinal movement of the SAA center also had another pattern where a shift is occurred, relative to the hourly succession.

Furthermore, since it was easier to explain the dual variations of the SAA B_{min} and the corresponding area, the reason behind the SAA diurnal variations would be better understood. It was remarked that when the SAA was located at nightside, the magnetotail field lines were more extended than when the SAA was located at dayside, due to the different geodipole tilting angle values, (a) $\mu \approx$ -5°at UT 15:00 and (b) $\mu \approx$ -25°at UT 03:00, as shown in Figure 4.10. Probably, this is the reason why the SAA B_{min} was decreased and that the SAA area was slightly increased at nightside. Once more, it is clear that the magnetotail structure is affecting the SAA magnetic response.

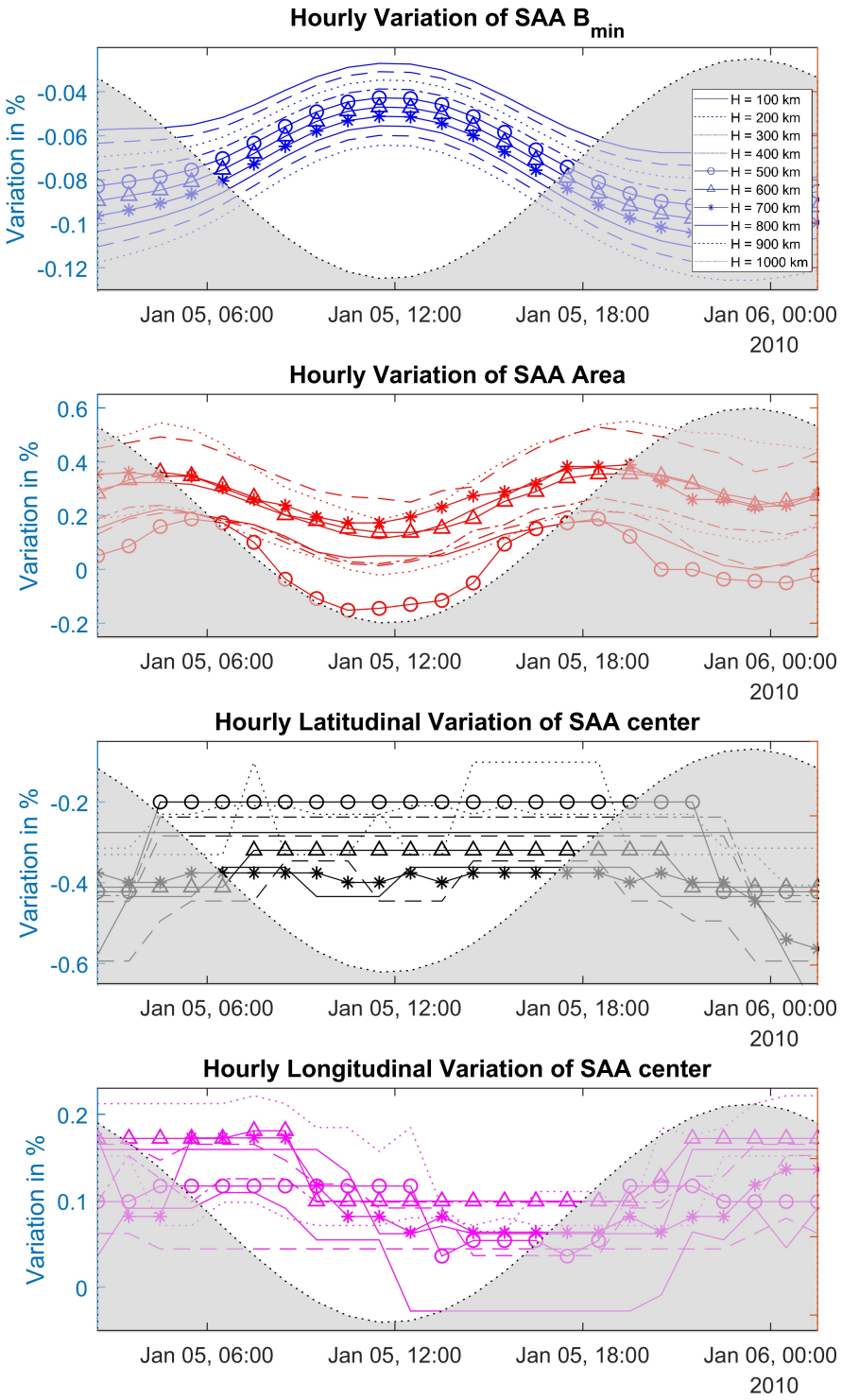

Figure 4.9: Diurnal variation of the SAA variables: the area, the B_{min}, the latitudinal and longitudinal center movements with respect to the altitude.

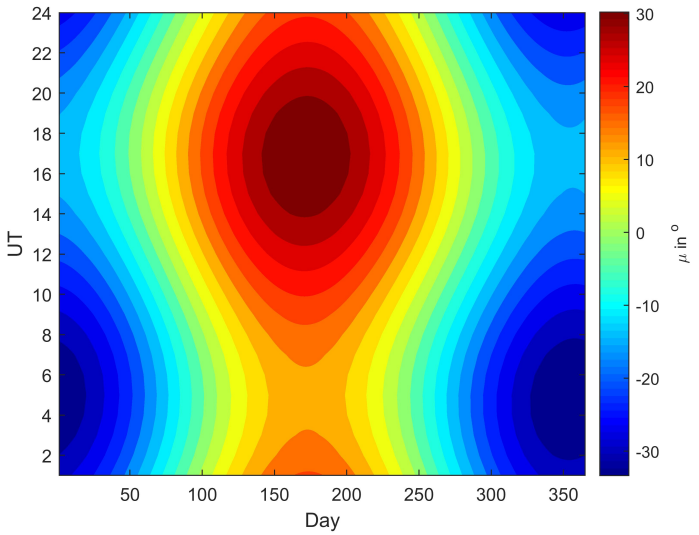

Figure 4.10: Daily and hourly variations of the geodipole tilting angle computed by GEOPACK package.

4.5.6 The effects of the magnetic field threshold on the SAA area

The effects of the magnetic field threshold to calculate the SAA area were studied. Three different values 1.08 B_{min}, 1.16 B_{min}, 1.25 B_{min} were selected, to describe the SAA magnetic boundary, as plotted in Panels (a) and (c) of Figure 4.11, with red, blue and green lines, respectively. Panel (a) demonstrates the temporal variation of the SAA area, while Panel (c) shows the contour plot levels of each boundary. Panels (b) and (d) illustrate the correlation coefficient of the SAA area, calculated based on the three different threshold values, with the Dst index, and the geodipole tilting angle (μ). It was concluded that each SAA area level, clearly and similarly, showed that both space weather parameters affected the anomaly. Furthermore, it was found that as the threshold values were decreased, the SAA area was more influenced by the Dst index. Thus, we can confirm that the SAA area was influenced by the space weather conditions, despite the selected threshold value.

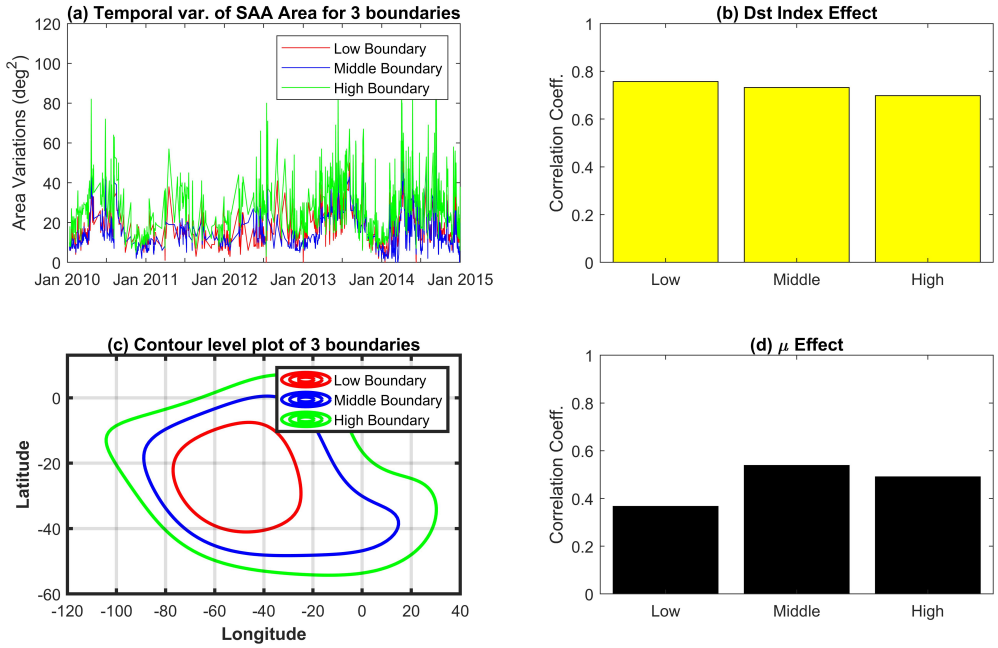

Figure 4.11: Panel (a) represents the SAA area temporal variation, while Panel (c) demonstrates the contour plot level of each boundary. Panels (b) and (d) illustrate the correlation coefficient between the SAA area, calculated based on the three different threshold values, and the Dst index, and the geodipole tilting angle (μ).

4.5.7 A note about proton flux observations inside the SAA

Figure 4.12 is an alternative representation of the statistical previous analysis, which is a comparison between the measured data from the spacecraft NOAA 17 (as shown in Panels (B)) and reported by [Zou et al., 2015], along with the numerical results obtained when implementing Tsyganenko models T01 and TS05 (Panels (A)). The two SAA observed variables were the maximum proton flux value and the corresponding area, whereas the other SAA variables were the SAA B_{min} and its associated area. It is remarked that the computed magnetic results agreed well with the flux observations, in that the Dst index was the main space weather parameter affecting the SAA response. Let one supposes that the magnetic field inside the SAA is acting like a cavity wall, where the immersed protons from the inner trapped belt would move relative to its variations. It has already been discussed that in intense space weather conditions, when the Dst index was $<$ -100 nT, the SAA B_{min} was decreased and the SAA area was increased. Therefore, it is expected that both SAA parameters should also be increased. However, observations have demonstrated the opposite of that, where the maximum protons flux value and the related area have been decreased. This apparent confusion was further interpreted by studying numerically the SAA proton flux variations by performing test particle simulations and by implementing a static magnetic field, calculated by Tsyganenko model. Briefly, the numerical results demonstrated that the maximum proton flux value and the corresponding area increased greatly at some altitudes, which was consistent with the current SAA magnetic response study. Although, the proton loss mechanism, the particle energy and event time-scale are considered as further significant factors that could affect the proton flux behavior inside the SAA region.

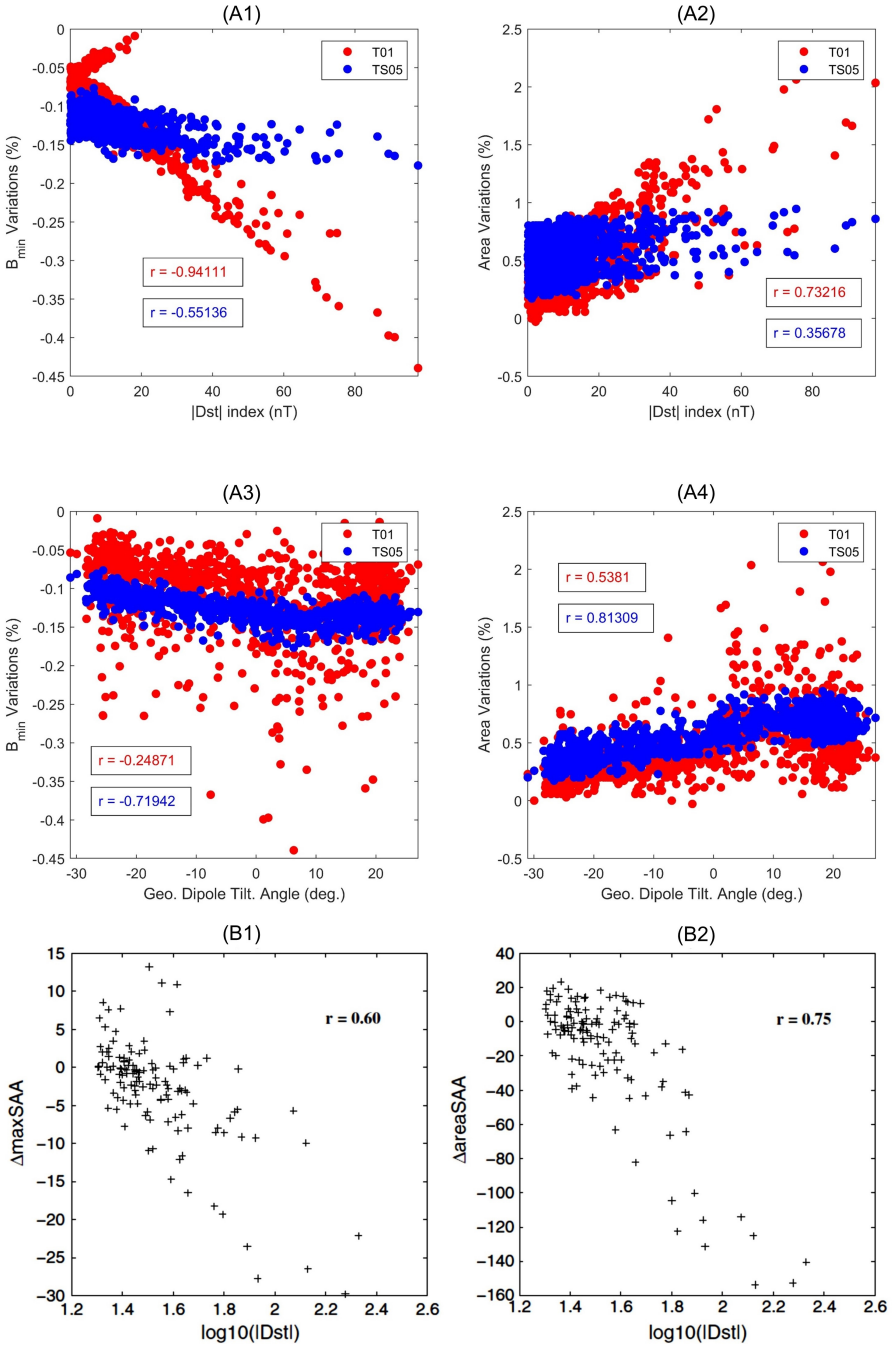

Figure 4.12: Panels (A) are scatter plots of the SAA B_{min} and the area, related to the Dst index and geodipole tilting angle, as computed from Tsyganenko models T01 and TS05, at 800 km. Panels (B) are scatter plots of $\Delta maxSAA$ and $\Delta areaSAA$, corresponding to the maximum flux values and the SAA proton flux area, respectively, with respect to the Dst index, as measured from NOAA 17 [Zou et al., 2015].

4.6 Conclusion and Summary

The magnetic field response inside the SAA with respect to the input space weather variations was investigated by implementing the following Tsyganenko models T96, T01 and TS05. The SAA variables introduced in this study were the SAA area, the B_{min} at the SAA center, and the movement of the SAA center. The main conclusions are summarized as follows:

1. The geodipole tilting angle and the Dst index were the most influencing space weather parameters on the variations of the magnetic field inside the SAA.

2. TS05, T01 and T96 enhanced the seasonal variations, the Dst index, and the ram pressure on the SAA magnetic field response, respectively.

3. The magnetotail dynamics were considered to play an important role affecting the SAA magnetic response.

4. The SAA magnetic field variations were mainly driven by both the magnetic poles due to the input space weather conditions (= the geodipole tilting angle variations and the Dst index).

5. It was found that the SAA magnetic field response was subjected to diurnal effects, where the maximum variations of the SAA area, B_{min} and the latitudinal movement were occurred at the dayside.

The main purpose of studying the magnetic response inside the SAA is considered as an important key that could help explaining the SAA proton flux variations, related to the magnetic storms events and the seasonal variations. This investigation will be carried out in our next study, where the proton trajectories in a time-fixed magnetic field provided by the Tsyganenko models, will be calculated.

Chapter 5

Test Particle Simulations: Calculation of SAA Proton Flux Response in Drift Period Time Scale

5.1 Introduction

In the previous chapter, we demonstrated the SAA magnetic response due to input space weather conditions. In this chapter, we proceed to investigate the SAA proton flux response due to the inner magnetosphere configurations, as computed by the Tsyganenko models, according to the geomagnetic conditions and tilting by implementing test particle simulations.

The proposed approach introduces several advantages as follows:

1. It reflects better the realistic situation of the particle dynamics, where the particles are precipitated from the inner radiation belt to the anomaly.

2. By implementing the classical Newton-Lorentz equations to compute the particle trajectories, the non-adiabatic behavior of the particles in the inner radiation belt could be reproduced; for example, the first adiabatic invariant violation could occur if the local field line curvature radius is comparable with or less than the particle gyroradius, as reported in several papers, e.g. the numerical study of the particle losses and trapping boundary in the realistic magnetic field configuration (IGRF+T79) [Sergeev and Tsyganenko, 1982] and [Tsyganenko, 2013], and the same subject was realized by using observational data of HEO-3 spacecraft [Selesnick et al., 2010]. The violation of the first adiabatic invariant could induce particle scattering in the loss cone, and therefore, particle loss in this region as shown by [Hudson et al., 1997, Engel et al., 2015]. Furthermore, [Zou et al., 2015] suggested that the decrease of both SAA parameters, the maximum proton flux value and the corresponding area at an altitude $\approx$ 800 km was occurred due to the proton losses by the violation of the first adiabatic invariant near the outer boundary of the inner proton radiation belt ($L > 1.7$). Regarding the third invariant, the authors [Sturrock, 1994], [Walt, 2005] and [Easly, 2007] examined the drift loss cone of the particles inside the SAA region. In addition, it was shown by [Antonova et al., 2003] and [Ukhorskiy and Sitnov, 2013], the second and the third invariants were more easily violated.

3. The particle trajectory calculation is believed to be reasonably efficient. The computation quality rely essentially on the accuracy of the implemented geomagnetic field models (IGRF+TSY); we consider that such accuracy is acceptable enough to evaluate the basic features of the proton flux response inside the SAA.

Actually, the same approach was already implemented by several research, namely [Engel et al., 2015], who investigated the proton loss in the inner proton radiation belt by performing test particle simulations where the time-varying magnetic field information was provided by the Tsyganenko model TS05; in addition [Saito et al., 2010] studied the relativistic electron drift losses occurring in the outer radiation belt by magnetopause shadowing, where the time-varying magnetic field information was also provided by the Tsyganenko model TS05; the mentioned authors implemented observed solar wind data and *Dst* index as inputs, and the relativistic electron trajectories were calculated by a three-dimensional test particle code.

In this study, we continue and estimate the variations of SAA proton flux under various space weather elements: the geodipole tilting angle, solar wind ram pressure, density, three velocity components, Interplanetary Magnetic Field components B_{yIMF} and B_{zIMF} and Dst index. As various parameters characterize the SAA proton flux, the study will consider (1) the area of the SAA (defined as the area where the proton flux exceeds a given threshold at a specific altitude) and (2) the maximum value of the proton flux (at specific altitudes).

The methodology implemented in this chapter is to provide first the background magnetic field described by Tsyganenko models T01, [Tsyganenko, 2002a, Tsyganenko, 2002b], and TS05, [Tsyganenko and Sitnov, 2005]. This is in order to define the external magnetic field under various space weather parameters, along with the IGRF-12 (International Geomagnetic Reference Field), in order to describe the main (internal) magnetic field. The second step is to perform test particle simulations to estimate the corresponding proton flux variations due to the magnetic field structure, considered as the only driver of the particle motion. The relativistic Boris-Buneman integrator scheme [Buneman, 1967, Boris, 1970] is implemented to solve the equations of proton motion. This scheme is essentially chosen for its great advantage of energy conservation.

5.2 Material and Methods

$$\frac{d\mathbf{p}}{dt} = \frac{d(\gamma m\mathbf{v})}{dt} = q(\mathbf{v}\times\mathbf{B}) \tag{5.1}$$

$$\frac{d\mathbf{r}}{dt} = \mathbf{v} \tag{5.2}$$

where $\mathbf{p}$ is the particle momentum, m the particle rest mass, c the speed of light, γ the Lorentz factor, q the particle charge, $\mathbf{B}$ the magnetic field, $\mathbf{v}$ the particle velocity, and $\mathbf{r}$ the particle position. In this chapter, we are focusing on the general structure of the proton flux distribution in the SAA, therefore the electric field is taken in to consideration. In the introduction section of this chapter, we demonstrated that the objective of this study is to reveal the basic features of the proton dynamics inside the SAA, by taking into account the magnetic field effect only. The static magnetic field was provided by TS05 and T01 for different input space weather conditions as shown in Table 5.1. The inclusion of the electric field and the study of its effect on proton flux in the SAA will be covered in the next chapter.

The simulation domain was a cubic grid, whose dimensions is 6 Re $\times$ 6 Re $\times$ 6 Re, with grid resolution was 0.075 Re and the Earth was located at the grid center.

We followed the same procedure as explained in [Saito et al., 2010] in order to distribute initially the protons almost uniformly in all L shells: this step was achieved by calculating the drift period of one single proton in a realistic field. Then, the drift period of every single proton was found by multiplying its drift period by a uniform random number from 0 to 1.

Two different sets of simulations were carried out:

1. **single overview run**, to demonstrate the SAA basic features, by plotting the final positions of the protons that were precipitated in the anomaly region from the inner trapped belt in a realistic magnetic field configuration (IGRF+TS05),
2. **multiple runs**, to study the SAA proton flux variations associated to various magnetic field configurations; the objective was to compare the SAA proton flux response with respect to selected geodipole tilting angles and geomagnetic storm events.

The magnetic field input parameters were shown in Table 5.1. The solar wind information were provided by ACE spacecraft database and the Dst index by WDC, Kyoto University. This simulation set was consisted of (2.a) three simulations, associated only to the seasonal variation by changing the geodipole tilting angle value; and (2.b) three additional simulations, corresponding to three selected real events in 2004, which reflected quiet conditions, moderate and intense geomagnetic storm conditions.

For each simulation set, two different initial proton distributions were established:

1. **single overview run**: 10^6 protons were initially distributed in a pure dipole field, the shell range (L) extended from 1 to 2 and the pitch angle range was from 10° to 170°. Then, this proton distribution was applied to the realistic magnetic field configuration (IGRF+TS05).
2. **multiple runs**: 10^5 protons were initially distributed in a realistic magnetic field (IGRF+T01/TS05) where the shell range (L) extended from 1 to 3 and the pitch angle range from 0° to 180°. The corresponding SAA features were achieved by capturing the proton inside the anomaly during the simulation time.

In all test particle simulations, the protons were assigned randomly a kinetic energy value from 140 to 400 MeV and a pitch angle value from 10˚ to 170˚. Each run was stopped at the same time, when protons with the lowest energy performed about 6 complete drifts periods, which corresponds to nearly 1 minute in the real time. The protons were captured below the altitude 960 km measured from the ground. Then, the proton positions were converted from Cartesian to geodetic systems (height, latitude and longitude). Next, the resulted 3D proton flux inside the SAA was interpolated, in height, latitude and longitude. The mapped grid resolution was selected to be 0.5˚× 0.5˚.

The main parameters to study the SAA proton flux were the maximum proton flux value in the mapped grid and its corresponding area, calculated below a proton flux threshold; this is equal to the total number of the area units, satisfying the condition that the SAA proton flux should be larger than the selected threshold in the grid.

To estimate the numerical error, the energy conservation of the protons was calculated for all energies and for all pitch angles at 1.5 Re. We have selected the time step resolution to be 1×10^{-4} s; the error in energy conservation was confirmed to be less than 2.5×10^{-11}%. The previous results indicate the strong advantage of implementing the Boris-Buneman integrator scheme.

The proton fluxes in the current study were considered as directional integral fluxes, where the protons pass inward through a unit area in 1 second for a 90˚solid angle and for all energy ranges. Thus, the corresponding flux unit would be cm^{-2} s^{-1} str^{-1}. The results shown in the next section are normalized by taking the speed and length scales as the speed of light and the Earth radius respectively.

5.3 Results

5.3.1 Overview Run

The resulted proton distributed extended from $L = 1$ to 2, a typical range for the inner radiation belt. Figure 5.1 demonstrates the initial and final proton distributions, in Panels (A) and (B), respectively. Panel (A) illustrates the initial proton distribution (blue points) in a dipole field configuration. On the other hand, in Panel (B) shows the final proton positions after one minute in real time are represented as red points, by implementing a static realistic magnetic field configuration (IGRF + TS05). The calculations indicated that ≈ 1% of the total trapped protons were precipitated inside the SAA.

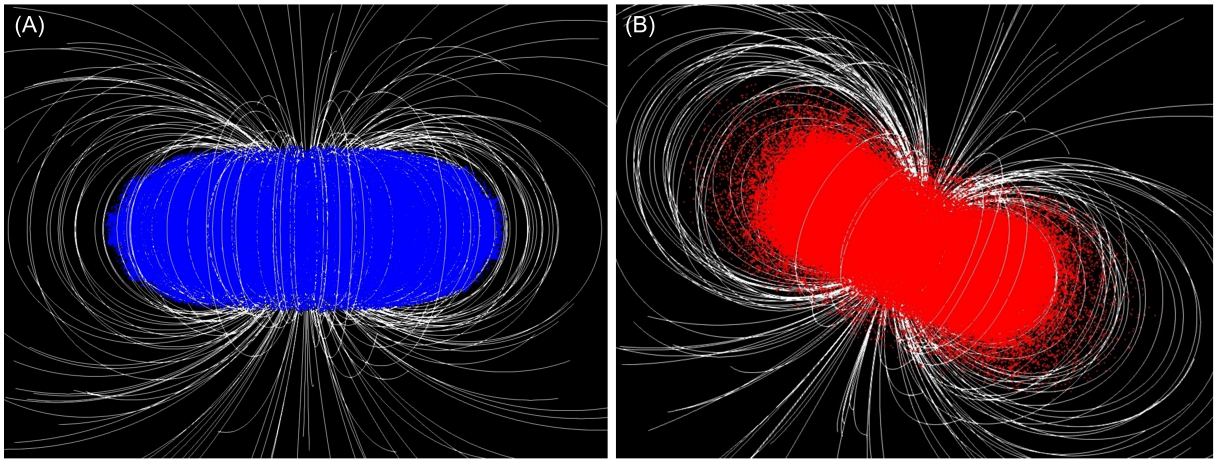

Figure 5.1: Panel (A) shows the initial distribution of the protons in a pure dipole magnetic field. Panel (B) shows the position of the protons after one minute in real time, in a time-fixed realistic magnetic field configuration (IGRF + TS05).

The anomaly effect on the inner radiation belt is illustrated in Figure 5.2. Three different views display the magnetic field configuration (field lines in white and the contour plots of the magnetic strength), with the trapped protons plotted as white points. The weakness of the magnetic field is represented as a blue area of the spherical contour plot at 1.1 *Re*, corresponding approximately to an altitude of 640 km. The protons, which were below 1.15 *Re* (≈ 960 km) are colored in magenta. From both Panels (B) and (C), the inner belt

was getting closer to the Earth's surface due to the SAA, reflecting the consistency of the model with existing knowledge.

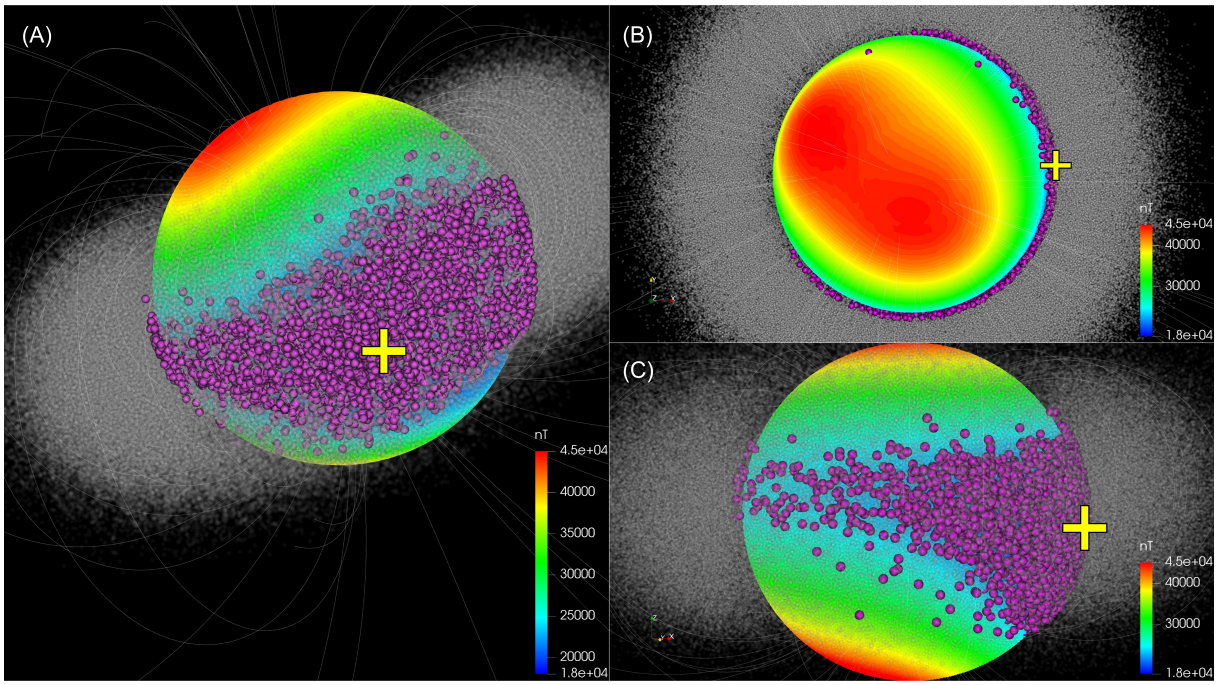

Figure 5.2: This figure shows three different views (general, top and side views, as demonstrated in Panels (A), (B) and (C), respectively) of the inner radiation belt simulation, including the magnetic field lines (white lines), the contour plots of the magnetic field strength at 1.1 *Re* (≈ 640 km altitude), and the proton distribution (white points). In addition, it can be detected visually the SAA (blue shaded area), and also the precipitated protons (magenta). The yellow cross in the panels locates the SAA center.

Further analysis was then continued by transforming the proton positions from Cartesian to geodetic coordinates: latitude, longitude and height, as shown in Panel (A) of Figure 5.3. From Panel (B), the same proton distribution is projected at all altitudes, covering Central and South America, the Atlantic Ocean, and also extending to Africa.

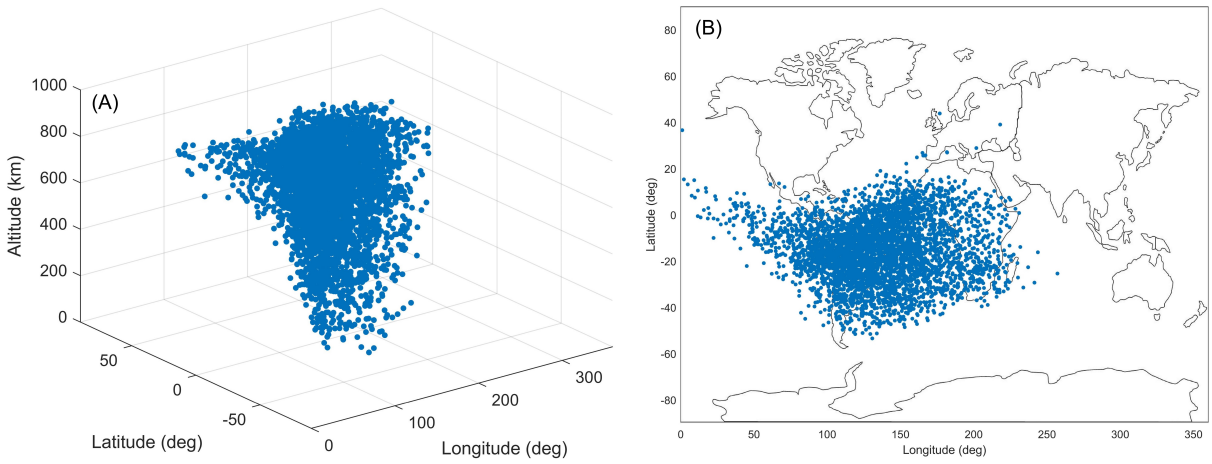

Figure 5.3: Panel (A) shows the final distribution of the protons in three-dimensional geodetic coordinates. Panel (B) is the corresponding map projection of the proton distribution for all altitudes.

In addition, Figure 5.4 displays the normalized proton flux contour plots at the altitudes 300, 500, 700, and 800 km, where it is clearly shown that when the altitude is increasing, the anomaly is expanding, while the flux strength is also increasing and the maximum flux position is slightly changed.

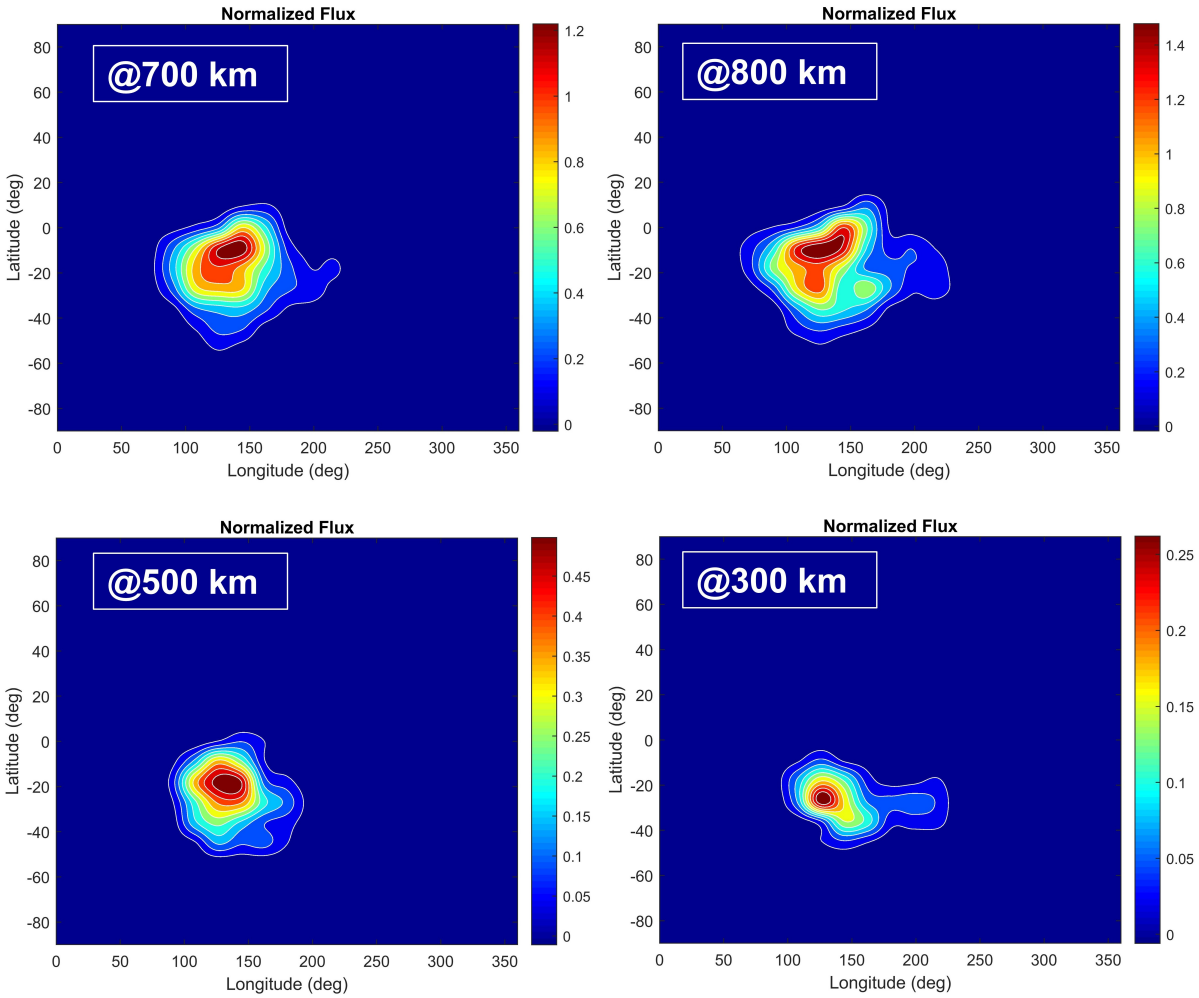

Figure 5.4: SAA proton flux maps plotted for several altitudes: 300, 500, 700, and 800 km.

[Qin et al., 2014] discussed that the one-dimensional Gaussian function was a convenient mathematical model to describe the 1D longitudinal and latitudinal flux distribution in the SAA. Figure 5.5 illustrates the Gaussian fitting as a function of the computed proton flux at the altitude 800 km, achieving nearly perfect correlations between the theoretical Gaussian function and the calculated latitudinal and longitudinal proton flux, respectively. Although, it should be noted that the latitudinal and longitudinal flux distribution range was more extended by about 10°, in comparison with [Qin et al., 2014]. This is might be due to the finite number of protons in the simulations, compared to the real situation.

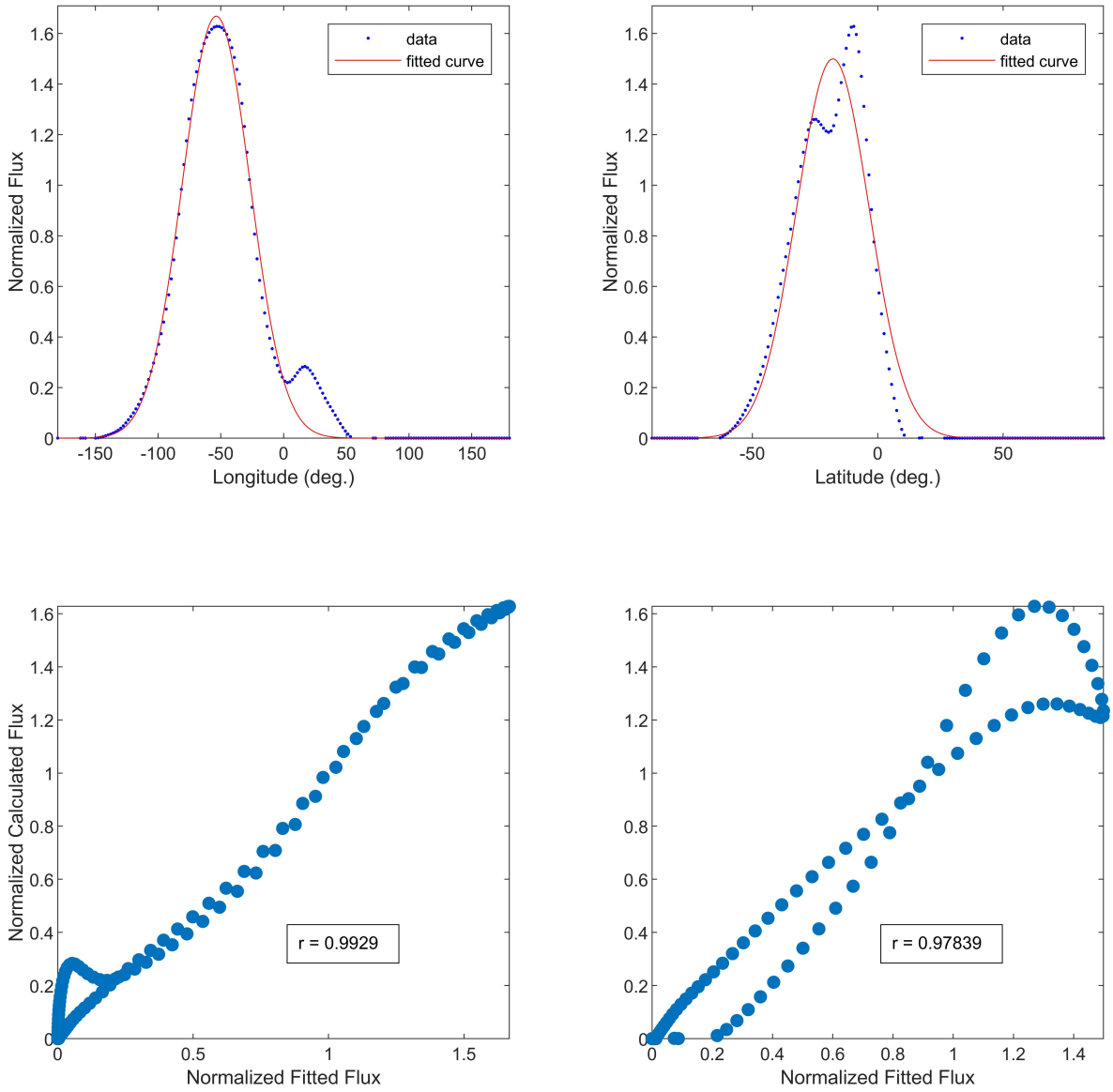

Figure 5.5: Gaussian fit representation of the longitudinal and latitudinal distributions of the proton flux in SAA at an 800 km altitude.

5.3.2 Geomagnetic Conditions/Tilt Runs

5.3.2.1 Input Conditions

The three panels of Figure 5.6 illustrate a typical and initial spatial (Panel (a)), pitch angle (Panel (b)) and energy (Panel (c)) proton distributions. It is clearly shown that the proton spatial distribution is well distributed radially along the L-shells, while the pitch angle and energy values are randomly distributed according to the desired ranges.

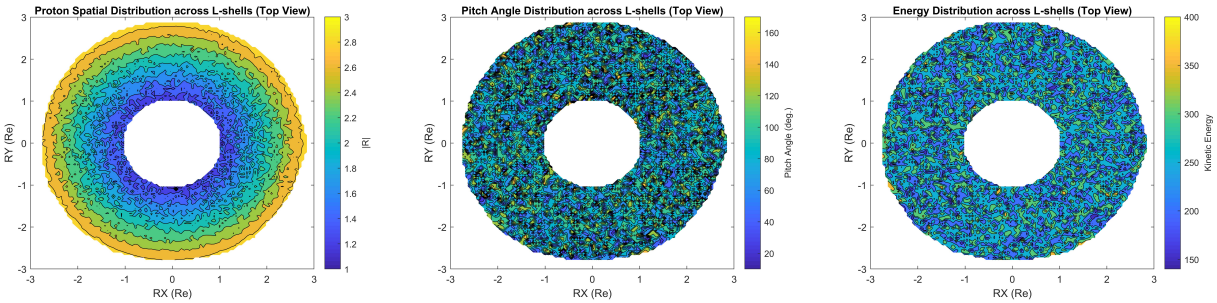

(a) Spatial Distribution (b) Pitch Angle Distribution (c) Energy Distribution

Figure 5.6: The figure represents the geodipole tilting angle effect on the SAA proton flux. The three panels show the longitudinal section contour plots of the SAA proton flux.

5.3.2.2 Geodipole Tilting Angle Effect

The seasonal variation effect on the proton flux inside the SAA was investigated by selecting three different geodipole tilting angles: μ = -20° (Case 1), $\mu = 3.89°$ (Case 2) and $\mu = 23.3°$ (Case 3).

Figures 5.7 and 5.8 represent the longitudinal and latitudinal section contour plot at the SAA center (= maximum flux). Panels (A) ($|\mu| = 20°$) and (C) ($|\mu| = 23.3°$) of both figures show that, as long as the magnitude of the geodipole tilting angle was increased, the maximum proton flux and the corresponding area were apparently decreased at all altitudes, in comparison with Panel (B) for the small tilting angle case ($|\mu| = 3.89°$), where the proton flux intensity was increased.

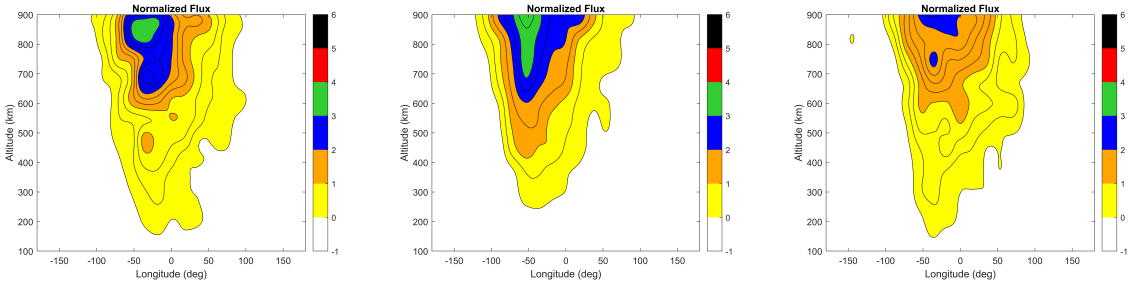

(a) Case 1: $|\mu| = 20°$ (b) Case 2: $|\mu| = 3.89°$ (c) Case 3: $|\mu| = 23.3°$

Figure 5.7: Geodipole tilting angle effect on the SAA proton flux: The three panels show the latitudinal section contour plots of the SAA proton flux.

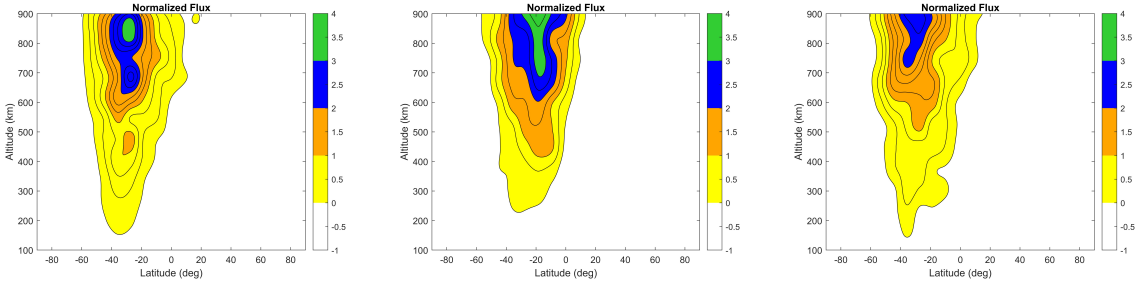

(a) Case 1: $|\mu| = 20°$ (b) Case 2: $|\mu| = 3.89°$ (c) Case 3: $|\mu| = 23.3°$

Figure 5.8: Geodipole tilting angle effect on the SAA proton flux: The three panels show the longitudinal section contour plots of the SAA proton flux.

Further error plots are introduced to quantify the geodipole tilting angle effect on the SAA with respect to altitude. Figure 5.9 displays the maximum proton flux value and the corresponding area variations for the second and third angle cases, relative to the first case. The red lines are the increase of both variables and the blue lines, the decrease. Simulation results showed clearly the SAA proton flux and area enhancements of Case 2 (bottom panel = low angle value) while both parameters were relatively decreased at both Cases 1 and 3 (top

pane; = high angle value).
To be more confident about the results, we have changed both random, initial energy and pitch angle distributions; as shown in the same figure, the different initial flux distributions did not affect the previous conclusion and the same pattern was clearly observed.
It was found that the maximum increases of both, the SAA maximum proton flux value and the corresponding area variations, could reach approximately 52 % and 73 % respectively.

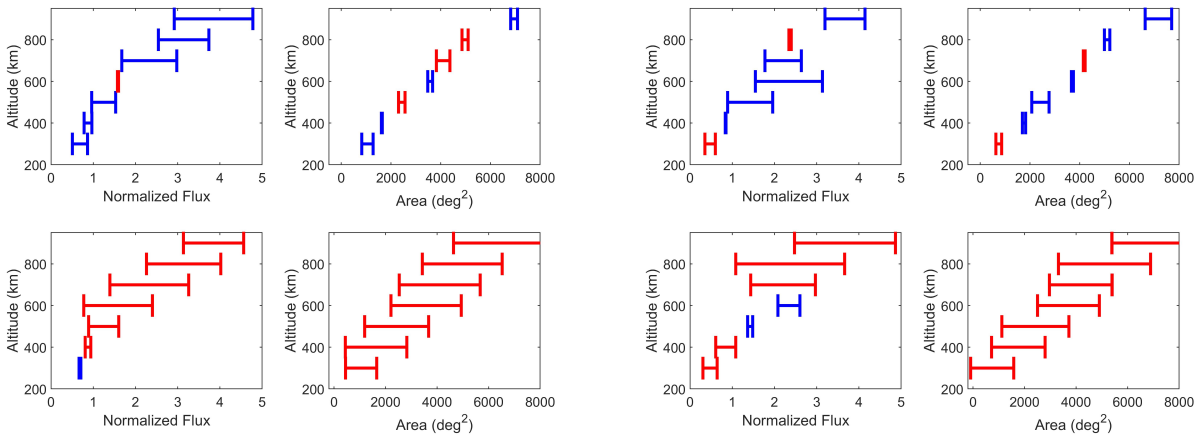

(a) Distribution 1

(b) Distribution 2

Figure 5.9: The error plots demonstrate both SAA parameters variations, maximum proton flux value and its corresponding area, with respect to altitude, for the second and third cases in comparison with the first case (μ = -20°). The red lines represent the increase in the maximum flux values and in the SAA area, that can create additional radiation doses, whereas the blue lines show the decrease in both of the SAA flux variables. The first two panels correspond to the third case ($\mu = 23.3°$) while the last two panels, the second case ($\mu = 3.89°$).

5.3.3 Geomagnetic Storm Event Effect

We have examined three events during the year 2004, corresponding to quiet conditions, moderate and intense geomagnetic storms. The Tsyganenko models T01 and TS05 were implemented to generate the desired magnetic field data.
The error plots are introduced to study quantitatively the variations of the SAA proton flux at the desired altitudes. Figure 5.10 displays the maximum proton flux values and the corresponding area variations for the second and third events, in comparison with the first event. The red lines correspond to the increase that occurred in both variables and the blue lines show the decrease.
Unfortunately, the simulation results did not agree with the observations carried out by [Zou et al., 2015] and [Dachev, 2018], who found that the SAA proton flux intensity was decreased during geomagnetic storms at the altitudes $\approx$ 800 and 400 km respectively. It is clear from the Figure 5.10 that the numerical results obtained, neither from TS05 or T01 at the selected altitudes, did not reveal such increases in both SAA parameters.

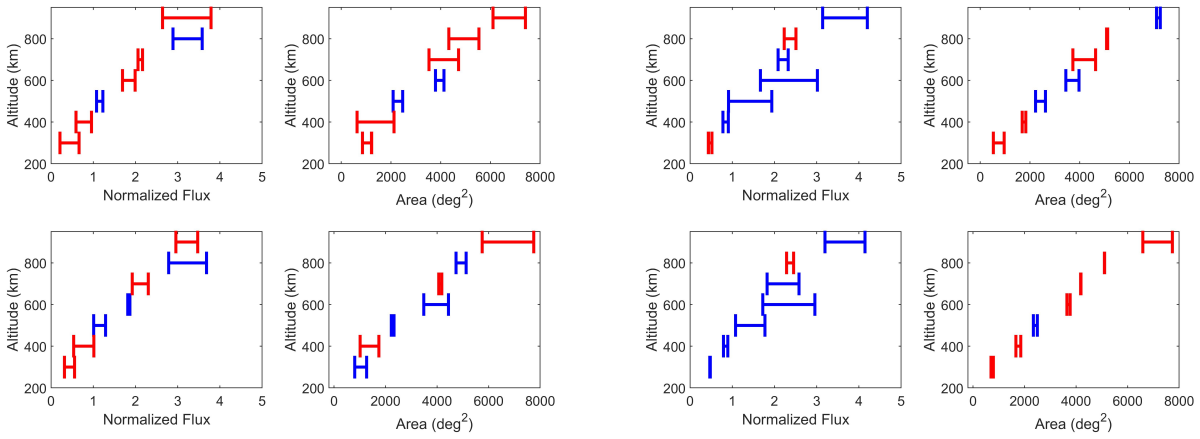

(a) T01 (b) TS05

Figure 5.10: The error plots demonstrate both SAA parameters variations, maximum proton flux value and its corresponding area, with respect to altitude, for the second and third event in comparison with the first event. The red lines represent the increase in the maximum flux values and in the SAA area, that can create additional radiation doses, whereas the blue lines show the decrease in both of the SAA flux variables.

5.4 Discussion

5.4.1 The Geodipole Tilting Angle Effects on the SAA Proton Flux Response

As demonstrated from the test particle simulations, the increase of the SAA proton flux intensity during equinox time (= low tilting angle) did agree with the observations analyzed and modeled by [Schaefer et al., 2016] from 2004 to 2008. Furthermore, the numerical results showed that the SAA proton flux was decreased in Case 3 in comparison with Case 1; as shown in Table 5.1, Case 3 was selected to be during summer while Case 1 during winter; this conclusion did again agree with [Schaefer et al., 2016] observations. Hence, the current simulation model could successfully determine the SAA proton flux according to seasonal variations.

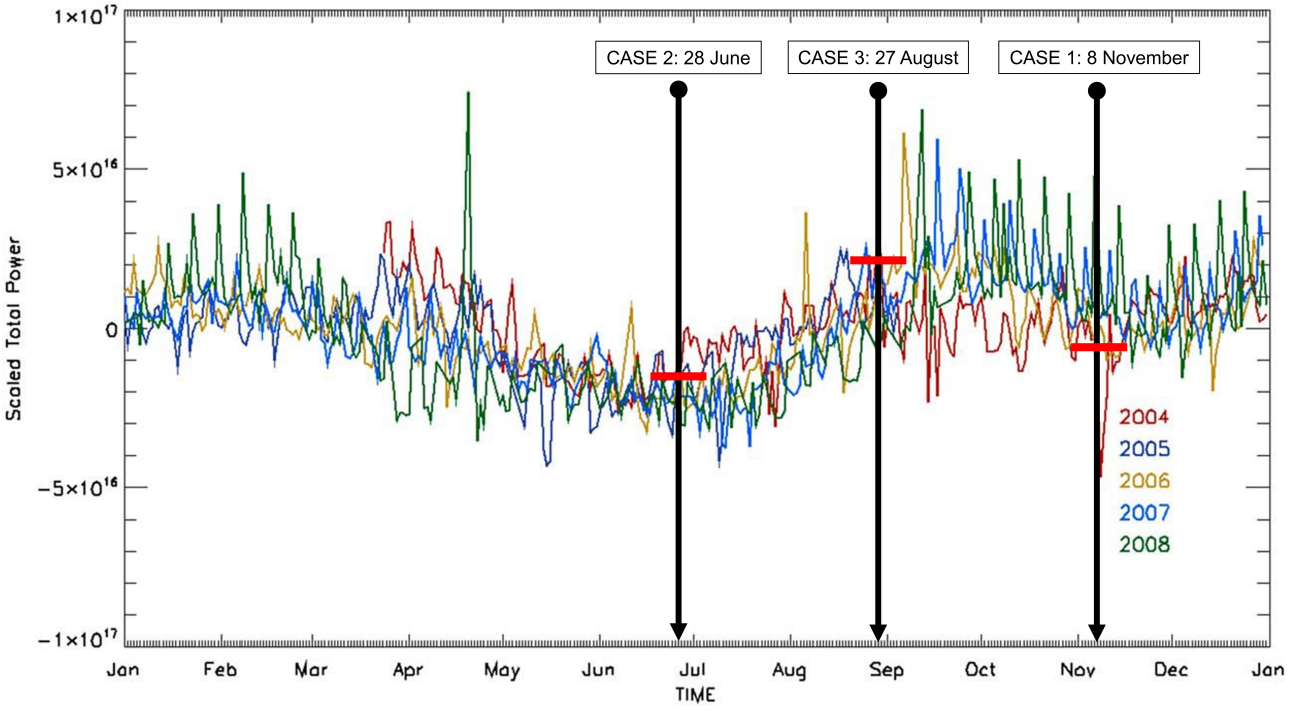

Figure 5.11: The figure illustrates the SAA intensity changes over the years 2004 to 2008. The yearly average counts were substracted and have been daily plotted. In our simulations, we selected three dates of the year 2004: 8 November (Case 1), 28 June (Case 3) and 27 August (Case 2).

From Figure 5.11, we can observe the trend of the SAA flux intensity during 2004. The related two maxima are located during equinox periods. In summer, the flux intensity is lower than in winter. As commented by [Schaefer et al., 2016], the observed spikes that appear with an 8 day period are likely an artifact of the DMSP orbital precession period.

5.4.2 Geomagnetic Storm Event Effects on the SAA Proton Flux Response

We would like to confirm also that by changing the initial random energy and pitch angle distributions, we obtained another different pattern of the proton flux variations in the SAA. Thus, a better numerical model should be carried out in order to match satellite observations.

The reasons behind the disagreement between the numerical results and the observations could be mainly due to the short simulation time we have selected. The geomagnetic storm effect on the inner radiation belts require a more detailed and extended simulations to reveal properly the proton dynamics inside the SAA. Another reason is the absence of the electric field in our simulations, which it might have a major effect on the SAA flux intensity. Such important aspects will be covered in the next chapter.

5.4.3 Threshold effect on SAA flux area

Since the SAA area calculations was depending on a chosen threshold, it is better to examine its variation on the result. Figure 5.12 demonstrates three different contour levels, selected at an altitude of 800 km, which correspond to three proton flux values of 0.3 (= low boundary), 0.7 (= mid boundary) and 1.1 (= high boundary). Generally speaking, for the four chosen thresholds, Figure 5.13 shows similar pattern. Therefore, the SAA area changes includes the effects of the real seasonal variations despite of the area threshold.

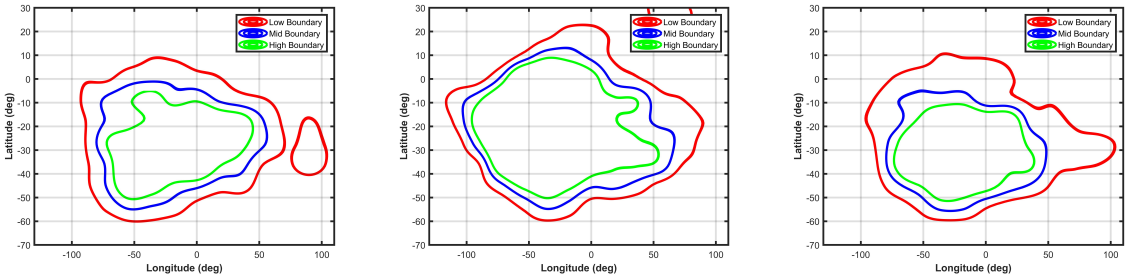

(a) Case 0: $|\mu| = 20°$ (b) Case 1: $|\mu| = 3.89°$ (c) Case 2: $|\mu| = 23.3°$

Figure 5.12: Panel (a) demonstrates three different boundaries at 800 km, corresponding to the three threshold values of the proton flux of 0.3, 0.7 and 1.1, so as to calculate the SAA proton flux area, whose flux values are greater than the selected threshold. Panels (b), (c), and (d) illustrate the effects of each boundary on the SAA flux expansion.

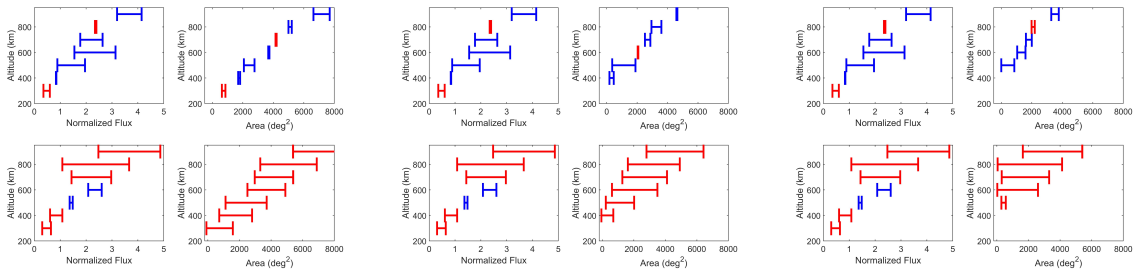

(a) Case 0: (b) Case 1: (c) Case 2:

Figure 5.13: Panel (A) demonstrates three different boundaries at 800 km, corresponding to the three threshold values (normalized proton flux) of0.25, 0.35 and 0.45, so as to calculate the SAA proton flux area, whose flux values are greater than the selected threshold. Panels (B), (C), and (D) illustrate the effects of each boundary on the SAA flux expansion.

5.5 Conclusion and Summary

The SAA high-energy proton flux response was numerically studied by performing test particle simulations, according to various magnetic field configurations, computed by the Tsyganenko models TS05 and T01. The main SAA proton flux variables were the maximum proton flux and the area. The conclusions are summarized as follows:

- **Basic features**: The current test particle model could successfully reveal the SAA basic features, such as: the capture of the particles in the anomaly due to the low magnetic intensity, the altitude effect and the 1D Gaussian fitting of the obtained proton flux.
- **Geodipole tilting angle effect**: The proton flux intensity in the SAA was significantly increased for small geodipole tilting angle values (during equinox time) and this result was confirmed by observations carried out by [Schaefer et al., 2016].
- **The increase rates**: The low geodipole tilting angle caused increases in the SAA maximum proton flux and in the corresponding area and could reach 52 % and 73 % respectively, in comparison with large tilting angles.
- **Geomagnetic storm effect**: The current numerical model could not reveal the same SAA flux variation pattern obtained from satellite observations made by [Zou et al., 2015] and [Dachev, 2018] at approximately 400 and 800 km where the SAA flux intensity should be decreased during geomagnetic storms.

From this study, the enhancement of the SAA proton flux can directly create an additional radiation dose on spacecraft electronic devices and on astronauts. Consequently, it is necessarily to include the effects of seasonal variations into radiation environment calculations, so as to be able to design better shielding.

Further work is still needed to deeply understand the proton dynamics of the SAA. This can take place by improving the current simulation model, such as by increasing the number of injected protons, by including electric field effects, and by extending simulation time, so that we could cover the proton flux variations inside the SAA within during a complete storm phase, and could obtain a better agreement between simulation results and observations. The better numerical model will be introduced in the next chapter.

Tables

Table 5.1: The following table shows the input conditions of each simulation. μ is the tilting dipole angle, N is the solar wind density, V_x, V_y, V_z are the three solar wind velocity components and B_{yIMF}, B_{zIMF} are Interplanetary Planetary Magnetic Field components. All simulations were performed at MIN = 0 and SEC = 0.

	Day	Hour	μ (deg)	P_{dyn} (nPa)	N (cc)	V_x (km/s)	V_y (km/s)	V_z (km/s)	B_{yIMF} (nT)	B_{zIMF} (nT)	Dst (nT)
Overview Run	304	15	-5	2.5	8.54	-418.10	-15.000	1.440	1.960	-1.320	-7
First Event	306	7	-20	1.06	3.60	-419.73	4.452	-19.372	-0.239	1.127	-7
Second Event	209	13	27.5	2.96	2.58	-825.78	36.937	-35.841	-7.666	-14.138	-141
Third Event	313	7	-25.1	2.53	2.98	-713.55	8.283	9.120	12.399	-16.312	-374
Case 0	306	7	-20	1.06	3.60	-419.73	4.452	-19.372	-0.239	1.127	-7
First Case	240	7	3.89	1.06	3.60	-419.73	4.452	-19.372	-0.239	1.127	-7
Second Case	180	10	23.3	1.06	3.60	-419.73	4.452	-19.372	-0.239	1.127	-7

Chapter 6

Test Particle Simulations: Calculation of SAA Proton Flux Response during a Geomagnetic Storm

6.1 Introduction

Even if the inner radiation belt is stable but it is not static [Barth, 1997]. One of the main source of disturbance is the solar wind, which drives the space weather and which is controlled by the solar activity. Any changes in the solar wind conditions is directly affecting the magnetosphere, hence, the radiation belts. On the another hand, particle loss evidence is a common feature while studying the radiation belts due to the non-adiabatic motion of the particle; the subject of the adiabatic invariant violation was widely discussed by many authors: for example the violation of the first adiabatic invariant due to the highly curvature magnetic field lines during geomagnetic storms [Sturrock, 1994], [Selesnick et al., 2010], [Zou et al., 2011] and [Zou et al., 2015], the second and third invariant violations by [Antonova et al., 2003], [Walt, 2005], [Easly, 2007] and [Ukhorskiy and Sitnov, 2013].

Since the SAA is one the main characteristics of the inner trapped radiation belt, it was found that the space weather can affect the anomaly. Observations carried out by the authors [Zou et al., 2015] using NOAA 17 data revealed the effect of the *Dst* index on the short-term response of the SAA proton maximum flux and the area of the SAA. Furthermore, another set of observations measured during the passage of the International Space Station (ISS) inside the SAA, [Dachev, 2018] investigated the geomagnetic storm effects on the anomaly as well. In addition, as discussed in the previous chapter, we have performed test particle simulations to study within several tens of drift periods the SAA proton flux response for several magnetic configurations with respect to various space weather conditions.
The framework of this research is to study the SAA proton flux response during a geomagnetic storm by implementing test particle simulations, where the background time-varying magnetic field is calculated by the combination of the realistic geomagnetic field computed by Tsyganenko model TS05 [Tsyganenko and Sitnov, 2005] and the internal (main) magnetic field model (IGRF-12), with the inclusion of the corresponding inductive electric field. The same approach was actually taken be by [Engel et al., 2015], who investigated the proton loss rate in the outer boundary of the inner radiation belt by carrying out test particle simulations where the time-varying magnetic field was calculated by the same Tsyganenko model with the corresponding inductive electric field, as well as [Ukhorskiy et al., 2006], who examined the radial transport of the electrons due to ULF pulsations in the outer radiation belt by calculating the inductive electric field from the time-varying realistic field given (IGRF+TS05).
This methodology is of great interest and several advantages could be taken in account, such as:

1. it is more approaching to the realistic situation, in another term, the dynamic nature of the inner radiation belt populated by the protons and electrons which are continuously precipitating and escaping from the anomaly.

2. the implementation of the guiding center model Tao-Chan-Brizzard model is solved by the Bulirsch-Stoer integrator which gives a better numerical accuracy by conserving the particle energy (if the magnetic field only was implemented) and better performance (because the method requires less computation time), especially for protons with high energy. Adding that, the efficiency of the particle trajectory calculations is based on the accuracy of the implemented Tsyganenko magnetic field model, which was previously explained by [Girgis et al., 2020]; we believe that the current magnetic model accuracy is adequate enough

to realize this study's objective, by assessing the variations of the proton flux inside the SAA with respect to disturbed space weather conditions.

3. The inclusion of the inductive the electric field with the realistic magnetic field can give us broader understanding about the inner radiation belt radial transport and particle energization.

For further details about the benefits of this technique, please refer to the section 2.3.6 as well as [Ukhorskiy et al., 2006].

6.2 Material and Methods

6.2.1 Guiding Center Equation Model

The relativistic formulation of the guiding center position and the parallel momentum are introduced by the authors [Tao et al., 2007], as follows:

$$\dot{\mathbf{X}} = \frac{p_{\parallel}}{\gamma m}\frac{\mathbf{B}^*}{B^*_{\parallel}} + \mathbf{E}^* \times \frac{\widehat{\mathbf{b}}}{B^*_{\parallel}}$$

$$\dot{p_{\parallel}} = q\mathbf{E}^* \cdot \frac{\mathbf{B}^*}{B^*_{\parallel}}, \tag{6.1}$$

where

$$\mathbf{B}^* = \mathbf{B} + \frac{p_{\parallel}}{q}\nabla \times \widehat{\mathbf{b}} \tag{6.2}$$

$$\mathbf{E}^* = \mathbf{E} - \frac{1}{q}\Big(p_{\parallel}\frac{\partial \widehat{\mathbf{b}}}{\partial t} + \frac{\mu}{\gamma}\nabla B\Big), \tag{6.3}$$

and,

$$B^*_{\parallel} = \mathbf{B}^* \cdot \widehat{\mathbf{b}} = B + \frac{p_{\parallel}}{q}\Big(\widehat{\mathbf{b}} \cdot \nabla \times \widehat{\mathbf{b}}\Big) \tag{6.4}$$

where $\mathbf{B}$ is the magnetic field, $\mathbf{E}$ is the electric field, $\mathbf{X}$ is the guiding center position, $p_{\parallel}$ is the parallel momentum, μ is the first invariant of the guiding center motion, m is the particle mass, q is the charge and γ is the relativity factor. The set of equations is solved numerically by the integrator Bulirsch-Stoer scheme [Stoer and Bulirsch, 1980].

6.2.2 Input Conditions

In this study, we have selected the geomagnetic storm event of 15 May 2015. We have simulated the first 12 hours of the storm that included the three storm phases: the initial, the main and the recovery phases as shown in Figure 6.1. The input parameters to the geomagnetic model IGRF+TS05 were the solar wind ram pressure, the density, the three velocity components, the Interplanetary Magnetic Field transversal components B_{yIMF} and B_{zIMF}, the *Dst* index and the geodipole tilting angle. As various parameters characterize the SAA proton flux, the study will consider:

1. the area of the SAA (defined as the area where the proton flux exceeds a given threshold)

2. the maximum value of the proton flux (at specific altitudes).

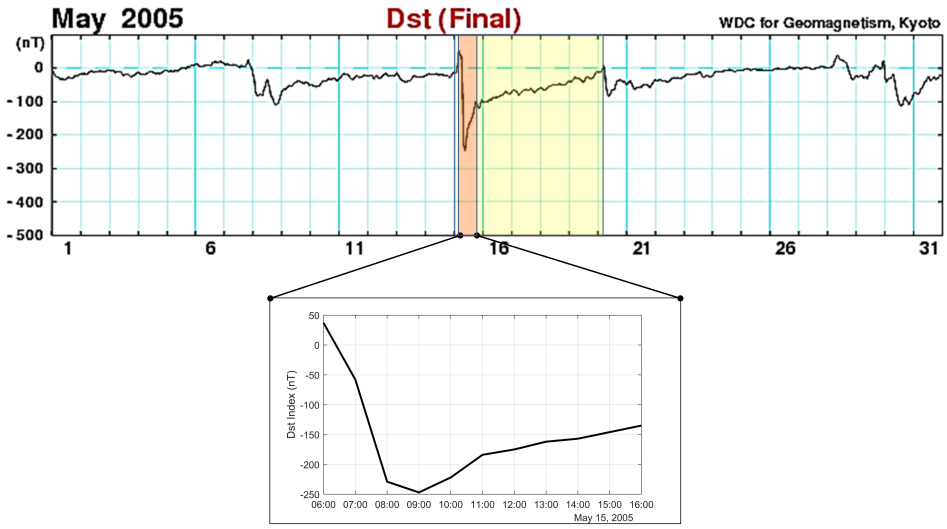

Figure 6.1: *Dst* index profile all over the year 2005

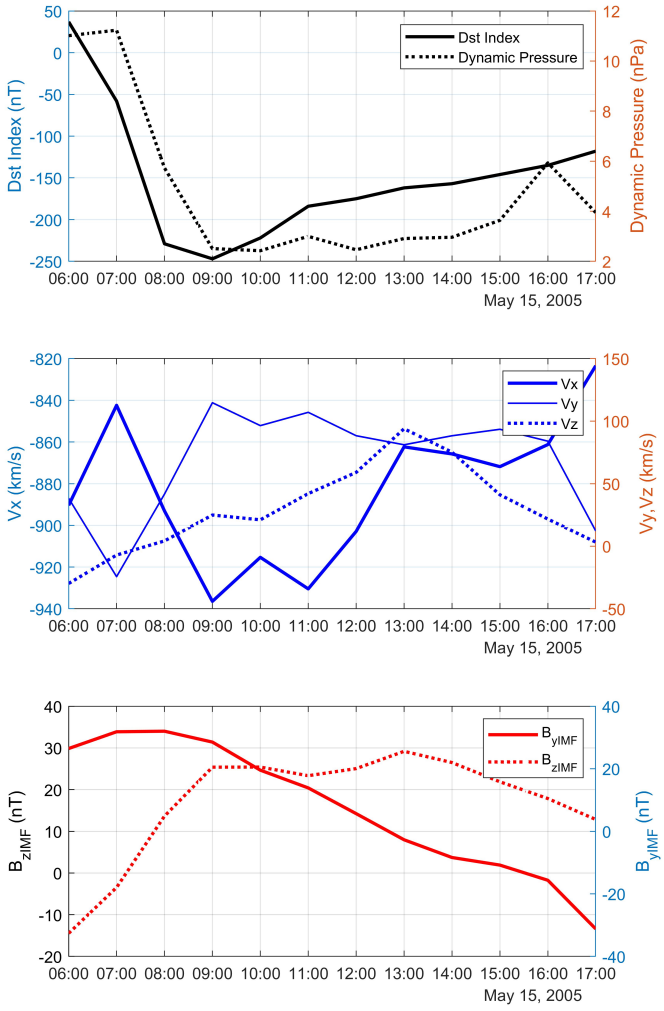

Figure 6.2: Hourly input data of geomagnetic storm event of 15 May 2015

6.2.3 Inductive Electric Field Formulation

We have solved the Biot-Savart integral to compute the inductive electric field from the given time-varying magnetic field generated by the realistic magnetic field TS05+IGRF. The mathematical expression is shown as follows:

$$\mathbf{E}(\mathbf{r},t) = -\frac{1}{4\pi}\frac{\partial}{\partial t}\int_V \frac{\mathbf{B}(\mathbf{r}^{'},t)\times(\mathbf{r}-\mathbf{r}^{'})}{|\mathbf{r}-\mathbf{r}^{'}|^3}d^3r^{'}, \tag{6.5}$$

where $\mathbf{E}$ is the electric field computed at the desired location $\mathbf{r}$ and time t, $\mathbf{B}$ is the magnetic field defined at all grid point $\mathbf{r}^{'}$; the integration was performed over the entire simulation domain of the selected geomagnetic field model.

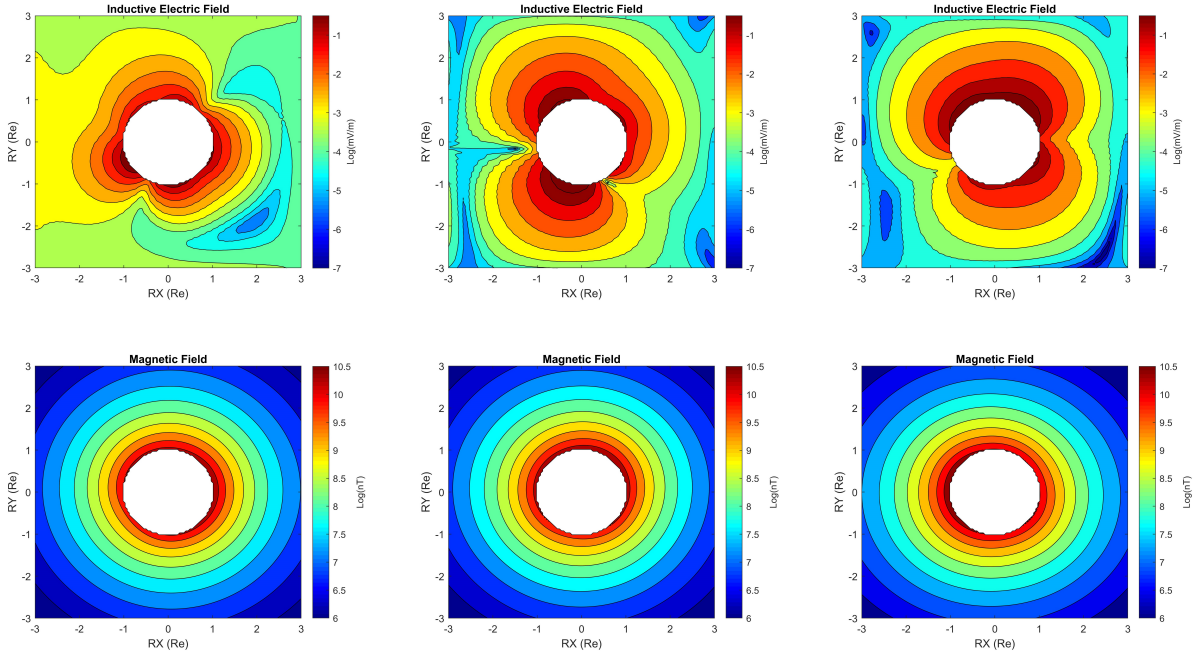

Figure 6.3: Equipotential contour plots of the magnitude of the inductive electric and (TS05+IGRF) magnetic fields at 07:00, 11:00 and 16:00 UT.

6.2.4 Simulation Setup

Two main test particle simulations had been performed. The first one the inner radiation belt proton had been simulated and the proton inside the SAA had been captured in order to estimate the corresponding proton flux; the only external field was the background magnetic field calculated by TS05+IGRF. The second run was realized by the inclusion of the inductive electric field. Then, a comparison was carried out in order to understand the effect of the electric field on the inner radiation belt proton in the SAA.

The background magnetic field was calculated by the TS05 for the input conditions of the geomagnetic storm of 15 May 2015, as demonstrated in Figures 6.1 and 6.2. The solar wind data were provided by ACE spacecraft and the *Dst* index by WDC, Kyoto University. In our simulations, 10^4 protons were initially distributed in a the realistic geomagnetic field (TS05+IGRF), with an energy range of 140 to 400 MeV, a pitch angle range of 10°to 170°, a shell range from 1 to 3 Re, and the magnetic field grid was a cube, with dimensions of 6 Re × 6 Re × 6 Re, with the Earth was located at its center, the grid space size resolution was 0.0468 Re. The study followed the same procedure as already shown in the previous chapter in order to initialize the proton position uniformly and distribute them in almost all L shells. The magnetic and electric field data were linearly interpolated in time and space.

The capturing time of the protons inside the anomaly was 3 seconds below 960 km as measured from the ground. The proton positions were then converted from Cartesian coordinates to geodetic coordinates: height, latitude and longitude. At the next step, the fluxes were calculated by a three-dimensional interpolation, being height, latitude and longitude. The mapped grid resolution was 0.5°× 0.5°.

The main parameters to study the SAA proton flux were the maximal value of the proton fluxes in the mapped grid and in its corresponding area, calculated below a certain threshold of the normalized proton flux value at

all altitudes. This is equal to the total number of the area units, satisfying the condition that the SAA proton flux should be larger than the selected threshold in the grid.

In order to estimate the numerical error, the energy conservation of the protons was calculated for the maximum proton energy (= 400 MeV) and for all pitch angles at 2.0 Re for 4 hours and the maximum energy conservation error was confirmed to be less than 7 %. The previous results indicate the strong advantage of the implementation of Bulirsch-Stoer integrator scheme.

The proton fluxes in the current study were considered as directional integral fluxes, where the protons pass inward through a unit area in 1 second for a 90˚solid angle value and for all energy ranges. Thus, the corresponding flux unit would be protons cm^{-2} s^{-1} str^{-1}. The values shown in the next section are normalized by selecting the speed and length scales to be the speed of light and the Earth radius respectively.

6.3 Results I: for 10^4 Implemented Protons

6.3.1 RUN A: Magnetic Field only (TS05+IGRF)

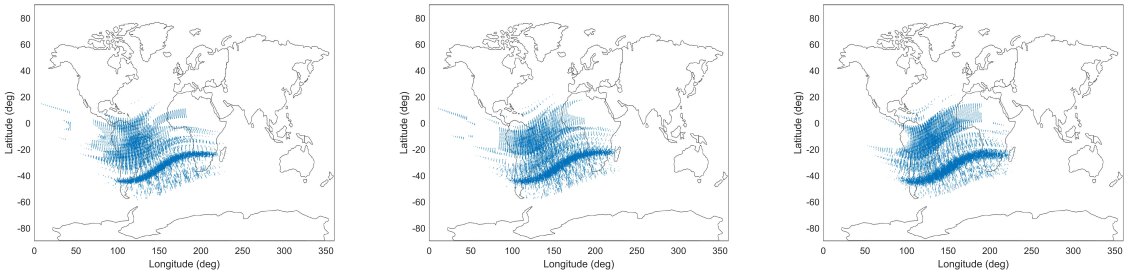

(a) (b) (c)

Figure 6.4: Proton distribution inside the SAA along the geomagnetic storm: (a) storm commencement (during the first storm hour), (b) storm main phase (after two hours from the storm commencement) and (c) recovery phase (after three hours from the storm commencement)

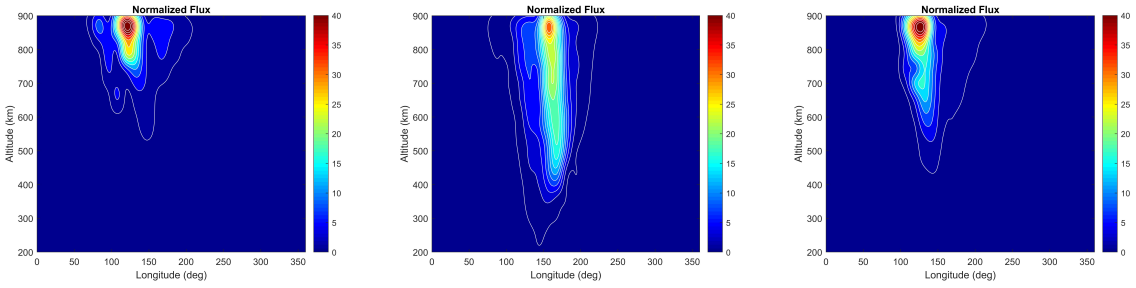

(a) (b) (c)

Figure 6.5: Latitudinal section contour plot of the proton flux distribution inside the SAA along the geomagnetic storm during: (a) storm commencement, (b) storm main phase and (c) recovery phase

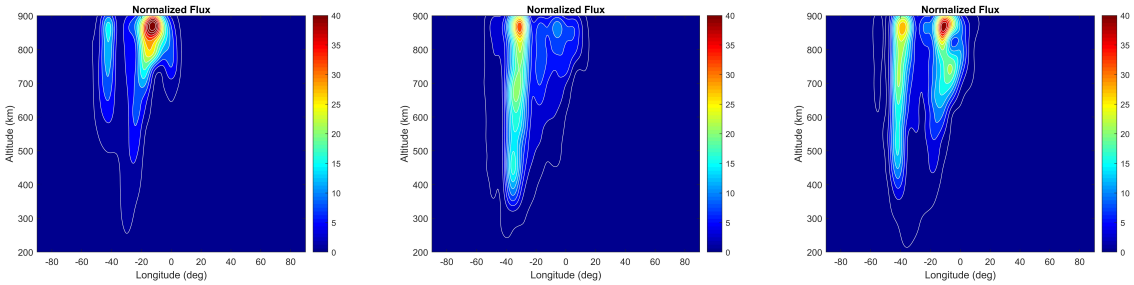

(a) (b) (c)

Figure 6.6: Longitudinal section contour plot of the proton flux distribution inside the SAA along the geomagnetic storm during: (a) storm commencement, (b) storm main phase and (c) recovery phase

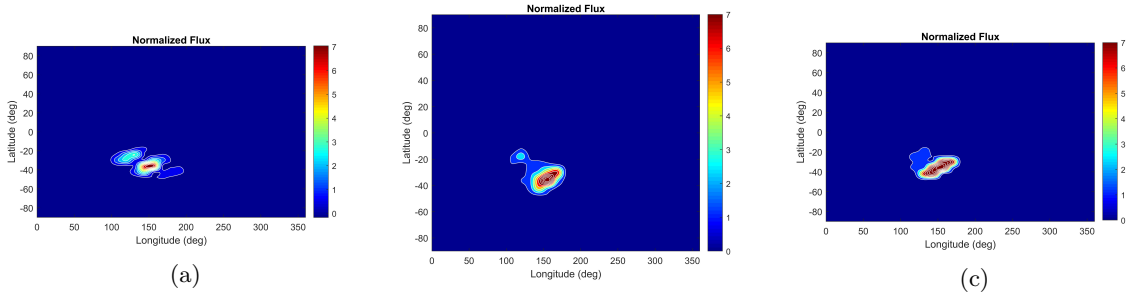

(a) (b) (c)

Figure 6.7: Contour plot of the proton flux distribution inside the SAA at the altitude of 400 km along the geomagnetic storm during: (a) storm commencement, (b) storm main phase and (c) recovery phase

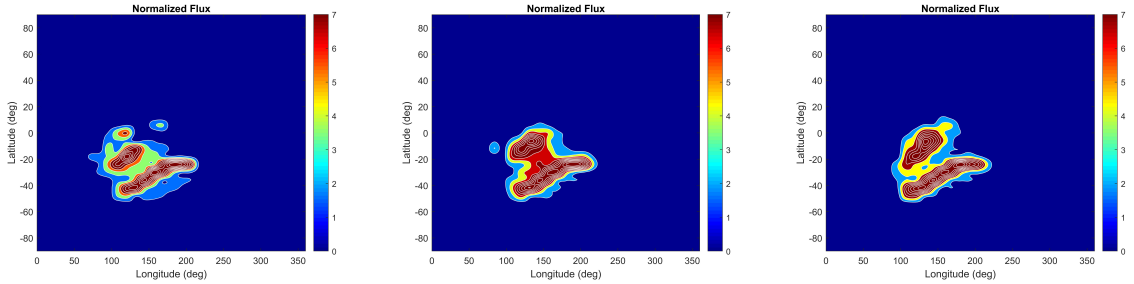

(a) (b) (c)

Figure 6.8: Contour plot of the proton flux distribution inside the SAA at the altitude of 800 km along the geomagnetic storm during : (a) storm commencement, (b) storm main phase and (c) recovery phase

The output numerical results are illustrated in several ways: Figure 6.4 shows the projection of the 3D proton distribution captured inside the anomaly during the three storm phases: (a) commencement, (b) main and (c) recovery phases; Figure 6.5, the 2D latitudinal section of the proton flux, Figure 6.6, the 2D longitudinal section. Figures 6.7 and 6.8 demonstrate the 2D proton flux distribution at the altitudes 400 and 800 lm respectively.

Several interesting aspects are remarked: (1) from Figures 6.6 and 6.5, we can observe that the proton flux during the recovery phase start to return gradually back to the commencement phase. (2) from Figure 6.6, a special feature could be detected which is a double-cell configuration; it is shown that first cell intensity is lower than the second during the commencement and recovery phase, while the opposite is during the main storm phase; (3) Figure 6.8 clearly show the merge of both cells during the main storm phase. (4) From the Figure 6.4 and again Figure 6.8, the main cell where the protons are mostly populated is the bottom one. Probably, the second cell is tending to be more sensitive to the geomagnetic storm conditions.

6.3.2 RUN B: Magnetic Field (TS05+IGRF) + Inductive Electric Field

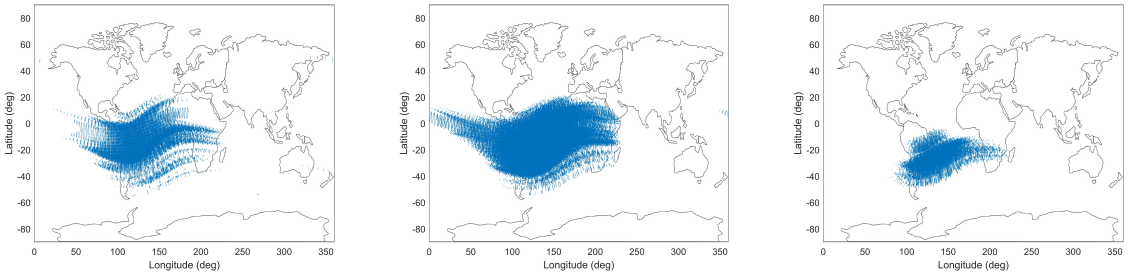

(a) (b) (c)

Figure 6.9: Proton distribution inside the SAA along the geomagnetic storm: (a) storm commencement (during the first storm hour), (b) storm main phase (after two hours from the storm commencement) and (c) recovery phase (after three hours from the storm commencement)

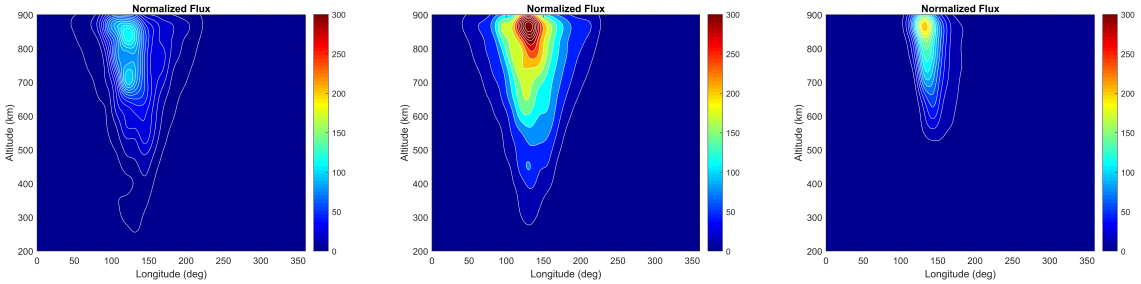

(a) (b) (c)

Figure 6.10: Latitudinal section contour plot of the proton flux distribution inside the SAA along the geomagnetic storm during : (a) storm commencement, (b) storm main phase and (c) recovery phase

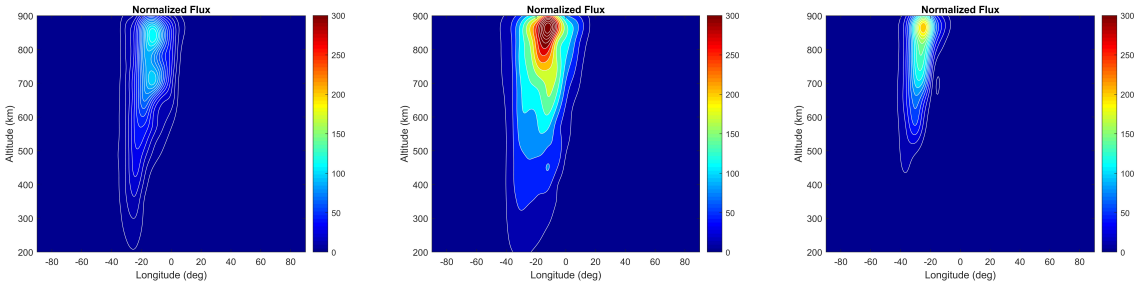

(a) (b) (c)

Figure 6.11: Longitudinal section contour plot of the proton flux distribution inside the SAA along the geomagnetic storm during : (a) storm commencement, (b) storm main phase and (c) recovery phase

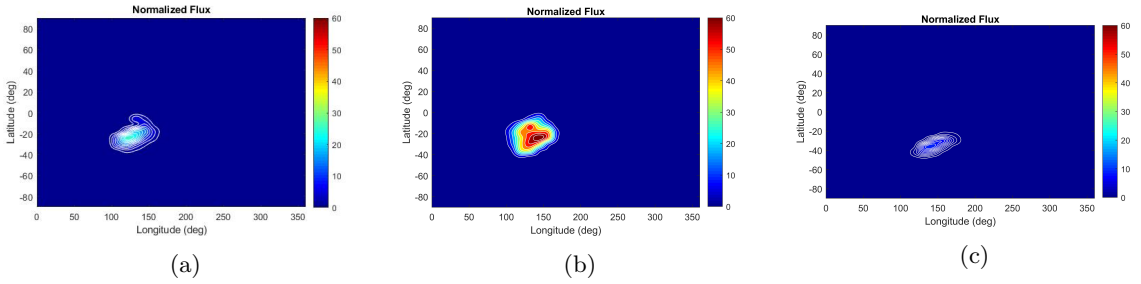

(a) (b) (c)

Figure 6.12: Contour plot of the proton flux distribution inside the SAA at the altitude of 400 km along the geomagnetic storm during: (a) storm commencement, (b) storm main phase and (c) recovery phase

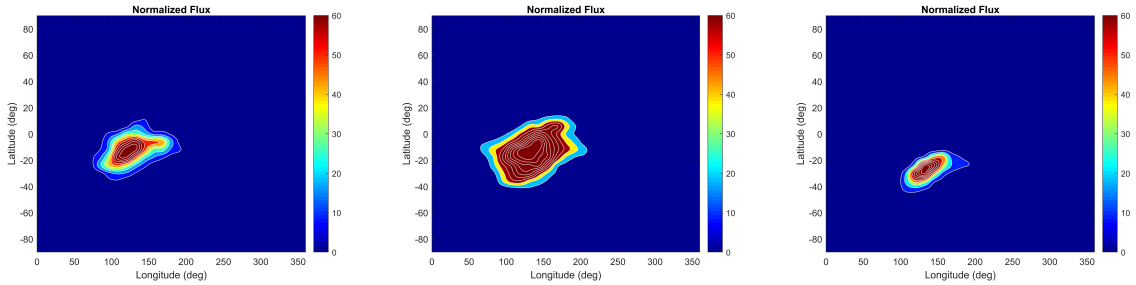

(a) (b) (c)

Figure 6.13: Contour plot of the proton flux distribution inside the SAA at the altitude of 800 km along the geomagnetic storm during: (a) storm commencement, (b) storm main phase and (c) recovery phase

The output numerical results are illustrated similarly as in the previous section corresponding to the three storm phases. The main features are summarized as follows: (1) by the inclusion of the inductive electric field, the protons were getting more captured inside the anomaly in comparison without the electric field case (previous section), from which we can understand that the inner proton belt is getting closer to the Earth's surface due to the radial transport. (2) From all the above figures, especially Panels (b), it is clearly demonstrated the enhancement of the proton flux intensity during the main storm phase, and totally the opposite during the recovery phase where the proton loss rate was significantly increasing. (3) The double cell configuration of the proton flux was nearly merged due to the high concentration of protons in comparison without the electric field case.

6.4 Discussion

The previous results demonstrated the proton flux response inside the anomaly for two different cases: without and with the inclusion of the electric field. Since the available observation data of the proton flux behavior inside the SAA during geomagnetic were related to both altitudes ≈ 400 and 800 km, we have extracted from the obtained numerical results the maximum proton flux value and the area at the same altitudes in order to carry out the comparison with the observations.

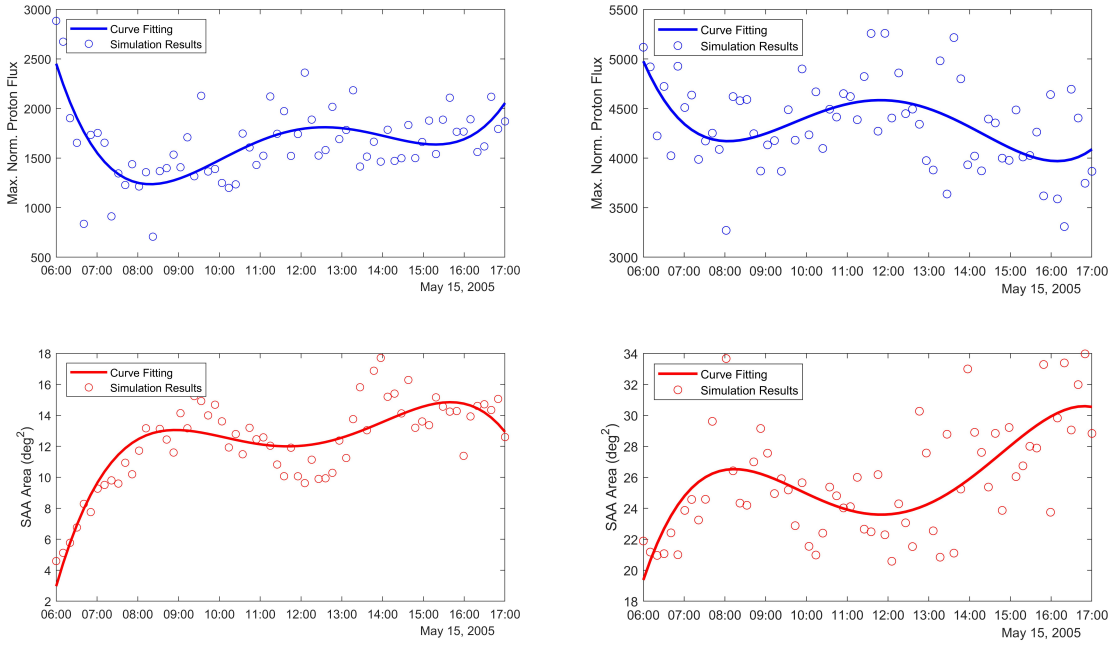

(a) @ 400 km (b) @ 800 km

Figure 6.14: The evolution of both SAA parameters, the maximum proton flux and the corresponding area at 400 and 800 km, without the inductive electric field.

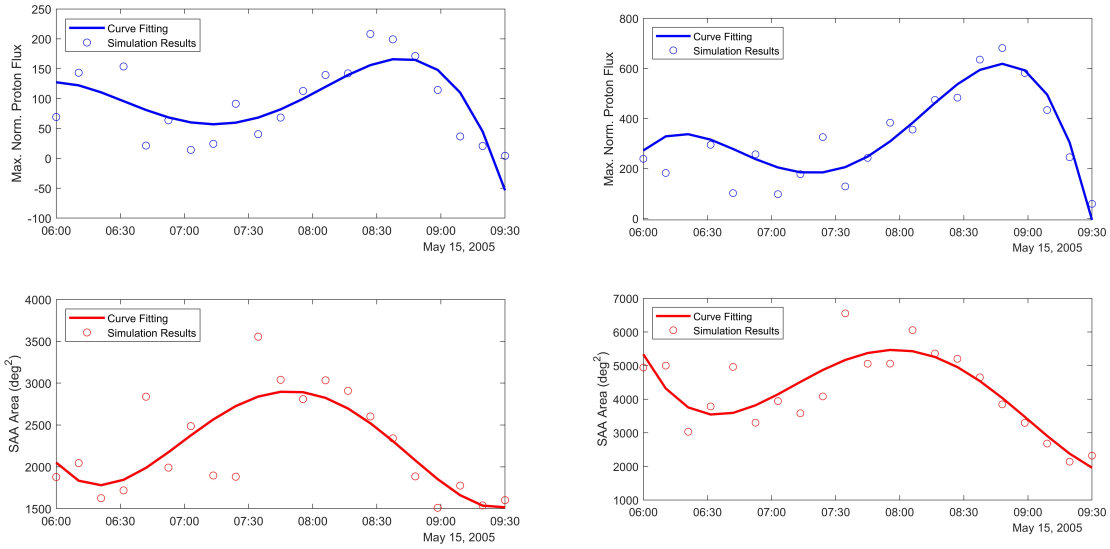

(a) @ 400 km

(b) @ 800 km

Figure 6.15: The evolution of both SAA parameters, the maximum proton flux and the corresponding area at 400 and 800 km, with the inclusion of the inductive electric field.

From figure 6.14, the investigation of the proton flux behavior at the specific altitudes 400 and 800 km from the numerical results revealed that the SAA proton flux was clearly decreased during the geomagnetic storm event; the latter conclusion was already confirmed from the observations analyzed by [Dachev, 2018] and [Zou et al., 2015] respectively. However, the trend of the maximum SAA proton flux variations with respect to the storm event was increasing, although there was a slight decrease in the recovery storm phase. Thus, a more realistic model is needed to better match the observation findings. This was achieved by adding the background electric field as shown in Figure 6.15.

At glance, due to the significant proton loss after the main storm phase, the numerical interpolation was carried out from the storm commencement until 09:30 UT due to the lack of number of counts. The main interesting aspect revealed from this simulation was that during the main storm phase, both SAA parameters were significantly increased at both altitudes and then were decreased drastically due to the proton loss during the recovery storm phase. This reduction in the proton flux intensity in the SAA does agree with the observations from satellites. From the output numerical results, it is also expected that extending the simulation time to cover the entire geomagnetic storm duration (about 5 days) the proton flux should return back to its normal situation during quiet conditions.

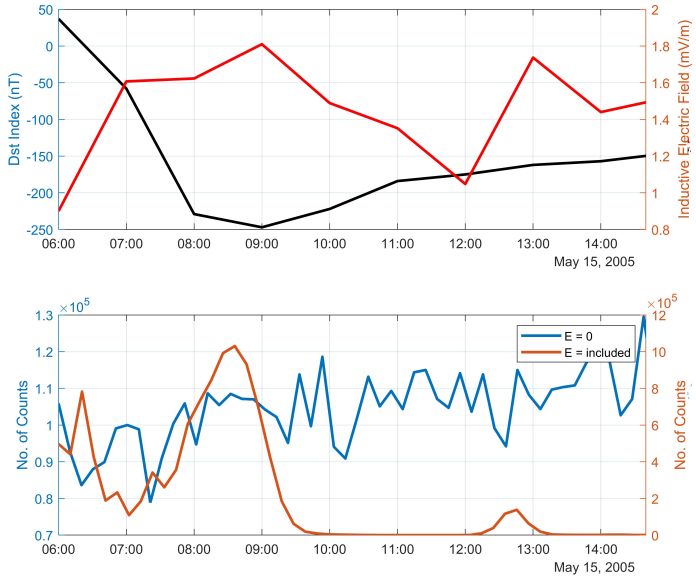

Figure 6.16: The upper panel shows the *Dst* index (black) profile and the maximum electric field value (red) in the SAA during the geomagnetic storm event. The lower panel represents the number of counts in the SAA during the event for the case with no electric field considered (blue) and including the electric field (orange).

Figure 6.16 emphasizes the electric field effect on the simulations. From the lower panel, since there was approximately no proton loss in the simulations (no electric field), it is clear the number of counts was slightly varying (average 1×10^5). On the other hand, regarding the electric field case, it is also clear that during the main storm phase, an overshoot in the number of counts was occurred corresponding directly to the increase in the electric field intensity in the SAA which was, by turn, associated with the large decrease of the *Dst* index. Furthermore, the small overshoot occurred during the storm commencement does agree also with observations of [Dachev, 2018].

The double-cell configuration of the proton flux obtained from the simulations including the magnetic field only, was similarly found for the high-energy proton > 50 MeV by [Stassinopoulos et al., 2015], who visualized the proton flux contour plots by implementing the AP8-MAX model as shown in Figure 6.17. As discussed by the previous authors, the magnetic field model IGRF was implemented to order the particle data, therefore, the three adiabatic invariants should be valid. This is probably the reason why this pattern was not observed in the simulations that included the electric field. As explained by [Ukhorskiy et al., 2006] and [Engel et al., 2015], the radial transport of the charged particles that are trapped in the geomagnetic field requires the violation of the third adiabatic invariant which is associated with the particle drift around the Earth due to the magnetic field gradient and curvature. From the last simulations, the inner high-energy proton belt was moving inward during the main phase of the storm due to the particle acceleration by the added induced electric field, then the inner belt moved outward and nearly disappeared from the low-altitude regions e.g. SAA. It is well known that the inward motion is accompanied by acceleration while the outward motion leads to energy loss; similarly, [Sauvaud et al., 2013] investigated the inner radiation belt particle acceleration and its energy structuring during geomagnetic storms by the drift resonance with the ULF waves using observational data from the polar orbiting Demeter spacecraft and also by performing numerical simulations.

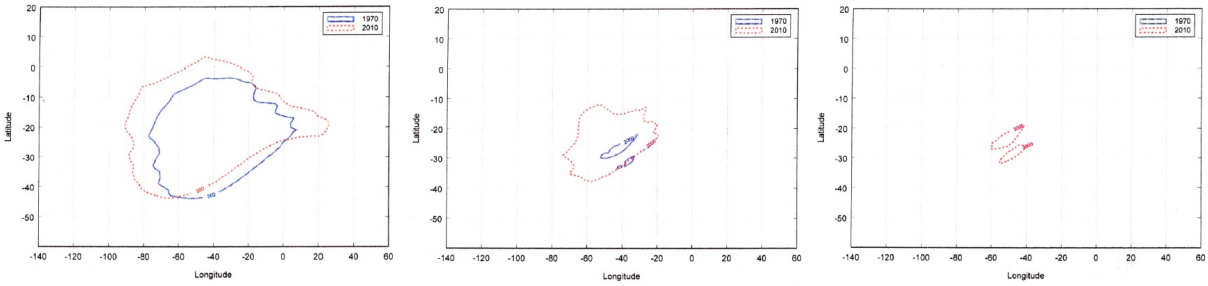

(a) Integral proton flux contour = 1000 proton cm^{-2} s^{-1}

(b) Integral proton flux contour = 2000 proton cm^{-2} s^{-1}

(c) Integral proton flux contour = 3000 proton cm^{-2} s^{-1}

Figure 6.17: Location of E > 100 MeV proton flux contours at 800 km altitude for epochs 1960 and 2010.

The last conclusion we would like to derive is that, even if the SAA proton flux trend is generally decreasing along the magnetic storms, it could be significantly increased at time scales (<= one hour) shorter than a single magnetic storm duration (several hours up to days), and hence, shorter than the available data from the satellite observational data. Such increases in both SAA parameters, the maximum proton flux and the corresponding area were found to be approximately 30 %, 50 % at 400 km and 50 %, 20 % at 800 km respectively.

6.5 Summary and Conclusion

We have developed a test particle simulation code to compute the proton trajectories of the inner trapped radiation belt and calculate the corresponding proton flux variations inside the SAA during the geomagnetic storm of 15 May 2015. The inductive electric field was calculated from the global time-dependent model output of the geomagnetic field (IGRF+TS05). The conclusions are summarized as follows:

1. According to the first simulation case when the magnetic field was only implemented without the inclusion of the electric field, the obtained numerical results revealed that the SAA area was decreased during the storm event and which did agree with observations at 400 and 800 km, however, the corresponding maximum SAA proton flux variations did not agree.

2. The inductive electric field intensity in the SAA was roughly anti-correlated with the *Dst* index variations.

3. Regarding the second simulation case when the inductive electric field was included, the inner radiation belt experienced a significant proton loss during the recovery phase. The SAA proton flux intensity was decreased and thus, did agree with observations.

4. Before the proton loss evidence, the SAA proton flux was remarkably enhanced during the main storm phase. At 400 km, the increase of the maximum proton flux value was about 30 % and the corresponding area, 50 %, while at 800 km, 50 % and 20 % respectively.

We would like to highlight that such enhancement could be a serious risk for the LEO orbit missions. As a result, the increased level of the radiation exposure can increase the probability of the Single Event Effect (SEE) occurrence. Hence, taking into account the small time-scale variations of the inner radiation belt can prevent a gradual decreased performance or even a failure of a vital electronic component mounted on LEO spacecrafts. Indeed, the assessment of the increased SEE rates according to geomagnetic storms is considered as a necessary task to be carried out as will be shown in the next chapter.

Chapter 7

Assessment of the LEO Spacecraft Radiation Environment due to its Passage in the SAA

7.1 Introduction

7.1.1 Space Radiation Environment

The space environment is greatly affecting spacecraft missions due to the presence of radiation consisting of electrons and protons trapped by the geomagnetic field. It was found that the International Space Station (ISS), is exposed to primary cosmic beam of approximately 85 % protons and 15 % heavy nuclei, which is partially converted into secondary neutrons by collisions the spacecraft material. The space radiation environment could impose a low dose rate of $\approx 10^{-4}$ to 10^{-2} rad/s. However, since mission durations are designed for several years, large accumulated doses are produced. Hence, during a typical spacecraft mission, the Total Ionizing Dose (TID) levels could be in the order of 10^5 rad. That is why it is crucial to select the candidate devices qualified to achieve successfully the requirements of a spacecraft mission. In general, the amount of energy of a particle that converts to ionization is given by the "stopping power" or "linear energy transfer (LET) function", which is defined as the energy per unit length (dE/dx). Therefore, the material in which the dose is deposited should always be determined, for example Silicon (Si) or Gallium-Arsenide (GaAs) for the solar cells. It is understood that for a given energy, the greater the mass and charge of the incident particle, the greater the amount of the deposited charge or energy produced over a path length inside the solid-state material [Maurer et al., 2008].

The radiation effects in a solid-state microelectronics can be categorized as:

1. **Cumulative Effects**: which produce gradual changes in the operational parameters of the devices, and,
2. **Single Event Effects (SEEs)**: which cause abrupt changes or transient behavior in the device circuits.

7.1.1.1 Cumulative Effects: *Enhanced Low-Dose-Rate Sensitivity*

The duration of a satellite mission may extend to several years, so a great TID is expected to be accumulated. Over the last decade, the development of the integrated circuit fabrication have led to produce some components with an enhanced sensitivity to radiation when exposed at low dose rate. This effect is called "Enhanced Low-Dose-Rate Sensitivity" (ELDRS). According to [Maurer et al., 2008], the standard TID dose rate for ground testing is ≈ 50 rad/s. This dose rate allows a qualification test to be run in an 8 hour shift. However, typical ELDRS testing is done with a dose rate of only 10 to 100 mrad/s; thus, test times are required on the order of weeks to months, which is much closer to the rate at which TID will be accumulated during a spacecraft mission. This extended and more realistic testing is certainly expensive and can affect a spacecraft program schedule. To solve this issue, some vendors who produce radiation-hardened devices, have determined the underlying cause of ELDRS for their parts and then could modified their manufacturing process to eliminate the problem.

7.1.1.2 Single-Event Effects (SEEs)

An SEE can be initiated if the amount of charges collected at a junction exceeds a threshold. The SEE could be destructive and results a catastrophic device failure, or nondestructive, which results in loss of data and/or control. The basic SEE mechanism is occurring when a charged particle travels through the device and loses

energy by ionizing the device material. Other mechanism can include elastic and inelastic nuclear reactions. Then, the charge generated by any single strike is collected, producing factitious voltage on a "sensitive" node that causes a circuit-level effect Figure 7.1. The number of electron-hole pairs generated is proportional to the stopping power of the incident particle in the target material. In silicon, it takes 22.5 MeV of energy to generate 1 pC of charge. The generated charge recombines or is collected at the various nodes within the region of the ion strike. The charge collection threshold for the single event is called the critical charge or Q_{crit}. If Q_{crit} for a device is reduced, then its SEE rate is increased.

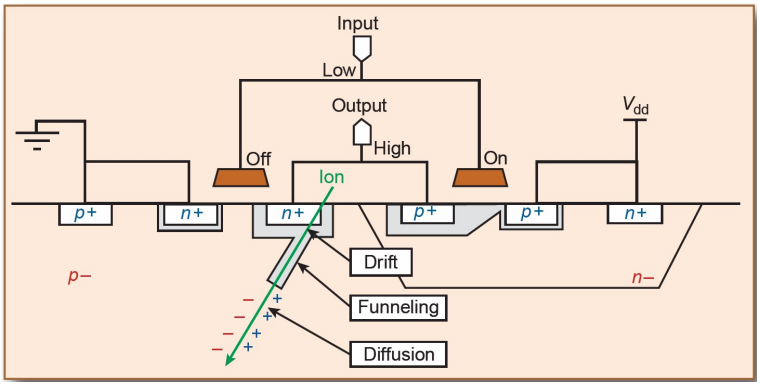

Figure 7.1: Schematic representation of a heavy ion strike on the cross-section of a bulk CMOS memory cell [Maurer et al., 2008].

Although TID testing is achievable, the access to off-site particle accelerators is required for SEE testing. SEE sensitivity is characterized as a function of LET versus equivalent cross-sectional area. The LET can be varied at a particle accelerator by changing the incident particle mass, incident energy, and angle of strike [Binder, 1988]. A particle entering a sensitive volume at 60° will deposit twice the energy of a particle entering at normal incidence; therefore, the LET is effectively doubled. The key measurement for these experiments is the number of single events that occur as function of the number of incident particles at a given LET. These data are combined with spacecraft trajectory information and used to predict a specific mission SEE rate [Maurer et al., 2008].
Several of SEEs types are summarized as follows:

- **Single Event Transient (SET):** SETs are momentary voltage excursions at a node in an integrated circuit caused by a transient current generated by the nearby passage of a charged particle. Most SETs are harmless and do not affect device operation. However, there are several types of SETs that can cause harm or corrupt data.

- **Single Event Upset (SEU):** A Single Event Upset (SEU) is the change of state of a bistable element, typically a flip-flop or other memory cell, caused by the impact of an energetic heavy ion or proton. The effect is nondestructive and may be corrected by rewriting the affected element. As with other SEEs, a single-particle strike may introduce enough charge to exceed a sensitive circuit node's Q_{crit} and change the logic state of the element. The resulting change of state is often known as a bit-flip and can occur in many different semi-conductor technologies. The vulnerability of a device to SEU is determined by two parameters: (i) the threshold LET, which is the minimum amount necessary to produce upset; and (ii) the saturation LET cross-section in square centimeters, which is a function of the surface area of all of the SEU sensitive nodes.
  Static Random Access Memory (SRAM) and Dynamic Random Access Memory (DRAM) are two common integrated circuit memories that experience SEUs. SRAMs have a structure consisting of an array of nearly identical memory cells. The cell is a cross-coupled inverter pair using four transistors in the inverters. An ion strike on the four transistor drains starts a mechanism potentially leading to upset (i.e., if the voltage pulse attributable to the ion strike is faster than the feedback loop between the two inverters, a change of logic state will occur until the next write to the cell). DRAM structures have cells using charge storage in a capacitor to represent data. Typically, only one state is susceptible to SEU (i.e., 1s can be upset but not 0s). Very dense memory circuits also may have multiple bit upsets when one ion strike causes upsets in multiple bits. As fabrication feature sizes are decreased, multiple upsets are more common because sensitive circuit nodes are closer together and Q_{crit} tends to be smaller [Petersen et al., 1982].
  At some time after an SEU or SET occurs, the device may operate in an unpredictable manner. In complicated devices such as microprocessors or flash memories, classes of SEEs that have been named single-event functional interrupts (SEFIs) have been observed. An SEFI is an SEE that places a device in an unrecoverable mode, often stopping the normal operation of the device. It is usually caused by a

particle strike but can be produced by other causes. SEFIs are not usually damaging but can produce data, control, or functional-interrupt errors that require a complex recovery action that may include reset of an entire spacecraft subsystem.

- **Single Event Latch-up (SEL):** A latched part in a circuit can be permanently damaged as a result of thermal runaway or failure of on-chip metallization or packaging bond wires. The targeted integrated circuits are the Complementary Metal–Oxide–Semiconductors (CMOS), which are very widely used in space electronics.

In this study, we will be focusing on the SEU assessment.

7.1.2 Mitigation of Radiation Effects

7.1.2.1 Mitigation of Cumulative Effects

Total dose effects are minimized by **shielding**, **derating** (the operation of a device at less than its rated maximum capability in order to prolong its life), and **conservative** circuit design. Radiation-hardened devices also may be used if available with suitable technical specifications. Dose–depth curves showing the ionizing dose at the range of shield depths for the spacecraft and radiation total dose testing are always necessary if parts without known total dose properties are used (Figure 7.2). Flight part qualification testing is usually done to two to three times the expected mission dose to provide margin given the uncertainty in the prediction of expected dose. This conservatism is necessary because of the dynamic variability of the natural environment for which static models are used and because of the variation of the hardness levels of the individual parts in the flight lot from which only a small sample size is used in the qualification test [Maurer et al., 2008].

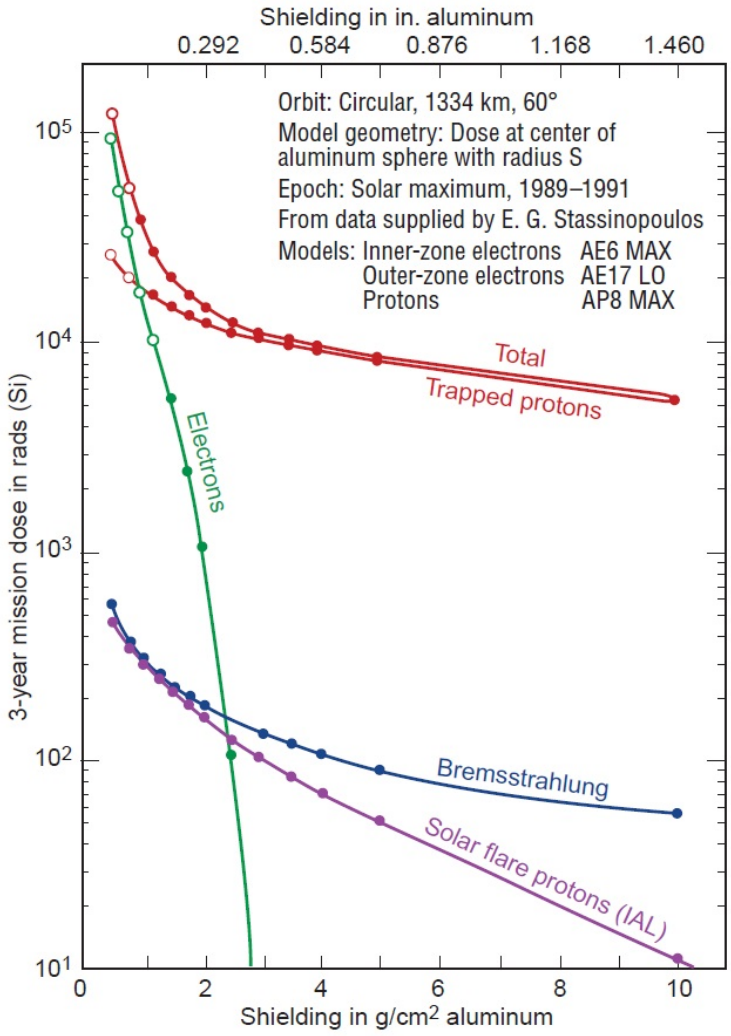

Figure 7.2: Schematic representation of a heavy ion strike on the cross-section of a bulk CMOS memory cell [Maurer et al., 2008].

7.1.2.2 Mitigation of Single Event Effects

Firstly, it is preferred to select circuit parts that are insensitive to the SEE, however, in many cases, such way could not be achievable. For the SEL mechanism, if the latch-up could be occurred frequently in a critical circuit of a spacecraft mission, then, the mitigation process should include full protection against device damage, automatic recovery from latch-up, and resumption of normal system operation. Regarding the SEU, the arrays of memory elements can often be mitigated by using some redundant cells and one of a large variety of error-detecting and -correcting codes; in addition, mitigation through coding is conceptually still feasible but is seldom used because encoding/decoding and signal routing overhead is substantial. Resynchronization of a processor affected by an upset is complex and is an area of active research in industry. Processor boards with very high throughput and modest power consumption compared to designs using fully SEU-immune components have been developed based on these principles [Maurer et al., 2008].

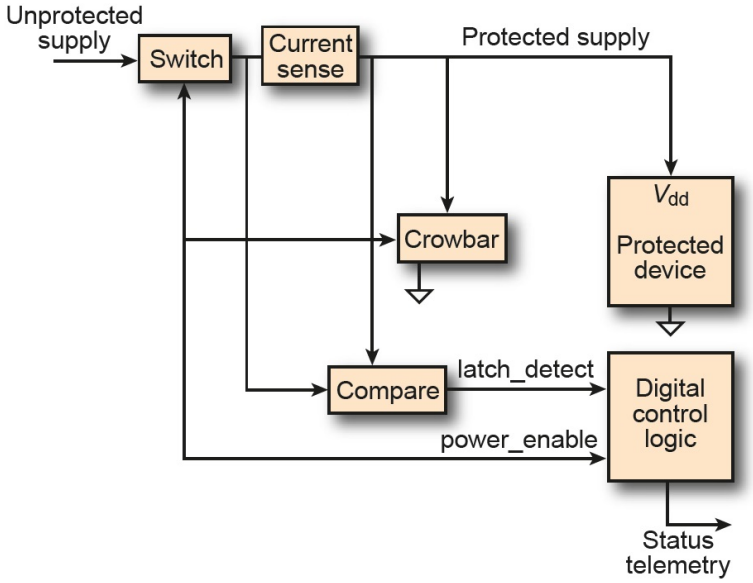

Figure 7.3: Latch-up protection circuit. The telemetry device susceptible to latch-up is called the protected device in the diagram. The current sense, comparator, and control logic detect any overcurrent and remove the applied voltage. The crowbar is enabled after overcurrent detection to shunt any charge to ground that remains on the protected supply line [Maurer et al., 2008].

7.2 Material and Methods

To estimate the radiation dose for the passage of a spacecraft inside the SAA, we calculate two parameters: the absorbed radiation dose and SEU rates.

From the previous chapter, it was concluded from the test particle simulation results that, during the geomagnetic storm, the SAA proton flux was significantly enhanced during the magnetic storm main phase and before the proton loss evidence. Consequently, such increase in the proton flux could induce a larger absorbed radiation dose and SEU rates. The objective of this chapter is to investigate the corresponding variations of the radiation environment in the SAA due to the enhancement of the proton flux during the geomagnetic storm main phase.

7.2.1 Dose Rates Calculations

According to [Da Silva and Rocco, 2017], the equation to estimate the absorbed radiation dose equivalent rate is shown as follows:

$$\dot{D}(E) = \omega_R \kappa \frac{\Phi(E) E^2}{\rho t} \tag{7.1}$$

where, ω_R is the radiation weighting factor, such that 1 is for electron and 2 is for proton, κ is a constant equal to $4.8065.10^{-11}$, Φ is the omnidirectional flux, in function of the energy E, t is the shielding thickness and ρ is the density of shielding material. The unit of absorbed radiation dose equivalent rate is rad/s, where rad is a unit of absorbed radiation dose defined as 1 rad = 0.01 J/kg. The selected material is Aluminum, whose material density is 0.002697 g/cm^2 and a thickness of 1 mm. The next step is to calculate the orbital motion

as well as the ground track of a selected spacecraft in order to assess the absorbed radiation doses when the spacecraft passes through the anomaly region; this step is achieved by implementing the orbit mechanical codes available in the textbook [Curtis, 2019].

7.2.2 SEU Calculations

We have adopted the following steps as explained in details by [Bendel and Petersen, 1983] in order to estimate the proton upset rates from RAM devices in a given spacecraft:

1. (a) Obtain the experimental proton upset cross section at one or more energies.
   (b) Determine the upset sensitivity parameter, A. The proton upset cross section equation is shown as follows:

$$\sigma = (24/A)^{14}[1 - \exp(-0.18Y^{0.5})]^4 \tag{7.2}$$

and,

$$Y = (18/A)^{0.5}[E - A] \tag{7.3}$$

where, Y is a linear function of energy in MeV and A is the apparent threshold for a given device in MeV. We have selected arbitrarily the parameter A to be equal to 18 [Bendel and Petersen, 1983]. Figure 7.8b demonstrates the corresponding upset cross section curve.

2. (a) Obtain the average proton spectrum in the orbit considered; this step is achieved by collecting the information of the proton flux inside the SAA from the output numerical results of the test particle simulations as demonstrated in the previous section as shown in Figure 7.5; in this problem, we selected a circular orbit at altitude of 800 km with respect to the incident energy; Figure 7.6 shows the related number of cell counts from the geographical map (shown in the previous section) with respect to flux and energy at the selected orbit. Next, a curve fit will be applied to follow the general pattern of the proton spectrum at LEO orbit which is:

$$\phi_o(E) = HE^{-q}; E_1 \leq E \leq E_2 \tag{7.4}$$

where, H and q are the curve fitting coefficients for a selected energy range from E_1 to E_2 and the corresponding flux unit is protons cm^{-2} s^{-1} MeV^{-1}, as shown by [Burrell, 1964] and [Beck and Divita, 1962]. Figure 7.7 demonstrates the curve fitting with respect to simulation results.

   (b) Obtain the shielding distribution for the devices in the spacecraft; for instance, the shielding distribution is 1.7, 3.3 and 5 g/cm^2.

   (c) Determine the proton spectrum at the devices; the corresponding differential energy spectrum formula at different depth in any material is:

$$\phi_X(E^*) = \frac{\phi_o(E)B\mathrm{E}^{*(r-1)}}{(A + B\mathrm{E}^{*r})^{(r-1)/r}} \tag{7.5}$$

knowing that E^* is the proton energy inside the slabs, A, B, r are coefficients defined for a specific material; in our calculations, we have selected the Aluminum. The previous coefficients were derived from empirical curves to determine the proton range in a given material. Figure 7.8a shows the proton energy inside the slabs with respect to its incident energy. The corresponding calculated fluxes inside the slabs are plotted in Figures 7.8c and 7.8d.

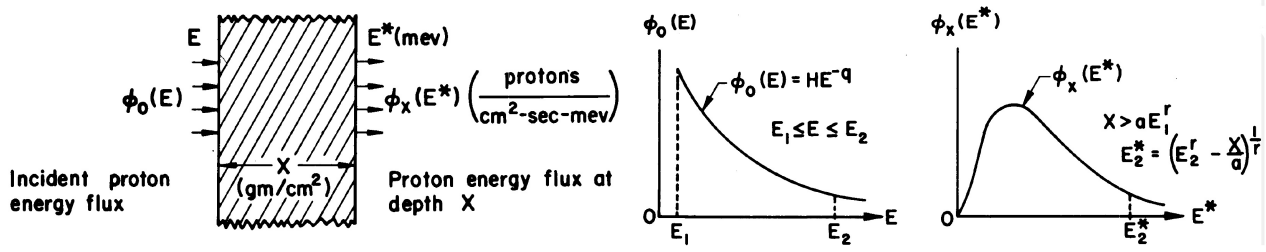

(a) Incident proton flux and penetration depth in a selected material

(b) Proton spectrum shape variation when protons penetrate a shield

Figure 7.4: Figures (a) and (b) demonstrate the effect of the incident proton and its propagation in a typical spacecraft shielding [Burrell, 1964]

3. Combine the upset cross sections with the flux-energy spectrum inside the slabs to find the upset rates; this step was achieved by multiplying the power spectrum in the device (obtained in previous step) by the upset cross sections (obtained in the first step). The resulted SEU rates are found in Figures 7.8e and 7.8f.

7.3 Results

7.3.1 Single Event Upset Rate Calculations

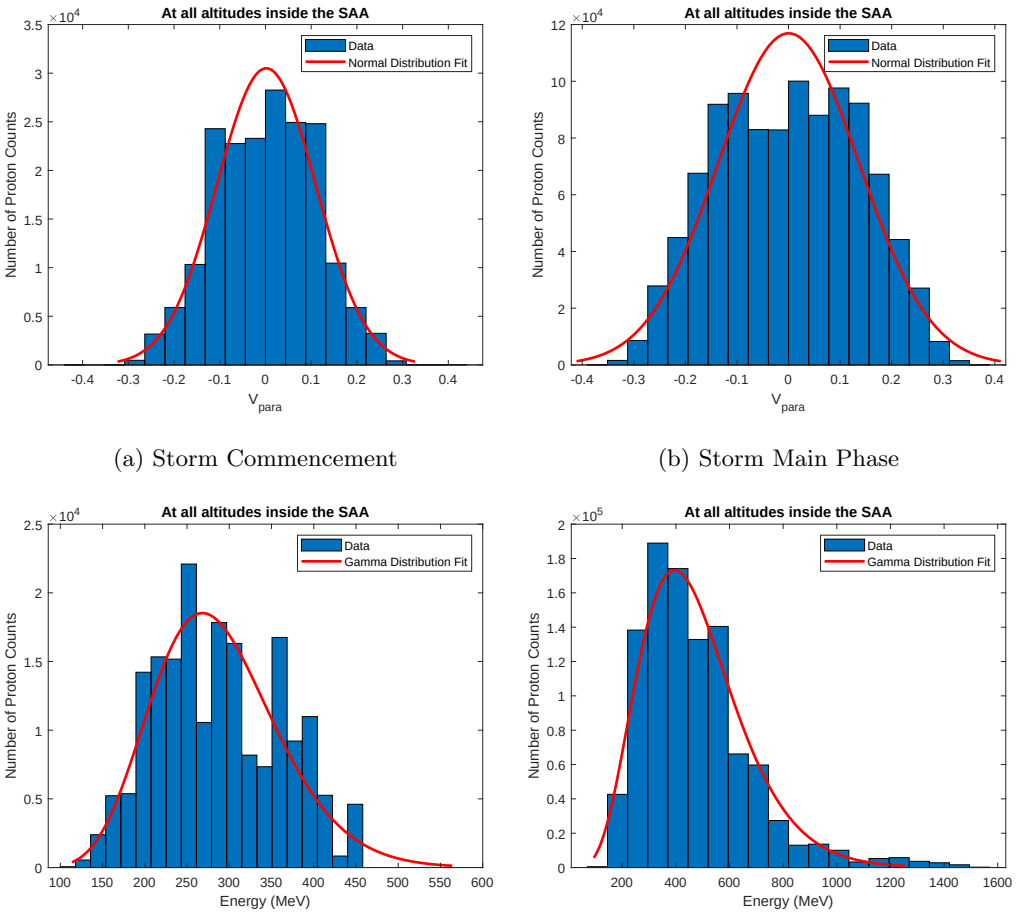

(a) Storm Commencement

(b) Storm Main Phase

(c) Storm Commencement

(d) Storm Main Phase

Figure 7.5: Statistical analysis illustrates the number of proton counts inside the SAA at all altitudes with respect to the corresponding parallel velocity and the kinetic energy at the storm commencement and storm main phases.

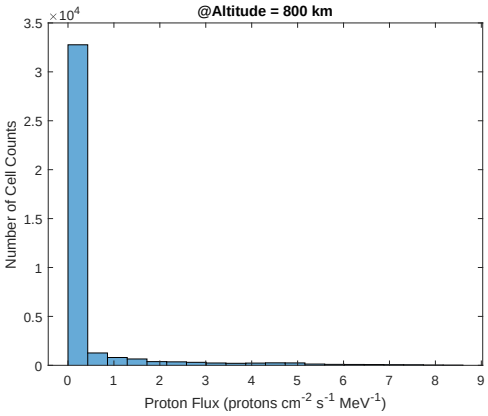

(a) Storm Commencement

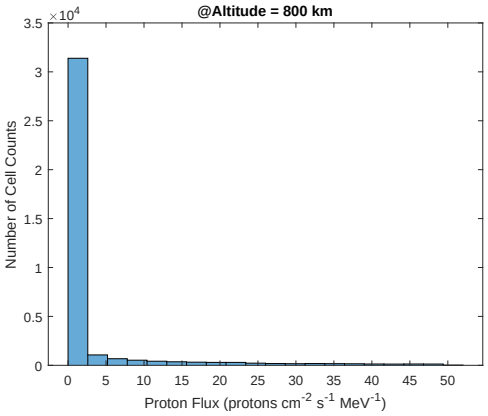

(b) Storm Main Phase

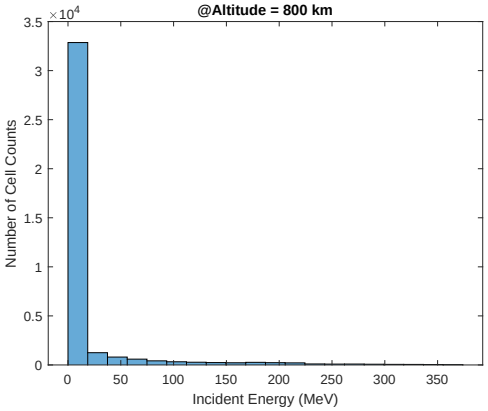

(c) Storm Commencement

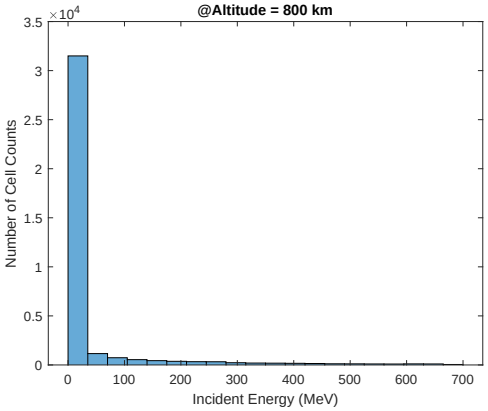

(d) Storm Main Phase

Figure 7.6: Statistical analysis illustrates the number of proton counts inside the SAA at altitude 800 km with respect to particle flux and kinetic energy at the storm commencement and storm main phases.

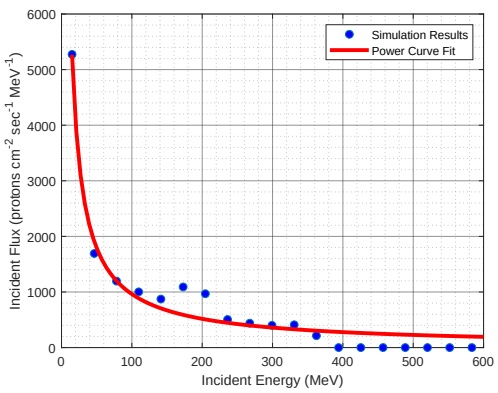

(a) Storm Commencement

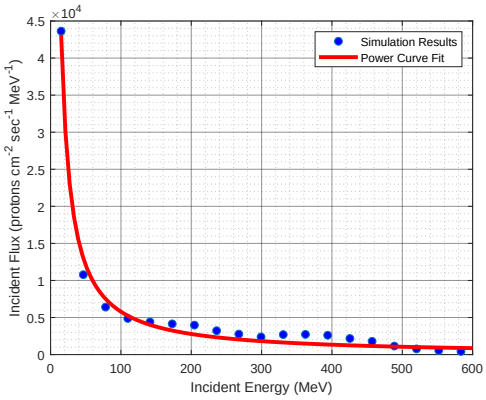

(b) Storm Main Phase

Figure 7.7: Power Spectrum @Altitude = 800 km

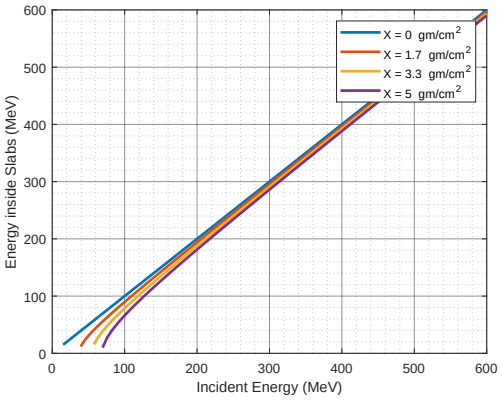

(a) Proton energy inside the slabs versus its incident energy

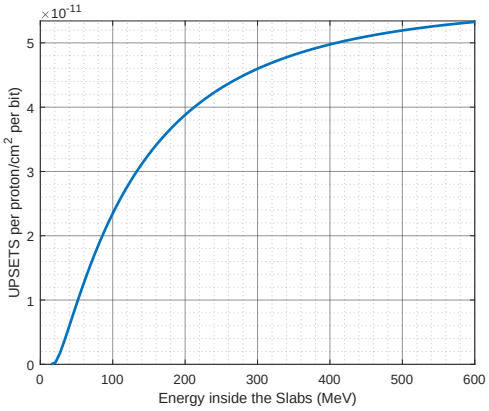

(b) Upset cross-section versus Energy inside the slabs

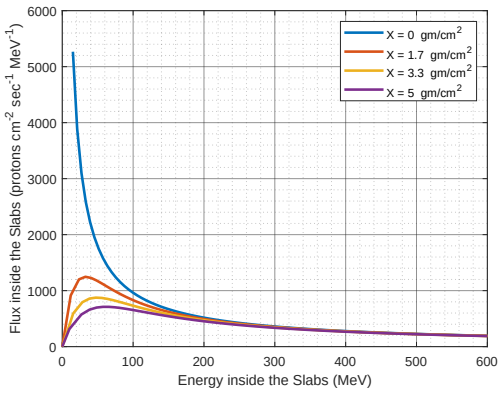

(c) Storm Commencement

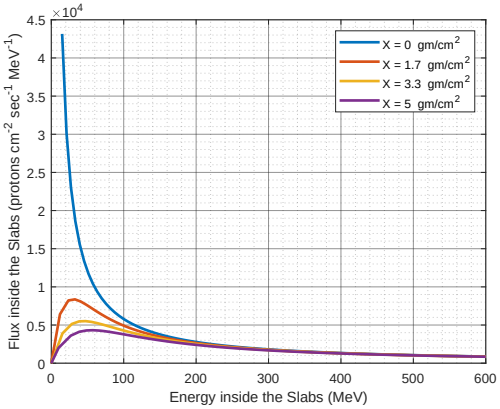

(d) Storm Main Phase

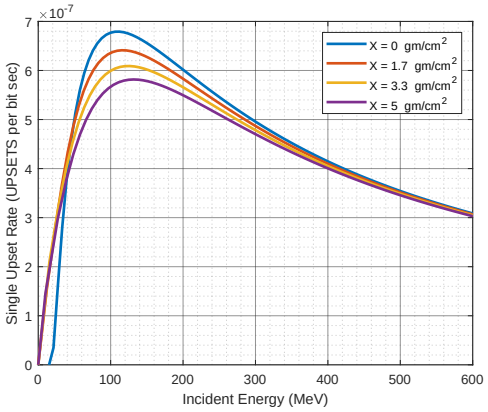

(e) Storm Commencement

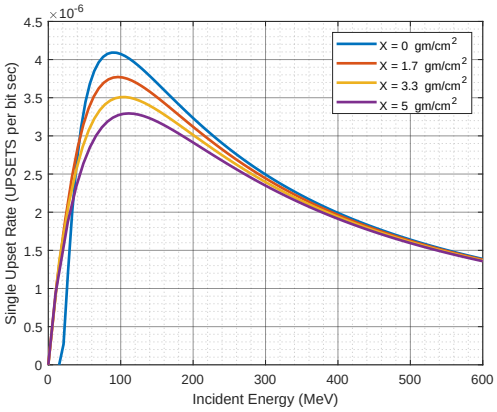

(f) Storm Main Phase

Figure 7.8: SEU calculation steps: (a) Particle Energy inside the slabs versus the incident energy, (b) SEU cross sections, (c,d) power spectrum obtained for the storm commencement and main phases, (e,f) final SEUs estimations.

7.3.2 Radiation Dose Rate Calculations

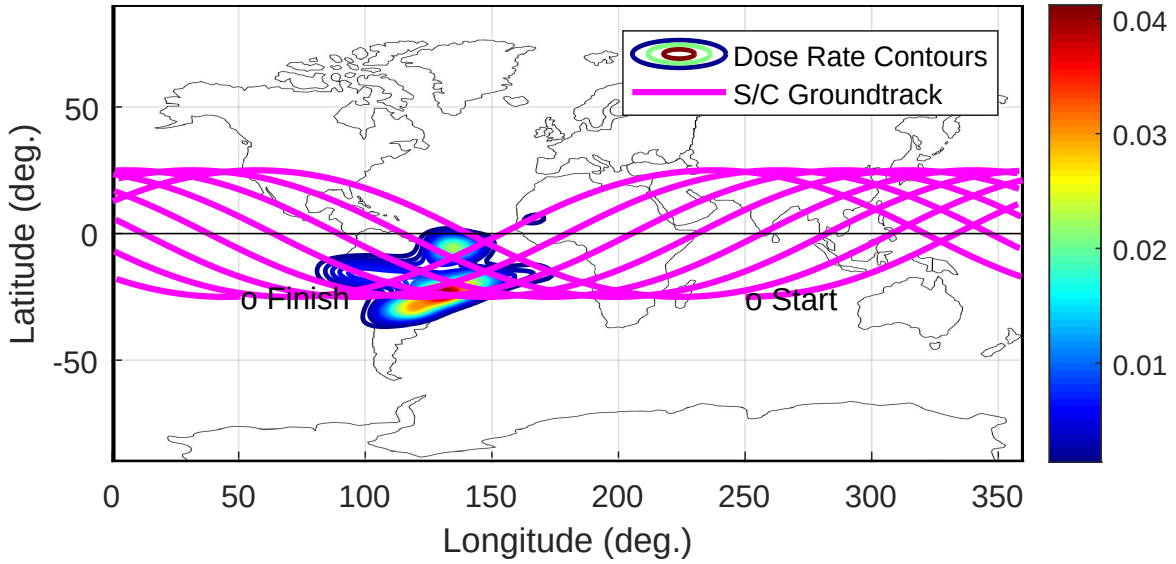

(a) A typical ground map showing the ground track of a low inclined satellite superposed with dose radiation maps

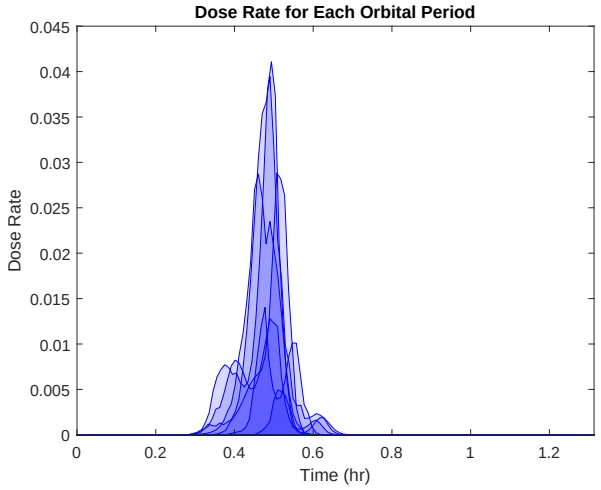

(b) The corresponding radiation doses imposed on the spacecraft during all its passages in the SAA; in this example, the number of orbits (= passage) was 8.

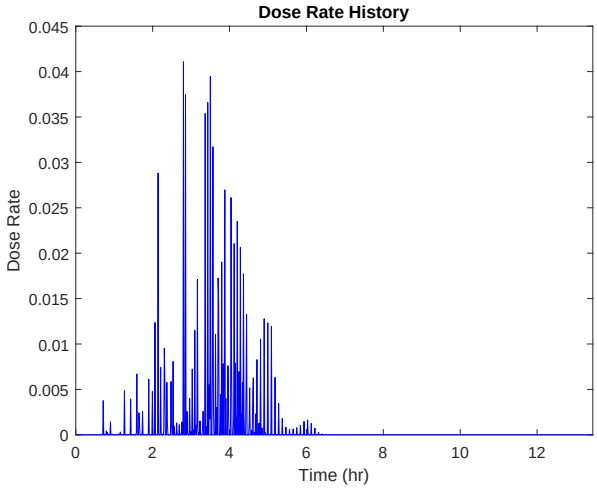

(c) The radiation doses plotted along the overall time slot of the spacecraft operation (during 8 passages inside the SAA).

Figure 7.9: The figure illustrates a typical LEO spacecraft groundtrack with the imposed radiation doses at altitude of 800 km.

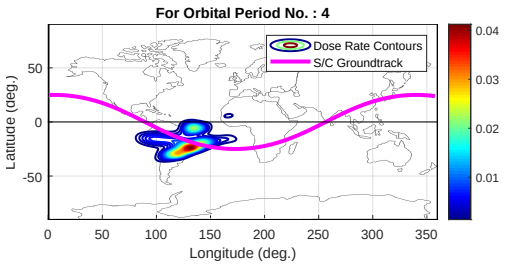

(a) Storm Commencement

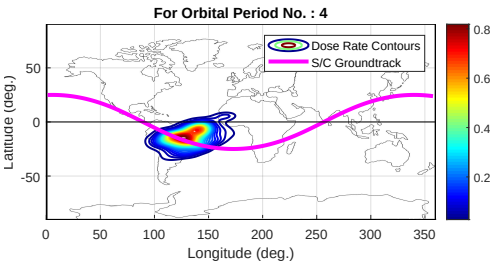

(b) Storm Main Phase

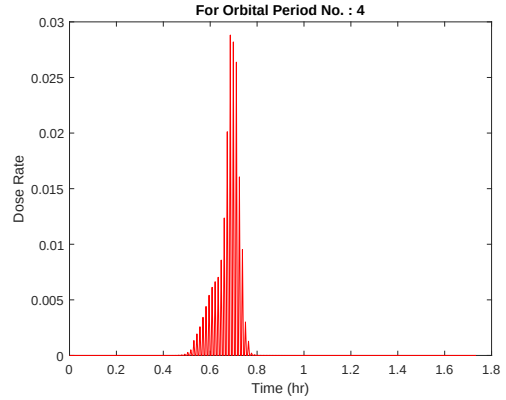

(c) Storm Commencement

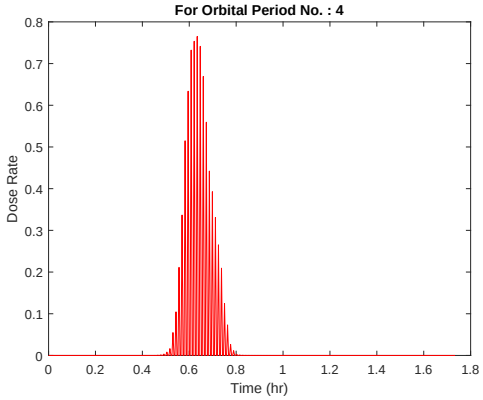

(d) Storm Main Phase

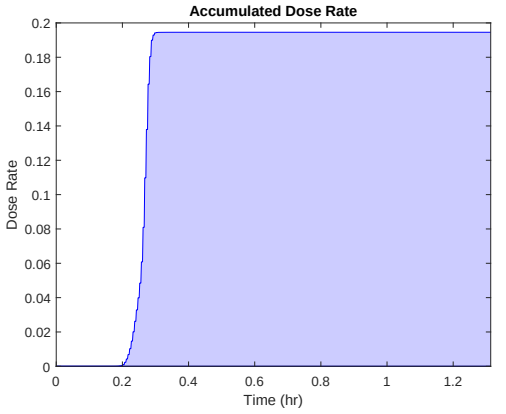

(e) Storm Commencement

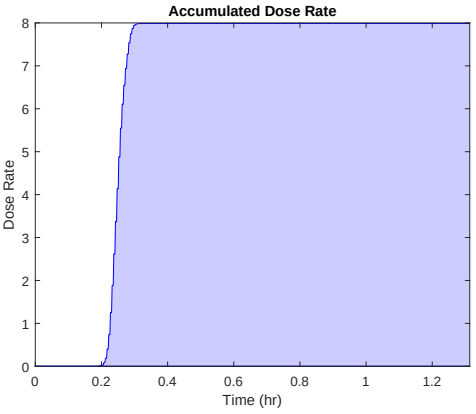

(f) Storm Main Phase

Figure 7.10: The estimation of the radiation doses of a typical LEO spacecraft during a single passage inside the SAA at altitude of 800 km.

7.4 Conclusions

From the previous results of the calculations of the absorbed radiation dose rates and the SEU rates at the given altitude 800 km during a geomagnetic storm, we found that the enhancement of the proton flux in the storm main phase during a short period (about 1 hour), can lead to significant growth in both radiation parameters: the increase ratio of the **SEU rates** (upsets per bit sec) of the storm main phase to the storm commencement was $\approx$ **6** and the corresponding **absorbed radiation dose rates** (rad/s) of the storm main phase to the storm commencement was $\approx$ **40**.

Chapter 8

Summary and Future Directions

8.1 Summary

In this research, we have investigated the SAA magnetic, proton flux responses with respect to space weather conditions, in addition of the estimation of the corresponding radiation environment. For each phase, we summarize the principal conclusions.

8.1.1 SAA Magnetic Response: Long-Term Study

In order to analyze the long-term magnetic variations (11 years) of the South Atlantic Anomaly (SAA), we have implemented the IGRF and T96 models to study the SAA magnetic response, by giving as input, the real solar wind data, from ACE spacecraft from the years 1999 to 2015. Our main conclusions can be summarized as follows:

- The anomaly was strongly correlated with the external magnetic field, even if the region of interest is lying below 1.15 Re ($\approx$ 1000 km). This was due to the variation of the magnetic field lines corresponding to the input solar wind conditions.
- SAA magnetic response was correlated to the variation of the geodipole tilting angle, since the magnetosphere structure and shape, are directly depending on it.
- All the SAA parameters, area, B_{min} and center movement, are more affected by the external magnetic field at the higher altitudes, because, as long as we move toward the Earth center, the internal magnetic field is more dominant and therefore, SAA becomes less dependent on the outer solar wind conditions.
- The solar wind dynamic pressure was more affecting the SAA than IMF when implementing T96 model.

8.1.2 SAA Magnetic Response: Medium-Term Study

The SAA magnetic field response to the space weather variations was studied by implementing the Tsyganenko models T96, T01 and TS05. The SAA variables introduced in this study were the SAA area, the B_{min}, and the movement of its center. The main conclusions are listed as follows:

1. The Dst index and the geodipole tilting angle were the most influencing space weather parameters on the magnetic field variations of the SAA.
2. TS05, T01 and T96 enhanced the seasonal variations, namely, the Dst index, and the solar wind dynamic pressure on the SAA magnetic field response, respectively.
3. The dynamics of the magnetotail were considered to be an important factor affecting the SAA magnetic field response.
4. The magnetic field variations of the SAA were mainly driven by both magnetic poles, in a response to the space weather conditions (the Dst index and the geodipole tilting angle variations).
5. The SAA magnetic field response was also subjected to diurnal effects, where the maximum variations of B_{min}, the area and the latitudinal movement occurred at dayside.

8.1.3 SAA Proton Flux Response: Short-Term Study

The SAA high-energy proton flux response was studied by performing test particle simulations, with respect to changes in the magnetic field configuration, as computed by the Tsyganenko model TS05 and T01 when using several geodipole tilting angles and geomagnetic conditions. The main SAA proton flux variables were the maximum proton flux and the area of the SAA. The conclusions are given as follows:

- **Basic features**: The current test particle model could successfully reveal the SAA basic features, such as: the capture of the particles in the anomaly due to the low magnetic intensity, the altitude effect and the 1D Gaussian fitting of the obtained proton flux.
- **Geodipole tilting angle effect**: The proton flux intensity in the SAA was significantly increased for small geodipole tilting angle cases (during equinox time) and this result was confirmed by observations carried out by [Schaefer et al., 2016].
- **The increase rates**: The low geodipole tilting angle caused increases in the SAA maximum proton flux and in the corresponding area and could reach 52 % and 73 % respectively, in comparison with large tilting angles.
- **Geomagnetic storm effect**: The current numerical model could not reveal the same SAA flux variation pattern obtained from satellite observations made by [Zou et al., 2015] and [Dachev, 2018] at approximately 400 and 800 km where the SAA flux intensity should be decreased during geomagnetic storms.

8.1.4 SAA Proton Flux Study: Geomagnetic Storm Effect

We have developed a test particle simulation code to compute the proton trajectories of the inner trapped radiation belt and to calculate the corresponding proton flux variations inside the SAA during the geomagnetic storm of 15 May 2015. The background magnetic field was carried out by Tsyganenko model TS05 and the associated inductive electric field was calculated from the global time-dependent model output of the geomagnetic field (TS05+IGRF). The conclusions are summarized as follows:

1. The first simulation case when the magnetic field was only implemented without the inclusion of the electric field, the obtained numerical results revealed that the maximum proton flux value was decreased during the storm event and which did agree with observations at 400 and 800 km, however, the corresponding SAA area variations did not agree.
2. The inductive electric field intensity in the SAA was roughly anti-correlated with the *Dst* index variations.
3. The second simulation case when the inductive electric field was included, the inner radiation belt experienced a significant proton loss during the recovery phase. The SAA proton flux intensity was decreased and thus, did agree with observations.
4. Before the proton loss evidence, the SAA proton flux was remarkably enhanced during the main storm phase. At 400 km, the increase of the maximum proton flux value was about 30 % and the corresponding area, 50 %, while at 800 km, 50 % and 20 % respectively.

8.1.5 SAA and Satellite Radiation Effects

The evaluation of the radiation environment of a LEO spacecraft due to the proton flux variations inside the SAA is considered as a direct engineering application for spacecraft shielding design. The proton flux information was obtained from the test particle simulations. The chosen radiation parameters in our study were the absorbed radiation dose rates and the SEU rates for a given altitude. It was found that of during a geomagnetic storm at altitude of 800 km, the enhancement of the proton flux in the storm main phase during a short period (about 1 hour), can lead to significant growth in both radiation parameters: the increase ratio of the **SEU rates** (upsets per bit sec) of the storm main phase to the storm commencement was $\approx$ **6** and the corresponding **absorbed radiation dose rates** (rad/s) was $\approx$ **40**.

8.2 Future Directions

The major purposes of the future research are the improvement of the modeling of the radiation belt dynamics and the study of their effects on the ionosphere, the atmosphere, spacecraft and aircraft. The following subjects consist the more detailed strategy:

1. **Wave-particle interaction**: The wave-particle interaction is considered as an important mechanism while modeling the radiation belts.Beside the inclusion of the inductive electric field, we would like to investigate the effect of (1) the quasi-sinusoidal ULF Pc5 and Pc4 waves, the model proposed e.g. by [Sauvaud et al., 2013] and also (2) the global convection electric e.g. Volland-Stern model [Volland, 1973] and [Stern, 1975]. It is worthy to investigate from the simulations the degree of influence of each electric model on the inner radiation belt dynamics.

2. **Fourrier transformation to calculate the induced electric field**: An alternative method to calculate the inductive electric field is by performing direct Fourrier transformation to the Faraday equation. The method used in the research was applied by performing integration following the Biot-Savart law over all the simulation domain, which makes it computationally very expensive, but has the advantage of being a straightforward calculation. We believe that Fourrier transformation could be faster than the Biot-Savart method.

3. **Inner Radiation Belt simulations, its corresponding effect in the SAA and its related radiation environment variations**: Estimating the radiation environment of a mission. (1) Assessing the Single Event Effects (SEE) probability: Since we estimated the SAA proton flux variations, we aim to calculate the associated probability of the occurrence of the Single Event Effects (SEE), corresponding to geomagnetic storms. The SEE is caused by a single, energetic particle, and can take on many forms. For example, Single Event Upsets (SEUs) are soft errors, and non-destructive. They normally appear as transient pulses in logic or support circuitry, or as bitflips in memory cells or registers. Several types of hard errors, potentially destructive, can appear: Single Event Latchup (SEL) results in a high operating current, above device specifications, and must be cleared by a power reset. The SEE probability can be calculated essentially from the proton flux and energy distribution information obtained from the test particle simulations. (2) Calculating the related radiation dose rate: The radiation dose rate is an important radiation parameter that is calculated for a particular mission at a specific orbit. In order to calculate this quantity, we need detailed information about the proton flux and the energy distributions of the protons at the selected altitude, which are also obtained from the test particle simulation results.

   Designing a more effective shielding of the satellite body and solar arrays: In order to mitigate the radiation effects, a better shield for the spacecraft can be conceived. The most common shielding material is the Aluminum and spacecraft engineers can increase the thickness to increase the protection. However, it was recently found that the Single Event Effect cannot be directly reduced by the conventional way. There are several alternative approaches such as changing the circuit designs or the material itself. Adding that, the solar cells are significantly affected by the SEE and its performance is a matter of great importance since the degraded generated power can affect the whole spacecraft mission lifetime. It is clear then, that applying the previous research outputs in developing space environment sensors for LEO spacecraft missions and astronaut suits is very important.

   Real-data forecasting of the Inner Proton and Electron Radiation Belts and their precipitations in the South Atlantic Anomaly: (1) It is worthy to monitor and thus, forecast the real situation of the inner radiation belt model driven regularly from the real space weather data, and comparing the obtained simulated results with spacecraft measurements. (2) Since the test particle code is already built, it can work for any particle type. The electron flux map beside the protons are of similar interest since the electron flux can also affect the spacecraft by increasing the internal charging and thus, can generate short circuits or arcs inside the vital satellite components. (3) Solar Proton Event (SPE) simulations: Additionally, as a matter of fact, the Solar Proton Event (SPE) could also be simulated and hence forecasted in the near-Earth environment. The solar proton event (SPE), or prompt proton event, occurs when particles (mostly energetic protons) emitted by solar flares or by coronal mass ejection shocks. Such particle can penetrate into geomagnetic field and again can cause a significant radiation hazard to spacecraft and astronauts.

4. **Outer Radiation Belt simulations and corresponding effects on satellites:** Coupling my test particle simulation code with REProduce Plasma Universe (REPPU) MHD code: Beside my study of the inner radiation belt, I would like to study the outer radiation belt using the same test particle simulation code, where the background magnetic field will be provided by REPPU MHD code and to compare output results with observations.

   Dipolarization Event in the Earth's magnetotail: By using the same test particle simulation code, we can also study the dipolarization events by computing the electron trajectories and their energizations in the magnetotail region and comparing the results with observations. The Dipolarization Fronts (DF)

are considered like narrow boundary layers consisting of electrons and ions with large spatial variations in velocity, temperature, and pressure anisotropy. The DF are generated by the self-consistent electric field resulting from global compression of the magnetic field at this region. Dipolarization phenomena are generally connected to particle acceleration, which makes them an important contributing factor to the near-Earth space weather.

5. **Further development of available magnetosphere, ionosphere, and atmosphere models, by including the SAA:** Including the realistic Earth's magnetic field model in REPPU MHD model: After a fruitful discussion with Professor Takashi Tanaka, the developer of the code, the inclusion of the non-dipole magnetic fields requires considerable modification of the code. I was advised that it is necessary to extend the simulation between 3*Re and 1*Re, and that this region cannot necessarily be calculated by the MHD alone, since the perpendicular field components are more dominant than the parallel field components for the particle motion, so the particle model or CGL approximation must be coupled with the MHD. Since I have an experience on MHD background during my Master research (by building my own 1D and 2D MHD codes), I would like also to extend and deepen my expertise in contributing to the REPPU code.

   Including a realistic Earth's magnetic field in the Whole Atmosphere-Ionosphere Coupled Model (GAIA): The current model is using a dipole field model. By including a more realistic magnetic field, we can investigate the effect of the South Atlantic Anomaly on the atmosphere-ionosphere coupling. Simulated results could also be compared with ionosonde data, operated by many institutes in Brazil.

   Improving WASAVIES model (air shower simulation): to observe if the SAA can affect the atmospheric species due to the precipitation of the high-energy protons, in quiet and in geomagnetic storm events; as mentioned by the code developers in their papers (Sato et. al, 2018), that WASAVIES model could be improved by selecting a more recent Tsyganenko model, and also, as explained in (Miyake, 2017), the Runge-Kutta 4th order scheme is implemented to calculate the particle position, from which it could be used as well, Boris-Buneman scheme, to minimize the numerical error. Since my academic background is aerospace engineering field, I am similarly interested in contributing to this project by improving WASAVIES model.

6. **Expected results and impacts:**

   The expected results are helpful and applicable in the improvement of the design of the satellite shielding body. More tests will be needed to make sure that spacecraft shielding techniques are effective in harmful environments. At least, the obtained numerical results can encourage the spacecraft engineers to re-evaluate again the technology performance and to better understand the dynamic space weather environment where the spacecraft and human missions are operating.

   The expected results can give a clearer image of the South Atlantic Anomaly (SAA) from the theoretical point of view. The simulations carried out have put insights on the particle dynamics inside the SAA. This subject is also essential for the researchers in general and for the theoreticians and plasma physicists in particular; the understanding of the physical processes inside this anomaly can reveal more clues in understanding the global picture of the space weather response in the near-Earth region with respect to the external perturbations occurring inside the magnetosphere due to flares and coronal mass ejections emitted from the Sun's surface.

   Through better improving our understanding toward the SAA and the trapped radiation belts in general, by both scientist and engineer groups, we believe that the society can widely benefit from the expected outcomes: better spacecraft design and performance, better services offered to research institutes and companies and citizens. For example, (1) several spacecrafts, when moving inside the SAA, cannot continue their regular measurements and sometimes they shut off their instruments, and so, important data could be missed. Finding a solution to complete the whole set of measurement can be of great value for the scientific community; (2) the development of the nowcast and forecast models of human exposure to Solar Energetic Protons at aircraft height (WASAVIES Program), to alert the airline companies to change the flight route or the flight cruising altitudes; (3) better designing the astronauts suits as well as the interior and exterior parts of the International Space Station (ISS), to prevent the external highly radiation environment, during quiet times and also during severe space weather events.

Bibliography

[Geo, 2010] (2010). Sun-Earth System Science (Original Text in Japanese Language). Geomagnetism and Geoscience Union Meeting School Education Working Group, Kyoto University.

[A. Tarduno et al., 2015] A. Tarduno, J., K. Watkeys, M., N. Huffman, T., D. Cottrell, R., G. Blackman, E., Wendt, A., A. Scribner, C., and L. Wagner, C. (2015). Antiquity of the South Atlantic Anomaly and evidence for top-down control on the geodynamo. Nature Communications, 6:7865.

[Antonova et al., 2003] Antonova, A., Gubar', Y., and Kropotkin, A. (2003). Effects in the radiation belts caused by the second adiabatic invariant violation in the presence of dayside off-equatorial magnetic field minima. Advances in Space Research, 31(5):1223–1228.

[Aubert, 2015] Aubert, J. (2015). Geomagnetic forecasts driven by thermal wind dynamics in the Earth's core. Geophysical Journal International, 203:1738–1751.

[Badavi, 2011] Badavi, F. F. (2011). A low earth orbit dynamic model for the proton anisotropy validation. Nuclear Inst. and Methods in Physics Research B, 269(21):2614–2622.

[Badavi, 2014] Badavi, F. F. (2014). Validation of the new trapped environment AE9 / AP9 / SPM at low Earth orbit. Advances in Space Research, 54(6):917–928.

[Badhwar, 1997] Badhwar, G. D. (1997). Drift rate of the South Atlantic Anomaly. J. Geophys. Res., 102(A2):2343–2349.

[Barratt and Pool, 2008] Barratt, M. R. and Pool, S. L. (2008). Principles of Clinical Medicine for Space Flight. Springer.

[Barth, 1997] Barth, J. (1997). Radiation Environments. In IEEE NSREC Short Course, Session I.

[Beck and Divita, 1962] Beck, A. J. and Divita, E. L. (1962). Evaluation of Space Radiation Doses Received Within a Typical Spacecraft. American Rocket Society Journal, 32(11):1668–1676.

[Bendel and Petersen, 1983] Bendel, W. L. and Petersen, E. L. (1983). Proton upsets in orbit. IEEE Transactions on Nuclear Science, 30(6):4481–4485.

[Bertotti and Farinella, 1990] Bertotti, B. and Farinella, P. (1990). Physics of the Earth and the Solar System. Kluwer Academic Publishers.

[Binder, 1988] Binder, D. (1988). Analytic SEU Rate Calculation compared to Space Data. IEEE Transactions on Nuclear Science, 35(6):1570–1572.

[Bone, 2007] Bone, N. (2007). Aurora: Observing and Recording Nature's Spectacular Light Show. Springer.

[Boris, 1970] Boris, J. (1970). Relativistic plasma simulation-optimization of a hybrid code. Proceeding of Fourth Conference on Numerical Simulations of Plasmas.

[Brizard and Chan, 1999] Brizard, A. J. and Chan, A. A. (1999). Nonlinear relativistic gyrokinetic Vlasov-Maxwell equations. Physics of Plasmas, 6(12):4548–4558.

[Brown et al., 2018] Brown, M., Korteb, M., Holme, R., Wardinski, I., and Gunnarson, S. (2018). Earth's magnetic field is probably not reversing. Proceedings of the National Academy of Sciences of the United States of America, 115(20):5111–5116.

[Buhler et al., 1997] Buhler, P., Zehnder, A., Desorger, L., Hajdas, W., Daly, E., and Adams, L. (1997). Measurements of the Radiation Belts from MIR and STRV 1994-1997. In on the High Energy Radiation Background in Space, C., editor, Conference on the High Energy Radiation Background in Space. Workshop Record, Snowmass, pages 108–113. USA.

[Buneman, 1967] Buneman, O. (1967). Time-reversible difference procedures. Journal of Computational Physics, 1(4):517–535.

[Burrell, 1964] Burrell, M. O. (1964). The calculation of proton penetration and dose rates. NASA Technical Memorandum, NASA TM X-(N64-30510):78.

[Campana et al., 2014] Campana, R., Orlandini, M., Del Monte, E., Feroci, M., and Frontera, F. (2014). The radiation environment in a low earth orbit: the case of BeppoSAX. Exp. Astron., 37:599–613.

[Campbell et al., 1992] Campbell, A., McDonald, P., and Ray, K. (1992). Single event upset rates in space. IEEE Transactions on Nuclear Science, 39(6):1828–1835.

[Casadio and Arino, 2011] Casadio, S. and Arino, O. (2011). Monitoring the South Atlantic Anomaly using ATSR instrument series. Adv. Space Res., 48(6):1056–1066.

[Chaisson, 1998] Chaisson, E. (1998). The Hubble Wars: Astrophysics Meets Astropolitics in the Two-billion-dollar Struggle Over the Hubble Space Telescope. Harvard University Press.

[Chulliat et al., 2015] Chulliat, A., Macmillan, S., Alken, P., Beggan, C., Nair, M., Hamilton, B., Woods, A., Ridley, V., Maus, S., and Thomson, A. (2015). The US/UK World Magnetic Model for 2015-2020: Technical Report. Technical report, National Geophysical Data Center, NOAA.

[Clément, 2007] Clément, G. (2007). Fundamentals of Space Medicine. Springer Science & Business Media.

[Cnossen and Matzka, 2016] Cnossen, I. and Matzka, J. (2016). Changes in solar quiet magnetic variations since the Maunder Minimum: A comparison of historical observations and model simulations. Journal of Geophysical Research : Space Physics, pages 520–535.

[Cnossen and Richmond, 2012] Cnossen, I. and Richmond, A. D. (2012). How changes in the tilt angle of the geomagnetic dipole affect the coupled magnetosphere-ionosphere-thermosphere system. Journal of Geophysical Research, 117.

[Cnossen et al., 2012] Cnossen, I., Wiltberger, M., and Ouellette, J. E. (2012). The effects of seasonal and diurnal variations in the earth's magnetic dipole orientation on solar wind–magnetosphere-ionosphere coupling. Journal of Geophysical Research, 117.

[Cottaar and Lekic, 2016] Cottaar, S. and Lekic, V. (2016). Morphology of seismically slow lower-mantle structures. Geophysical Journal International, 207:1122–1136.

[Curtis, 2019] Curtis, H. D. (2019). Orbital Mechanics for Engineering Students. Butterworth-Heinemann.

[Da Silva and Rocco, 2017] Da Silva, M. R. and Rocco, E. M. (2017). Analysis of the passage of a spacecraft between the Van Allen belts considering a low and high solar activity. Journal of Physics: Conference Series, 911(1).

[Dachev et al., 2002] Dachev, T., Tomov, B., Matviichuk, Y., Dimitrov, P., Lemaire, J., Gregoire, G., Cyamukungu, M., Schmitz, H., Fujitaka, K., Uchihori, Y., Kitamura, H., Reitz, G., Beaujean, R., Petrov, V., Shurshakov, V., Benghin, V., and Spurny, F. (2002). Calibration results obtained with liulin-4 type dosimeters. Advances in Space Research, 4:917–925.

[Dachev, 2018] Dachev, T. P. (2018). South-Atlantic Anomaly magnetic storms effects as observed outside the International Space Station in 2008–2016. Journal of Atmospheric and Solar-Terrestrial Physics, 179:251–260.

[de Pater and Lissauer, 2010] de Pater, I. and Lissauer, J. J. (2010). Planetary Sciences. Cambridge University Press.

[Domingos et al., 2017] Domingos, J., Jault, D., Alexandra Pais, M., and Mandea, M. (2017). The South Atlantic Anomaly throughout the solar cycle. Earth and Planetary Science Letters, 473:154–163.

[Dragt, 1971] Dragt, A. J. (1971). Solar cycle modulation of the radiation belt proton flux. Journal of Geophysical Research, 76(10):2313–2344.

[Easly, 2007] Easly, S. M. (2007). Anisotropy in the South Atlantic Anomaly. Master's thesis, Department of Engineering Physics, Graduate School of Engineering and Management, Air Force Institute of Technology, Ohio.

[Elkington et al., 2002] Elkington, S. R., Hudson, M. K., Wiltberger, M. J., and Lyon, J. G. (2002). MHD/particle simulations of radiation belt dynamics. Journal of Atmospheric and Solar-Terrestrial Physics, 64(5-6):607–615.

[Engel et al., 2015] Engel, M. A., Kress, B. T., Hudson, M. K., and Selesnick, R. S. (2015). Simulations of inner radiation belt proton loss during geomagnetic storms. Journal of Geophysical Research: Space Physics, 120:9323–9333.

[Federico et al., 2015] Federico, C. A., Gonçalez, O. L., Caldas, L. V. E., Pazianotto, M. T., Dyer, C., Caresana, M., and Hands, A. (2015). Radiation measurements onboard aircraft in the South Atlantic region. Radiation Measurements, 82:14–20.

[Fennelly et al., 2015] Fennelly, J. A., Ober, D. M., Wilson, G. R., Paul, T., Brien, O., and Huston, S. L. (2015). South Atlantic Anomaly and CubeSat Design Considerations. Solar Physics and Space Weather Instrumentation VI: Conference 9604, The International Society for Optics and Photonics, pages 1–15.

[Feshchenko et al., 2000] Feshchenko, E. Y., Maltsev, Y. P., and Ostapenko, A. A. (2000). Dependence of the magnetospheric magnetic field on the storm activity. In SP-443, A. W. E., editor, Congress Center of the Arctic and Antarctic Research Institute, page 431. ESA, ESA.

[Finlay, 2011] Finlay, C. (2011). Observational geomagnetism. Technical report, ETH, Zurich.

[Finlay et al., 2016] Finlay, C. C., Olsen, N., Kotsiaros, S., Gillet, N., and Tøffner-Clausen, L. (2016). Recent geomagnetic secular variation from Swarm and ground observatories as estimated in the CHAOS-6 geomagnetic field model Swarm Science Results after two years in Space 1. Geomagnetism. Earth, Planets and Space, 68(1):1–18.

[Ganushkina et al., 2018] Ganushkina, N. Y., Liemohn, M. W., and Dubyagin, S. (2018). Current Systems in the Earth's Magnetosphere. Reviews of Geophysics, 56(2):309–332.

[Ganushkina et al., 2005] Ganushkina, N. Y., Pulkkinen, T. I., Kubyshkina, M. V., Sergeev, V. A., Lvova, E. A., Yahnina, T. A., Yahnin, A. G., and Fritz, T. (2005). Proton isotropy boundaries as measured on mid- and low-altitude satellites. Annales Geophysicae, 23:1839–1847.

[Gemelos, 2011] Gemelos, E. S. (2011). Global Assessment of Precipitation of Radiation Belt Electrons by Electromagnetic Waves from Lightning. PhD thesis, Stanford University.

[Girgis and Hada, 2018] Girgis, K. M. and Hada, T., editors (2018). Long-Term Variations of the Solar Wind Effects on South Atlantic Anomaly (SAA) using Tsyganenko Model, volume 4. Kyushu University, International Exchange and Innovation Conference on Engineering & Sciences (IEICES).

[Girgis et al., 2020] Girgis, K. M., Hada, T., and Matsukiyo, S. (2020). Solar wind parameter and seasonal variation effects on the South Atlantic Anomaly using Tsyganenko Models. Earth Planets Space, 72(100).

[Gradwell and Rainford, 2016] Gradwell, D. and Rainford, D. J. (2016). Ernsting's Aviation and Space Medicine 5E. CRC Press.

[Grigoryan et al., 2008] Grigoryan, O. R., Romashova, V. V., and Petrov, A. N. (2008). SAA drift: Experimental results. Adv. Space Res., 41(1):76–80.

[Hada and Matsukiyo, 2017] Hada, T. and Matsukiyo, S. (2017). Lecture notes: Numerical methods in space plasma physics. Technical report, Department of Earth System Science and Technology (ESST), Interdisciplinary Graduate School of Engineering Sciences (IGSES), Kyushu University.

[Heckman and Nakano, 1963] Heckman, H. H. and Nakano, G. H. (1963). East-west asymmetry in the flux of mirroring geomagnetically trapped protons. Journal of Geophysical Research, 68(8):2117–2120.

[Heirtzler et al., 2002] Heirtzler, J. R., Allen, J. H., and Wilkinson, D. C. (2002). Ever-present South Atlantic Anomaly damages spacecraft. EOS, Transactions, American Geophysical Union, 83(15):165–172.

[Hudson et al., 1997] Hudson, M. K., Elkington, S. R., Lyon, J. G., Marchenko, V. A., Roth, I., Temerin, M., Blake, J. B., Gussenhov, M. S., and Wygant, J. R. (1997). Simulations of radiation belt formation during storm sudden commencements. Journal of Geophysical Research, 102(A7):14087–14102.

[Huston et al., 1996] Huston, S., Kuck, G., and Pfitzer, K. (1996). Low-altitude trapped radiation model using TIROS/NOAA data. Radiation Belts: Models and Standards, 97:119–122.

[Huston and Pfitzer, 1998] Huston, S. and Pfitzer, K. (1998). Space environment effects: Low-altitude trapped radiation model. Technical Report, NASA/CR-1998-208593.

[Jones et al., 2017] Jones, A. D., Kanekal, S. G., Baker, D. N., Klecker, B., Looper, M. D., Mazur, J. E., and Schiller, Q. (2017). SAMPEX observations of the South Atlantic anomaly secular drift during solar cycles 22–24. Space Weather, 15:44–52.

[Kamide et al., 1999] Kamide, Y., Kokubun, S., Bargatze, L. F., and Frank, L. A. (1999). The size of the polar cap as an indicator of substorm energy. Physical Chemical Earth, 24(1-3):119–127.

[Kress et al., 2015] Kress, B. T., Hudson, M. K., Selesnick, R. S., Mertens, C. J., and Engel, M. (2015). Modeling geomagnetic cutoffs for space weather applications. Journal of Geophysical Research: Space Physics, 120:5694–5702.

[Kronberg et al., 2015] Kronberg, E. A., Grigorenko, E. E., Haaland, S. E., Daly, P., Delcourt, D. C., Luo, H., Kistler, L. M., and Dandouras, I. (2015). Distribution of energetic Oxygen and Hydrogen in the near-Earth plasma sheet. Journal of Geophysical Research: Space Physics, 120:3415–3431.

[Kubyshkina et al., 2009] Kubyshkina, M., Sergeev, V., Tsyganenko, N., Angelopoulos, V., Runov, A., Singer, H., Glassmeier, K. H., Auster, H. U., and Baumjohann, W. (2009). Toward adapted time-dependent magnetospheric models: A simple approach based on tuning the standard model. Journal of Geophysical Research, 114(A00C21).

[Limousin et al., 2015] Limousin, O., Renaud, D., Horeau, B., Dubos, S., Laurent, P., Lebrun, F., Chipaux, R., Polo, C. B., Marcinkowski, R., Kawaharada, M., Watanabe, S., Ohta, M., Sato, G., and Takahashi, T. (2015). Nuclear Instruments and Methods in Physics Research A ASTRO-H CdTe detectors proton irradiation at PIF. Nuclear Inst. and Methods in Physics Research, A, 787:328–335.

[Logsdon, 1998] Logsdon, T. (1998). Orbital Mechanics: Theory and Applications. John Wiley & Sons.

[Looper and Blake, 2005] Looper, M. D. and Blake, J. B. (2005). Response of the inner radiation belt to the violent sun-earthconnection events of october–november 2003. GEOPHYSICAL RESEARCH LETTERS, 32.

[Lorentzen et al., 2002] Lorentzen, K. R., Mazur, J. E., Looper, M. D., Fennell, J. F., and Blake, J. B. (2002). Multisatellite observations of mev ion injections during storms. JOURNAL OF GEOPHYSICAL RESEARCH, 107(A9).

[Lowman, 2002] Lowman, P. D. (2002). Exploring Space, Exploring Earth: New Understanding of the Earth from Space Research. Cambridge University Press.

[Lühr et al., 2017] Lühr, H., Xiong, C., Olsen, N., and Le, G. (2017). Near-Earth Magnetic Field Effects of Large-Scale Magnetospheric Currents. Space Science Reviews, 206(1-4):521–545.

[Malin and Isikara, 1976] Malin, S. and Isikara, A. (1976). Annual variation of the geomagnetic field. Geophys. J. R. Astron. Soc., 47:445–457.

[Matzner, 2001] Matzner, R. A. (2001). Dictionary of Geophysics, Astrophysics, and Astronomy. CRC Press.

[Maurer et al., 2008] Maurer, R. H., Fraeman, M. E., Martin, M. N., and Roth, D. R. (2008). Harsh environments: Space radiation environment, effects, and mitigation. Johns Hopkins APL Technical Digest (Applied Physics Laboratory), 28(1):17–29.

[Meng, 1982] Meng, C.-I. (1982). Latitudinal variation of the polar cusp during a geomagnetic storm. Geophysical Research Letters, 9(1):60–63.

[Meng, 1984] Meng, C.-I. (1984). Dynamic variation of the auroral oval during intense magnetic storms. Journal of Geophysical Research, 89(A1):227–235.

[Messenger and Ash, 2013] Messenger, G. and Ash, M. (2013). Single Event Phenomena. Springer Science & Business Media.

[Nakano and Heckman, 1968] Nakano, G. and Heckman, H. (1968). Evidence for solar-cycle changes in the inner-belt protons. Phys. Rev. Lett., 20(15):806–809.

[Narici et al., 2015] Narici, L., Casolino, M., Fino, L. D., Larosa, M., Picozza, P., and Zaconte, V. (2015). Radiation survey in the International Space Station. Journal of Space Weather and Space Climate, 37:1–14.

[NASA, 1967] NASA (1967). GEMINI Summary Conference. Technical report, Manned Spacecraft Center, Scientific and Technical Information Division, Office of Technology Utilization, NASA.

[Norberg, 2013] Norberg, C. (2013). Human Spaceflight and Exploration. Springer Science & Business Media.

[Northrop, 1963a] Northrop, T. G. (1963a). Adiabatic charged-particle motion. Reviews of Geophysics, 1.

[Northrop, 1963b] Northrop, T. G. (1963b). The Adiabatic Motion of Charged Particles. Interscience Publishers, John Wiley and Sons, New York.

[Okpala and Ogbonna, 2018] Okpala, K. C. and Ogbonna, C. E. (2018). On the mid-latitude ionospheric storm association with intense geomagnetic storms. Advances in Space Research, 61(7):1858–1872.

[Olsen et al., 2006] Olsen, N., Lühr, H., Sabaka, T. J., Mandea, M., Rother, M., Tøffner-Clausen, L., and Choi, S. (2006). CHAOS - A model of the Earth's magnetic field derived from CHAMP, Ørsted, and SAC-C magnetic satellite data. Geophysical Journal International, 166(1):67–75.

[Öztürk, 2012] Öztürk, M. K. (2012). Trajectories of charged particles trapped in Earth's magnetic field. American Journal of Physics, 80(5):420–428.

[Pavón-Carrasco and De Santis, 2016] Pavón-Carrasco, F. J. and De Santis, A. (2016). The South Atlantic Anomaly: The Key for a Possible Geomagnetic Reversal. Frontiers in Earth Science, 4:40.

[Petersen, 2011] Petersen, E. (2011). Single Event Effects in Aerospace. John Wiley & Sons.

[Petersen et al., 1982] Petersen, F. L., Shapiro, P., Adams, J. H., and Burke, E. A. (1982). Calculation of cosmic-ray induced soft upsets and scaling in VLSI devices. IEEE Transactions on Nuclear Science, 29(6):2055–2063.

[Pierrard et al., 2014] Pierrard, V., Lopez Rosson, G., Borremans, K., Lemaire, J., Maes, J., Bonnewijn, S., Van Ransbeeck, E., Neefs, E., Cyamukungu, M., Benck, S., Bonnet, L., Borisov, S., Cabrera, J., Grégoire, G., Semaille, C., Creve, G., De Saedeleer, J., Desoete, B., Preud'homme, F., Anciaux, M., Helderweirt, A., Litefti, K., Brun, N., Pauwels, D., Quevrin, C., Moreau, D., Punkkinen, R., Valtonen, E., Hajdas, W., and Nieminen, P. (2014). The energetic particle telescope: First results. Space Sci. Rev., 184:87–106.

[Pisacane, 2014] Pisacane, V. (2014). Space radiation and its effects on space systems and astronauts. Applied Technology Institute (ATI) Courses.

[Pisacane, 2005] Pisacane, V. L. (2005). Fundamentals of Space Systems. Oxford University Press.

[Press et al., 1997] Press, W. H., Teukolsky, S. A., Vetterling, W. T., and Flannery, B. P. (1997). Numerical Recipes in Fortran 77: The Art of Scientific Computing. Cambridge University Press.

[Qin et al., 2014] Qin, M., Zhang, X., Ni, B., Song, H., Zou, H., , and Sun, Y. (2014). Solar cycle variations of trapped proton flux in the inner radiation belt. Journal of Geophysical Research: Space Physics.

[Rauschenbakh et al., 2006] Rauschenbakh, V., Ovchinnikov, M. Y., and McKenna-Lawlor, S. M. (2006). Essential Spaceflight Dynamics and Magnetospherics. Springer Science & Business Media.

[Ridpath, 2012] Ridpath, I. (2012). A Dictionary of Astronomy. OUP Oxford.

[Saito et al., 2010] Saito, S., Miyoshi, Y., and Seki, K. (2010). A split in the outer radiation belt by magnetopause shadowing: Test particle simulations. Journal of Geophysical Research, 115.

[Sauvaud et al., 2013] Sauvaud, J. A., Walt, M., Delcourt, D., Benoist, C., Penou, E., Chen, Y., and Russell, C. T. (2013). Inner radiation belt particle acceleration and energy structuring by drift resonance with ULF waves during geomagnetic storms. Journal of Geophysical Research: Space Physics, 118(4):1723–1736.

[Schaefer et al., 2016] Schaefer, R. K., Paxton, L. J., Selby, C., Ogorzalek, B., Romeo, G., Wolven, B., and et al. (2016). Observation and modeling of the south atlantic anomaly in low earth orbit using photometric instrument data. Space Weather-the International Journal of Research and Applications, 14(5):330–342.

[Scherer et al., 2005] Scherer, K., Fichtner, H., and Bernd Heber, U. M. (2005). Space Weather: The Physics Behind a Slogan. Springer Science & Business Media.

[Selesnick et al., 2010] Selesnick, R. S., Hudson, M. K., and Kress, B. T. (2010). Injection and loss of inner radiation belt protons during solar proton events and magnetic storms. Journal of Geophysical Research, 115.

[Sergeev, 1990] Sergeev, V. A. (1990). Polar cap and cusp boundaries at day and night. J. Geomag. Geoelectr., 42:683–695.

[Sergeev and Tsyganenko, 1982] Sergeev, V. A. and Tsyganenko, N. A. (1982). Energetic particle losses and trapping boundaries as deduced from calculations with a realistic magnetic field model. Planet. Space Sci., 30(10):999–1006.

[Shevchenko et al., 2010] Shevchenko, I. G., Sergeev, V., Kubyshkina, M., Angelopoulos, V., Glassmeier, K. H., and Singer, H. J. (2010). Estimation of magnetosphere-ionosphere mapping accuracy using isotropy boundary and themis observations. Journal of Geophysical Research, 115(A11206).

[Shore et al., 2016] Shore, R. M., Whaler, K. A., Macmillan, S., Beggan, C., Velímský, J., , and Olsen, N. (2016). Decadal period external magnetic field variations determined via eigenanalysis. J. Geophys. Res. Space Physics, 121:5172–5184.

[Smart and Shea, 1994] Smart, D. F. and Shea, M. A. (1994). Geomagnetic cutoffs: a review for space dosimetry applications. Advances in Space Research, 14(10):1994.

[Smart and Shea, 2005] Smart, D. F. and Shea, M. A. (2005). A review of geomagnetic cutoff rigidities for earth-orbiting spacecraft. Advances in Space Research, 36:2012–2020.

[SP., 1962] SP., N. (1962). Astronomy and Space Sciences, volume 404. Scientific and Technical Information Office, NASA.

[Stasiewicz, 1991] Stasiewicz, K. (1991). Polar cusp topology and position as a function of interplanetary magnetic field and magnetic activity: Comparison of a model with Viking and other observations. Journal of Geophysical Research, 96(A9):15789–15800.

[Stassinopoulos et al., 2015] Stassinopoulos, E. G., Xapsos, M. A., and Stauffer, C. A. (2015). Forty-Year "Drift" and Change of the SAA. NASA Technical Memorandum, 217547(December 2015):78.

[Stauning et al., 2008] Stauning, P., Troshichev, O., and Janzhura, A. (2008). The Polar Cap (PC) indices: Relations to solar wind parameters and global magnetic activity. Journal of Atmospheric and Solar-Terrestrial Physics, 70:2246–2261.

[Stern, 1975] Stern, D. P. (1975). The motion of a proton in the equatorial magnetosphere. Journal of Geophysical Research, 80(4):595–599.

[Stoer and Bulirsch, 1980] Stoer, J. and Bulirsch, R. (1980). Introduction to Numerical Analysis. Springer-Verlag Berlin Heidelberg.

[Stubbs et al., 2004] Stubbs, T. J., Cargill, P. J., Lockwood, M., Grande, M., Kellett, B. J., and Perry, C. H. (2004). Extended cusp-like regions and their dependence on the polar orbit, seasonal variations and interplanetary conditions. Journal of Geophysical Research, 109(A09210).

[Sturrock, 1994] Sturrock, P. (1994). Plasma Physics: An Introduction to the Theory of Astrophysical, Geophysical and Laboratory Plasmas, chapter 4, page 47. Cambridge University Press.

[Suparta et al., 2017] Suparta, W., Gusrizal, Karel, K., and Isa, Z. (2017). A hierarchical Bayesian spatio-temporal model to forecast trapped particle fluxes over the SAA region. Terr. Atmos. Ocean. Sci., 28(3):357–370.

[Takagi et al., 1993] Takagi, S., Nakamura, T., Kohno, T., Shiono, N., and Makino, F. (1993). Observation of Space Radiation Environment with EXOS-D. IEEE Transactions on Nuclear Science, 40(6):1491–1497.

[Tao et al., 2007] Tao, X., Chan, A. A., and Brizard, A. J. (2007). Hamiltonian theory of adiabatic motion of relativistic charged particles. Physics of Plasmas, 14(9):1–20.

[Terra-Nova et al., 2017] Terra-Nova, F., Amit, H., A. Hartmann, G., I.F. Trindade, R., and J. Pinheiro, K. (2017). Relating the South Atlantic Anomaly and geomagnetic flux patches. Physics of the Earth and Planetary Interiors, 266:39–53.

[Thébault et al., 2015] Thébault, E., C Finlay, C., D Beggan, C., and Alken, P. (2015). International Geomagnetic Reference Field: the 12th generation. Earth, Planets and Space, page 67:79.

[Toggweiler, 2011] Toggweiler, M. (2011). An adaptive time integration method for more efficientsimulation of particle accelerators. Master's thesis, Swiss Federal Institute of Technology in Zurich (ETH).

[Tsyganenko, 1979] Tsyganenko, N. A. (1979). Subroutines and tables for calculation of the geomagnetic field. WDC-B2 issue.

[Tsyganenko, 1989] Tsyganenko, N. A. (1989). A magnetospheric magnetic field model with awarped tail current sheet. Planet. Space Sci., 37:5–20.

[Tsyganenko, 1995] Tsyganenko, N. A. (1995). Modeling the earth's magnetospheric magnetic field confined within a realistic magnetopause. Journal of Geophysical Research.

[Tsyganenko, 1996] Tsyganenko, N. A., editor (1996). Effects of the solar wind conditions in the global magnetospheric configurations as deduced from data-based field models. European Space Agency, International Conference on Substorms, Proceedings of the 3rd International Conference.

[Tsyganenko, 2002a] Tsyganenko, N. A. (2002a). A model of the near magnetosphere with a dawn-dusk asymmetry 1. Mathematical structure. Journal of Geophysical Research: Space Physics, 107.

[Tsyganenko, 2002b] Tsyganenko, N. A. (2002b). A model of the near magnetosphere with a dawn-dusk asymmetry 2. Parameterization and fitting to observations. Journal of Geophysical Research: Space Physics, 107.

[Tsyganenko, 2013] Tsyganenko, N. A. (2013). Data-based modelling of the earth's dynamic magnetosphere: a review. Annales Geophysicae, 31:1745–1772.

[Tsyganenko and Sitnov, 2005] Tsyganenko, N. A. and Sitnov, M. I. (2005). Modeling the dynamics of the inner magnetosphere during strong geomagnetic storms. Journal of Geophysical Research: Space Physics, 110.

[Ukhorskiy et al., 2006] Ukhorskiy, A. Y., Anderson, B. J., Takahashi, K., and Tsyganenko, N. A. (2006). Impact of ULF oscillations in solar wind dynamic pressure on the outer radiation belt electrons. Geophysical Research Letters, 33(6):2–5.

[Ukhorskiy and Sitnov, 2013] Ukhorskiy, A. Y. and Sitnov, M. I. (2013). Dynamics of radiation belt particles. Space Science Reviews, 179:545–578.

[Underwood et al., 1993] Underwood, C. I., Ecoffet, R., Duzellier, S., and Faguere, D. (1993). Observations of single-event upset and multiple-bit upset in non-hardened high-density srams in the TOPEX/Poseidon orbit. IEEE Radiation Effects Data Workshop, pages 85–92.

[Volland, 1973] Volland, H. (1973). A Semiempirical Model of Large-Scale Magnetospheric Electric Fields. Journal of Geophysical Research, 78(1):171–180.

[Walt, 2005] Walt, M. (2005). Introduction to Geomagnetically Trapped Radiation, chapter 4, page 47. Cambridge University Press.

[Weimer, 1995] Weimer, D. R. (1995). Models of high-latitude electric potentials derived with a least error fit of spherical harmonic coefficients. Journal of Geophysical Research, 100(A10):19595.

[Weimer, 2005] Weimer, D. R. (2005). Improved ionospheric electrodynamic models and application to calculating Joule heating rates. Journal of Geophysical Research: Space Physics, 110(A5):1–21.

[Weiss et al., 1997] Weiss, L. A., Thomsen, M. F., D., R. G., and McComas, D. J. (1997). An examination of the tsyganenko (t89a) field model using a database of two-satellite magnetic conjunctions. Journal of Geophysical Research, 102(A3):4911–4918.

[Ye et al., 2017] Ye, Y., Zou, H., Zong, Q., Chen, H., Wang, Y., Yu, X., and Shi, W. (2017). The secular variation of the center of geomagnetic South Atlantic Anomaly and its effect on the distribution of inner radiation belt particles. Space Weather, 15.

[Yu et al., 2017] Yu, Y., Jordanova, V. K., Ridley, A. J., Toth, G., and Heelis, R. (2017). Effects of electric field methods on modeling the midlatitude ionospheric electrodynamics and inner magnetosphere dynamics. Journal of Geophysical Research: Space Physics, 122(5):5321–5338.

[Zou et al., 2015] Zou, H., Li, C., Zong, Q., Parks, G. K., Pu, Z., Chen, H., Xie, L., and Zhang, X. (2015). Short-term variations of the inner radiation belt in the South Atlantic Anomaly. Journal of Geophysical Research: Space Physics.

[Zou et al., 2011] Zou, H., Zong, Q. G., Parks, G. K., Pu, Z. Y., Chen, H. F., and Xie, L. (2011). Response of high-energy protons of the inner radiation belt to large magnetic storms. Journal of Geophysical Research, 116.